Multicomponent, Multiphase Thermodynamics with Interfacial Curvature

by

Nadia Shardt

A thesis submitted in partial fulfillment of the requirements for the degree of

Doctor of Philosophy

in

Chemical Engineering

Department of Chemical and Materials Engineering

University of Alberta

© Nadia Shardt, 2019

Abstract

The interface between two phases—for example, a liquid and a vapor phase—influences the properties of the phases it separates. When the interface is flat, the phase properties of both single- and multicomponent systems can be reliably predicted by applying well-established thermodynamic principles. When the interface is curved, phase properties change according to the extent of the curvature, and this curvature-dependent effect has been studied extensively in single-component systems. This thesis investigates the intersection where multicomponent, multiphase systems contain interfacial curvature. Contributions are made to three questions at this intersection: (1) how does the surface tension of a multicomponent mixture vary as a function of composition and temperature? (2) how does the vapor–liquid phase diagram of a multicomponent system change when there is a curved interface between the vapor and liquid phases? and (3) how does the contact angle of a liquid drop change when it is on a chemically heterogeneous or physically rough solid phase compared to a homogeneous, smooth solid? Considering the first question, a new equation is developed to predict the surface tension of multicomponent liquid mixtures, and it is validated against experimental data for a wide range of temperatures, pressures, and mixture types (those containing one supercritical compound (*e.g.*, carbon dioxide) and those containing two subcritical compounds (*e.g.* organic and aqueous mixtures)). In pursuing the second and third questions, the postulates of Gibbsian composite-system thermodynamics—a mathematical framework that describes relationships between energy and the properties of matter—are applied to each studied system. For calculating the phase diagrams of multicomponent systems with nanoscale interfacial curvature, an activity-coefficient model is developed and applied to both ideal and nonideal systems; the newly-

developed surface tension model is incorporated into this system of equations. For describing contact angle, a rigorous mathematical approach is presented, which demonstrates that the properties at the circumference of the liquid drop determine the contact angle—that is, a line fraction for a chemically heterogeneous surface and a line roughness for a physically rough surface. As a whole, this thesis develops fundamental mathematical equations to quantify the effect of interfacial curvature on the properties of multicomponent, multiphase systems for use in the multitude of applications where curved interfaces are present, such as atmospheric physics, medicine, catalysis, and soft matter nanotechnology.

Preface

Chapters 2 to 7 of this thesis have been published or have been submitted for publication. I performed all research under the direction and supervision of J. A. W. Elliott.

Chapter 2 of this thesis has been published, with minor modifications, as N. Shardt and J. A. W. Elliott. "A Model for the Surface Tension of Dilute and Concentrated Binary Aqueous Mixtures as a Function of Composition and Temperature". *Langmuir* 33 (2017), pp. 11077–11085. http://pubs.acs.org/articlesonrequest/AOR-NkAqpDtYAHIVUiaXdP6d Copyright 2017 American Chemical Society.

Chapter 3 and Appendix A of this thesis have been submitted for publication as N. Shardt, Y. Wang, Z. Jin, and J. A. W. Elliott. "Surface Tension as a Function of Temperature and Composition for a Broad Range of Mixtures". I performed all research and composed the first draft of this chapter under the direction and supervision of J. A. W. Elliott. Y. Wang and Z. Jin provided motivation for this work and gave assistance with Peng–Robinson equation of state phase equilibrium calculations for hydrocarbon mixtures. All authors contributed to the version of the chapter presented in this thesis. In performing this research, I received advice from Dr. J. M. Shaw on the critical composition of multicomponent mixtures and assistance from Dr. A. Komrakova in translating Kharin *et al.* [140].

Chapter 4 of this thesis has been published, with minor modifications, as N. Shardt and J. A. W. Elliott. "Thermodynamic Study of the Role of Interface Curvature on Multicomponent Vapor–Liquid Phase Equilibrium". *Journal of Physical Chemistry A* 120.14 (2016), pp. 2194–2200. http://pubs.acs.org/articlesonrequest/AOR-Kgv8I2tpBEfqdH9e5aKX Copyright 2016 American Chemical Society. J. A. W. Elliott conceived the original idea.

Chapter 5 of this thesis has been published, with minor modifications, as N. Shardt and J. A. W. Elliott. "Isobaric Vapor–Liquid Phase Diagrams for Multicomponent Systems with Nanoscale Radii of Curvature". *Journal of Physical Chemistry B* 122.8 (2018), pp. 2434–2447. https://pubs.acs.org/articlesonrequest/AOR-TvK85VGmsbiNcqZRPZrx Copyright 2018 American Chemical Society. In performing this research, some recent literature was brought to our attention by Dr. William R. Smith of the University of Guelph.

Chapter 6 of this thesis has been published, with minor modifications, as N. Shardt and J. A. W. Elliott. "Gibbsian Thermodynamics of Cassie–Baxter Wetting (Were Cassie and Baxter Wrong? Revisited)". *Langmuir* 34.40 (2018), pp. 12191–12198. https://pubs.acs.org/articlesonrequest/AOR-tif5N8X82K2tVuR94pTk Copyright 2018 American Chemical Society. J. A. W. Elliott conceived the original idea. In performing this research, I had valuable discussions with Leila Zargarzadeh, who shared pertinent literature, and the anonymous reviewers brought additional literature to our attention.

Chapter 7 of this thesis has been submitted for publication as N. Shardt and J. A. W. Elliott. "Gibbsian Thermodynamics of Wenzel Wetting (Was Wenzel Wrong? Revisited)". In performing this research, I had a valuable discussion with Dr. Orest Shardt on the expression for solid–liquid interfacial area.

To my family

Acknowledgments

To Dr. Janet Elliott, thank you for your boundless enthusiasm and generous guidance of my academic and professional development. Your commitment to mentoring, supervising, and teaching is inspiring.

To Drs. John Shaw and Jason Olfert, thank you for your help and continuous support throughout the course of this thesis as members of my supervisory committee.

To Drs. Martin Trusler, Mohtada Sadrzadeh, and Tony Yeung, thank you for your time in reading my work and willingness to be part of my examining committee.

To Drs. William R. Smith, Leila Zargarzadeh, and Alexandra Komrakova, thank you for our helpful and motivational conversations.

To Dr. Zhehui Jin, Yingnan Wang, Dr. Peichun Amy Tsai, and Masoud Bigdeli, thank you for our stimulating discussions and collaborations.

To all past and present members of the Elliott, McGann, and Jomha research groups I have been lucky to get to know, thank you for sharing your knowledge, advice, and passion.

To all undergraduate and graduate students, postdoctoral researchers, faculty, and administrative staff I have had the pleasure of meeting or working with, thank you for enriching my graduate school experience.

To the Natural Sciences and Engineering Research Council of Canada (NSERC), Alberta Innovates and Alberta Advanced Education, and the University of Alberta, thank you for your financial support of this thesis.

Table of Contents

List of Figures

List of Tables

List of Symbols

Acronyms

AAD	Average absolute deviation
CI	Confidence interval
MW	Molar weight
PR-EOS	Peng–Robinson equation of state
SD	Standard deviation
SSE	Sum of squared errors
TSS	Total sum of squared deviations from the mean
VLE	Vapor–liquid equilibrium

Constants

R	Universal gas constant

Greek Symbols

α, β	Fitting parameters for the Li et al. [56] surface tension model
α_i, β_i	Fitting coefficients for surface tension *vs.* temperature of pure component i
β	Vapor fraction
χ	Empirical parameter for the volume shift parameter correlation by Ahlers and Gmehling [3]
γ_i	Activity coefficient of component i
κ	Parameter in the Peng–Robinson equation of state

λ, λ_i	Line fraction at a radius along the bottom of a drop's spherical cap; line fraction of solid i
Λ_{21}	Dimensionless parameter for the Li et al. [56] surface tension model
μ_i^j, μ_i^{jk}	Chemical potential of component i in bulk simple system j or interfacial system jk
ω	Acentric factor
ϕ_i	Fugacity coefficient of component i
ψ_i	Angle of a tangent line to the solid at an intersection point
ρ	Line roughness, defined in Equation (7.41)
σ, $\hat{\sigma}_i$, $\bar{\sigma}$	Surface tension; predicted surface tension; mean surface tension
σ^{ij}	Interfacial tension between phase i and j
H	Dimensionless quantity defined as $h\lambda_{\text{liquid}}/R$
θ	Contact angle
$\theta_{0,i}$, $\theta_{1,i}$	Fitting parameters used in a linear equation for surface tension of component i
$\theta_{j,i}$, p_i	Empirical parameters for each order j of a p_i degree polynomial for component i describing surface tension
ε	Tolerance for relative error
φ_i	Angle of the ith intersection between a liquid drop and a pillar side
ζ	Integral number of pillar sides at a radius along the bottom of a drop's spherical cap

Latin Symbols

ΔF_{s}	Free energy change for the Shereshefsky [257] surface tension model
ℓ	Length of a line
$\mathscr{P}_i$	Parachor of pure component i
A	Surface area per mole for the Li et al. [56] surface tension model

a	Radius of the bottom of a drop's spherical cap; $a = R\sin\theta$
A, B	Parameters in the Peng–Robinson equation of state
a, b	Fitting parameters for our new model of surface tension and for the Connors–Wright [63] surface tension model
a^{PR}, a_i^{PR}, a_{ij}^{PR}	Parameters for the attractive term in the Peng–Robinson equation of state for the system, pure component i, or two components i and j, respectively
A^{jk}	Area of the jk interface
A_i, B_i, C_i, D_i, E_i	Empirical parameters for an extended Antoine equation
a_i, b_i, c_i, and n_i	Empirical parameters for a generalized Rackett equation
A_{12}, A_{21}	Empirical constants for use in the Margules activity coefficient model
a_{ji}, b_{ji}	Fitting coefficients for a binary mixture made up of components j and i where $\sigma_j > \sigma_i$
B	Free energy
b^{PR}, b_i^{PR}	Parameters for the repulsive term in the Peng–Robinson equation of state for the system or pure component i, respectively
C	Proportionality constant
c	Volume shift parameter
d, d_s	Relative percent deviation; average relative percent deviation
f	Arbitrary function
f_i	Area fraction of component i on a solid surface ($A_i/A^{\mathrm{projected}}$) in Part III; fugacity of component i in Appendix A
h	Height of a pillar
j	Number of data points
k	Number of components in Chapter 5; collection of three terms in Equation (7.42)
K_i	Equilibrium ratio between vapor and liquid mole fractions of component i

k_{ij}	Binary interaction coefficient for the Peng–Robinson equation of state
L	Length of the contact line that is solid or liquid
m	Number of components in the reservoir
$m(r)$	Sum of all orientation factors m_i at a radius r
m_i	Number of terms in the Mulero et al. [196] correlation in Part I; orientation factor at the ith intersection of a pillar side in Part III
n	Number of points used for fitting, number of solid phases, number of components, or number of accurate significant figures
N_i^j, N_i^{jk}	Number of moles of component i in bulk simple system j or interfacial system jk
p	Number of parameters
P^j	Pressure of bulk simple system j
R	Radius of curvature of the liquid drop in Part III
r	Radius of curvature in Part II; radius along the bottom of a drop's spherical cap in Part III
R^2	Coefficient of determination
R_1, R_2	Principal radii of curvature
r_f	Roughness factor based on area; $A^\mathrm{SL}/A^\mathrm{projected}$
r_p	Pore radius
s	Arc length along the side of a pillar
S^j, S^{jk}	Entropy of bulk simple system j or interfacial system jk
T	Absolute temperature
T^j, T^{jk}	Absolute temperature of bulk simple system j or interfacial system jk
U^j, U^{jk}	Internal energy of bulk simple system j or interfacial system jk
v^PR	Molar volume as calculated by the Peng–Robinson equation of state

V^j	Volume of bulk simple system j
v_i^{L}	Molar liquid volume of pure component i
x_i	Liquid-phase mole fraction of component i; can also be vapor-phase mole fraction when used with the Peng–Robinson equation of state
$x_{i,\mathrm{cr}}$	Liquid-phase mole fraction of component i at the critical point
$x_{i,\mathrm{r}}$	Reduced mole fraction of component i in the liquid phase; equals $x_i/x_{i,\mathrm{cr}}$
$x_{i\mathrm{f}}$	Liquid-phase mole fraction of component i for a flat interface
y_i	Vapor-phase mole fraction of component i
Z	Compressibility factor
z_i	Overall system mole fraction of component i

Subscripts

i, j	An index for summation or related to the ith or jth component
0	Reference state; used with B and R
b	Bubble point; used with P and T
bf	Bubble point for a flat interface; used with P and T
CB	Cassie–Baxter; used with θ
cr	Critical; used with T, P, Z, and x_i
CW, ex-CW	Connors–Wright model and extended Connors–Wright model; used with σ
d	Dew point; used with P and T
df	Dew point for a flat interface; used with P and T
eq	Equilibrium state; used with R and θ
fit	Of a fit; used with T
liquid	Liquid; used with λ
lv	Liquid–vapor; used with f and θ

LWW	Li, Wang, and Wang [56] (or Li et al.) model, where a prefix of ex1- or ex2- refers to an extension of this model; used with σ
max, min	Maximum and minimum, respectively; used with T
mix	Mixture; used with σ
ref	Reference point; used with T
S	Shereshefsky [257] model, where a prefix of ex1- or ex2- refers to an extension of this model; used with σ
sl	Solid–liquid; used with f
solid	Solid; used with λ
W	Wenzel; used with θ
Y	Young; used with θ

Superscripts

L	Liquid phase; used with S, T, U, P, V, μ, N, L, r, and v
LV	Liquid–vapor interface; used with S, T, U, σ, A, μ, and N
projected	Projected quantity; used with ℓ and A
R	Reservoir; used with S, T, U, P, V, μ, and N
SL, S_iL	Solid–liquid interface; ith solid–liquid interface; used with S, T, U, σ, A, μ, and N
SLV	Solid–liquid–vapor; used with ℓ
S, S_i	Solid phase and solid phase i; used with S, T, U, P, V, μ, and N
SV, S_iV	Solid–vapor interface; ith solid–vapor interface; used with S, T, U, σ, A, μ, and N
V	Vapor phase; used with S, T, U, P, V, μ, N, r, and v
cap	Spherical cap; used with A
sat	At saturated conditions with a flat interface between phases; used with P to denote the saturated vapor pressure

Chapter 1

Introduction

I would like to start by emphasizing the importance of surfaces.

Walter Houser Brattain
Nobel Laureate in Physics

The physical world can be roughly categorized into macroscopic phases of matter: solids, liquids, and gases. When, for example, a liquid and a vapor phase coexist, each phase is described by a set of properties, such as pressure and density, and there is a region between these phases with a density that varies as a function of location. This region can be conceptualized as a two-dimensional mathematical entity that separates the two phases—an interface—with a surface area (but no thickness or volume) and a characteristic property called interfacial tension (analogous to the pressure that is associated with a phase). Around two centuries ago, the significance of interfacial tension became apparent through the work of scientists such as Thomas Young [321], Agnes Pockels [218], and Josiah Willard Gibbs [108]. The importance of interfacial tension has not diminished in the intervening years, but rather it has grown, particularly in light of (*i*) emerging technologies that rely on, or are governed by, interfacial forces and (*ii*) our increased awareness of natural processes that are also dictated by interfacial tension. Interfacial science is the study of any system or process where interfaces play an important role.

One specific topic of interest within interfacial science is the effect of a curved interface on the behavior and properties of the phases it separates. In many natural and industrial environments, the interface between two phases is flat, and as a consequence of this, the pressure in one phase is equal to the pressure in the other. However, when a curved interface is present—such as for a bubble of vapor or a droplet of liquid—the pressures in each phase are no longer

equal. As described by the Young–Laplace equation, the difference in pressures is proportional to the interfacial tension and inversely proportional to the radius of curvature (*e.g.*, the radius of a spherical bubble), so that the effect of curvature becomes increasingly relevant as the curvature of the interface becomes more extreme. That is, as the radius of curvature approaches the nanoscale, the behavior and properties of the phases in the system will deviate from those expected if a flat interface were instead present. For example, the boiling temperature of water is 100°C at a pressure of 101 kPa when there is a flat interface between the vapor and liquid phases. If a droplet of water has a radius of 10 nm, its boiling point is lower—96°C—when it is in a surrounding vapor phase at the same pressure of 101 kPa [70]. For the same reason, a vapor bubble with a highly curved interface will condense at a temperature higher than the condensation temperature of a flat vapor phase. Solid porous structures such as capillaries facilitate the creation of a curved liquid–vapor interface, leading to a phenomenon known as capillary condensation. With the addition of a solid phase, solid–liquid and solid–vapor interfaces are created, and the curvature of the liquid–vapor interface is influenced by the magnitudes of the interfacial tensions associated with these new interfaces.

Another area of interest in interfacial science is the interaction between fluids and solids and its impact on interfacial curvature. For instance, will a liquid spread out on and completely wet a particular solid, or will it adopt a spherical shape and not wet the surface at all? The wetting behavior of a liquid on a certain solid phase is characterized by a contact angle measured through the liquid at the location where the liquid–vapor interface touches the solid, where a contact angle of 0° corresponds to a perfectly wetting liquid and a contact angle of 180° corresponds to a perfectly non-wetting liquid for that solid. Generally, the chemical and physical properties of each phase influence the resultant contact angle, and by manipulating these properties, desired contact angles can be attained. A common method of controlling wetting behavior is to introduce roughness to the solid substrate. By doing so, the liquid may either rest on top of the rough features with trapped pockets of air or it may completely fill the surface with no air entrapment. The level of roughness can be tuned to achieve the preferred state of wetting and corresponding contact angle. For example, a liquid-repellent material with high contact angles is desirable for waterproof food packaging [296], nonstick coatings, and concrete with anti-icing and anti-corrosion properties [267]. In other circumstances, the liquid should preferentially wet a surface, such as in painting, ink-jet printing, and cosmetics.

Specific fields where interfacial curvature between two or three phases is pertinent include atmospheric science [164, 246], hydrocarbon extraction [88, 97, 295], and catalysis [24, 209, 308], among others. Cloud microphysics aims to describe how cloud droplets form, followed by growth mechanisms such as condensation and coalescence. Condensation generally occurs on atmospheric nuclei with highly curved surfaces. Depending on the chemistry and size of

these nuclei, water condensation or evaporation may occur. On a slightly larger scale, the concentration of nuclei influences the equilibrium number of water droplets and the size of these droplets, which in turn, determine the size and lifetime of clouds. The size of these clouds can affect both local and global weather patterns. In the subsurface of the Earth, porous media span the micro- and mesoporous scale (0.2–2 nm and 2–50 nm) [232], and hydrocarbon recovery operations are dependent on the accurate prediction of vapor–liquid equilibrium in these underground formations [88, 97, 295]. With average pore throat diameters down to 10 nm [178], shale reservoirs significantly alter the phase behavior of the fluids they contain (*e.g.*, whether the fluid is a gas, a liquid, or split into one liquid and one vapor phase). In catalysis, certain pore sizes and structures can induce capillary condensation within the catalyst, leading to changes in the reaction rate and conversion [24, 209, 308]. Capillary condensation may also affect the rate of catalyst deactivation [14, 39, 40]. Emerging technologies such as micro- and nanofluidics have been used to probe the nanoscale, together with established tools such as atomic force microscopy [29] and the surface forces apparatus [149]. At these nanoscale dimensions, surface forces arising from interfacial tension dominate the behavior of fluids compared to gravitational or inertial forces. It is vital to understand and control nanoscale processes so that these tools can be designed to achieve desirable effects—such as encapsulating one medium in another medium or separating these media—for application in medicine (diagnosis [162] and drug delivery [75]), molecular biology [125], water filtration [261], and nanoreactor chemistry [309].

In each of these environments and applications from atmospheric science to nanofluidics, multiple phases coexist, and often, one or more of the phases contain multiple components. A theoretical framework for understanding the behavior of multicomponent, multiphase systems is well-established in chemical engineering, and numerous mathematical tools for prediction and design have been developed, but this fundamental knowledge has been developed extensively for systems with flat interfaces. On the other hand, our theoretical understanding of interfacial tension on phase behavior has often focused on single-component systems. In recent decades, research has begun to bridge these theoretical descriptions, motivated by the variety of systems and processes consisting of several components separated by curved interfaces that often require interdisciplinary understanding.

How can we understand, predict, and control processes and systems that contain multiple phases, multiple components, and curved interfaces? Thermodynamics provides such a framework. It is a set of mathematical relationships that describes the properties of matter and how energy can be transformed. Through these relationships, thermodynamics can be used to predict whether a process can occur, and if it does occur, how the properties of matter will change when subjected to the defined constraints of the process. This thesis applies thermodynamics—more specifically, Gibbsian composite-system thermodynamics—to two types of multiphase, mul-

ticomponent systems with interfacial curvature: (*i*) two-phase vapor–liquid systems and (*ii*) three-phase solid–liquid–vapor systems. This thesis lies at the intersection of multicomponent, multiphase thermodynamics and interfacial thermodynamics, and it will bring researchers in both fields to a more complete understanding of thermodynamics as a whole.

1.1 Gibbsian Composite-System Thermodynamics

Over the 19th century, the field of thermodynamics materialized into a set of laws that govern matter and energy. Near the end of the century, Gibbs pioneered a comprehensive mathematical blueprint for thermodynamics and how it relates a system's thermal, mechanical, and chemical properties with transfers of energy, while also placing limitations on spontaneous processes [108]. Out of the Gibbsian blueprint presented in *On the Equilibrium of Heterogeneous Substances* [108], Callen [46] communicated a postulatory approach for thermodynamics as an alternative to the historical presentation of the 1st, 2nd, and 3rd laws of thermodynamics.

In thermodynamics, a **system** is any collection of matter that is being investigated, and it is contained within a defined system boundary. Usually, the system interacts with a **reservoir**, which is a collection of matter that is located outside the system boundary. An *open system* can exchange matter and energy with the surrounding reservoir, while a *closed system* can only exchange energy. An *isolated system* is one whose boundary does not permit mass or energy transfer with the reservoir. The **state** of a system can be defined as the unique aggregate of its properties, including—but not limited to—temperature, pressure, and volume. If a property does not change with the amount of matter in the system, then that property is **intensive** (*e.g.*, temperature and pressure). A property that changes with the amount of matter in the system is **extensive** (*e.g.*, volume, internal energy, and number of moles). If an isolated system is in a state where its macroscopic properties do not change over a prolonged period of time, then it is in a stable **equilibrium state**—one goal of thermodynamics is determining the properties of systems in their stable equilibrium state(s).

Gibbs established several additional concepts. First, a **simple system** is a collection of matter that is homogeneous, isotropic, uncharged, and not under the influence of external fields, such as gravity or electromagnetism [46, 108]. A **composite system** is a group of simple systems. If each simple system in a composite system is in an equilibrium state and there is no net transfer of matter or energy between the simple systems, then the composite system is in an equilibrium state. This concept of a composite system is particularly useful for analyzing systems with multiple phases and interfaces that can each be a simple system.

Next, to include the interfacial region in the mathematical framework of thermodynamics, Gibbs accounted for the variation in density and composition between phases by describing

such a system as two phases with constant properties (*e.g.*, density, composition, and internal energy) and an interface with its own set of properties (*e.g.*, surface area, composition, and internal energy). For a flat interface, the mathematical interface is placed in such a way that the number of moles of one of the constituent components are completely accounted for by the bulk phases. All other components in the system are assigned some number of moles that belong to a "surface excess" in the interface, which may be a positive or negative value. This choice of interfacial placement where one component has a surface excess of zero is known as the **Gibbs dividing surface approach**. For a curved interface, the mathematical interface is placed so that the interfacial tension does not depend on the curvature of the interface, and as a result, each component is present in the interface with a nonzero surface excess. This approach for curved interfaces where all components have a nonzero number of moles in the interface is known as the **Gibbs surface of tension approach**.

The postulates of thermodynamics, as described by Callen are [46]:

I. A simple system in an equilibrium state is completely defined by the internal energy U, volume V for a bulk phase or area A for an interface, and mole numbers $N_1, N_2, \ldots, N_n$, where n is the number of components.

II. A quantity called entropy S is a function of the extensive properties of any composite system. Entropy is defined for all equilibrium states. In the absence of internal constraints, a stable equilibrium state is one where entropy is maximized compared to all other equilibrium states.

III. The entropy of a composite system is additive over its subsystems. Entropy is a continuous, differentiable, and monotonically increasing function of internal energy.

IV. At a temperature of 0 K, the entropy of a system is zero (if the system is a pure crystal [121]).

As a consequence of postulates I–III, the following fundamental thermodynamic equation applies to every bulk simple system j:

$$\mathrm{d}U^j = T^j\,\mathrm{d}S^j - P^j\,\mathrm{d}V^j + \sum_{i=1}^{n} \mu_i^j\,\mathrm{d}N_i^j, \tag{1.1}$$

where T is absolute temperature and μ_i is the chemical potential of component i. Each of T, P, and μ_i are intensive properties, while U, S, V, and N_i are extensive.

For the interface between simple bulk systems j and k, the fundamental equation has the

following form for a flat interface according to the Gibbs dividing surface approach:

$$\mathrm{d}U^{jk} = T^{jk}\,\mathrm{d}S^{jk} + \sigma^{jk}\,\mathrm{d}A^{jk} + \sum_{i=2}^{n} \mu_i^{jk}\,\mathrm{d}N_i^{jk}, \tag{1.2}$$

and the following form for a curved interface according to the Gibbs surface of tension approach:

$$\mathrm{d}U^{jk} = T^{jk}\,\mathrm{d}S^{jk} + \sigma^{jk}\,\mathrm{d}A^{jk} + \sum_{i=1}^{n} \mu_i^{jk}\,\mathrm{d}N_i^{jk}, \tag{1.3}$$

where σ^{jk} is the interfacial tension of the jk interface and A^{jk} is the area of the interface. The term *surface tension* is commonly used to refer to the interfacial tension of a liquid–vapor interface. For a pure liquid in equilibrium with its vapor, surface tension generally decreases with temperature. In systems with multiple components, surface tension varies as a function of both composition and temperature.

To identify and categorize stable equilibrium states, postulate II indicates that the entropy of a composite system must be at a maximum subject to the physical constraint that energy is constant. Given postulate III, this requirement is mathematically equivalent to minimizing energy subject to constant entropy. A state that has the global minimum in energy at constant entropy is categorized as a stable equilibrium state. If the state is in a local minimum in energy, it is a metastable equilibrium state. The third possibility is an unstable equilibrium state, which has a local or global maximum in energy. Depending on the trend in energy as a function of a variable of interest (such as volume), there may be an energy barrier between metastable/stable equilibrium states that the system will need to overcome before reaching a different metastable/stable equilibrium state. By virtue of Legendre transformations, the identification of equilibrium states can be done by defining a free energy that eliminates entropy from being an independent variable, and this free energy will also be extremized at an equilibrium state [46]. Thus, a recipe for thermodynamic analysis consists of the following steps: (*i*) defining the system, (*ii*) defining the constraints (physical or geometric), (*iii*) extremizing entropy subject to the defined constraints to solve for the equilibrium conditions, (*iv*) determining the free energy of the system, and (*v*) using the free energy, evaluating the stability of the equilibrium states.

1.1.1 Vapor–Liquid Phase Diagrams of Multicomponent Systems

Using the Gibbsian framework of thermodynamics, the equilibrium conditions for multicomponent systems can be determined. Phase diagrams summarize the expected composition, quantity, and state of matter for a given system at a certain temperature and pressure. For a pure substance, a phase diagram delineates the expected phase as a function of both temperature and pressure.

Another commonly varied system property is volume, and this extends the pure substance's phase diagram into three dimensions. For a binary mixture, a three-dimensional plot is needed to show the phase as a function of composition in addition to the temperature and pressure axes. Slices of such a 3D plot are typically taken at a specific temperature or pressure to illustrate the equilibrium phase as a function of mixture composition.

Given a constant system temperature, a qualitative phase diagram for an ideal binary liquid mixture is illustrated in Figure 1.1. Here, the system pressure is plotted as a function of composition where x_1 is the mole fraction of component 1 in the liquid phase and y_1 is the mole fraction of component 1 in the vapor phase. The overall composition of the mixture is denoted by z_1. Generally, the composition is in terms of the more volatile compound so that the vapor pressure at $x_1 = 1$ will be greater than the vapor pressure at $x_1 = 0$. For given z_1 values, the bubble line is the pressure at which the first bubble of vapor forms from a single liquid phase. The dew line is the pressure at which the first droplet of liquid forms from a single vapor phase. The shaded area enclosed by the bubble line and dew line is the two-phase region where a liquid phase and a vapor phase are in equilibrium. At any point within this phase envelope (for example, the '$\times$' at an overall composition of z_1 in Figure 1.1), a horizontal tie line can be drawn to determine the composition in each phase and the quantity of each phase using the lever rule based on the relative lengths of the line segments, as illustrated in Figure 1.1.

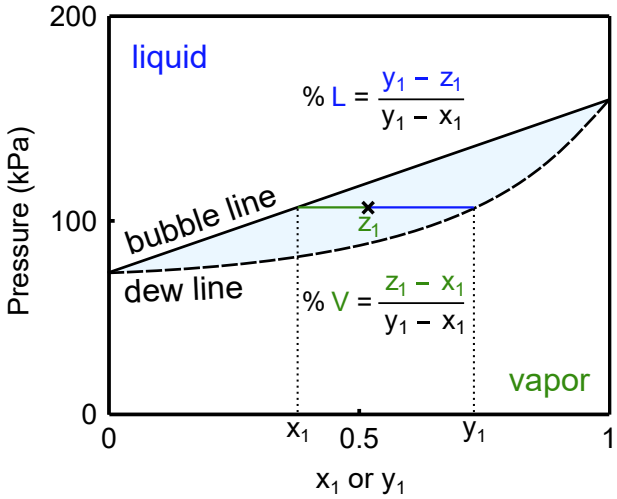

Figure 1.1: A qualitative isothermal phase diagram for an ideal binary mixture.

Figure 1.2 illustrates the phase diagram for an ethanol + water system and corresponding isothermal and isobaric slices. Figure 1.2(a) shows a surface plot with the complete dataset as a function of pressure, temperature, and composition (data taken from Ohe [208]). The shaded volume is the 3D depiction of the phase envelope where liquid and vapor phases coexist. Outside this region, there will be a single liquid phase at high pressures and low temperatures,

and there will be a single vapor phase at low pressures and high temperatures. Figure 1.2(b) shows five isothermal slices from the 3D phase envelope, and Figure 1.2(c) shows two isobaric slices. These isothermal and isobaric phase diagrams are most familiar to chemical engineers.

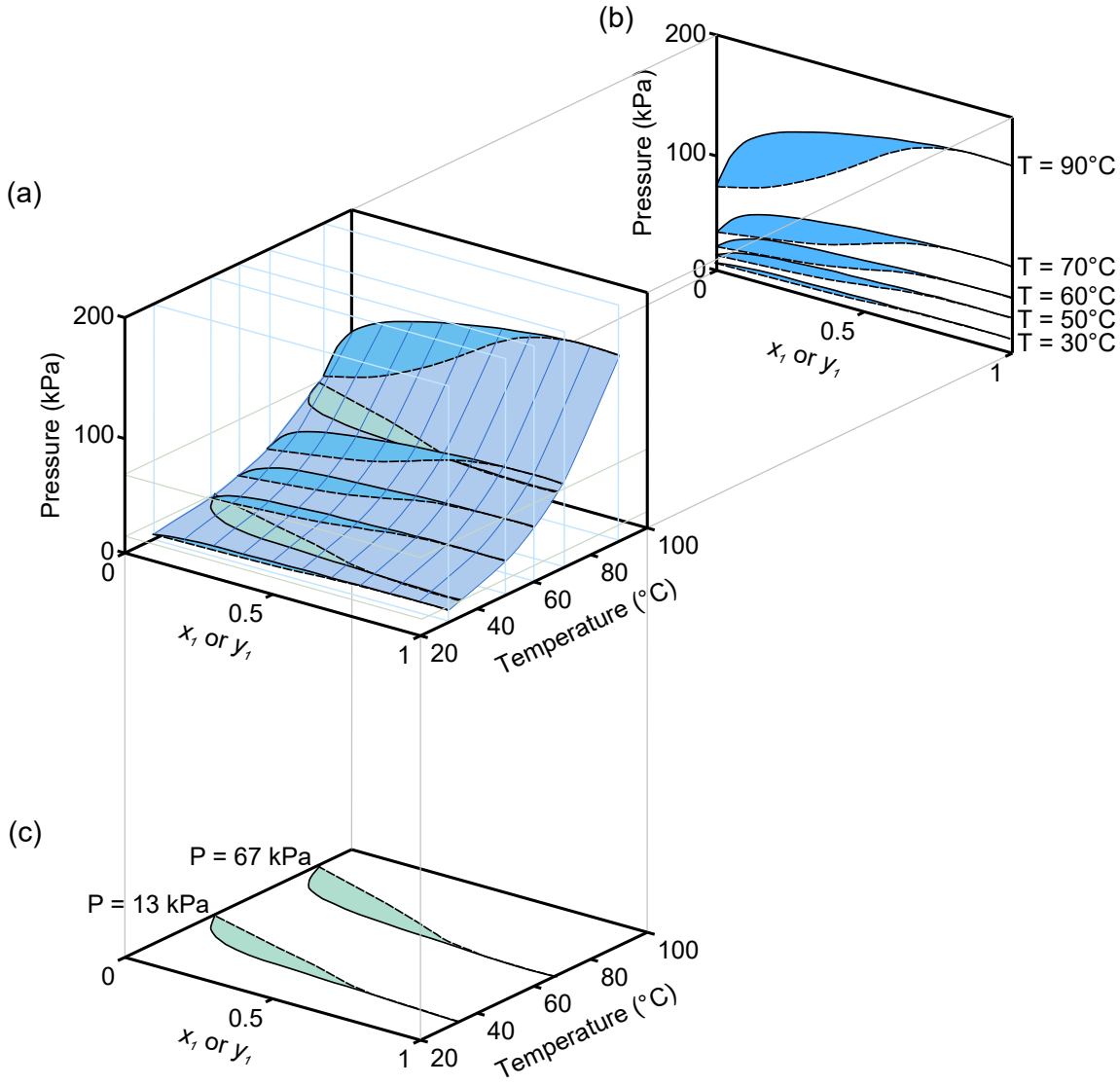

Figure 1.2: Phase diagram of ethanol + water. (a) The complete phase diagram as a function of temperature, pressure, and composition (data taken from Ohe [208]); (b) isothermal slices of the 3D phase envelope; and (c) isobaric slices of the 3D phase envelope.

The shape of the phase envelope is dictated by how different the strengths of the intermolecular bonds are between dissimilar molecules compared to similar molecules. The more similar these bonds are, the closer the mixture is to ideality. In Figure 1.2, it can be seen that the ethanol + water system exhibits nonideal behavior. An ideal system follows Raoult's Law, which states that the total vapor pressure in equilibrium with a liquid mixture is a simple

linear combination of mole fraction and saturation vapor pressure for each pure component in the mixture, as illustrated by the straight bubble line in Figure 1.1. This would give a planar shape for the upper surface of the 3D phase envelope, but the ethanol + water system shows a highly nonlinear shape due to the differences between water–water bonding, ethanol–ethanol bonding, and water–ethanol bonding. In fact, there is a certain mixture composition at which the ethanol + water system has a higher equilibrium bubble pressure than either of the individual components, or alternatively, it has a lower equilibrium bubble temperature. At this point, the composition in the liquid phase is equal to the composition in the vapor phase. This composition is termed the azeotrope, and conventional distillation past this point is not possible.

The illustrated data in Figure 1.2 were collected under the condition that there is a flat interface between the vapor and liquid phases. As a result, the pressure in the vapor phase is equal to that in the liquid phase, and this single pressure defines the system, as plotted along the vertical axis. When a curved interface is present, this convention cannot be followed because of the difference in pressure between the phases. For a flat interface at a constant temperature, the following established equations are used to calculate the bubble and dew pressures, $P_{\mathrm{b}}^{\mathrm{V}}$ and $P_{\mathrm{d}}^{\mathrm{V}}$ respectively, as given in thermodynamics textbooks [78, 266]:

$$P_{\mathrm{b}}^{\mathrm{V}} = \sum_i x_i \gamma_i P_i^{\mathrm{sat}} \exp\left(\frac{v_i^{\mathrm{L}} \left(P_{\mathrm{b}}^{\mathrm{V}} - P_i^{\mathrm{sat}} \right)}{RT} \right) \tag{1.4}$$

$$P_{\mathrm{d}}^{\mathrm{V}} = \left(\sum_i \frac{y_i}{\gamma_i P_i^{\mathrm{sat}} \exp\left(\frac{v_i^{\mathrm{L}} \left(P_{\mathrm{d}}^{\mathrm{V}} - P_i^{\mathrm{sat}} \right)}{RT} \right)} \right)^{-1}, \tag{1.5}$$

where x_i and y_i are the liquid mole fraction and vapor mole fraction of component i, γ_i is the activity coefficient of each component, P_i^{sat} is the saturation vapor pressure of each component, v_i^{L} is the liquid molar volume of pure component i, R is the universal gas constant, and T is the absolute temperature. Equations (1.4) and (1.5) can be derived from the conditions for equilibrium obtained *via* Gibbsian composite-system thermodynamics for a flat vapor–liquid interface, including the equality of chemical potential for each component and the equality of temperature and pressure between all phases. The exponential factor in Equations (1.4) and (1.5) is known as the Poynting correction [222, 305], and at low pressures and high temperatures, this factor becomes unity. For an ideal system, the activity coefficients will be equal to 1, whereas for a nonideal binary system, they can be modeled by, for example, the following Margules

equations [266]

$$\ln(\gamma_1) = x_2^2 \left[A_{12} + 2(A_{21} - A_{12})x_1\right] \tag{1.6a}$$

$$\ln(\gamma_2) = x_1^2 \left[A_{21} + 2(A_{12} - A_{21})x_2\right], \tag{1.6b}$$

where A_{12} and A_{21} are empirical constants for a given system under either isothermal or isobaric conditions at a specific temperature or pressure, respectively.

1.1.2 Single-Component Systems with Interfacial Curvature: The Kelvin Equation

When there is a curved interface between a vapor and a liquid phase, the Young–Laplace equation describes the relationship between pressure and the radius of curvature

$$P^{\mathrm{L}} - P^{\mathrm{V}} = \sigma\left(\frac{1}{R_1} + \frac{1}{R_2}\right), \tag{1.7}$$

where σ is the surface tension, and R_1 and R_2 are the two principal radii of curvature. For Equation (1.7) as written the radii of curvature are defined as positive when they are in the liquid (*e.g.*, for a droplet). Equation (1.7) can be derived from a mechanical force balance [26, p. 53], or it can be obtained as an equilibrium condition through the extremization of entropy using the Gibbsian approach [87].

For a pure liquid in equilibrium with its vapor, the Kelvin equation describes how a spherical vapor–liquid interface alters the vapor phase pressure [283]; it was later corrected by Gibbs to the following thermodynamically consistent form for a spherical interface *via* the equality of chemical potential in each phase combined with the Young–Laplace equation [77, 108]:

$$\frac{RT}{v^{\mathrm{L}}} \ln\left(\frac{P^{\mathrm{V}}}{P^{\mathrm{sat}}}\right) = \frac{2\sigma}{r} + \left(P^{\mathrm{V}} - P^{\mathrm{sat}}\right), \tag{1.8}$$

where P^{V} is the pressure in the vapor phase for a given interfacial radius of curvature r, P^{sat} is the saturated vapor pressure for a flat interface, and σ is the surface tension. The Kelvin equation (Equation (1.8)) is valid when the vapor phase can be treated as an ideal gas and the liquid phase is incompressible. Equation (1.8) is written such that in the case of a drop of liquid in a bulk vapor phase, the radius is a positive value, and thus the vapor pressure is greater than the vapor pressure in equilibrium with a flat interface. In contrast, for a bubble of vapor, the radius of curvature is negative, which means that the vapor pressure is lower than the flat-interface vapor pressure. Equation (1.8) has been experimentally verified by several researchers in a variety of

systems. Some highlights include verification for a cyclohexane system and an *n*-hexane system for radii as small as 4 nm between crossed mica cylinders [101], with a slight discrepancy for water between silica surfaces down to a 9-nm radius [99]. La Mer and Gruen studied solutions made up of one non-volatile and one volatile compound (dioctyl phthalate + toluene and oleic acid + chloroform) and also achieved close agreement with the Kelvin equation [154].

1.1.3 Wetting of Liquids on Smooth, Chemically Homogeneous Solids

While the previous section discussed two-phase systems with interfacial curvature, curved interfaces can also be found in three-phase systems, such as a solid–liquid–vapor system. The term wetting describes how the liquid phase interacts with the solid, and the angle that the liquid–vapor interface makes with a solid phase is defined to be the contact angle (θ). When the solid surface is physically smooth and chemically homogeneous and the liquid is in the shape of a spherical cap (in the absence of any external forces, including pinning and gravity), the contact angle is dictated by the Young equation [321]:

$$\cos\theta_{\mathrm{Y}} = \frac{\sigma^{\mathrm{SV}} - \sigma^{\mathrm{SL}}}{\sigma^{\mathrm{LV}}}, \tag{1.9}$$

where θ_{Y} is the Young contact angle and σ is the interfacial tension of the solid–vapor (SV), solid–liquid (SL), or liquid–vapor (LV) interfaces. Equation (1.9) has been derived by balancing mechanical forces [321], minimizing free energy under a constraint of constant liquid volume [43, pp. 144–147], and maximizing entropy subject to physical and geometric constraints using Gibbsian composite-system thermodynamics [87]. Each of these approaches concludes with Equation (1.9) being the condition for mechanical equilibrium.

1.2 Literature Review on Multicomponent Systems with Interfacial Curvature

In this thesis, three main topics are investigated. The subsequent sections provide an overview of the prior literature for each of these areas.

1.2.1 Surface Tension of Multicomponent Systems

Any model of vapor–liquid equilibrium that accounts for interfacial curvature between liquid and vapor phases must necessarily involve an accurate estimation of surface tension for substitution into the Young–Laplace equation. Models for the surface tension of multicomponent systems

can be broadly categorized into algebraic equations and differential equations. In the first category are the parachor model (Weinaug–Katz equation [302]) and a range of models derived out of thermodynamics (*e.g.*, the Shereshefsky model [257] and the Connors–Wright model [63]). In the second category, distributions of molecules through the interfacial region are calculated using statistical mechanics *via*, for example, density gradient theory [35, 64, 66] or density functional theory [144, 167, 175]. The parachor model and the statistical mechanics models require inputs of the density of each phase (vapor and liquid) and pure-component fitting parameters for predicting surface tension as a function of composition and temperature.

While the parachor model is straightforward to use, it is often inaccurate for mixtures over a wide range of temperatures and compositions [7, 170, 191, 216]. Although the statistical mechanics models are more accurate than the parachor model, they are limited by their time-consuming computational intensity [157] and occasional issues with convergence [167]. The algebraic thermodynamic models are both accurate and computationally simple, but they are only applicable for mixtures where all constituent compounds are below their individual critical points.

There is thus a need for the development of mathematical tools to describe multicomponent surface tension for a wide array of mixture types, compositions, and temperatures. This thesis proposes a new algebraic equation for the surface tension of multicomponent systems as a function of composition and temperature based on a minimal amount of experimental data. This new equation avoids the drawbacks of other approaches in the literature, namely inaccuracy, computational intensity, or requirement for subcriticality. It also does not require knowledge of liquid phase density at the composition and temperature of interest, an important benefit given the difficulty in accurately calculating this density.

1.2.2 Phase Diagrams of Multicomponent Systems with Interfacial Curvature

To describe the effect of interfacial curvature on a multicomponent system's pressure in the vapor phase, Defay and Prigogine [70] and Vehkmäki [292] derived a multicomponent version of the Kelvin equation assuming that the vapor phase is an ideal gas and the liquid phase is an ideal, incompressible mixture. Moving beyond the restrictions of ideality and incompressibility, recent approaches have combined equations of state with the Young–Laplace equation and the equality of chemical potential condition required at equilibrium using, for example, the Peng–Robinson equation of state [204] and the perturbed chain-statistical associating fluid theory (PC-SAFT) equation of state [278, 279]. In the model developed by Tan and Piri [278, 279], an adsorption layer was considered to be present for multicomponent vapor–liquid equilibrium in

porous media. To obtain the extent of this adsorption layer, their model was fit to experimental data of pure components, and the adsorption layer was fit to be a function of pore radius and temperature. An alternative method for modeling vapor–liquid equilibrium in pores is with a version of the Peng–Robinson equation of state modified to account for fluid–solid interactions by Travalloni *et al.* [285], also requiring fitting coefficients obtained from pure-component data.

However, the equations of state combined with the Young–Laplace equation may not always correctly predict the change in liquid-phase and vapor-phase composition, such as for the isothermal vapor–liquid equilibrium measurements of cyclohexane + fluorobenzene mixtures conducted by Brown [37]. When the Tan–Piri approach was applied with the Peng–Robinson equation of state, predictions indicated that compositions in the vapor and liquid phases were identical, but experimental measurements showed otherwise [37]. As also identified by Brown [37], there does not appear to be any model for predicting the effect of interfacial curvature for mixtures whose bulk vapor–liquid equilibrium behavior cannot be described by the Peng–Robinson or PC-SAFT equations of state.

In other words, there is an unmet need for an activity-coefficient phase equilibrium model for multicomponent systems with interfacial curvature. In this thesis, such a model is developed.

1.2.3 Contact Angles on Heterogeneous and Rough Surfaces

In Section 1.1.3, the Young equation was presented to describe the contact angle of a liquid on a smooth, chemically homogeneous solid, as shown in Figure 1.3(a). In reality, the solid surface can be any combination of (*i*) physically smooth or rough and (*ii*) chemically homogeneous or heterogeneous.

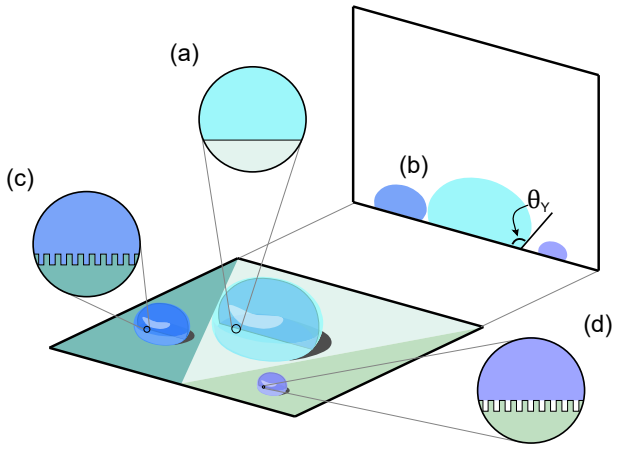

Figure 1.3: Illustration of the Young, Wenzel, and Cassie–Baxter wetting states. (a) Schematic diagram of a liquid droplet on a smooth surface with a contact angle θ_Y as illustrated in (b). Droplets on rough surfaces are shown in the (c) Wenzel and (d) Cassie–Baxter states of wetting.

When the solid is rough and chemically homogeneous, a fluid can either fill the space between the surface asperities or the fluid can rest on top of the asperities, as shown in Figure 1.3(c) and 1.3(d), respectively. Wenzel [303] first investigated the state where the fluid completely fills the rough surface features and proposed the following equation to predict the contact angle of a liquid drop in such a state:

$$\cos\theta_{\mathrm{W}} = r_{\mathrm{f}}\cos\theta_{\mathrm{Y}}, \tag{1.10}$$

where θ_{W} is the Wenzel contact angle, θ_{Y} is the Young contact angle of a drop on a smooth surface of the same material, and r_{f} is the roughness factor—the actual area (A) of the solid–liquid interface divided by the projected area of the solid–liquid interface ($r_{\mathrm{f}} = A^{\mathrm{SL}}/A^{\mathrm{projected}} > 1$). Equation (1.10) states that as the solid–liquid area increases, the contact angle will (*i*) decrease until it reaches 0° if $\theta_{\mathrm{Y}} < 90^\circ$ or (*ii*) increase if $\theta_{\mathrm{Y}} > 90^\circ$. The Wenzel equation (Equation (1.10)) has been derived from a free energy minimization approach by Johnson and Dettre [133], who showed that it is the condition for mechanical equilibrium because the free energy is at an extremum (a global minimum in free energy) under the constraint of constant volume.

Based on the work of Wenzel [303], Cassie and Baxter [49] studied the state where the liquid rests on top of the rough surface features, and they derived the following equation to predict the contact angle of a liquid in such a state

$$\cos\theta_{\mathrm{CB}} = f_{\mathrm{sl}}\cos\theta_{\mathrm{Y}} - f_{\mathrm{lv}}, \tag{1.11}$$

where θ_{CB} is the Cassie–Baxter contact angle, f_{sl} is the ratio between the solid–liquid interfacial area and the projected bottom area of the spherical cap (that is, $f_{\mathrm{sl}} = A^{\mathrm{SL}}/A^{\mathrm{projected}}$), and f_{lv} is the ratio between bottom liquid–vapor interfacial area and the projected area. In the special case that the bottom of the spherical cap is completely flat, $f_{\mathrm{sl}} + f_{\mathrm{lv}} = 1$. Physically, Equation (1.11) is a cosine average of contact angle over the solid–liquid and liquid–vapor fractions, where $\theta_{\mathrm{lv}} = 180^\circ$. As mentioned by Cassie and Baxter [49], the Wenzel equation (Equation (1.10)) is obtained in the limiting case when $f_{\mathrm{sl}} = r_{\mathrm{f}}$ and $f_{\mathrm{lv}} = 0$.

When the solid is physically smooth and chemically heterogeneous, a general form of the Cassie–Baxter equation (Equation (1.11)) has been used to predict the contact angle of a liquid on such a surface [188]:

$$\cos\theta_{\mathrm{CB}} = \sum_{i=1}^{n} f_i \cos\theta_{\mathrm{Y},i}, \tag{1.12}$$

where n is the number of components in the solid phase, f_i is the ratio between the liquid–ith solid interfacial area and the projected area of the spherical cap's bottom ($f_i = A^{\mathrm{S}_i\mathrm{L}}/A^{\mathrm{projected}}$), and $\theta_{\mathrm{Y},i}$ is the Young contact angle for the liquid on a smooth surface composed entirely of

component i.

However, the applicability of the Wenzel and Cassie–Baxter equations (Equations (1.10) and (1.12)) to all surfaces has been questioned, and a debate has emerged on which portion of the contact region dictates the contact angle [82]. Does the whole solid–liquid contact area determine the value of the contact angle, or is it only the solid–liquid region close to or at the three-phase contact line that is important?

To test the Cassie–Baxter equation (Equation (1.12)), Gao and McCarthy [103] and Extrand [90] measured the contact angles of drops on surfaces with a central island of one component, where the volume of the drop exceeded the size of the central island. They showed that the area fraction under the drop clearly does not determine the contact angle of such a large liquid drop, because the inner heterogeneity does not affect the state at the contact line. In response, theoreticians suggested that the area fractions in Equation (1.12) should be determined in the region close to the drop's contact line [185, 206, 248]. Others proposed that line fractions at the contact line should be used instead [120, 212, 275, 314], and this approach predicted contact angles that were in close agreement with those measured experimentally [65, 158]. The Wenzel equation has been similarly questioned with experiments [103], and theoretical responses have been limited to suggesting the use of an area roughness in the region close to the three-phase line [32, 185, 206, 248]. Recently, the concept of a line roughness been suggested by Xu and Wang [312, 313].

Thus, there is an opportunity to address the debate and misconceptions that persist in the literature on the Cassie–Baxter and Wenzel states of wetting. This thesis proposes the use of fundamental Gibbsian composite-system thermodynamics to do so.

1.3 Thesis Scope

The focus of this thesis is in deriving fundamental mathematical relationships that can predict the properties or behavior of multicomponent systems with interfacial curvature. It is divided into three parts.

Part I investigates the surface tension of liquid mixtures as a simultaneous function of composition and temperature. Chapter 2 outlines a model to predict the surface tension as a function of liquid-phase composition and temperature for mixtures with two components that are below their individual critical points. The developed model is tested against 15 aqueous mixtures. Chapter 3 extends the model from Chapter 2 to multicomponent mixtures where one component may be above its critical point. The considered systems in this chapter include binary methane + n-alkane mixtures, carbon dioxide + n-alkane mixtures, other organic subcritical mixtures, as well as a ternary methanol + ethanol + water mixture. Part I of this thesis thus

proposes a new equation for calculating surface tension as a function of composition and temperature over a wide range of mixture types with a high level of accuracy, and this equation uses parameters that can be considered composition- and temperature-independent.

Part II investigates the effect of curvature on the phase diagrams of multicomponent mixtures from fundamental Gibbsian composite-system thermodynamics. Chapter 4 proposes an activity-coefficient model for determining the bubble and dew pressures of a multicomponent system as a function of composition and radius of curvature. Predictions are made for two systems, one ideal (methanol + ethanol) and the other nonideal (ethanol + water). The azeotrope (equal volatility point) of the nonideal mixture is shown to shift as a function of interfacial curvature. Chapter 5 extends the activity-coefficient model to determine the bubble and dew temperatures of a multicomponent system with the inclusion of the surface tension model developed in Chapter 2. In this chapter, the activity-coefficient model with interfacial curvature is used to make accurate predictions of dew temperature for a nitrogen + argon mixture as a function of composition and radius of curvature (down to a radius of 2 nm). Additionally, further predictions are made for methanol + ethanol and ethanol + water. Part II of this thesis thus provides a framework for predicting the vapor–liquid equilibrium behavior of mixtures with interfacial curvature using activity coefficients.

Part III is a theoretical investigation into the contact angle of liquid drops on rough or heterogeneous surfaces. Chapter 6 puts forward a new derivation of the Cassie–Baxter equation within the framework of Gibbsian composite-system thermodynamics, confirming the use of a line fraction in place of an area fraction. The applicability of the area- and line-fraction Cassie–Baxter equations is assessed for a variety of surface designs. Chapter 7 proposes a new derivation of the Wenzel equation using the same Gibbsian framework, concluding with a version that uses a line roughness instead of an area roughness. A dimensionless number is introduced to quantify how large the radius of curvature of the liquid phase needs to be for a simplified version of the equation to be valid, and a thermodynamic free energy analysis is completed. Part III is a mathematical proof that the properties of the solid–liquid–vapor contact line dictate the contact angle for both the Cassie–Baxter and Wenzel states of wetting.

The last chapter of this thesis, Chapter 8, highlights the main outcomes of this work.

PART I

SURFACE TENSION

Chapter 2

Model for the Surface Tension of Dilute and Concentrated Binary Aqueous Mixtures as a Function of Composition and Temperature[1]

Abstract

Surface tension dictates fluid behavior, and predicting its magnitude is vital in many applications. Equations have previously been derived to describe how the surface tension of pure liquids changes with temperature, and other models have been derived to describe how the surface tension of mixtures changes with liquid-phase composition. However, the simultaneous dependence of surface tension on temperature and composition for liquid mixtures has been less studied. Past approaches have required extensive experimental data to which models have been fit, yielding a distinct set of fitting parameters at each temperature or composition. Herein, we propose a model that requires only three fitting procedures to predict surface tension as a function of temperature and composition. We achieve this by analyzing and extending the Shereshefsky (*J. Colloid Interface Sci.* 24.3 (1967), pp. 317–322), Li *et al.* (*Fluid Phase Equilib.* 175 (2000), pp. 185–196), and Connors–Wright (*Anal. Chem.* 61.3 (1989), pp. 194–198), models to high temperatures for 15 aqueous systems. The best extensions of the Shereshefsky, Li *et al.*, and Connors–Wright models achieve average relative deviations of 2.11%, 1.20%, and 0.62%, respectively, over all systems. We thus recommend the extended Connors–Wright model for predicting the surface tension of aqueous mixtures at different temperatures with the tabulated coefficients herein. An additional outcome of this chapter is the previously-unreported equivalence of the Li *et al.* and Connors–Wright models in describing experimental data of surface tension as a function of composition at a single temperature.

[1]Reproduced, with minor modifications, with permission from N. Shardt and J. A. W. Elliott. "A Model for the Surface Tension of Dilute and Concentrated Binary Aqueous Mixtures as a Function of Composition and Temperature". *Langmuir* 33 (2017), pp. 11077–11085. http://pubs.acs.org/articlesonrequest/AOR-NkAqpDtYAHIVUiaXdP6d Copyright 2017 American Chemical Society.

2.1 Introduction

Surface tension plays a key role in both static and dynamic phenomena such as the contact angle of a liquid on a solid and the separation of a liquid stream into droplets [106]. It is a significant factor in studies of atmospheric physics [17, 184, 224, 288], pharmacy [62], liquid chromatography [52], ink-jet printing [270], microfluidics [84–86, 195], emulsions [27], wetting [145–147], nucleation [87, 323, 324], and phase diagrams that include the effects of interfacial curvature [254, 278, 279]. For pure liquids, it is known that surface tension is a linear function of temperature for low temperatures, as first described by the Eötvös equation [81]. Guggenheim and Katayama later developed other empirical equations that are more accurate for temperatures approaching the liquid's critical temperature [114].

For liquid mixtures, the prediction of surface tension as a function of composition is crucial. Many empirical models have been proposed to achieve this, such as the Shereshefsky (S) model [257], the Li *et al.* (LWW) model [56], and the Connors–Wright (CW) model [63]. However, the temperature dependence of surface tension for liquid mixtures has been studied less than for pure liquids. In the work that has been completed, there have been two common approaches. The first approach for a liquid mixture is to fit a linear temperature dependence separately at each mole fraction [9, 11, 180, 229, 289–291]. As an illustrative example, for the formic acid + water system, a total of 28 fitting parameters are needed to describe the complete experimental dataset using this approach [9]. The second approach is to choose a model that describes the composition-dependence of surface tension for a mixture and then apply this model separately to experimental data at each considered temperature [9, 11, 229, 289]; for the same dataset of formic acid + water, 14 fitting parameters are needed when using the CW model [9]. A linear fit can then be performed on the model parameters as a function of temperature [122, 123, 278]. This second approach reduces the number of fitting parameters needed to describe the data, but it still relies on experimental knowledge of surface tension at all combinations of composition and temperature. It would thus be beneficial to avoid such extensive data collection and numerous iterations of fitting and instead have a model that can accurately predict surface tension at any composition and temperature from a minimal number of experimental data points.

In this chapter, the S, LWW, and CW models are compared for aqueous binary mixtures as a function of composition at room temperature. Through this analysis, we discover that the LWW and CW models are mathematically identical when describing composition dependence at a single temperature. Next, using solely the model parameters obtained at room temperature and the temperature dependence of the pure components' surface tension, we propose extensions of each model to predict each mixture's surface tension for temperatures up to 373 K for propylene glycol(1) + water(2) and up to 323 K for all other mixtures, and the accuracy of each extended

model is assessed. We consider two different extensions of the S and LWW models and one extension of the CW model in our analysis for a total of five extended models. We propose that the temperature dependence of a mixture's surface tension arises primarily from the temperature dependence of its pure components' surface tensions for the majority of the studied aqueous systems, as supported by the extended CW model.

2.2 Governing Equations

2.2.1 Surface Tension as a Function of Composition

The model proposed by Shereshefsky (S model) is given by [257, 276]

$$\sigma_{\mathrm{S}} = \sigma_2 - \frac{\exp\left(\frac{\Delta F_{\mathrm{s}}}{RT}\right)}{1 + x_1\left[\exp\left(\frac{\Delta F_{\mathrm{s}}}{RT}\right) - 1\right]} x_1\left(\sigma_2 - \sigma_1\right), \tag{2.1}$$

where σ_{S} is the predicted mixture surface tension, σ_1 and σ_2 are the surface tensions of the pure components (in this chapter, σ_2 is the surface tension of pure water), x_1 is the mole fraction of the nonaqueous compound, ΔF_{s} is the free energy change associated with the exchange of one mole of water with one mole of the second compound at the surface, R is the universal gas constant, and T is the absolute temperature.

The model proposed by Li *et al.* (LWW model) is given by [56]

$$\sigma_{\mathrm{LWW}} = x_1\sigma_1 + x_2\sigma_2 - \frac{x_1 x_2 RT}{x_2 + x_1\Lambda_{21}}\left(\frac{\partial\Lambda_{21}}{\partial A}\right)\left(1 - \frac{1}{\Lambda_{21}}\right), \tag{2.2}$$

where Λ_{21} is a dimensionless parameter for the system and A is surface area per mole. Substituting expressions for Λ_{21} and its partial derivative into Equation (2.2) and redefining the fitting parameters gives the following form of the LWW model

$$\sigma_{\mathrm{LWW}} = x_1\sigma_1 + x_2\sigma_2 + \frac{x_1 x_2}{x_2 + \exp\left(-\frac{\alpha}{RT}\right)x_1}\beta\exp\left(-\frac{\alpha}{RT}\right)\left[1 - \exp\left(\frac{\alpha}{RT}\right)\right], \tag{2.3}$$

where α and β are re-defined fitting parameters related to the original parameters by the following expressions

$$\Lambda_{21} = \exp\left(-\frac{\alpha}{RT}\right) \tag{2.4}$$

$$\frac{\partial\alpha}{\partial A} = \beta. \tag{2.5}$$

The LWW model has been used successfully to describe the surface tension of both binary and multicomponent systems as a function of composition [56, 241]. It was initially considered to have approximately temperature-independent parameters, but in the reported results [56], it can be seen that the percent deviation between predictions and experimental data increases as the temperature increases, and for mixtures of organic acids with water, the parameters have been shown to be functions of temperature [18].

The model proposed by Connors and Wright (CW model) is given by [63]

$$\sigma_{\mathrm{CW}} = \sigma_2 - \left(1 + \frac{b(1-x_1)}{1-a(1-x_1)}\right) x_1(\sigma_2 - \sigma_1), \tag{2.6}$$

where a and b are fitting parameters. The CW model can be simplified to the S model by setting $b = a$ and rearranging.

Each of the above three models (Equations (2.1), (2.3), and (2.6)) is fit to literature data at the lowest reported temperature (T_{ref}). To compare the accuracy of each model at T_{ref}, the standard deviation (SD) is calculated in MATLAB (R2016b Natick, USA) using [18, 255]

$$\mathrm{SD} = \sqrt{\frac{\sum_{i=1}^{n} (\hat{\sigma}_i - \sigma_i)^2}{n-p}}, \tag{2.7}$$

where $\hat{\sigma}_i$ is the predicted value of surface tension, σ_i is the experimental value of surface tension, n is the number of experimental data points used in the fitting, and p is the number of fitting parameters in the model. The lower the standard deviation the better the model agrees with experimental values.

2.2.2 Surface Tension as a Function of Composition and Temperature

The temperature dependence of each pure component's surface tension is chosen for this chapter to be a linear fit of experimental data from each literature source:

$$\sigma_i = \theta_{0,i} + \theta_{1,i} T, \tag{2.8}$$

where $\theta_{0,i}$ and $\theta_{1,i}$ are fitting parameters for component i. For ordinary least squares regression, the coefficient of determination R^2 can be used to evaluate the goodness of fit, and it is given by

$$R^2 = 1 - \frac{\mathrm{SSE}}{\mathrm{TSS}} = 1 - \frac{\sum_{i=1}^{n} (\hat{\sigma}_i - \sigma_i)^2}{\sum_{i=1}^{n} (\sigma_i - \bar{\sigma}_i)^2}, \tag{2.9}$$

where SSE is the sum of squared errors and TSS is the total sum of squared deviations from the mean, where the mean is given by

$$\bar{\sigma}_i = \frac{1}{n}\sum_{i=1}^{n}\sigma_i. \tag{2.10}$$

We propose to extend the S, LWW, and CW models by combining Equation (2.8) for each pure component with the original models (Equations (2.1), (2.3), and (2.6)) to create new models that can predict the surface tension of a mixture as a function of both composition and temperature. Each original model is fit to literature data at the lowest reported temperature (T_{ref}), and then only the pure component surface tensions are allowed to vary with temperature in the extended models. In total, five extended models to higher temperatures are considered, and the accuracy of their predictions is assessed.

First, we extend the S and LWW models (Equations (2.1) and (2.3), respectively) by assuming that the fitting parameters ΔF_{s}, α, and β are constant with temperature. The models obtained using this assumption will be referred to as the ex1-S and ex1-LWW models.

Next, we extend the S and LWW models by nondimensionalizing two of the parameters ($\Delta F_{\text{s}}/RT$ and α/RT) and assuming that these dimensionless parameters are constant with temperature. The models obtained using this assumption will be referred to as the ex2-S and ex2-LWW models. The motivation behind using dimensionless parameters comes from previous studies of mixtures' surface tension as a function of temperature. Tahery *et al.* [276] showed that while ΔF_{s} in the S model depends on temperature, $\Delta F_{\text{s}}/RT$ can be temperature independent for many aqueous systems. Since the value of ΔF_{s} for each system is determined at T_{ref}, the dimensionless counterpart of ΔF_{s} is $\Delta F_{\text{s}}/RT_{\text{ref}}$, and the ex2-S model is calculated using the following equation

$$\sigma_{\text{ex2-S}} = \sigma_2 - \frac{\exp\left(\frac{\Delta F_{\text{s}}}{RT_{\text{ref}}}\right)}{1 + x_1\left[\exp\left(\frac{\Delta F_{\text{s}}}{RT_{\text{ref}}}\right) - 1\right]} x_1\left(\sigma_2 - \sigma_1\right). \tag{2.11}$$

In the LWW model, Bagheri *et al.* [18] showed that the fitting parameters are functions of temperature for organic acid + water systems, but the functional forms of these relationships were not investigated. Based on the success of a dimensionless parameter in the S model, we investigate whether a dimensionless LWW parameter α/RT is constant with temperature. For the ex2-LWW model, the dimensionless counterpart of α is α/RT_{ref}, yielding

$$\sigma_{\text{ex2-LWW}} = x_1\sigma_1 + x_2\sigma_2 + \frac{x_1 x_2}{x_2 + \exp\left(-\frac{\alpha}{RT_{\text{ref}}}\right)x_1}\beta\exp\left(-\frac{\alpha}{RT_{\text{ref}}}\right)\left[1 - \exp\left(\frac{\alpha}{RT_{\text{ref}}}\right)\right]. \tag{2.12}$$

In Equations (2.11) and (2.12), the pure component surface tensions (σ_i) are calculated as a function of temperature using Equation (2.8).

The final extended model combines Equation (2.8) with the original CW model (Equation (2.6)), and this extended model will be referred to as the ex-CW model.

To compare the accuracy of each extended model, the relative percent deviation (d_i) between a prediction at a specific composition and temperature and the experimental value at the same composition and temperature can be calculated using

$$d_i = \frac{|\hat{\sigma}_i - \sigma_i|}{\sigma_i} \times 100\%, \tag{2.13}$$

and the average relative deviation for a system or group of systems can be calculated using

$$d_s = \frac{1}{j} \sum_{i=1}^{j} d_i, \tag{2.14}$$

where j is the number of experimental points over all compositions and/or temperatures for that system or group of systems. All experimental data were taken from the tables reported in each literature source for a total of 1315 data points over all considered aqueous systems. Two experimental data points were identified as outliers and were not used for comparison to predictions: for monoethanolamine(1) + water(2), the measurement [289] at $x_1 = 0.069$ and $T = 308$ K, and for methanol(1) + water(2), the measurement [290] at $x_1 = 0.090$ and $T = 313$ K. These outliers were identified because at those compositions and temperatures the surface tensions do not follow the otherwise monotonically decreasing trend as a function of temperature.

2.3 Results and Discussion

2.3.1 Pure-Component Surface Tension as a Function of Temperature

Table 2.1 summarizes the fitting coefficients for each pure substance used in this chapter to describe how surface tension changes as a function of temperature (Equation (2.8)). For propylene glycol(1) + water(2), the equation for water is taken from Hoke and Patton [122], but the goodness of fit for this equation is not given in the reference; the listed coefficients for this equation have been converted for use with temperatures in Kelvin. For all other compounds, the coefficients were determined by fitting Equation (2.8) to the tabulated experimental data in each listed reference using the built-in MATLAB *fit()* function that uses QR factorization for a linear polynomial curve.

Table 2.1: Coefficients ± their 95% confidence intervals to describe the effect of temperature on the surface tension of pure compounds for T in K and σ_i in mN/m obtained from a linear fit ($\sigma_i = \theta_{0,i} + \theta_{1,i}T$) to the experimental data reported in the listed reference. n is the number of data points.

Compound	n	$\theta_{0,i}$ [mN/m]	$\theta_{1,i}$ [mN/m/K]	R^2	Reference
Monoethanolamine (MEA)	6	98.1 ± 2.0	-0.165 ± 0.006	0.9992	Vázquez *et al.* [289]
Diethanolamine (DEA)	6	96.0 ± 2.4	-0.163 ± 0.008	0.9989	Vázquez *et al.* [291]
Triethanolamine (TEA)	6	94.2 ± 2.2	-0.162 ± 0.007	0.9990	Vázquez *et al.* [291]
2-Amino-2-methyl-1-propanol (AMP)	6	66.3 ± 0.5	-0.117 ± 0.002	0.9999	Vázquez *et al.* [289]
Formic acid	7	69.2 ± 0.4	-0.108 ± 0.001	0.9999	Álvarez *et al.* [9]
Acetic acid	7	56.5 ± 0.4	-0.099 ± 0.001	0.9999	Álvarez *et al.* [9]
Propionic acid	7	55.8 ± 0.2	-0.099 ± 0.001	1.0000	Álvarez *et al.* [9]
Methanol	7	50.0 ± 1.0	-0.092 ± 0.003	0.9991	Vázquez *et al.* [290]
Ethanol	7	46.3 ± 0.9	-0.082 ± 0.003	0.9990	Vázquez *et al.* [290]
1-Propanol	7	46.9 ± 0.3	-0.079 ± 0.001	0.9999	Vázquez *et al.* [290]
2-Propanol	7	51.4 ± 0.3	-0.101 ± 0.001	0.9999	Vázquez *et al.* [290]
Propylene glycol	8	56.4 ± 1.5	-0.068 ± 0.004	0.9960	Hoke and Patton [122]
N-Methyl diethanolamine (MDEA)	6	61.1 ± 9.5	-0.076 ± 0.031	0.9214	Álvarez *et al.* [11]
1-Amino-2-propanol (1-AP)	6	109.4 ± 2.1	-0.242 ± 0.007	0.9996	Álvarez *et al.* [10]
3-Amino-1-propanol (3-AP)	6	112.3 ± 0.5	-0.229 ± 0.002	1.0000	Álvarez *et al.* [10]
Water	6	120.5 ± 2.2	-0.163 ± 0.007	0.9991	Álvarez *et al.* [10, 11]; Vázquez *et al.* [289, 291]
Water	7	119.9 ± 1.6	-0.161 ± 0.005	0.9992	Álvarez *et al.* [9]; Vázquez *et al.* [290]
Water	N/A	116.2	-0.148	N/A	Hoke and Patton [122]

2.3.2 Surface Tension as a Function of Composition

To describe how a mixture's surface tension depends on composition at a single temperature, the S, LWW, and CW models (Equations (2.1), (2.3), and (2.6)) are fit to reported experimental data. Table 2.2 lists the fitting parameters, their 95% confidence intervals, and the standard deviation (SD) for the S, LWW, and CW models for each binary mixture at the lowest reported temperature (T_{ref}). The pure component surface tensions (σ_i in Equations (2.1), (2.3), and (2.6)) were evaluated at T_{ref} using Equation (2.8), and then each model's fitting parameters were determined using the built-in MATLAB *fit()* function with the Levenberg–Marquardt algorithm for nonlinear regression.

Table 2.2: Parameters ± their 95% confidence intervals for the S, LWW, and CW models (Equations (2.1), (2.3), and (2.6), respectively) fit to the surface tension of the listed systems at the lowest reported temperature (T_{ref}) using n experimental points. Equation (2.8) was used to calculate the surface tension of each pure component at T_{ref} using the fit coefficients in Table 2.1. The standard deviation (SD; Equation (2.7)) of each model is listed in brackets. Compound 1 refers to the first component of the binary aqueous mixture.

			S model	LWW model		CW model	
Compound 1	n	Temp. T_{ref} [K]	ΔF_s [J/mol] (SD [mN/m])	α [J/mol] (SD [mN/m])	β [J/m^2]	a [unitless] (SD [mN/m])	b [unitless]
MEA [289]	13	298	4940 ± 520 (1.32)	−7260 ± 40 (0.03)	−15.28 ± 0.08	0.9466 ± 0.0008 (0.03)	0.6274 ± 0.0028
DEA [291]	11	298	5520 ± 550 (1.40)	−7680 ± 30 (0.02)	−17.36 ± 0.07	0.9550 ± 0.0006 (0.02)	0.6694 ± 0.0023
TEA [291]	11	298	7790 ± 20 (0.05)	−7840 ± 20 (0.02)	−25.87 ± 0.06	0.9576 ± 0.0003 (0.02)	0.9510 ± 0.0020
AMP [289]	14	298	8460 ± 430 (1.94)	−9740 ± 40 (0.09)	−34.47 ± 0.15	0.9803 ± 0.0004 (0.09)	0.8315 ± 0.0035
Formic acid [9]	14	293	4130 ± 130 (0.55)	−4780 ± 120 (0.16)	−29.93 ± 0.81	0.8595 ± 0.0070 (0.16)	0.7302 ± 0.0144
Acetic acid [9]	14	293	6460 ± 330 (1.77)	−7680 ± 30 (0.07)	−37.17 ± 0.16	0.9571 ± 0.0006 (0.07)	0.7873 ± 0.0029
Propionic acid [9]	14	293	9500 ± 280 (1.26)	−10210 ± 40 (0.10)	−42.67 ± 0.16	0.9848 ± 0.0003 (0.10)	0.9109 ± 0.0032
Methanol [290]	14	293	4780 ± 60 (0.34)	−4990 ± 110 (0.21)	−47.59 ± 1.02	0.8709 ± 0.0056 (0.21)	0.8314 ± 0.0130
Ethanol [290]	14	293	7440 ± 100 (0.56)	−7740 ± 80 (0.19)	−48.39 ± 0.46	0.9583 ± 0.0013 (0.19)	0.9176 ± 0.0076
1-Propanol [290]	14	293	11360 ± 140 (0.46)	−11230 ± 190 (0.41)	−49.66 ± 0.59	0.9900 ± 0.0008 (0.41)	1.0011 ± 0.0113
2-Propanol [290]	14	293	9650 ± 130 (0.60)	−9500 ± 200 (0.55)	−51.87 ± 0.95	0.9798 ± 0.0017 (0.55)	0.9954 ± 0.0169
Propylene glycol [122]	9	303	6230 ± 520 (1.33)	−7520 ± 480 (0.45)	−29.70 ± 1.61	0.9495 ± 0.0096 (0.45)	0.7885 ± 0.0362
MDEA [11]	14	298	7280 ± 580 (2.33)	−9360 ± 520 (0.78)	−24.71 ± 1.47	0.9771 ± 0.0048 (0.78)	0.7227 ± 0.0401
1-AP [10]	12	298	5660 ± 560 (1.97)	−7800 ± 40 (0.05)	−24.87 ± 0.13	0.9571 ± 0.0007 (0.05)	0.6858 ± 0.0030
3-AP [10]	12	298	4530 ± 200 (0.58)	−5430 ± 10 (0.01)	−23.06 ± 0.06	0.8884 ± 0.0007 (0.01)	0.7287 ± 0.0015

Figure 2.1 shows some representative examples of the model fits to experimental surface tension data as a function of composition. The S model performs well when a and b in the CW model are close to the same value, such as in the TEA(1) + water(2) system; this is expected because the CW model simplifies to the S model when $a = b$. As the values of a and b become more different, the S model cannot mathematically describe the curvature of the experimental data with a single fitting parameter. The S model becomes less and less accurate, as seen by the larger standard deviation for systems such as acetic acid(1) + water(2) and MDEA(1) + water(2) compared to the standard deviation for TEA(1) + water(2). This means that it is better to use a 2-parameter model to more accurately capture how surface tension changes as a function of composition for a wider variety of systems. The 2-parameter CW and LWW models have the same standard deviation for the studied systems, and therefore, either model can be selected for the fitting of experimental data of surface tension as a function of liquid mole fraction at constant temperature.

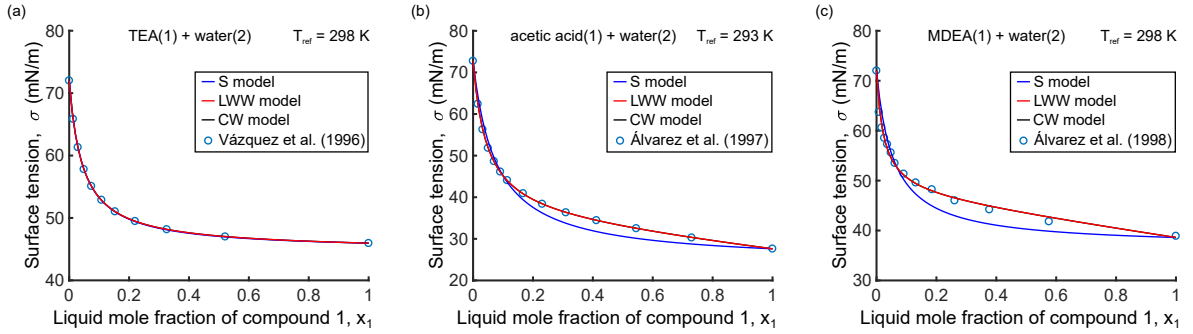

Figure 2.1: Fits of the S, LWW, and CW models (Equations (2.1), (2.3), and (2.6), respectively) to experimental data of surface tension as a function of liquid mole fraction for aqueous mixtures: (a) TEA, (b) acetic acid, and (c) MDEA. Equation (2.8) was used to calculate the surface tension of each pure component at T_{ref} with the fit coefficients in Table 2.1. The best-fit parameters of the S, LWW, and CW models at T_{ref} are listed in Table 2.2.

The fact that the LWW and CW models yield the same predictions of surface tension as a function of liquid mole fraction at a single temperature suggests that these models are mathematically identical. After some algebraic manipulation, the following relationships between the LWW and CW fitting coefficients can be derived:

$$\alpha = -RT \ln\left(\frac{a}{1-a} + 1\right) = -RT \ln\left(\frac{1}{1-a}\right) \tag{2.15a}$$

$$\beta = \frac{b}{a}\left(\sigma_1 - \sigma_2\right). \tag{2.15b}$$

Even though the CW model was derived based on Langmuir adsorption and the LWW model

was derived from a free energy analysis, the final models are of the same mathematical form to describe the dependence of surface tension on liquid-phase composition.

2.3.3 Surface Tension as a Function of Composition and Temperature

We propose to extend the original S, LWW, and CW models to predict the surface tension of mixtures at higher temperatures by combining Equation (2.8) for each pure component with each of the original models (Equations (2.1), (2.3), and (2.6), respectively). A total of five extended models are considered, depending on whether the fitting parameters or their dimensionless versions are assumed constant with temperature.

The best-fit parameters in Table 2.2 were determined at the lowest reported temperature (T_{ref}), so all surface tension values calculated above this temperature for the mixtures are true predictions based solely on the temperature-dependent pure component surface tension and the single fit to data as a function of composition at T_{ref}. Using the parameters in Table 2.1 and Table 2.2, surface tension can then be calculated as a function of composition and temperature for each extended model and compared to experimental data. Table 2.3 summarizes the maximum and average relative percent deviations of the predictions over all compositions and temperatures for each extended model applied to each system. Over all the systems, the ex-CW model has the lowest average percent deviation of 0.62% between predictions and experimental measurements, and such a high level of accuracy is comparable to the reported average deviation of 0.54% for the LWW model fit to data at a single temperature over 124 systems [56]. The maximum relative deviation is also lowest for the ex-CW model compared to the other extended models. For propylene glycol, the highest temperature considered is 373 K, and for all other systems, the highest temperature is 323 K.

Table 2.3: Maximum and average relative percent deviation are listed for predictions calculated using the ex1-S, ex2-S, ex1-LWW, ex2-LWW, and ex-CW models compared to experimental data for each aqueous system over all compositions and temperatures. The last row considers the performance of each extended model over all systems. The number of points (j) used in each calculation of average relative deviation is also listed. The gradient in background colors for average relative deviation is a scale from blue (0%) to white to red (4%). White text on a blue background indicates that the average relative deviation is less than 0.5%.

		ex1-S model		ex2-S model		ex1-LWW model		ex2-LWW model		ex-CW model	
Compound 1	j	Max deviation $d_{i,\max}$ (%)	Average deviation d_s (%)	Max deviation $d_{i,\max}$ (%)	Average deviation d_s (%)	Max deviation $d_{i,\max}$ (%)	Average deviation d_s (%)	Max deviation $d_{i,\max}$ (%)	Average deviation d_s (%)	Max deviation $d_{i,\max}$ (%)	Average deviation d_s (%)
MEA	77	3.74	1.95	3.89	1.95	1.45	0.36	0.25	0.07	0.27	0.08
DEA	66	4.49	2.11	4.42	2.07	1.98	0.49	0.20	0.08	0.19	0.08
TEA	66	3.12	0.85	0.27	0.10	3.04	0.85	0.20	0.08	0.18	0.08
AMP	84	8.01	3.98	8.32	3.81	3.40	0.66	2.46	0.90	1.50	0.29
Formic acid	98	3.15	1.03	2.10	0.87	1.70	0.46	1.69	0.47	0.74	0.21
Acetic acid	98	8.93	4.03	8.54	3.72	4.49	1.00	2.86	0.83	0.66	0.13
Propionic acid	98	13.84	3.99	6.41	3.10	8.80	1.73	4.43	1.27	3.17	0.37
Methanol	97	5.77	1.58	1.95	0.78	3.95	1.02	3.59	0.91	0.96	0.40
Ethanol	98	10.04	2.57	3.23	1.37	6.04	1.40	5.69	1.54	1.26	0.36
1-Propanol	98	12.99	3.21	3.58	1.16	10.16	2.89	9.88	3.10	2.98	1.30
2-Propanol	98	15.68	3.72	4.42	1.43	11.39	3.36	8.91	2.48	3.66	1.64
Propylene glycol	109	12.58	3.56	6.08	2.81	7.15	1.63	6.65	2.10	2.94	0.96
MDEA	84	8.68	3.24	6.83	2.97	4.59	1.43	3.62	1.27	6.09	1.49
1-AP	72	12.28	4.12	9.33	3.91	9.14	2.59	6.14	1.85	4.64	1.20
3-AP	72	5.75	1.73	4.35	1.56	5.42	1.29	3.74	0.82	3.04	0.68
Over all systems	1315	15.68	2.80	9.33	2.11	11.39	1.42	9.88	1.20	6.09	0.62

Figure 2.2 illustrates the trends in surface tension as a function of composition at 323 K as predicted by each extended model for systems of TEA(1) + water(2), acetic acid(1) + water(2), and MDEA(1) + water(2). Compared to Figure 2.1, the surface tensions of the mixtures are lower at 323 K for all system compositions. This is expected since the surface tension of each pure component decreases with temperature, and therefore the mixture's surface tension also decreases. In Figure 2.1, the LWW and CW models give identical predictions, but as the temperature reaches 323 K in Figure 2.2, the ex-CW model agrees more closely with experimental data than the ex1-LWW or ex2-LWW model for the illustrated TEA(1) + water(2) and acetic acid(1) + water(2) systems.

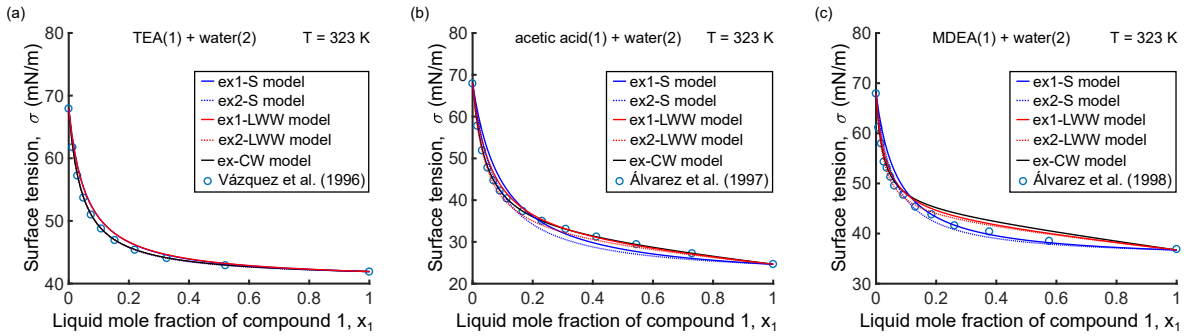

Figure 2.2: Predictions of five extended models for surface tension as a function of liquid mole fraction for aqueous mixtures: (a) TEA, (b) acetic acid, and (c) MDEA compared to experimental data at 323 K. For each extended model, the best-fit parameters listed in Table 2.2 were used for the composition dependence of surface tension at T_{ref}, and the coefficients listed in Table 2.1 were used to determine the pure components' surface tension at 323 K with Equation (2.8).

Figure 2.1 and Figure 2.2 show snapshots of fits of each original model at the lowest reported temperature and of predictions of each extended model at the highest reported temperature, respectively. To gain insight into how each extended model performs in the intermediate temperatures, the average relative deviation can be calculated at every temperature for each aqueous system. Three main patterns emerge when these average relative deviations are plotted as a function of temperature.

All systems exhibiting Pattern I are shown in Figure 2.3. Here, the ex1-LWW model's deviation increases with temperature, but the ex2-LWW model's deviation is constant with temperature. Considering extensions of the S model, the ex1-S model's deviation is either constant or increasing with temperature, but the ex2-S deviation is constant with temperature for all systems. The ex-CW model yields constant relative deviation with temperature. For these systems, it can thus be concluded that $\Delta F_{\text{s}}/RT_{\text{ref}}$, α/RT_{ref}, β, a, and b are constant. Equation (2.15a) supports the fact that α/RT_{ref} is constant for systems for which a from the CW

model is also constant with temperature. By considering α/RT_{ref} as a constant, the magnitude of the temperature dependence of β can be isolated and assessed. For systems in Pattern I, the average percent deviation of the ex2-LWW model matches that of the ex-CW model at all temperatures, and therefore β is essentially temperature independent. This can be explained with Equation (2.15b), which shows that the value of β will only change if the difference in surface tension between the two components changes as a function of temperature. That is, when the pure component surface tension is represented by a linear polynomial, β will not change very much if the slopes ($\theta_{1,i}$) of each pure component are similar; if the slopes are very different, β will change with temperature. The systems exhibiting Pattern I have slopes closer to that of water than those systems in Pattern II.

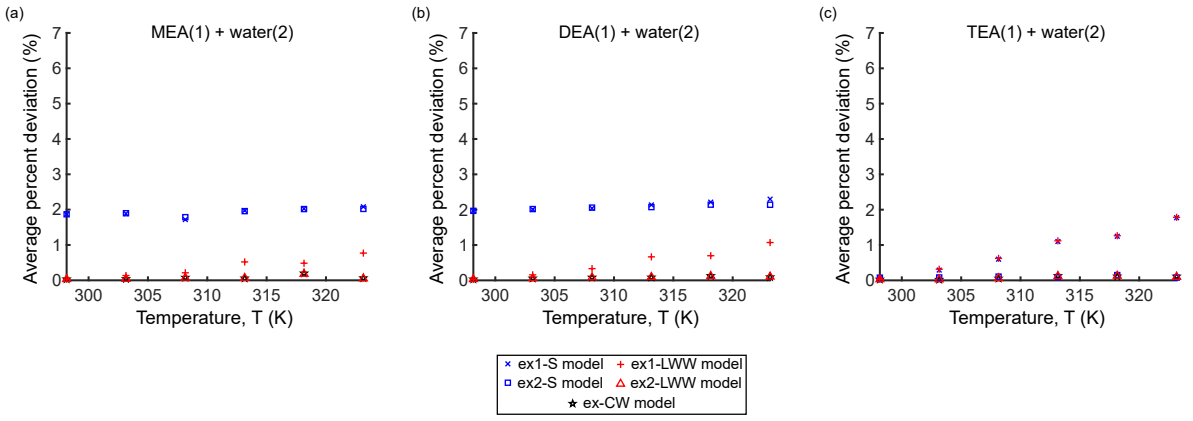

Figure 2.3: Average relative percent deviation between model predictions and experimental data as a function of temperature for aqueous mixtures exemplifying Pattern I: (a) MEA, (b) DEA, and (c) TEA. For each extended model, the best-fit parameters listed in Table 2.2 were used for the composition dependence of surface tension at T_{ref}, and the coefficients listed in Table 2.1 were used to determine the pure components' surface tension at each temperature.

Pattern II, as shown in Figure 2.4, is characterized by increasing relative deviation with increasing temperature for the ex1-LWW model and ex2-LWW model, increasing relative deviation for the ex1-S model, and constant relative deviation for the ex2-S and ex-CW models. For these systems, therefore, $\Delta F_{\text{s}}/RT_{\text{ref}}$, α/RT_{ref}, a, and b are constant. The observation that α and β are not constant is in agreement with Bagheri *et al.* [18], who previously studied the original LWW model and concluded that its fitting parameters are functions of temperature for organic acid + water systems. The temperature dependence of β worsens the accuracy of the extended LWW models for systems in Pattern II. The pure components in each system exhibiting this pattern have significantly different $\theta_{1,i}$ compared to $\theta_{1,\text{water}}$, and thus the ex2-LWW model shows increasing relative deviation with increasing temperature, as given by Equation (2.15b).

Pattern III shows varying relative deviation as a function of temperature for all five of the

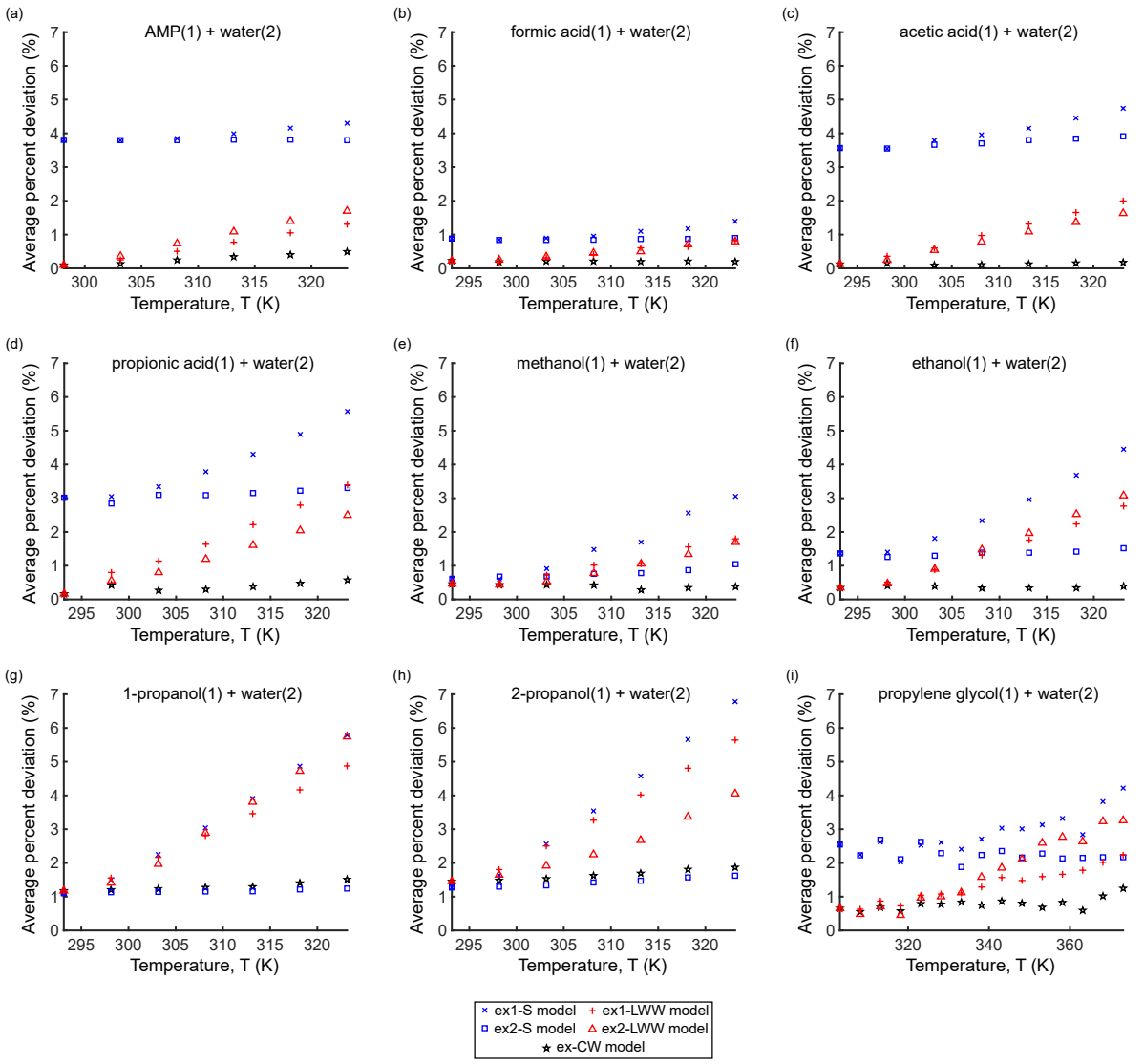

Figure 2.4: Average relative percent deviation between model predictions and experimental data as a function of temperature for aqueous mixtures exemplifying Pattern II: (a) AMP, (b) formic acid, (c) acetic acid, (d) propionic acid, (e) methanol, (f) ethanol, (g) 1-propanol, (h) 2-propanol, and (i) propylene glycol. For each extended model, the best-fit parameters listed in Table 2.2 were used for the composition dependence of surface tension at T_{ref}, and the coefficients listed in Table 2.1 were used to determine the pure components' surface tension at each temperature.

extended models, as illustrated in Figure 2.5. None of the models describe the temperature dependence of MDEA(1) + water(2) very well, although the ex2-LWW and ex-CW models are both within approximately 2% of experimental data at all temperatures. The model predictions for the MDEA(1) + water(2) system may be compromised by the relatively worse fit for the temperature dependence of the surface tension of pure MDEA compared to the other systems (R^2 of 0.9214 for MDEA compared to $R^2 > 0.99$ for all other systems in Table 2.1). For

aqueous mixtures of 1-AP and 3-AP, all extended models have increasing relative deviation as the temperature increases. This suggests that there is an additional temperature dependence that is not captured by the proposed extended models for these mixtures.

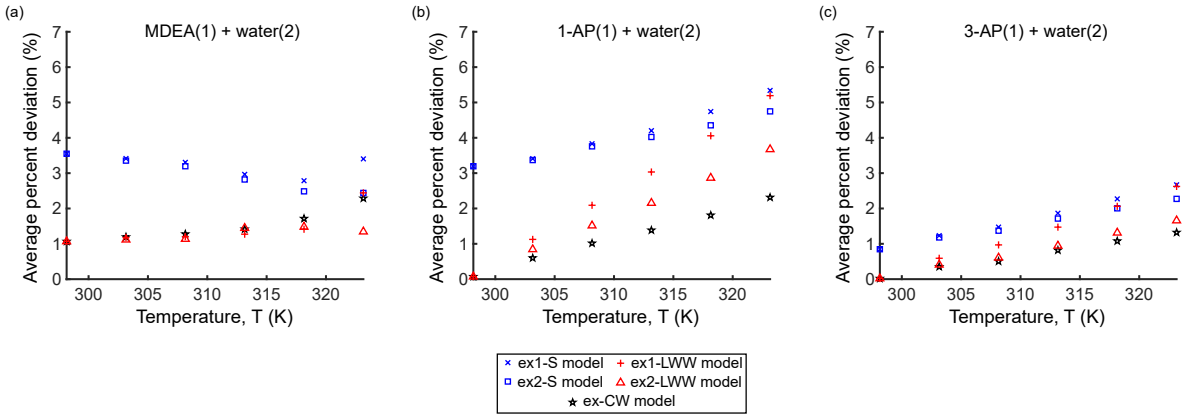

Figure 2.5: Average relative percent deviation between model predictions and experimental data as a function of temperature for aqueous mixtures exemplifying Pattern III: (a) MDEA, (b) 1-AP, and (c) 3-AP—where all extended models show varying deviation as a function of temperature. For each extended model, the best-fit parameters listed in Table 2.2 were used for the composition dependence of surface tension at T_{ref}, and the coefficients listed in Table 2.1 were used to determine the pure components' surface tension at each temperature.

Depending on the extended model and system, the predictions of surface tension can maintain the same level of accuracy seen at the lowest temperature. In order to achieve the same level of accuracy as the ex-CW model, the ex1-LWW and ex2-LWW model parameters need to be recalculated at different temperatures, as dictated by Equations (2.15a) and (2.15b). To eliminate any temperature-dependence of the fitting parameters, it would thus be easier to initially select the ex-CW model form for fitting to experimental data and then for extrapolating to higher temperatures. The ex-CW model performs best in terms of describing the curvature of the composition dependence of surface tension and in terms of describing the temperature dependence.

Thus, we propose the use of the following ex-CW model for prediction of surface tension as a function of composition and temperature:

$$\sigma_{\text{ex-CW}}(x_1,T) = \sigma_2(T) - \left(1+\frac{b(1-x_1)}{1-a(1-x_1)}\right) x_1\left[\sigma_2(T)-\sigma_1(T)\right], \tag{2.16}$$

where the parameters a and b can be fit to data collected as a function of composition at one reference temperature. For the systems considered herein, these parameters can be found in Table 2.2, and the pure component surface tension can be calculated using Equation (2.8) with the coefficients listed in Table 2.1 at any temperature between T_{ref} and 373 K for propylene

glycol or 323 K for all other systems.

2.4 Conclusions

For experimental data at a single temperature, the Connors–Wright (CW) model and the Li *et al.* (LWW) model perform equally well to describe the dependence of surface tension on composition for the studied aqueous systems. We have shown that the CW and LWW models are mathematically equivalent, and we have derived the equations for converting the fitting parameters of one model to the other. The Shereshefsky (S) model has only one fitting parameter, and it is generally not as accurate as the other two studied models in describing the surface tension as a function of composition.

Our proposed extension of the CW model is superior for extrapolating experimental data as a function of mixture composition from a single temperature to higher temperatures for the studied aqueous systems compared to our proposed extensions of the S and LWW models. Thus, when there is limited experimental data as a function of temperature, the extended CW model should preferentially be selected for predicting the surface tension of binary mixtures. While the CW model and the LWW model are mathematically identical when describing the effect of composition at a fixed temperature, the LWW parameters are temperature-dependent, and thus the LWW model should not be used for extrapolation to other temperatures.

Previous studies have used extensive experimental data to determine empirical correlations that cover a wide range of temperatures and compositions. In this chapter, we show that the only experimental measurements of surface tension needed for many aqueous systems are, in fact, (*i*) the pure components' surface tensions as a function of temperature and (*ii*) the mixture's surface tension as a function of composition at a single temperature. Since the effect of temperature on many pure substances is usually tabulated in databases, the only additional experimental data needed is the composition dependence for the mixture of interest at a single reference temperature. Once this experimental data is collected, a single fitting procedure can be completed to determine the parameters a and b, and our proposed extended CW equation (Equation (2.16)) can be used to calculate the surface tension of a mixture at any composition and any temperature (as long as this temperature is not outside the range of validity for the pure component surface tension equations).

Chapter 3

Surface Tension as a Function of Temperature and Composition for a Broad Range of Mixtures[1]

Abstract

It is desirable to predict the surface tension of liquid mixtures for a wide range of compositions, temperatures, and pressures, but current state-of-the-art calculations (*e.g.*, density gradient theory or density functional theory) are computationally expensive. We propose a computationally simple—but accurate—semi-empirical mathematical model of surface tension for a wide variety of multicomponent mixtures. Previously, we showed excellent accuracy for subcritical aqueous systems across mole fractions x_1 between 0 and 1 (an average deviation of 0.62% relative to experimental data for 15 mixtures). In this chapter, we show that our approach can be used for various nonaqueous systems, including those with a supercritical compound when coupled with an equation of state (by introducing a reduced mole fraction $x_{1,\mathrm{r}} = x_1/x_{1,\mathrm{cr}}$ that varies between 0 and 1, where $x_{1,\mathrm{cr}}$ is the critical composition of compound 1). Our predictions for binary systems with one supercritical component (methane + *n*-alkanes for temperatures of 173–442 K and pressures of 0.1–35.9 MPa; carbon dioxide + *n*-alkanes for temperatures of 323–378 K and pressures of 0.1–11.2 MPa) are an average absolute deviation of 0.22 mN/m away from experimental data (466 data points) in the literature, and those for systems with two subcritical components (293–333 K) are within 0.10 mN/m (236 data points). We make predictions for methanol + ethanol + water using binary coefficients, each obtained at one temperature, within an average of 0.71 mN/m away from 196 data points. Given its computational simplicity and wide applicability, the model proposed herein will be useful for many applications.

[1]This chapter and Appendix A have been submitted for publication as N. Shardt, Y. Wang, Z. Jin, and J. A. W. Elliott. "Surface Tension as a Function of Temperature and Composition for a Broad Range of Mixtures". I performed all research and composed the first draft of this chapter under the direction and supervision of JAWE. YW and ZJ provided motivation for this work and gave assistance with Peng–Robinson equation of state calculations for hydrocarbon mixtures. All authors contributed to the version of the chapter presented in this thesis. In performing this research, I received advice from Dr. J. M. Shaw on the critical composition of multicomponent mixtures and assistance from Dr. A. Komrakova in translating Kharin *et al.* [140].

3.1 Introduction

The way a fluid behaves—how it flows, how it rests, and how it nucleates—is influenced by the magnitude of its surface tension. The importance of an equation that describes the surface tension of multicomponent systems as a function of composition and temperature is far-reaching. A vast array of applications and fundamental phenomena involve liquid mixtures whose behavior is driven by the magnitude of surface tension. For instance, the surface tension of fluid mixtures influences how food packaging is designed [139, 173], how drugs are delivered [15, 62, 148, 160], and how shale gas can be extracted from porous media underground [98, 131, 278, 279, 295]. Technologies such as micro-/nanofluidic chips [84–86, 260, 310] and ink-jet printers [69, 161] also handle multicomponent mixtures. More widely, researchers in the fields of atmospheric physics [17, 34], catalysis [37], heat transfer [23], nucleation [20, 30, 153, 297], and vapor–liquid phase equilibrium [240, 253, 254, 278, 279] or phase change [74, 142, 210, 322] all examine mixtures at varying temperatures. Thus, surface tension must be accurately quantified so that diverse phenomena can be better understood, predicted, and controlled when, for example, temperatures, pressures, and/or compositions vary.

For a pure compound's surface tension, accurate theoretical descriptions have been obtained by fitting to experimental data. The mathematical form of fitted equations in the literature ranges from a linear equation (the Eötvös equation [81]) or other algebraic forms (*e.g.*, the principle of corresponding states [36, 114] and the parachor model (Macleod–Sugden equation [179]) to a differential equation that describes the distribution of molecules through the interfacial region (*e.g.*, density gradient theory [35, 45, 64, 170, 190, 287] or density functional theory [109, 167, 280] combined with a Helmholtz free energy approximation to calculate interfacial properties).

A similarly broad range of approaches has been investigated to describe how surface tension varies as a function of composition. Simpler models include the parachor model (Weinaug–Katz equation [302]) and those derived from a thermodynamic approach (*e.g.*, the Shereshefsky model [257], the Connors–Wright (CW) model [63], the Fu *et al.* model [135], and the Li *et al.* model [56]). More computationally intensive models of mixture surface tension employ principles of statistical mechanics, and this group of approaches includes density gradient theory [35, 64, 66, 80, 104, 168, 170, 189, 202, 216, 239, 327], linear gradient theory [168, 216, 328], density functional theory [144, 167, 175, 242, 277], and Monte Carlo or molecular dynamics simulations [47, 192, 200].

The parachor model for mixtures relates the quartic-root of surface tension to phase compositions, densities, and pure-component parachor values. It has been used extensively in the petroleum industry for predicting the surface tension of hydrocarbon mixtures [94, 131, 216, 244, 256]. Although the parachor model may be easy to use, its inconsistent predictive power

over a wide range of compositions has been reported [7, 170, 191, 216], and numerous variations have been proposed where the quartic root is modified or the pure-component parachor values are adjusted [7, 83, 244] to improve its accuracy.

The thermodynamic models have been used for liquid mixtures where all components are in a subcritical state with respect to their critical temperatures and pressures, including aqueous and nonaqueous solutions. Each of these models—Shereshefsky [257], Connors–Wright (CW) [63], Fu *et al.* [135], and Li *et al.* [56]—require semi-empirical parameters that are obtained from fitting to experimental data of surface tension as a function of liquid-phase composition. The CW [63], Fu *et al.* [135], and Li *et al.* [56] models have two adjustable parameters in a mathematical form that can accurately capture the trend of surface tension as a function of composition, including for nonideal aqueous mixtures. The Shereshefsky model [257] uses only one fitting parameter and can be used to accurately predict surface tension for a narrower range of mixtures than the models with more parameters.

For the statistical mechanics models that calculate molecular distributions through the interface, the presence of each additional compound in a mixture expands the system of differential equations, which are usually solved via time-consuming iterations, bringing the required number of calculations to the millions [157]. These density-theory models need to be coupled with a series of judiciously-chosen Helmholtz free energy functionals which are dependent on density distributions to predict the interfacial properties. Importantly, the accuracy of surface tension predictions made by the density-theory models depends directly on whether the selected Helmholtz free energy functionals accurately predict the liquid-phase density at each composition of interest [327].

The parachor model and the statistical mechanics approaches are capable of predicting the surface tension of mixtures as a function of both composition and temperature (*vs.*, for example, the Li *et al.* [56] and Shereshefsky [257] composition models that must be fit to experimental data separately at each temperature, because their coefficients vary with temperature [251]). However, the accuracy of the parachor model for temperature-dependence is limited by its deficiencies for capturing composition-dependence. The primary drawbacks of the statistical mechanics models are their computational complexity and dependence on the Helmholtz free energy approximations whose accuracy must span wide ranges of temperature and pressure (often, temperature-dependent parameters are used). Thus, there remains a gap in the literature for an easy-to-use, accurate model that reliably describes the surface tension of a broad range of mixtures as a function of both composition and temperature with parameters that can be assumed composition and temperature independent.

In Chapter 2, we proposed an extension of the Connors–Wright model for predicting the surface tension of binary aqueous mixtures (σ_{mix}; N/m) as a function of liquid-phase composition

and temperature, and the equation had the following form:

$$\sigma_{\text{mix}}(x_1, T) = \sigma_2(T) - \left(1 + \frac{b(1-x_1)}{1-a(1-x_1)}\right) x_1 \left(\sigma_2(T) - \sigma_1(T)\right), \tag{3.1}$$

where x_1 is the liquid mole fraction of the nonaqueous compound varying between 0 and 1 (that is, both components are below their pure species critical points), T is the absolute temperature, σ_2 is the surface tension of water, and σ_1 is the surface tension of the nonaqueous compound. The unitless coefficients a and b were obtained by fitting to surface tension data as a function of composition at a reference temperature (any temperature for which there is a sufficient number of experimental data points to adequately capture the trend in surface tension) and then used predictively at other temperatures (the coefficients could be assumed temperature independent). To make predictions of surface tension, our method needs accurate experimental data as inputs, including: (*i*) each pure component's surface tension as a function of temperature, and (*ii*) the mixture's surface tension as a function of composition at one temperature.

To briefly summarize the results of Chapter 2, when we tested predictions from Equation (3.1) against experimental surface tension data for 15 aqueous mixtures, we obtained an average relative deviation from experimental measurements of 0.62% (where the relative deviation is given by $|\hat{\sigma}_i - \sigma_i| / \sigma_i$ given $\hat{\sigma}_i$ is the prediction and σ_i is the measurement) over all available temperatures (a minimum temperature of 293 K or 298 K with a maximum temperature of 323 K for all systems except for one that spanned 303 K to 373 K) [251]. Importantly, in Chapter 5, we use Equation (3.1) to make predictions of surface tension for nitrogen(1) + argon(2) mixtures at temperatures for which experimental data is lacking [253]; this equation enables us to accurately predict the experimentally-determined vapor–liquid equilibrium behavior (dew temperatures) of this mixture in nanopores [5]. (See Appendix A, Section A.8 for a more detailed discussion on the importance of surface tension in these predictions.)

In this chapter, we further extend Equation (3.1) to apply to nonaqueous systems that may contain a supercritical component by introducing a reduced mole fraction. Empirical parameters are assumed constant (independent of temperature) so that predictions can be made at temperatures other than the one used for determining the fitting coefficients. In addition to the two inputs listed for Equation (3.1), we need one additional input: (*iii*) the critical composition of the binary mixture obtained from an equation of state. For this input, we develop a numerical method to calculate the value of the critical composition at a given temperature. An important benefit of our approach is that the molar volumes of the liquid and vapor phases are not needed for predictions, whereas the parachor model and the statistical mechanics models (density gradient theory and density functional theory) all require accurate values for the molar volumes over all compositions and temperatures of interest.

If experimentally measured surface tensions as a function of composition at even a single temperature are unavailable for a specific mixture of interest, a statistical mechanics model could instead be used to obtain these values, which could be used as an input to our model for predictions at any composition and temperature. In this way, a hybrid approach that uses our equation together with inputs from a statistical mechanics model would reduce the overall computational cost required to calculate surface tension as a function of all compositions and temperatures.

We note that throughout this chapter, the use of "supercritical" to describe a mixture does not indicate that it is in a state above the critical point of the mixture; rather, we use this term to denote that one of the components is in a supercritical state with respect to its pure-component critical point, while the mixture is still within the two-phase vapor–liquid phase envelope. The use of "subcritical" refers to a mixture where each pure component is below its individual critical point.

3.2 Results

Based on Equation (3.1), we propose the following equation for the surface tension of a binary mixture as a function of liquid mole fraction and temperature:

$$\sigma_{\text{mix}}(x_{1,\text{r}}, T) = \sigma_2(T) - \left(1 + \frac{b\left(1 - x_{1,\text{r}}(T)\right)}{1 - a\left(1 - x_{1,\text{r}}(T)\right)}\right) x_{1,\text{r}}(T)\left(\sigma_2(T) - \sigma_1(T)\right), \tag{3.2}$$

where σ_{mix} is the surface tension of the mixture at an absolute temperature T, σ_i is the surface tension of pure component i (where $\sigma_2 > \sigma_1$), the reduced mole fraction of component 1 is $x_{1,\text{r}}(T) = x_1/x_{1,\text{cr}}(T)$ where $x_{1,\text{cr}}$ is the critical composition of component 1 at the given temperature (*i.e.*, the maximum liquid-phase composition on the isothermal phase diagram of the binary mixture). Although there are numerous approaches in the literature for calculating the critical temperature and pressure of a multicomponent system given its composition [98, 214, 274], the reverse calculation—determining the critical composition at a given temperature—is less studied. We develop a numerical method for calculating the critical composition of a mixture, and in implementing this method, we choose the Peng–Robinson equation of state (PR-EOS) [213, 230] (see Appendix A, Section A.2 for details on our iterative numerical method). The values of a and b are specific to each binary mixture, and they are determined by fitting to experimental data as a function of mole fraction at one temperature. Note that when $T > T_{\text{cr},1}$ (or equivalently, $x_{1,\text{cr}} < 1$), $\sigma_1 = 0$. Equation (3.2) can also be used for subcritical mixtures in the limiting case where $x_{1,\text{cr}} = 1$, in which case the equation reduces to Equation (3.1).

To apply our approach beyond binary mixtures, we develop a multicomponent form of Equation (3.2). To do so, we start with the multicomponent equation for surface tension proposed by Li *et al.* [56] and convert the proposed coefficients to those proposed by Connors and Wright (CW) [63] (see Chapter 2 [251] for equations to convert between the Li *et al.* and CW models). Then, we introduce a reduced mole fraction for each component of the multicomponent mixture to yield the following equation:

$$\sigma_{\text{mix}}(x_{1,\text{r}},T) = \sum_{i=1}^{n} \sigma_i(T) x_{i,\text{r}}(T) + \sum_{i=1}^{n} \left[\frac{x_{i,\text{r}}(T)}{\sum_{j=1}^{n} \frac{x_{j,\text{r}}(T)}{1-a_{ji}}} \sum_{j=1}^{n} \frac{b_{ji}}{a_{ji}} \left(\frac{1}{1-a_{ji}} \right) \left(\sigma_i(T) - \sigma_j(T) \right) x_{j,\text{r}}\,(T) \right], \quad (3.3)$$

where the reduced mole fractions for all components $i > 1$ are $x_{i>1,\text{r}} = \frac{x_i}{\sum_{j=2}^{n} x_j}(1-x_{1,\text{r}})$, n is the number of components, and a_{ji} and b_{ji} are fitting coefficients obtained from fitting to surface tension data of a binary mixture made up of components j and i where $\sigma_j > \sigma_i$ at a single temperature for each mixture. Note that the following relationships apply to the coefficients in Equation (3.3):

$$a_{ii} = 0 \quad (3.4a)$$

$$b_{ii} = 0 \quad (3.4b)$$

$$\frac{a_{ii}}{b_{ii}} = 1 \quad (3.4c)$$

$$b_{ij} = b_{ji} \quad (3.5a)$$

$$\left(1-a_{ij}\right) = \left(1-a_{ji}\right)^{-1}. \quad (3.5b)$$

While Equations (3.2) and (3.3) show the dependence of surface tension on liquid mole fraction, the surface tension of supercritical mixtures is instead commonly reported in the experimental literature as a function of pressure at a given temperature. Pressure only affects the surface tension of the supercritical mixtures in an indirect way, as it directly changes the liquid-phase composition through a shift in the equilibrium state of the vapor–liquid system; it is because of this change in composition that the surface tension changes. To obtain the composition-dependence of experimental surface tension in the literature, we use the PR-EOS with appropriate binary interaction parameters to calculate the liquid-phase compositions of supercritical binary mixtures at the reported temperatures and pressures. (See Appendix A, Section A.1 for all governing equations and validation of our calculations against experimental vapor–liquid equilibrium data from the literature.)

We make predictions of surface tension for six methane(1) + *n*-alkane(2) systems and two carbon dioxide(1) + *n*-alkane(2) systems for a total of 466 experimental points over a wide range of temperatures (173–442 K) and pressures (0.1–35.9 MPa), obtaining an average absolute

difference between experiments and predictions of 0.22 mN/m over all systems. In addition, we use our equation for seven subcritical mixtures (236 data points), obtaining predictions that are an average absolute difference of 0.10 mN/m away from experimental measurements. For the ternary mixture methanol(1) + ethanol(2) + water(3), surface tension predictions using Equation (3.3) are an average absolute deviation of 0.71 mN/m away from 196 experimental measurements at various concentrations (both dilute and concentrated) and at temperatures between 278 K and 333 K. Because our equation is computationally simple, it can be easily implemented in any application of interest and in any process simulation software for liquid mixtures. Significantly, our equation achieves an accuracy that is comparable to that achieved by the density gradient and density functional theories (reported average absolute deviations obtained with these theories include: 0.05 mN/m for carbon dioxide(1) + *n*-decane(2) at 344.3 K [144]; 0.23 mN/m for a variety of binary hydrocarbon mixtures (403 data points for T between 278.28 K and 442.55 K) [327]; and 0.23 mN/m for a variety of binary halogenated hydrocarbon mixtures (885 points for T between 223.15 K and 343.16 K) [170]).

Our first set of results is the fitting coefficients for the composition dependence of surface tension at a single temperature for a range of supercritical and subcritical mixtures available in the literature. First, we calculate pure component surface tensions at the temperature of interest where we use either: (*i*) the Mulero *et al.* correlation [196] for the supercritical mixtures (those containing methane or carbon dioxide):

$$\sigma_i = \sum_{j=0}^{m_i} \sigma_{j,i} \left(1 - \frac{T}{T_{\mathrm{cr},i}}\right)^{p_{j,i}}, \tag{3.6}$$

where $T_{\mathrm{cr},i}$ is the critical temperature (K) and the values of $\sigma_{j,i}$, $p_{j,i}$ and m_i are specific to each compound (see Appendix A, Table A.4); or (*ii*) a linear equation fit to the reported data for each pure component comprising the subcritical mixtures (all coefficients used are summarized in Table 3.1). Substituting these pure component values into Equation (3.2), we fit Equation (3.2) to experimental data of surface tension as a function of composition at a single temperature with critical composition $x_{\mathrm{cr},1}$ to obtain the coefficients a and b listed in Table 3.2. Given that the fit of surface tension *vs.* liquid mole fraction is a nonlinear equation (Equation (3.2)), the goodness of fit is indicated by the standard deviation (SD), which is calculated by $\mathrm{SD} = \sqrt{\frac{\sum(\hat{\sigma}_i - \sigma_i)^2}{n-p}}$, where n is the number of points used in the fit, $p = 2$ is the number of fitting coefficients, $\hat{\sigma}_i$ is predicted surface tension, and σ_i is experimental surface tension. A list of systems available in the literature is included in Appendix A, Section A.5.1 with detailed notes on the reliability and suitability of data for fitting (briefly, some datasets are in disagreement with other literature sources and others report insufficient data points for fitting purposes).

Table 3.1: For mixtures with both components below their critical point, fitting coefficients with 95% confidence intervals (CI) are listed for each pure component for T in K and σ_i in mN/m with a linear fit ($\sigma_i = \theta_{0,i} + \theta_{1,i}T$) to n experimental data points from each reference. Note, for some datasets, all experimental data lies exactly on the linear fit, the standard deviation (SD) is zero, and the confidence interval cannot be calculated.

Component	n	Temperatures [K]	$\theta_{0,i} \pm 95\%$ CI	$\theta_{1,i} \pm 95\%$ CI	SD [mN/m]	Data Reference
dodecane(1)	4	298–313	50.23 ± 3.09	-0.086 ± 0.010	0.026	Schmidt *et al.* [245]
benzene(2)	4		68.10	-0.134	0	
n-hexane(1)	4	298–313	49.01 ± 0.70	-0.104 ± 0.002	0.006	Schmidt *et al.* [245]
benzene(2)	4		68.10	-0.134	0	
cyclohexane(1)	4	293–313	57.35 ± 11.70	-0.111 ± 0.039	0.133	Wohlfarth [119, 306]
benzene(2)	4		64.85 ± 4.90	-0.123 ± 4.898	0.056	
carbon tetrachloride(1)	5	288–308	66.26	-0.134	0	Teixiera *et al.* [281]
methyl iodide(2)	5		67.13 ± 0.19	-0.123 ± 0.190	0.003	
carbon tetrachloride(1)	5	298–318	66.26	-0.134	0	Teixiera *et al.* [281]
acetonitrile(2)	5		66.41 ± 0.20	-0.127 ± 0.196	0.003	
carbon tetrachloride(1)	6	293–318	62.92 ± 0.18	-0.122 ± 0.001	0.004	Luengo *et al.* [176]
carbon disulfide(2)	6		73.48 ± 1.42	-0.140 ± 1.418	0.035	
dichloromethane(1)	4	293–308	65.54 ± 0.45	-0.129 ± 0.002	0.004	Aracil *et al.* [13]
carbon disulfide(2)	4		75.71	-0.148	0	

Table 3.2: Fitting coefficients (a and b) with 95% confidence intervals for Equation (3.2) for binary organic systems with corresponding fitting temperature (T_{fit}), critical composition of component 1 ($x_{\text{cr},1}$), number of points used (n), and standard deviation of the fit (SD). The literature source for experimental data is listed under the heading "Data Reference".

Component 1	Component 2	n	T_{fit} [K]	$x_{\text{cr},1}(T_{\text{fit}})$	$a \pm 95\%$ CI	$b \pm 95\%$ CI	SD [mN/m]	Data Reference
methane	ethane	6	133	1.000	0.52 ± 0.89	0.50 ± 0.44	0.49	[19]
	propane	6	258	0.776	-1.42 ± 0.81	1.53 ± 0.34	0.07	[302]
	n-butane	6	311	0.730	-2.43 ± 0.54	2.06 ± 0.22	0.01	[201, 215]
	n-hexane	8	298	0.846	-1.49 ± 0.77	2.08 ± 0.55	0.05	[183]
	n-heptane	16	311	0.860	-1.44 ± 0.26	1.53 ± 0.09	0.11	[12]
	n-decane	23	311	0.902	-2.01 ± 0.21	1.49 ± 0.05	0.09	[271]
carbon dioxide	*n*-butane	18	319	0.871	0.70 ± 0.13	0.41 ± 0.06	0.12	[127]
	n-heptane	6	323	0.957	-1.91 ± 2.69	0.91 ± 0.59	0.21	[202]
dodecane	benzene	5	298	1.000	0.86 ± 0.07	1.06 ± 0.13	0.04	[245]
n-hexane	benzene	7	298	1.000	0.80 ± 0.04	0.51 ± 0.03	0.05	[245]
cyclohexane	benzene	11	293	1.000	0.43 ± 0.20	0.84 ± 0.13	0.07	[119, 306]
carbon tetrachloride	methyl iodide	5	288	1.000	0.66 ± 0.08	1.00 ± 0.10	0.03	[281]
	acetonitrile	9	298	1.000	0.82 ± 0.06	0.69 ± 0.07	0.03	[281]
	carbon disulfide	10	293	1.000	0.56 ± 0.18	0.77 ± 0.15	0.11	[176]
dichloromethane	carbon disulfide	8	293	1.000	0.45 ± 0.22	1.05 ± 0.20	0.09	[13]

Having obtained fitting coefficients at one temperature, we assume that these coefficients (a and b) are temperature-independent, and we make predictions of surface tension as a function of liquid-phase composition using Equation (3.2) for all elevated temperatures studied experimentally. At each considered temperature, the critical composition is calculated, with values summarized in Table 3.3 and Table 3.4. For the pure-component surface tensions in Equation (3.2), we use the Mulero *et al.* correlation [196] for pure components comprising supercritical mixtures or the linear equation in Table 3.1 for those comprising subcritical mixtures. For comparison, we also make surface tension predictions using the parachor model [302] with volume-shifted PR-EOS phase densities of the mixture [3] and pure-component parachor values obtained from fitting pure-component PR-EOS phase densities (also volume-shifted) to temperature-dependent surface tension data retrieved from the DIPPR database ([72]; see Appendix A, Section A.4.1). We compile the performance of our new model and the parachor model in Table 3.5 with a list of the average absolute deviation $\left(\text{AAD} = \frac{1}{j}\sum_{i=1}^{j}|\hat{\sigma}_i - \sigma_i|\right)$ and maximum absolute deviation for each studied mixture. Over the broad range of supercritical hydrocarbon mixtures and subcritical organic mixtures, our new model has an AAD of 0.17 mN/m compared to the parachor model's AAD of 0.44 mN/m.

Table 3.3: Our calculated critical composition of carbon dioxide as a function of temperature for carbon dioxide(1) + *n*-alkane(2) mixtures.

carbon dioxide(1) +	Temperature [K]	Critical Composition $x_{1,\text{cr}}$	Data Reference
n-butane(2)	319.30 344.30 377.60	0.871 0.725 0.517	Hsu *et al.* [127]
n-heptane(2)	323.15 353.15	0.957 0.885	Niño-Amézquita *et al.* [202]
	323.00 353.00	0.958 0.885	Jaeger *et al.* [130]

Table 3.4: Our calculated critical composition of methane as a function of the temperatures listed in each literature source for methane(1) + *n*-alkane(2) mixtures.

methane(1) +	Temperature [K]	Critical Composition $x_{1,\mathrm{cr}}$	Data Reference
ethane(2)	133.15	1.000	Baidakov *et al.* [19]
	173.15	1.000	
	193.15	0.985	
	213.15	0.869	
	233.15	0.737	
	253.15	0.589	
	263.15	0.505	
	273.15	0.412	
	283.15	0.305	
propane(2)	258.15	0.776	Weinaug and Katz [302]
	283.15	0.685	
	303.15	0.596	
	318.15	0.513	
	338.15	0.370	
	272.20	0.727	Seneviratne *et al.* [247]
	285.50	0.675	
	303.34	0.595	
n-butane(2)	310.93	0.730	Pennington and Hough [201, 215]
	327.59	0.685	
	335.93	0.660	
	344.26	0.631	
n-hexane(2)	298.15	0.846	Massoudi and King [183]
	300.00	0.845	Niño–Amézquita *et al.* [203]
	350.00	0.796	
n-heptane(2)	310.93	0.860	Warren and Hough [301]
	327.59	0.850	
	344.26	0.838	
	360.93	0.823	
	377.59	0.806	
	394.26	0.787	
	410.93	0.763	
	427.59	0.734	
	310.93	0.860	Amin and Smith [12]
	338.71	0.842	
	366.48	0.818	
	394.26	0.787	
n-decane(2)	310.93	0.902	Stegemeier *et al.* [271]
	327.59	0.898	
	344.26	0.893	
	360.93	0.887	
	310.93	0.902	Amin and Smith [12]
	366.48	0.884	
	410.93	0.862	
	313.30	0.901	Pereira *et al.* [216]
	343.20	0.893	
	392.60	0.873	
	442.30	0.841	

Table 3.5: Average absolute deviations from experimental data $\left(\frac{1}{j}\sum_{i=1}^{j}|\hat{\sigma}_i - \sigma_i|\right)$ and maximum absolute deviations ($|\hat{\sigma}_i - \sigma_i|$) of surface tension predictions obtained using either our new model (Equation (3.2)) or the parachor model (see Appendix A, Section A.5.2) for each considered binary mixture over a range of temperatures and pressures with j points from each listed literature source. The last row considers all studied systems. The columns for average absolute deviation are shaded with a color gradient from dark blue (0 mN/m) to white (0.6 mN/m) to dark red (1.2 mN/m). White text on a blue background indicates that the value is less than 0.2 mN/m.

					Parachor model absolute deviation		New model absolute deviation		
Component 1	Component 2	Temperatures [K]	Pressures [MPa]	j	Average [mN/m]	Max [mN/m]	Average [mN/m]	Max [mN/m]	Data Reference
methane	ethane	173–283	0.1–3.9	58	0.56	1.26	0.16	0.45	[19]
	propane	283–338	1.4–8.5	36	0.33	0.48	0.17	0.27	[302]
		272–303	1.0–8.7	24	0.26	0.32	0.22	0.26	[247]
	n-butane	328–344	9–10	9	0.23	0.32	0.08	0.11	[201, 215]
	n-hexane	300–350	2–10	9	0.26	0.36	0.34	0.49	[203]
	n-heptane	311–428	2.8–24.8	101	0.44	0.62	0.16	0.24	[301]
		339–394	2.8–24.1	37	0.28	0.41	0.08	0.13	[12]
	n-decane	328–361	10.3–35.9	52	0.27	0.51	0.06	0.12	[271]
		311–411	2.8–34.5	55	1.24	1.58	0.46	0.76	[12]
		313–442	0.5–30.5	39	0.69	0.89	0.59	0.82	[216]
carbon dioxide	*n*-butane	344–378	2.9–8.0	24	0.26	0.40	0.12	0.21	[127]
	n-heptane	353	0.1–11.2	8	0.21	0.42	0.15	0.29	[202]
		323–353	0.1–11.2	14	0.53	0.55	0.26	0.29	[130]
dodecane	benzene	303–313	–	12	0.27	0.40	0.10	0.20	[245]
n-hexane	benzene	303–313	–	10	0.61	0.87	0.14	0.22	[245]
cyclohexane	benzene	293–303	–	28	0.43	0.44	0.09	0.13	[156]
		293–333	–	33	0.66	0.94	0.10	0.18	[151, 306]
		298–313	–	27	0.37	0.55	0.08	0.14	[119, 306]
carbon tetrachloride	methyl iodide	293–308	–	34	0.47	0.61	0.05	0.09	[281]
	acetonitrile	303–318	–	29	0.42	0.56	0.04	0.08	[281]
	carbon disulfide	298–318	–	40	0.14	0.31	0.10	0.19	[176]
dichloromethane	carbon disulfide	298–308	–	23	0.83	1.15	0.18	0.29	[13]
all systems		173–442		702	0.44	1.58	0.17	0.82	

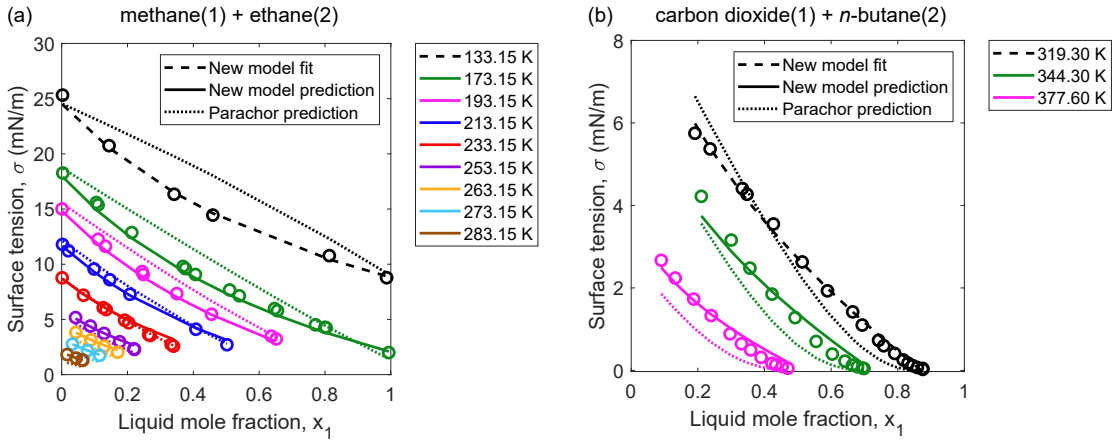

Figure 3.1: Fits (dashed black lines using Equation (3.2) and predictions of surface tension (solid lines using Equation (3.2); dotted lines using the parachor model (Appendix A, Equation (A.22))) as a function of liquid-phase composition for (a) methane(1) + ethane(2) and (b) carbon dioxide(1) + *n*-butane(2). Experimental data points (○) that are used in fits are shown in black; all other symbol colors serve as comparisons to theoretical predictions in the same color at the listed temperatures. Data in (a) are from Baidakov *et al.* [19] and in (b) are from Hsu *et al.* [127].

As representative systems of the supercritical set of studied mixtures, we show detailed results for methane(1) + ethane(2) and carbon dioxide(1) + *n*-butane(2) in Figure 3.1, where the dashed black lines show the fit of Equation (3.2) to experimental data (black circles) at the lowest available temperature. All solid lines are predictions using Equation (3.2) at elevated temperatures with critical compositions calculated from the PR-EOS and with pure-component surface tensions evaluated using Equation (3.6) (coefficients in Appendix A, Table A.4); these predictions closely agree with experimental trends of surface tension. Dotted lines are predictions calculated using the parachor model for mixtures ([302]; Appendix A, Equation (A.22)), which performs with mixed accuracy.

Figure 3.2 shows detailed results for two representative systems from the group of studied subcritical organic mixtures: dodecane(1) + benzene(2) and dichloromethane(1) + carbon disulfide(2). The fit of Equation (3.2) to experimental data of surface tension is shown at the lowest temperature (dashed black line), along with predictions using Equation (3.2) at all elevated temperatures (see Table 3.1 for the linear equation used for each pure component's surface tension *vs.* temperature). The parachor model predictions are shown with dotted lines. Our model predictions consistently outperform the parachor model over the available range of experimental temperatures and compositions.

Figure 3.3 graphically summarizes the accuracy of predictions for all binary systems to which we have applied our model: methane(1) + *n*-alkane(2), carbon dioxide(1) + *n*-alkane(2),

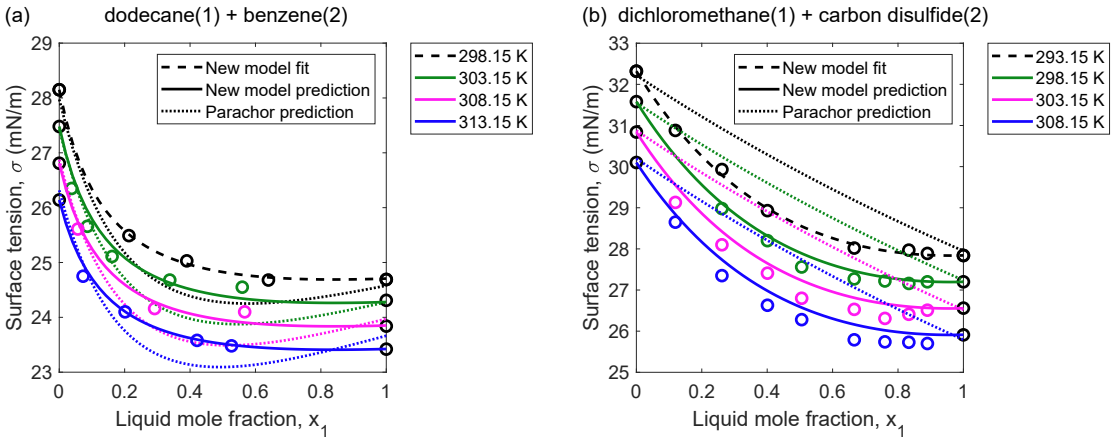

Figure 3.2: Fits (dashed black lines using Equation (3.2) and predictions of surface tension (solid lines using Equation (3.2); dotted lines using the parachor model (Appendix A, Equation (A.22))) as a function of liquid-phase composition for (a) dodecane(1) + benzene(2) and (b) dichloromethane(1) + carbon disulfide(2). Experimental data points are shown by open circles (○; black symbols are used in fits: both pure components *vs.* temperature and mixture data at one temperature; all other symbol colors serve as comparisons to theoretical predictions in the same color at the listed temperatures). Data in (a) are from Schmidt *et al.* [245] and in (b) are from Aracil *et al.* [13].

various subcritical organic mixtures, and aqueous mixtures. Fitting coefficients to describe the composition-dependence of surface tension for all nonaqueous systems are listed in Table 3.2, and the temperature-dependence of each pure component is obtained using the Mulero *et al.* correlation (Equation (3.6)) [196] or the linear equation using the coefficients in Table 3.1. For the coefficients obtained for aqueous systems, refer to Chapter 2. All points used for fitting purposes are excluded from this figure (any at T_{fit} listed in Table 3.2 and any pure component values). Figure 3.3 highlights that our model accurately predicts the surface tension of a wide variety of nonideal mixtures (nonideal in the sense that $\sigma_{\text{mix}} \neq \sigma_1 x_1 + \sigma_2 x_2$) over a range of temperatures and pressures, and this accuracy is of the same order of magnitude as predictions obtained using density gradient theory or density functional theory [144, 170, 327]. Such close agreement is the result of fitting coefficients that can be assumed to be independent of temperature. As previously noted by Li and Firoozabadi [167, 216] and Pereira *et al.* [216], we likewise note the unexpectedly high surface tension measurements at low pressures for methane(1) + *n*-decane(2) from Amin and Smith [12] that are within the dashed oval in Figure 3.3. For details of each individual system in Table 3.5, refer to Appendix A, Section A.5.2 for plots of vapor–liquid equilibrium, critical composition, surface tension as a function of composition (and pressure for supercritical systems), and the difference between predictions and experimental data.

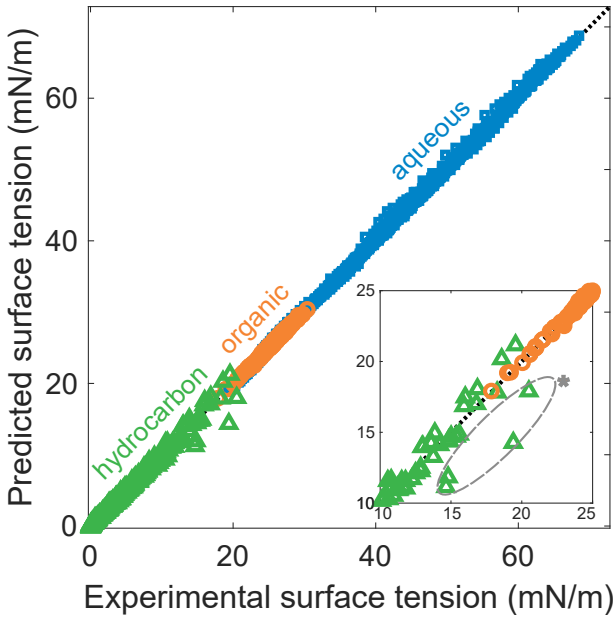

Figure 3.3: Predicted surface tension *vs.* experimental surface tension for all methane(1) + *n*-alkane(2) and carbon dioxide(1) + *n*-alkane(2) mixtures (hydrocarbon, △), as well as all binary mixtures where both components are below their pure critical points (organic, ○). We also include all aqueous mixtures (□) from Chapter 2 [251], highlighting the applicability of our approach to a broad range of systems, temperatures, and pressures. This figure contains the 702 points from the 15 supercritical and subcritical systems in Table 3.5 and 961 points from the 15 aqueous mixtures in Chapter 2 [251]. The four points within the dashed circle from the methane(1) + *n*-decane(2) system at low pressures are likely experimental outliers [12].

Finally, we make predictions for the surface tension of the ternary mixture methanol(1) + ethanol(2) + water(3) as a function of composition and temperature using Equation (3.3), as illustrated in Figure 3.4. The inputs to these predictions are (*i*) coefficients to describe surface tension as a function of temperature for each pure component and (*ii*) coefficients to describe surface tension for each binary mixture as a function of composition at a single temperature (obtained from fitting Equation (3.1)). All coefficients used in the predictions illustrated in Figure 3.4 are taken from Chapter 2 [251] for binary aqueous systems and are summarized in Appendix A, Tables A.14 and A.15, and all illustrated experimental data are from Kharin *et al.* [140]. Surface tension predictions using Equation (3.3) are an average absolute deviation of 0.71 mN/m and 2.54% away from experimental measurements of the methanol(1) + ethanol(2) + water(3) mixture for 196 data points at various concentrations (both dilute and concentrated) and at temperatures between 278 K and 333 K. We additionally present ternary predictions for the supercritical ternary mixture carbon dioxide(1) + *n*-butane(2) + *n*-decane(3) in comparison to experimental data obtained by Nagarajan *et al.* [198] in Appendix A, Section A.7.2.

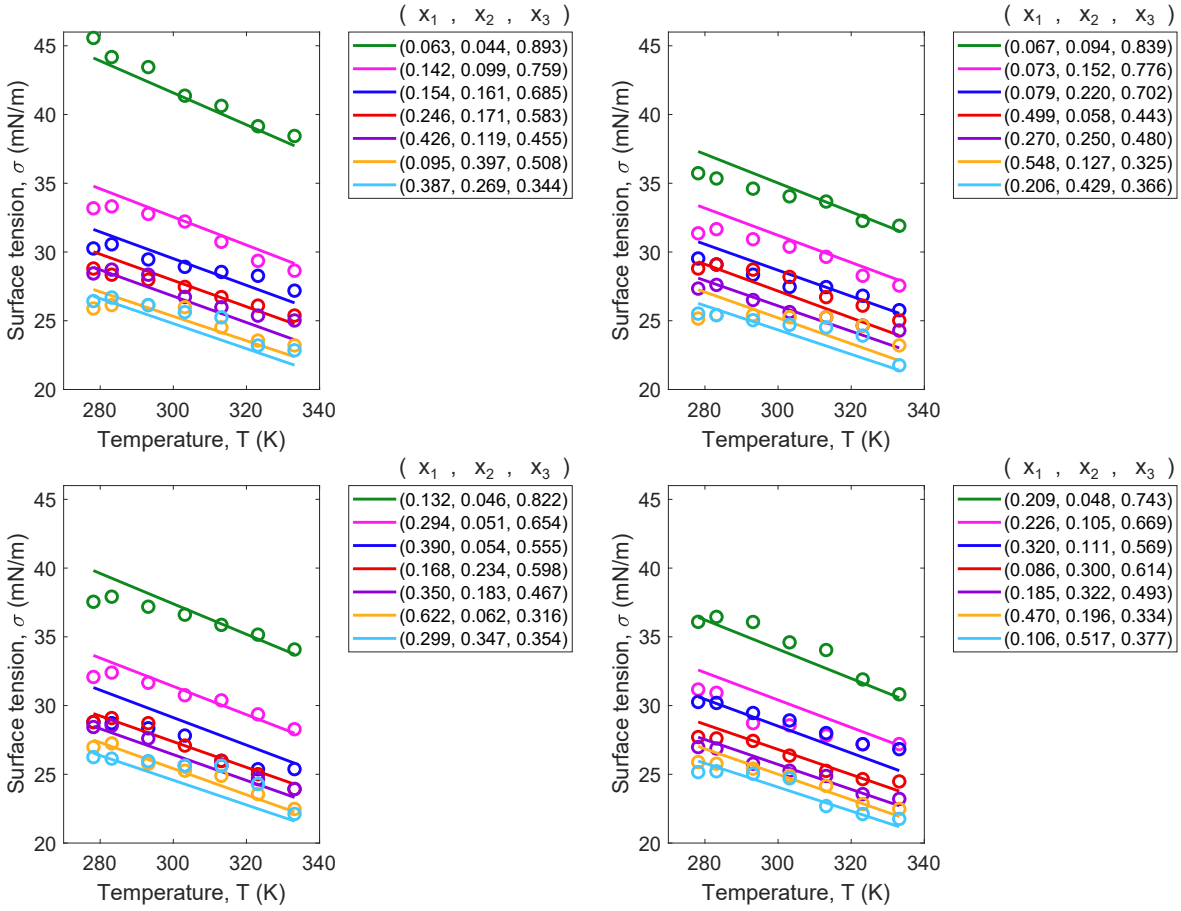

Figure 3.4: Surface tension as a function of temperature for mixtures containing methanol(1) + ethanol(2) + water(3), as measured experimentally (symbols) by Kharin *et al.* [140] and as predicted by Equation (3.3) (lines) with coefficients for each pure component and each aqueous binary mixture at a single temperature from Chapter 2 [251], as summarized in Appendix A, Tables A.14 and A.15. The mixture compositions (mole fractions of each component computed from the reported weight fractions) are shown in the legend of each graph. No fitting coefficients need to be extracted from surface tension data of the ternary mixture to make predictions.

3.3 Discussion

Our new model (Equation (3.2)) can be used to predict the surface tension of a wide spectrum of mixtures: those containing supercritical hydrocarbons, subcritical organic compounds, or water. A key benefit of these predictions is that they bypass the calculation of molar volumes for each phase at every temperature, unlike both the parachor model and density gradient theory predictions. This is significant because the estimation of liquid molar volumes in particular can be a challenge depending on which equation of state is selected (*e.g.*, for the PR-EOS, a volume shift obtained from fitting to experimental data is needed). In contrast to the parachor model and density gradient theory, we constrain our use of the PR-EOS to only determining vapor–liquid phase equilibrium states (compositions of the liquid phase) and the critical compositions of each mixture as a function of temperature. We also demonstrated that our model can be applied to multicomponent mixtures through Equation (3.3) for predicting surface tension as a function of composition and temperature. The coefficients used to make these predictions are obtained from each binary mixture that constitutes the ternary one, and these coefficients can be assumed composition- and temperature-independent. No coefficients need to be extracted from the ternary data.

We note that Equation (3.2) may predict an unphysical negative surface tension as the critical composition of a supercritical mixture is approached, and we attribute this partly to the empirical nature and functional form of the equation, but also to our use of the PR-EOS in calculating the critical composition of the mixture, which may be different from the true critical composition. Nevertheless, for the wide range of systems, temperatures, and compositions considered, Equation (3.2) and its multicomponent form Equation (3.3) provide a straightforward approach for accurately predicting surface tension in the diverse applications that are governed by surface effects.

Most importantly, the practical utility of such an equation is in its application to systems for which no experimental data is available. For example, in Chapter 5 [253], we predict the dew temperatures of a mixture containing nitrogen(1) + argon(2) in nanopores within 0.45% of experimental measurements [5]; surface tension is the key variable in the system of equations that is used to make these predictions. Since experimental measurements of the surface tension for nitrogen(1) + argon(2) mixtures over a wide range of compositions were available at only a single temperature, we use Equation (3.1) to extrapolate to higher temperatures around the dew point of the mixture. If the surface tension is instead assumed to be constant with either temperature or composition, predictions of dew point become increasingly inaccurate (see Appendix A, Section A.8).

3.4 Conclusions

Experimentally, it is feasible to perform surface tension measurements for a pure component at multiple temperatures or for various mixture compositions at a single temperature, but the shear number of experimental measurements required for mixtures over many compositions and temperatures is both time-consuming and costly. Therefore, accurate theoretical predictions of surface tension as a function of both composition and temperature are advantageous for the wide range of mixtures present across various applications and fields of study. The computational simplicity of a theoretical approach is particularly important when surface tension is one piece of a larger system of equations that describe, for example, phase equilibrium [253, 254].

We present a model of surface tension as a function of composition and temperature applicable to a wide range of supercritical hydrocarbon mixtures, subcritical organic systems, and subcritical aqueous solutions. As a case study, we additionally extend the model to a mixture of cryogenic gases (nitrogen(1) + argon(2)) and investigate the importance of an accurate representation of surface tension for the phase equilibrium of the system in nanopores. Because the coefficients in our model can be assumed composition- and temperature-independent, accurate predictions can be made for conditions where experimental data is unavailable. The development of a simple equation for $\sigma(x_1, T)$ should prove to be useful in understanding, designing, and controlling both natural and industrial processes. For example, concentration and temperature can both be treated as design parameters instead of being limited to either a pure component at any temperature or a mixture at a single temperature.

The only experimental data needed for using our surface tension model for multicomponent systems are: (*i*) surface tension *vs.* temperature for each pure component (*e.g.*, from DIPPR [72]) and (*ii*) surface tension *vs.* composition for each constituent binary mixture of interest at one temperature, which may be found in the literature (*e.g.*, Wohlfarth and Wohlfarth [306]). Alternatively, if experimental data of surface tension is lacking, predictions obtained from a statistical mechanics model for each binary mixture as a function of composition at one temperature could be used as inputs instead. Our model lowers the overall computational cost required to make predictions of surface tension for each binary mixture at other temperatures and compositions. Additionally, our model can predict the surface tension of mixtures with more than two components *via* Equation (3.3) using coefficients obtained from every constituent binary mixture, each at a single temperature (no fitting coefficients need to be extracted from surface tension data of the multicomponent mixture).

If the mixture contains a supercritical compound, the critical composition of this compound needs to be calculated as a function of temperature using an appropriate equation of state. For any of the studied systems, pure-component surface tension *vs.* temperature can be substituted

into Equation (3.2), the critical composition can be calculated (see Appendix A, Section A.2 for a flowchart of our numerical method), and the tabulated coefficients a and b can be used to predict surface tension. Our model is advantageous compared to those in the literature that rely on accurate phase density predictions from equations of state (*e.g.*, the parachor model and density gradient theory predictions), because density predictions are unnecessary as inputs to Equation (3.2) or Equation (3.3).

Finally, we note a vital need for ensuring the accuracy of experimental measurements for the surface tension of mixtures, particularly those containing supercritical compounds (*e.g.*, methane and carbon dioxide), and a need for a larger database of experimental systems with which predictions can be compared.

PART II

PHASE DIAGRAMS

Chapter 4

Isothermal Vapor–Liquid Phase Diagrams for Multicomponent Systems with Nanoscale Radii of Curvature[1]

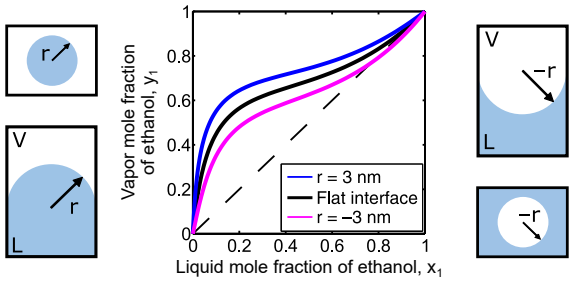

Abstract

The effect of interface curvature on phase equilibrium has been much more studied for single-component than multicomponent systems. We isolate the effect of curvature on multicomponent vapor–liquid equilibrium (VLE) phase envelopes and phase composition diagrams using the ideal system methanol + ethanol and the nonideal system ethanol + water as illustrative examples. An important finding is how nanoscale interface curvature shifts the azeotrope (equal volatility point) of nonideal systems. Understanding of the effect of curvature on VLE can be exploited in future nanoscale prediction and design.

[1]Reproduced, with minor modifications, with permission from N. Shardt and J. A. W. Elliott. "Thermodynamic Study of the Role of Interface Curvature on Multicomponent Vapor–Liquid Phase Equilibrium". *Journal of Physical Chemistry A* 120.14 (2016), pp. 2194–2200. http://pubs.acs.org/articlesonrequest/AOR-Kgv8I2tpBEfqdH9e5aKX Copyright 2016 American Chemical Society. J. A. W. Elliott conceived the original idea.

4.1 Introduction

Vapor–liquid equilibrium (VLE) drives chemical processes that occur under conditions yielding two phases. A phase diagram outlines the temperature or pressure at which a liquid, vapor, or mixture of phases will exist. Curvature of the vapor–liquid interface alters equilibrium pressure in the vapor phase, as described first by the Kelvin equation [283] and later corrected by Gibbs [77, 108, 138]. This equation is valid for a pure component assuming an incompressible liquid and an ideal gas. The Kelvin equation and its liquid–liquid and liquid–solid analogs describe capillary condensation, adsorption hysteresis [41, 42, 55, 60, 67, 126, 186, 193], nucleation [79, 84–87, 205, 292, 297, 323, 324], and emulsion stability [136]. Single component systems have been extensively examined theoretically [38, 87, 155, 186, 297, 323, 324]. Early experimental work [113, 265, 282] and more recent work [100, 101, 150, 154] verified the Kelvin equation, with discrepancies observed for systems containing water [99, 258]. Using certain capillary plates results in deviations from the Kelvin equation [61, 234–237, 307, 318, 319] due to molecular interactions between the liquid and the capillary walls [236], adsorption, or surface contamination [99]. Closer experimental agreement was achieved by Shin and Simandl [249, 250, 262, 263] for multicomponent mixtures.

In this chapter, we apply Gibbsian thermodynamics to multicomponent mixtures to calculate phase envelopes as a function of curvature. We gain an understanding of how an azeotrope shifts with curvature. The thermodynamics of curved interfaces can be applied in atmospheric science [164, 246], hydrocarbon recovery [88, 97], distillation [143, 233, 318], and catalyst design [24, 209, 308].

4.2 Governing Equations

Gibbsian composite-system thermodynamics [108] provides a framework to determine the equilibrium states of a given composite system—a system that is made up of simple systems, but that itself is not a simple system, such as a multicomponent multiphase system. A stable equilibrium state occurs when the entropy of the composite system is at a maximum [46]. That is, for an isolated system consisting of a vapor and a liquid phase separated by an interface, the following equation determines equilibrium states:

$$\mathrm{d}S^{\mathrm{L}} + \mathrm{d}S^{\mathrm{V}} + \mathrm{d}S^{\mathrm{LV}} = 0, \tag{4.1}$$

where S is entropy and the superscripts L, V, and LV denote the liquid phase, the vapor phase, and the liquid–vapor interface, respectively. Substituting the physical constraints of an isolated

multicomponent system into Equation (4.1) yields equations for thermal, mechanical, and chemical equilibrium. For an isolated n-component liquid–vapor system with a flat liquid–vapor interface, the conditions for equilibrium (in accordance with Gibbs' dividing surface approach) are found to be:

$$T^{\mathrm{V}} = T^{\mathrm{L}} = T^{\mathrm{LV}} \tag{4.2}$$

$$P^{\mathrm{V}} = P^{\mathrm{L}} \tag{4.3}$$

$$\mu_i^{\mathrm{L}} = \mu_i^{\mathrm{V}} \text{ for } i = 1 \tag{4.4}$$

$$\mu_i^{\mathrm{L}} = \mu_i^{\mathrm{V}} = \mu_i^{\mathrm{LV}} \text{ for } i = 2, 3, ..., n, \tag{4.5}$$

where T is absolute temperature, P is pressure, μ is chemical potential, and the subscript i refers to the ith component.

For a spherical liquid–vapor interface, the conditions for equilibrium (in accordance with Gibbs' surface of tension approach) are:

$$T^{\mathrm{V}} = T^{\mathrm{L}} = T^{\mathrm{LV}} \tag{4.6}$$

$$P^{\mathrm{L}} - P^{\mathrm{V}} = 2\sigma/r \tag{4.7}$$

$$\mu_i^{\mathrm{L}} = \mu_i^{\mathrm{V}} = \mu_i^{\mathrm{LV}} \text{ for } i = 1, 2, 3, ..., n. \tag{4.8}$$

Equation (4.7) is the Young–Laplace equation for a spherical interface [194], where σ is the surface tension of the liquid mixture and r is the radius of curvature of the interface. As illustrated in Figure 4.1, the radius of curvature appearing in Equation (4.7) is defined here to be positive for a convex liquid surface in a capillary or for a droplet of liquid in vapor, and to be negative for a concave liquid surface in a capillary or for a bubble of vapor in liquid.

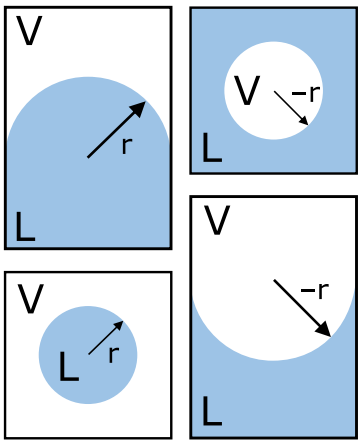

Figure 4.1: System configurations of positive and negative radii of curvature.

The equations for equilibrium can be solved by inserting the equilibrium pressures and temperatures of the phases into the equality of chemical potentials of the liquid and vapor phases (Equation (4.4) and the first equivalence of Equations (4.5) and (4.8)) and used to determine the composition and quantity of vapor and liquid phases. Equations of state are used to write chemical potentials as functions of temperature, pressure, and composition.

For a multicomponent system with assumptions of an ideal gas and an incompressible liquid, the chemical potentials of the vapor and liquid phases for each component are given by [78, 298]

$$\mu_i^{\mathrm{V}}(T,P^{\mathrm{V}}) = \mu_i^{\mathrm{V}}(T,P_i^{\mathrm{sat}}) + RT\ln\left(y_i P^{\mathrm{V}}/P_i^{\mathrm{sat}}\right) \tag{4.9}$$

and

$$\mu_i^{\mathrm{L}}(T,P^{\mathrm{L}}) = \mu_i^{\mathrm{L}}(T,P_i^{\mathrm{sat}}) + v_i^{\mathrm{L}}(P^{\mathrm{L}} - P_i^{\mathrm{sat}}) + RT\ln(\gamma_i x_i), \tag{4.10}$$

respectively. Here, y_i is the mole fraction of component i in the vapor phase, x_i is the mole fraction in the liquid phase, P_i^{sat} is the saturation pressure at a given temperature, v_i^{L} is the liquid molar volume of pure component i [78], R is the universal gas constant, and γ_i is the species-dependent activity coefficient. The activity coefficient γ_i can be modeled, for example, by the Margules equations for a two-component system as follows [266]

$$\ln(\gamma_1) = x_2^2\left[A_{12} + 2\left(A_{21} - A_{12}\right)x_1\right] \tag{4.11}$$

and

$$\ln(\gamma_2) = x_1^2\left[A_{21} + 2\left(A_{12} - A_{21}\right)x_2\right], \tag{4.12}$$

where A_{12} and A_{21} are species-dependent empirical constants at a given temperature. The activity coefficient captures the nonideality of liquid mixtures (*e.g.*, ethanol + water) where the magnitudes of intermolecular interactions are unequal between the components of the mixture.

Substituting Equations (4.9) and (4.10) into the equality of chemical potentials between the vapor and liquid phases (Equations (4.4), (4.5), and (4.8)) results in a generalized modified Raoult's Law [78]:

$$y_i P^{\mathrm{V}} = \gamma_i x_i P_i^{\mathrm{sat}} \exp\left[v_i^{\mathrm{L}}(P^{\mathrm{L}} - P_i^{\mathrm{sat}})/(RT)\right]. \tag{4.13}$$

If the liquid phase is an ideal mixture ($\gamma_i = 1$), Equation (4.13) becomes generalized Raoult's Law:

$$y_i P^{\mathrm{V}} = x_i P_i^{\mathrm{sat}} \exp\left[v_i^{\mathrm{L}}(P^{\mathrm{L}} - P_i^{\mathrm{sat}})/(RT)\right]. \tag{4.14}$$

The exponential term in Equation (4.13) or Equation (4.14) is known as the Poynting correction [78, 222, 305], and at low pressures and high temperatures, this term becomes unity. Setting the Poynting correction to 1 in Equation (4.14) results in Raoult's Law, which is commonly used in

designing equipment that operates at such moderate conditions.

4.2.1 Flat Interface Vapor–Liquid Equilibrium

Vapor–liquid equilibrium calculation procedures for flat interfaces are described in textbooks [78, 266]. For example, Raoult's Law given by

$$y_i P^{\mathrm{V}} = x_i P_i^{\mathrm{sat}} \tag{4.15}$$

is used under conditions for which the Poynting correction can be neglected, and it is valid when assuming an ideal gas in the vapor phase and an ideal incompressible solution in the liquid phase. The bubble pressure is the pressure at which the first bubble of vapor appears, *i.e.* the equilibrium pressure in the vapor phase for known x_i. For a flat interface, the equilibrium pressure in the vapor phase is equal to the pressure in the liquid phase. The bubble pressure can be calculated by combining Equation (4.15) for i components with $\sum_i y_i = 1$:

$$P_{\mathrm{b}}^{\mathrm{V}} = \sum_i x_i P_i^{\mathrm{sat}}, \tag{4.16}$$

where the subscript 'b' stands for bubble.

The dew pressure is the pressure at which the first drop of liquid appears for known y_i, *i.e.* the equilibrium pressure in the vapor phase. Rearranging Equation (4.15) in terms of x_i for each component and using $\sum_i x_i = 1$ gives the following equation to calculate the dew pressure:

$$P_{\mathrm{d}}^{\mathrm{V}} = \left(\sum_i y_i / P_i^{\mathrm{sat}} \right)^{-1}, \tag{4.17}$$

where the subscript 'd' stands for dew.

A more general expression of Raoult's Law should be used in cases of high liquid phase pressure. For a flat interface between an ideal liquid mixture and an ideal vapor phase, the pressure in the vapor equals the pressure in the liquid ($P^{\mathrm{V}} = P^{\mathrm{L}}$), and an expression for bubble pressure can be obtained by combining Equation (4.14) and $\sum_i y_i = 1$, as shown in Equation (4.18):

$$P_{\mathrm{b}}^{\mathrm{V}} = \sum_i x_i P_i^{\mathrm{sat}} \exp\left[v_i^{\mathrm{L}} (P_{\mathrm{b}}^{\mathrm{V}} - P_i^{\mathrm{sat}}) / (RT) \right]. \tag{4.18}$$

To obtain an expression for the dew pressure, Equation (4.14) is rearranged to the form

$$x_i = \frac{y_i P^{\mathrm{V}}}{P_i^{\mathrm{sat}} \exp\left[v_i^{\mathrm{L}} (P^{\mathrm{V}} - P_i^{\mathrm{sat}}) / (RT) \right]}, \tag{4.19}$$

where again the fact that $P^{\mathrm{V}} = P^{\mathrm{L}}$ for a flat interface is used. Equation (4.19) is then combined with $\sum_i x_i = 1$ to obtain the following dew pressure expression:

$$P_{\mathrm{d}}^{\mathrm{V}} = \left(\sum_i \frac{y_i}{P_i^{\mathrm{sat}} \exp\left[v_i^{\mathrm{L}} (P_{\mathrm{d}}^{\mathrm{V}} - P_i^{\mathrm{sat}})/(RT) \right]} \right)^{-1}. \tag{4.20}$$

Iteration is used to solve Equation (4.18) and Equation (4.20) with an initial guess of $P_{\mathrm{d}}^{\mathrm{V}}$ calculated from Equation (4.16) and Equation (4.17), respectively, until the value for pressure in the vapor phase converges.

For a flat interface between a nonideal liquid mixture and an ideal vapor phase, $P^{\mathrm{V}} = P^{\mathrm{L}}$ and using $\sum_i y_i = 1$ and Equation (4.13), the bubble pressure is

$$P_{\mathrm{b}}^{\mathrm{V}} = \sum_i \gamma_i x_i P_i^{\mathrm{sat}} \exp\left[v_i^{\mathrm{L}} (P_{\mathrm{b}}^{\mathrm{V}} - P_i^{\mathrm{sat}})/(RT) \right]. \tag{4.21}$$

By first assuming a Poynting correction value of 1, the bubble pressure can be calculated iteratively using Equation (4.21) together with Equations (4.11) and (4.12). Then this calculated value for bubble pressure is used in the exponential term of Equation (4.21) for the next iteration, and this is repeated until the bubble pressure value converges.

The dew pressure expression is derived similarly to that of Equation (4.20), where Equation (4.13) is now rearranged and combined with $\sum_i x_i = 1$ and $P^{\mathrm{V}} = P^{\mathrm{L}}$, to obtain

$$P_{\mathrm{d}}^{\mathrm{V}} = \left(\sum_i \frac{y_i}{\gamma_i P_i^{\mathrm{sat}} \exp\left[v_i^{\mathrm{L}} (P_{\mathrm{d}}^{\mathrm{V}} - P_i^{\mathrm{sat}})/(RT) \right]} \right)^{-1}. \tag{4.22}$$

Iteration can also be used to calculate the dew pressure from Equations (4.11), (4.12), and (4.22). An initial guess of $\gamma_i = 1$ and a Poynting correction of 1 are used to estimate the dew pressure in Equation (4.22). For a flat interface, an expression for liquid mole fraction is obtained by using $P^{\mathrm{V}} = P^{\mathrm{L}}$ and rearranging Equation (4.13) for components 1 and 2, followed by equating these expressions to yield

$$\frac{\gamma_1 x_1 P_1^{\mathrm{sat}} \exp\left[v_1^{\mathrm{L}} (P_{\mathrm{d}}^{\mathrm{V}} - P_1^{\mathrm{sat}})/(RT) \right]}{y_1} = \frac{\gamma_2 x_2 P_2^{\mathrm{sat}} \exp\left[v_2^{\mathrm{L}} (P_{\mathrm{d}}^{\mathrm{V}} - P_1^{\mathrm{sat}})/(RT) \right]}{y_2}. \tag{4.23}$$

Rearranging for x_1 gives

$$x_1 = \left(\frac{\gamma_1 P_1^{\text{sat}} \exp\left[v_1^{\text{L}} (P_{\text{d}}^{\text{V}} - P_1^{\text{sat}})/(RT) \right] y_2}{\gamma_2 P_2^{\text{sat}} \exp\left[v_2^{\text{L}} (P_{\text{d}}^{\text{V}} - P_2^{\text{sat}})/(RT) \right] y_1} + 1 \right)^{-1} . \tag{4.24}$$

The values of the Margules activity coefficients and the exponential Poynting correction are updated in the next iteration of evaluating Equation (4.22), followed again by Equation (4.24), until the values of dew pressure and liquid mole fraction converge.

4.2.2 Curved Interface Vapor–Liquid Equilibrium

Whereas the equations and calculation procedures for flat interfaces summarized in the preceding section are well known to chemical engineers, the analogous equations and calculation procedures for curved interfaces have not been developed previously. For a flat interface, the pressures in the liquid and vapor phases are equal, but as the curvature of the interface varies, the pressure changes in the vapor phase according to Equation (4.7), where the surface tension of the liquid mixture, σ, must be evaluated as a function of liquid mole fraction (x_1).

For the ideal multicomponent VLE of curved interfaces, Equation (4.14) is used with $\sum_i y_i = 1$, and Equation (4.7) is substituted for P^{L} to give the expression

$$P_{\text{b}}^{\text{V}} = \sum_i x_i P_i^{\text{sat}} \exp\left[v_i^{\text{L}} (P_{\text{b}}^{\text{V}} + 2\sigma/r - P_i^{\text{sat}})/(RT) \right] \tag{4.25}$$

to calculate the vapor phase pressure at the bubble point of a multicomponent system with curvature.

The vapor phase pressure at the dew point is determined by using Equation (4.14) with $\sum_i x_i = 1$ and the relationship in Equation (4.7) to obtain

$$P_{\text{d}}^{\text{V}} = \left(\sum_i \frac{y_i}{P_i^{\text{sat}} \exp\left[v_i^{\text{L}} (P_{\text{d}}^{\text{V}} + 2\sigma/r - P_i^{\text{sat}})/(RT) \right]} \right)^{-1} . \tag{4.26}$$

Equations (4.25) and (4.26) are both solved iteratively with an initial guess of 1 for the Poynting correction.

For a nonideal liquid mixture, Equation (4.13) is used with $\sum_i y_i = 1$ and Equation (4.7) to create an expression for the pressure in the vapor phase of a curved interface at the bubble point:

$$P_{\mathrm{b}}^{\mathrm{V}} = \sum_i x_i \gamma_i P_i^{\mathrm{sat}} \exp\left[v_i^{\mathrm{L}}(P_{\mathrm{b}}^{\mathrm{V}} + 2\sigma/r - P_i^{\mathrm{sat}})/(RT)\right]. \tag{4.27}$$

Equation (4.13) and Equation (4.7), along with $\sum_i x_i = 1$, are combined to obtain the following expression for the pressure in the vapor phase of a curved interface at the dew point:

$$P_{\mathrm{d}}^{\mathrm{V}} = \left(\sum_i \frac{y_i}{\gamma_i P_i^{\mathrm{sat}} \exp\left[v_i^{\mathrm{L}}(P_{\mathrm{d}}^{\mathrm{V}} + 2\sigma/r - P_i^{\mathrm{sat}})/(RT)\right]}\right)^{-1}. \tag{4.28}$$

In Equation (4.28), the values of γ_i and the exponential Poynting correction are functions of liquid mole fraction, which is initially unknown. Therefore, an iterative method is used to calculate the dew pressure and the composition in the liquid and vapor phases. To determine the value of the liquid mole fraction for the dew pressure calculation, Equation (4.13) can be written for each of the two components, each rearranged to form an expression for pressure, and equated. Then, combining this result with Equation (4.7) and simplifying gives

$$x_1 = \left(\frac{\gamma_1 P_1^{\mathrm{sat}} \exp\left[v_1^{\mathrm{L}}(P_{\mathrm{d}}^{\mathrm{V}} + 2\sigma/r - P_1^{\mathrm{sat}})/(RT)\right] y_2}{\gamma_2 P_2^{\mathrm{sat}} \exp\left[v_2^{\mathrm{L}}(P_{\mathrm{d}}^{\mathrm{V}} + 2\sigma/r - P_2^{\mathrm{sat}})/(RT)\right] y_1} + 1\right)^{-1}. \tag{4.29}$$

First, initial guesses of 1 are used for the Poynting correction and Margules activity coefficients in Equations (4.28) and (4.29) to estimate the dew pressure and liquid mole fraction values. These estimated dew pressure and liquid mole fraction values are then substituted into Equation (4.28) to update the value for dew pressure, followed by Equation (4.29) to update the liquid mole fraction value. Iteration is repeated until the values of $P_{\mathrm{d}}^{\mathrm{V}}$ and x_1 converge.

Each pair of liquid mole fraction and vapor mole fraction values can be plotted to form an *x*-*y* composition diagram, a useful tool in the design of chemical processes. It gives a qualitative indication of the ease of separation based on the distance of the *x*-*y* curve from a 45° line that indicates equal composition in the two phases—the smaller the distance, the harder the separation. If the *x*-*y* curve intersects the 45° line, an azeotrope exists at this composition and indicates that conventional distillation past this point is not possible.

4.2.3 Composition of the Azeotrope

A defining property of an azeotrope is exactly that the mole fraction of each species is the same in the vapor phase as in the liquid phase. That is, $x_i = y_i$, so that for a two-component mixture

$$\frac{y_1/x_1}{y_2/x_2} = 1. \tag{4.30}$$

Rearranging and substituting generalized modified Raoult's Law (Equation (4.13)) for each component into the numerator and denominator of Equation (4.30) and combining with Equation (4.7) gives

$$\frac{\gamma_1 P_1^{\text{sat}} \exp\left[v_1^{\text{L}}(P^{\text{V}} + 2\sigma/r - P_1^{\text{sat}})/(RT)\right]}{\gamma_2 P_2^{\text{sat}} \exp\left[v_2^{\text{L}}(P^{\text{V}} + 2\sigma/r - P_2^{\text{sat}})/(RT)\right]} = 1. \tag{4.31}$$

The pressure in the vapor phase at the azeotropic composition can be calculated from the bubble pressure equation (Equation (4.27)). First, the built-in MATLAB (Natick, USA) function *fsolve()* is used to solve Equation (4.31) with an initial guess of 1 for the exponential Poynting correction factor. Then the calculated x_1 is used to determine the value of P^{V} from Equation (4.27). This pressure in the vapor is then substituted back into Equation (4.31), and an updated x_1 is calculated. Such an iterative procedure is repeated until the values of azeotropic composition and vapor phase pressure converge.

4.2.4 Surface Tension

The surface tension of a liquid becomes a function of curvature when the radius of curvature approaches the atomic scale [284], with notable deviations for radii less than 10 nm [4]. However, in Gibbsian composite system thermodynamics, the convention of placing the dividing surface according to Gibbs' surface of tension removes this dependence and allows a constant interfacial tension to be used down to the nanometer scale [108]. In the current chapter, for lack of experimental data or theoretical approximations to the contrary for binary systems containing methanol, ethanol, and water, we assume that the surface tension is independent of curvature.

Surface tension varies with liquid mole fraction. For the ideal system of methanol(1) + ethanol(2), a linear combination of each component's surface tension and its liquid mole fraction can be used. The pure liquid surface tension values of methanol and ethanol differ from each other by less than 1 mN/m. For nonaqueous liquid mixtures with such close values of surface tension, a linear composition dependence accurately describes the mixture's surface tension [70, 219]:

$$\sigma = x_1\sigma_1 + x_2\sigma_2. \tag{4.32}$$

Table 4.1: Flat surface saturation pressure in the vapor phase, molar liquid volume, and surface tension values for pure methanol, ethanol, and water [116, 169, 290].

	Flat surface saturation pressure in the vapor, P_i^{sat} @ 298 K [kPa]	Molar liquid volume, v_i^{L} @ 298 K [cm^3/mol]	Surface tension, σ_i @ 298 K [mN/m]
Methanol	16.94	40.73	22.07
Ethanol	7.87	58.69	21.97
Water	3.17	18.07	72.01

However, for the nonideal system of ethanol(1) + water(2), surface tension is not a linear combination of the two components' surface tension values [31, 107, 141, 194]. We therefore fit a function to the experimental data from Vázquez *et al.* [290] as seen in Figure 4.2 to obtain

$$\sigma(\text{in mN/m}) = \frac{2.46 \pm 0.14}{x_1 + (0.048 \pm 0.003)} + (20.1 \pm 0.5). \tag{4.33}$$

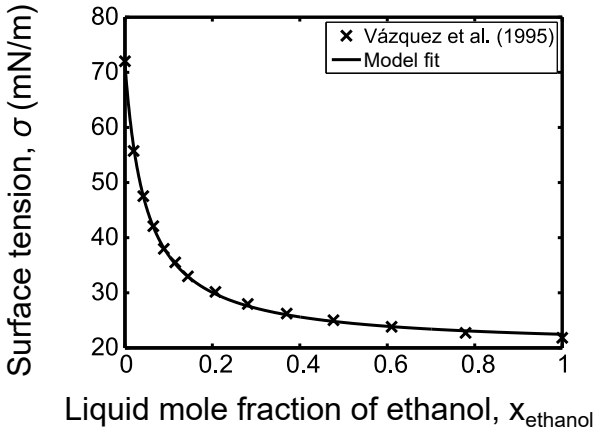

Figure 4.2: Surface tension as a function of ethanol composition in the ethanol(1) + water(2) system, as measured experimentally by Vázquez *et al.* [290] and as given by the model fit to this data.

Table 4.1 includes the values of flat surface saturation pressures, molar liquid volumes, and surface tensions of pure methanol, ethanol, and water all at 298 K [116, 169, 290]. For the ethanol(1) + water(2) system, the two-parameter Margules equation is used to calculate activity coefficients with constants $A_{12} = 1.4473$ and $A_{21} = 0.9395$ at 298 K [110].

4.3 Results and Discussion

In the above theoretical framework, the Poynting correction accounts for the change in chemical potential of a liquid component with pressure assuming incompressibility. Modified Raoult's Law takes into account nonideality in the liquid phase with activity coefficients. In this chapter, we use the Margules form of the activity coefficients for the ethanol(1) + water(2) system. Limitations of our analysis include assuming an ideal gas in the vapor phase and neglecting the effect of any external forces, such as gravity. The hydrogen-bonding in water may alter vapor–liquid phase equilibrium at higher pressures in the vapor phase, but at the low pressures considered in the vapor phase, we treat the vapor ideally.

The effect of curvature on VLE can be seen for the ideal methanol(1) + ethanol(2) phase envelopes presented in Figure 4.3, where pressure in the vapor phase is plotted as a function of methanol liquid mole fraction. The solid and dashed thick black lines show the bubble and dew pressures, respectively, for a methanol(1) + ethanol(2) system with a flat interface. It can be seen that, as expected, the pressures in the vapor phase increase for positive radii of curvature (liquid inside the curvature), and decrease for negative radii of curvature (vapor inside the curvature). Visually, it appears that the phase envelope is simply translated vertically as a function of radius of curvature, but Figure 4.4 shows that composition is slightly altered by curvature. As a result, it is more difficult to separate the methanol(1) + ethanol(2) system when the interface has a positive radius of curvature since the *x*-*y* curve lies closer to the 45° line, and separation is easier when the interface has a negative radius of curvature.

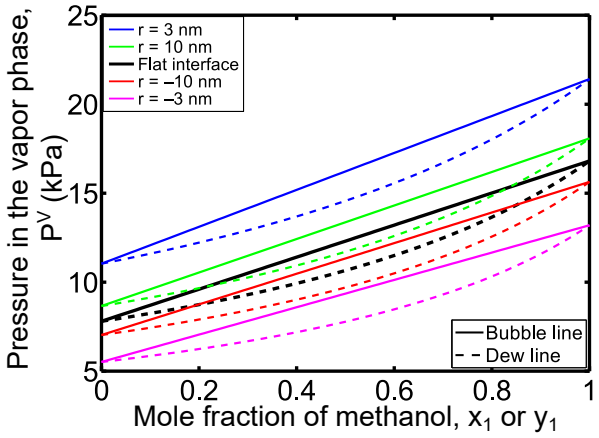

Figure 4.3: Phase envelopes of the methanol(1) + ethanol(2) system for a flat interface and for interfaces with radii of curvature of ±3 nm and ±10 nm.

Figure 4.5 illustrates the nonideal ethanol(1) + water(2) phase envelopes for flat and curved vapor–liquid interfaces. As seen for the methanol(1) + ethanol(2) system, a positive radius of curvature increases the pressure in the vapor phase, and a negative radius of curvature decreases

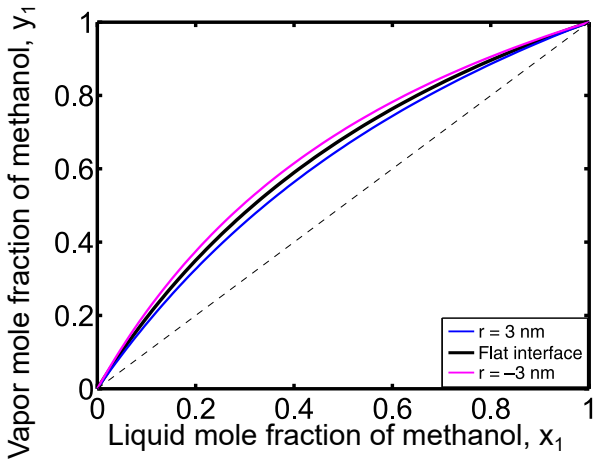

Figure 4.4: Vapor mole fraction as a function of liquid mole fraction for methanol(1) + ethanol(2) phase equilibrium for a flat interface and for interfaces with radii of curvature of ± 3 nm. The 45° line for the plot is the thin dashed line.

pressure in the vapor phase. Most importantly, for the flat interface at a constant temperature of 298 K, the azeotrope lies at 97.75 mol% ethanol, whereas for positive radii of curvature, the azeotrope shifts towards a liquid composition of ethanol closer to 100 mol%. This is highlighted by Figure 4.6, where the *x*-*y* curve for positive radii of curvature intersects the 45° line at values closer to $x_1 = 1$. In contrast, negative radii of curvature result in azeotropic compositions less than that observed for a flat interface in the ethanol(1) + water(2) system.

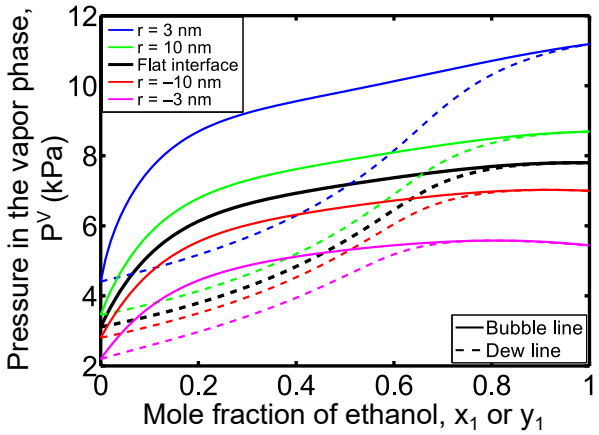

Figure 4.5: Phase envelopes of the ethanol(1) + water(2) system for a flat interface and for interfaces with radii of curvature of ± 3 nm and ± 10 nm.

In Figure 4.7, as the radius of curvature approaches infinity, the limit of the composition is that of a flat interface (97.75 mol% ethanol), shown by the dashed black line. To achieve an azeotropic composition >99 mol% ethanol, a radius of curvature smaller than 66 nm would be desired. Figure 4.8 shows azeotropic composition plotted as a function of the inverse radius of

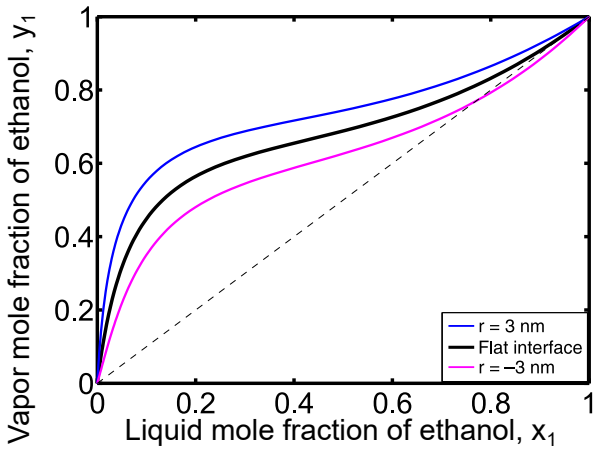

Figure 4.6: Vapor mole fraction as a function of liquid mole fraction for ethanol(1) + water(2) phase equilibrium for a flat interface and for interfaces with radii of curvature of ± 3 nm. The 45° line for the plot is the thin dashed line.

curvature. This variable transformation highlights that a flat interface ($1/r = 0$) has an azeotropic composition of 97.75 mol% ethanol and that the azeotropic composition increases or decreases for positive or negative radii of curvature, respectively.

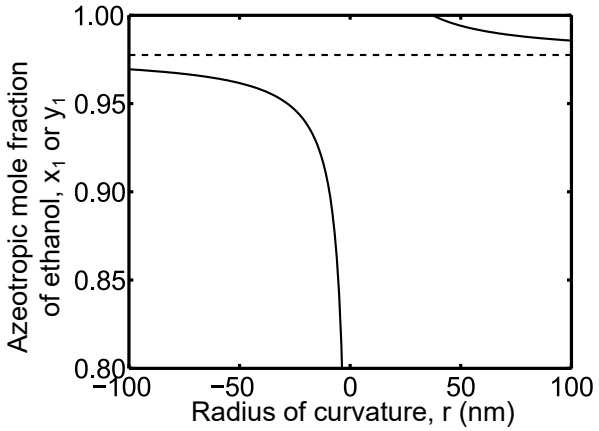

Figure 4.7: Azeotropic composition as a function of radius of curvature. The dashed line indicates the azeotropic composition for a flat interface between phases.

It may be surprising that the azeotropic composition at a curvature of ± 100 nm has not yet reached that of a flat interface. Observable departures from flat interface equilibrium values can in fact occur at radii of curvature less than 1000 nm; for a 100 nm pure water droplet in air, the Kelvin equation predicts a vapor pressure 12% higher than the vapor pressure for a flat interface between air and water [26]. Also at a radius of curvature of 100 nm, Defay *et al.* predict a decrease in azeotropic composition from 0.40 to 0.395 for a mixture of *n*-hexane + ethyl iodide, where the value of surface tension and its dependence on composition were arbitrarily chosen

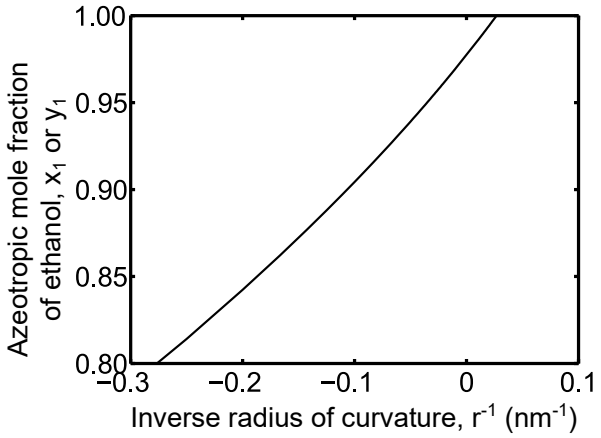

Figure 4.8: Azeotropic composition of an ethanol(1) + water(2) system as a function of the inverse radius of curvature.

[70]. In addition to illustrating curvature-dependent phase diagrams, this chapter lends insight into the predicted change in azeotropic composition with the use of an actual function fit to experimentally measured values of surface tension for ethanol(1) + water(2).

4.4 Conclusions

We ultimately investigated the effect of curvature on VLE in methanol(1) + ethanol(2) and ethanol(1) + water(2) mixtures, as well as its effect on the location of the azeotrope for the nonideal mixture. This analysis can be applied to capillaries whose solid–liquid interactions with the binary mixtures are negligible and to droplets or bubbles contained in their respective vapor or liquid phase. For a positive radius of curvature (liquid inside the curvature), the azeotropic composition approaches 100 mol% ethanol, whereas for a negative radius of curvature (vapor inside the curvature), the azeotropic composition shifts in the opposite direction. This chapter provides new fundamental understanding and calculation procedures for multicomponent phase equilibrium across curved interfaces, and it introduces curved-interface phase envelope and phase composition diagrams based on Gibbsian thermodynamics. The insight gained can be used to describe a variety of phenomena and provides the foundation needed for accurate prediction and design. For example, the results of this chapter indicate that curvature could be used to distill past the azeotrope of nonideal liquid mixtures. Additionally, phase composition in multicomponent systems with curved phase boundaries can be predicted, which is vital in atmospheric physics, material processing, and soft matter nanotechnology.

Chapter 5

Isobaric Vapor–Liquid Phase Diagrams for Multicomponent Systems with Nanoscale Radii of Curvature[1]

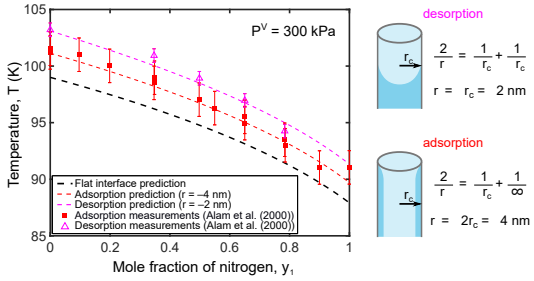

Abstract

At any given temperature, pressure, and composition, a compound or a mixture of compounds will exist either in a single phase, whether solid, liquid, or vapor, or in a combination of these phases coexisting in equilibrium. For multiphase systems, it is known that the geometry of the interface impacts the equilibrium state; this effect has been well-studied in single component systems with spherical interfaces. However, multicomponent phase diagrams are usually calculated assuming a planar interface between phases. Recent experimental and theoretical work has started to investigate the effect of curved interfaces on multicomponent phase equilibrium, but these analyses have been limited to isothermal conditions or to a portion of the isobaric phase diagram. Herein, we consider complete vapor–liquid phase diagrams (both bubble and

[1]Reproduced, with minor modifications, with permission from N. Shardt and J. A. W. Elliott. "Isobaric Vapor–Liquid Phase Diagrams for Multicomponent Systems with Nanoscale Radii of Curvature". *Journal of Physical Chemistry B* 122.8 (2018), pp. 2434–2447. https://pubs.acs.org/articlesonrequest/AOR-TvK85VGmsbiNcqZRPZrx Copyright 2018 American Chemical Society. In performing this research, some recent literature was brought to our attention by Dr. William R. Smith of the University of Guelph.

dew lines) under isobaric conditions. We use Gibbsian composite-system thermodynamics to derive the equations governing vapor–liquid equilibrium for systems with a spherical interface separating the phases. We validate our approach by comparing the predicted nitrogen + argon dew points with reported literature data. We then predict complete isobaric phase diagrams as a function of radius of curvature for an ideal methanol + ethanol system and for a nonideal ethanol + water system. We also determine how the azeotropic composition of ethanol + water changes. The effect of curvature on isobaric phase diagrams is similar to that seen on isothermal phase diagrams. This chapter extends the study of curved-interface multicomponent phase equilibrium to isobaric systems, expanding the conditions under which nanoscale systems, such as nanofluidic systems, shale gas reservoirs, and cloud condensation nuclei, can be understood.

5.1 Introduction

Just 31 articles were published on nanofluidics in 2006; in 2016, researchers around the world published 1392 articles in this field (articles with "nanofluidics" in the title, abstract, or keywords, Scopus, Dec. 19, 2017). Such a rapid increase in publications over the decade underscores the growing interest in fluid phenomena that occur at the nanoscale. One common feature of many nanoscale systems is the presence of curved interfaces in the form of nanobubbles, nanodroplets, or nanopores. As a result of the nanoscale curvature, the phase behavior of fluids in these nanoscale systems differs drastically from that of bulk systems without curved interfaces. The phase behavior of nanoscale systems is particularly important to understand because fluid properties are governed by which phase or phases are present, and predicting fluid properties accurately is important for the design and control of nanoscale systems. Interfacial thermodynamics has been previously used to study the phase behavior of single-component systems with interfaces that have nanoscale radii of curvature. There still lies much opportunity for research in extending the framework of interfacial thermodynamics to multicomponent, multiphase systems.

In the natural environment, multicomponent systems with highly curved interfaces can be found from 4 km below the Earth's crust in hydrocarbon reservoirs [57] up to 15 km above the surface in the troposphere [227, 246]. In the subsurface, porous structures can have pore throat diameters in the nanometer range [6, 97, 197, 295]. These nanopores influence phase equilibrium, and if their effect is unaccounted for, predictions for unconventional hydrocarbon recovery operations may be inaccurate [8, 21, 174, 177, 204]. Phase diagrams are vital tools in recovering oil and natural gas from shale formations, and the effect of nanoscale curvature on phase diagrams has been calculated for specific compositions of hydrocarbons as a function of temperature and pressure [6, 73, 199, 204, 217, 240]. In the atmosphere, clouds can form

when water condenses on highly curved nuclei with diameters in the nanometer range [246, 326]. The number, size, and composition of these nuclei determine the number and size of water droplets, which dictate the size and lifetime of clouds [272]. Thus, nanoscale processes can have a significant role in macroscopic properties and phenomena.

In industry, catalysts may deactivate if liquid condenses in pores with nanoscale diameters, altering the rate and extent of reaction [24, 39, 40, 308]. The atomic force microscope (AFM) and surface forces apparatus (SFA) can be affected by condensation between the probe tip and the surface, and the radii of curvature of the condensed phase can reach nanometer scales [29, 149]. The manufacturing of cosmetics, food, and paint can also be described by multicomponent, multiphase thermodynamics with interfacial curvature [44, 105]. In medicine, nanoscale drug delivery systems show potential for targeting tumors [115, 124, 211, 259]. The effect of nanoscale curvature is also pertinent in fluid flow through nanochannels [117, 195] and in phase changes occurring in porous media [105, 320]. Such phase changes can occur in molecular sieves such as MCM-41 and SBA-15, which are commonly used adsorbents that have pores with diameters less than 10 nm [21, 53, 105, 126, 152].

Extensive theoretical analyses have been carried out for single-component systems with interfacial curvature [87, 155, 187, 297, 323, 324], and the effect of curvature on single component systems is outlined in detail by Defay and Prigogine for both constant temperature and constant pressure conditions [70]. Single-component phase equilibrium has been investigated for water [207, 286] and carbon dioxide [273] with nanoscale curvature between phases. Recent molecular simulations suggest that the Kelvin equation that describes the increase in vapor-phase pressure as a function of radius of curvature is accurate for water droplets down to a radius of 0.6 nm [92].

Defay and Prigogine [70] and Vehkmäki [292] derived a multicomponent Kelvin equation assuming ideal behavior in the vapor and liquid phases. Another multicomponent form of the Kelvin equation was derived by Shapiro and Stenby [249, 250] but it is only valid in the region close to the dew point. It was extended to the bubble point region by Sandoval *et al*. [240]. The derivation of the proposed multicomponent form of the Kelvin equation uses a linear approximation in both the dew and bubble point regions. Using the Shapiro–Stenby approach, Chen *et al*. [51] studied the shift in the dew point, and Sandoval *et al*. [240] calculated the shift in the phase envelope for hydrocarbon mixtures. Gelb *et al*. [105] have summarized theoretical and experimental work on phase equilibria in nanoporous material, while Barsotti *et al*. [21] have reviewed research dealing specifically with the phase behavior of hydrocarbon mixtures. Curvature also affects the equilibrium between solid and liquid phases of single and multicomponent systems [2, 105, 221] and the effect of confinement in nanoscale capillaries on the phase diagram and the eutectic point of glycerol + water has been studied [171].

To predict the phase diagrams of multicomponent systems with interfacial curvature, Tan and Piri [279] proposed an empirical model that combines an equation of state with a modified capillary pressure expression that accounts for an adsorbed layer at the capillary wall. However, the model can only be implemented when vast experimental datasets are available, because it relies on a fitting parameter for each pure component that is a function of pore radius and temperature. Using this empirical model, dew temperatures for a binary mixture of nitrogen + argon and bubble temperatures for krypton + argon were predicted and compared to experimental data. Predictions of the complete phase diagrams for nitrogen + argon under isothermal conditions were also made [279]. The model was then extended to associating fluids under isothermal conditions [278].

Molecular simulations have been used to predict the effect of confinement on both single and multicomponent phase diagrams [105] through approaches including density functional theory, Monte Carlo [16, 59, 68, 93, 118, 217, 293, 294], and molecular dynamics [105] for cylindrical pores [89, 118] and slit pores [58, 59, 68, 89, 293]. Many of these simulations have been limited to simpler fluids such as nitrogen [16], argon and krypton [59, 93, 118], methane [16, 58, 217], and ethane [217] because of the computational intensity that would be required for more complex fluids. Considering confinement in a slit pore, Coasne *et al*. [58] simulated the solid–liquid phase diagram for a Lennard–Jones azeotropic mixture of Ar + CH_4, and Li *et al*. [166] studied how the azeotrope shifts for a Lennard–Jones mixture.

For nonideal systems with an azeotrope, Defay and Prigogine [70] outline the effect of curvature on the location of the azeotrope under isothermal conditions. Experimental work indicates that the azeotrope of nonideal multicomponent mixtures can be altered by introducing curvature between the vapor and liquid phases [234, 316, 317]. Several binary mixtures have been distilled with porous plates, and in the theoretical analysis, solid–liquid interactions between the solution and pore walls were identified to significantly alter vapor–liquid equilibrium [1, 234, 236, 316–318].

The previous chapter examined the effect of interfacial curvature on the isothermal phase diagrams of both ideal and nonideal multicomponent systems [254]. Through the framework of Gibbsian thermodynamics, we determined that the pressure in the vapor phase increases for a liquid droplet in a bulk vapor phase and decreases for a vapor bubble in a bulk liquid phase, similar to the trends seen for pure components. Significant effects on the phase envelope were only observed at nanoscale radii of curvature. We also calculated the shift in azeotropic composition as a function of radius of curvature for the nonideal ethanol(1) + water(2) system and determined that the azeotrope can vanish for some radii under isothermal conditions. Conventional separation processes have limited applicability for nonideal systems that exhibit an azeotrope, but new processes could shift the azeotrope by exploiting the effects of nanoscale

curvature.

The past literature on multicomponent systems with curvature has been limited to isothermal phase diagrams or to a portion of the isobaric phase diagram; in this chapter, we now extend the scope of study to complete vapor–liquid phase diagrams under isobaric conditions. Under isothermal conditions, liquid properties are generally invariant as a function of pressure and are commonly treated as constant parameters. Isobaric phase diagrams are more challenging to compute, because the liquid properties that govern vapor–liquid phase equilibrium are nonlinear functions of temperature. In other words, the bubble and dew temperatures of a system are more difficult to calculate than the bubble and dew pressures [78]. It is important to note that for systems with interfacial curvature, the meaning of the term isobaric may be unclear because each phase has a different pressure; in the current chapter, the term isobaric will refer to systems that have constant pressure in the vapor phase.

In this chapter, we derive the equations governing vapor–liquid equilibrium of multicomponent, nonideal systems with interfacial curvature using Gibbsian composite-system thermodynamics, and we choose models that accurately describe the relevant parameters of the system components. We predict the dew temperatures of a nitrogen(1) + argon(2) system and compare the results to experimental measurements as a function of composition. Then, we predict the complete isobaric phase diagrams for an ideal system (methanol(1) + ethanol(2)) and a nonideal system (ethanol(1) + water(2)). Finally, the azeotropic composition of ethanol + water is calculated as a function of radius of curvature under isobaric conditions.

5.2 Governing Equations

The equilibrium states of a composite system can be determined from Gibbsian thermodynamics. Consider a system consisting of one phase in contact with a second phase separated by a spherical interface. This two-phase system is in a piston–cylinder device, forming a closed system within a surrounding reservoir. Figure 5.1 illustrates two examples of vapor–liquid systems with curved interfaces that will be analyzed in this chapter. Figure 5.1(a) shows a liquid droplet within a bulk vapor phase (radius of curvature in the liquid phase), and Figure 5.1(b) shows a cylindrical capillary tube containing a liquid phase in contact with a bulk vapor phase, but with a different direction of interfacial concavity compared to Figure 5.1(a) (radius of curvature in the vapor phase). In both cases, the piston–cylinder device imposes the pressure of the reservoir on the vapor phase.

An equilibrium state occurs when the entropy (S) of the system is at an extremum; mathematically, this means that

$$\mathrm{d}S^{\mathrm{L}} + \mathrm{d}S^{\mathrm{V}} + \mathrm{d}S^{\mathrm{LV}} + \mathrm{d}S^{\mathrm{R}} = 0, \tag{5.1}$$

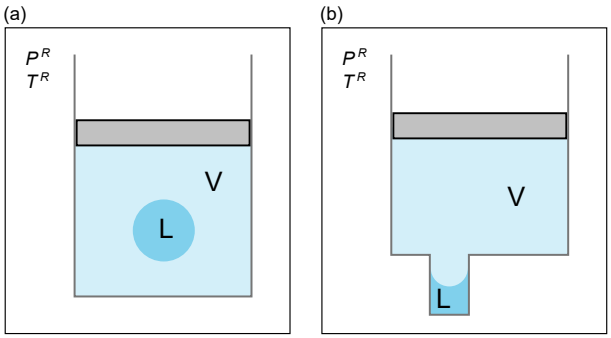

Figure 5.1: Schematic diagrams of vapor(V)–liquid(L) systems contained in a reservoir that has pressure P^{R} and temperature T^{R}. The piston–cylinder device imposes the reservoir pressure on the vapor phase. Diagram (a) shows a system with a convex liquid surface and (b) illustrates a system with a concave liquid surface.

where superscripts L and V denote the liquid and vapor phases, respectively, LV denotes the vapor–liquid interface, and R denotes the reservoir surrounding the vapor–liquid system. The entropies are functions of internal energy (U), volume (V), and number of moles (N).

The differential changes of these variables in the bulk vapor and liquid phases are related by the following equations, respectively, [46, 87, 108, 323]

$$\mathrm{d}U^{\mathrm{V}} = T^{\mathrm{V}}\,\mathrm{d}S^{\mathrm{V}} - P^{\mathrm{V}}\,\mathrm{d}V^{\mathrm{V}} + \sum_{i=1}^{k} \mu_i^{\mathrm{V}}\,\mathrm{d}N_i^{\mathrm{V}} \tag{5.2}$$

$$\mathrm{d}U^{\mathrm{L}} = T^{\mathrm{L}}\,\mathrm{d}S^{\mathrm{L}} - P^{\mathrm{L}}\,\mathrm{d}V^{\mathrm{L}} + \sum_{i=1}^{k} \mu_i^{\mathrm{L}}\,\mathrm{d}N_i^{\mathrm{L}}, \tag{5.3}$$

where T is the absolute temperature, P is the pressure, μ_i is the chemical potential of component i, and k is the number of components. The differential change in internal energy for a curved vapor–liquid interface is [87, 108, 323]

$$\mathrm{d}U^{\mathrm{LV}} = T^{\mathrm{LV}}\,\mathrm{d}S^{\mathrm{LV}} + \sigma^{\mathrm{LV}}\,\mathrm{d}A^{\mathrm{LV}} + \sum_{i=1}^{k} \mu_i^{\mathrm{LV}}\,\mathrm{d}N_i^{\mathrm{LV}}, \tag{5.4}$$

where σ is the surface tension and A is the area of the vapor–liquid interface. Using Gibbs' surface of tension approach for a curved interface ensures that the surface tension is independent of radius of curvature [108, 292], and this means that each component is present at the interface.

The differential change in the internal energy of the reservoir is

$$\mathrm{d}U^{\mathrm{R}} = T^{\mathrm{R}}\,\mathrm{d}S^{\mathrm{R}} - P^{\mathrm{R}}\,\mathrm{d}V^{\mathrm{R}} + \sum_{i=1}^{m} \mu_i^{\mathrm{R}}\,\mathrm{d}N_i^{\mathrm{R}}, \tag{5.5}$$

where m is the number of components in the reservoir.

Rearranging Equations (5.2)–(5.5) in terms of dS and substituting into Equation (5.1) gives

$$\frac{1}{T^{\mathrm{L}}}\,\mathrm{d}U^{\mathrm{L}} + \frac{P^{\mathrm{L}}}{T^{\mathrm{L}}}\,\mathrm{d}V^{\mathrm{L}} - \sum_{i=1}^{k}\frac{\mu_i^{\mathrm{L}}}{T^{\mathrm{L}}}\,\mathrm{d}N_i^{\mathrm{L}} + \frac{1}{T^{\mathrm{V}}}\,\mathrm{d}U^{\mathrm{V}} + \frac{P^{\mathrm{V}}}{T^{\mathrm{V}}}\,\mathrm{d}V^{\mathrm{V}} - \sum_{i=1}^{k}\frac{\mu_i^{\mathrm{V}}}{T^{\mathrm{V}}}\,\mathrm{d}N_i^{\mathrm{V}}$$
$$+ \frac{1}{T^{\mathrm{LV}}}\,\mathrm{d}U^{\mathrm{LV}} - \frac{\sigma^{\mathrm{LV}}}{T^{\mathrm{LV}}}\,\mathrm{d}A^{\mathrm{LV}} - \sum_{i=1}^{k}\frac{\mu_i^{\mathrm{LV}}}{T^{\mathrm{LV}}}\,\mathrm{d}N_i^{\mathrm{LV}} + \frac{1}{T^{\mathrm{R}}}\,\mathrm{d}U^{\mathrm{R}} + \frac{P^{\mathrm{R}}}{T^{\mathrm{R}}}\,\mathrm{d}V^{\mathrm{R}} - \sum_{i=1}^{m}\frac{\mu_i^{\mathrm{R}}}{T^{\mathrm{R}}}\,\mathrm{d}N_i^{\mathrm{R}} = 0. \quad (5.6)$$

Equation (5.6) will yield equilibrium conditions for a system once appropriate constraints are defined.

5.2.1 Equilibrium Conditions for a Droplet of Liquid within a Vapor Phase

First, applying the law of conservation of energy to the vapor–liquid system and reservoir gives the following mathematical constraint:

$$\mathrm{d}U^{\mathrm{V}} = -\,\mathrm{d}U^{\mathrm{L}} - \mathrm{d}U^{\mathrm{LV}} - \mathrm{d}U^{\mathrm{R}}. \quad (5.7)$$

Next, there is no mass transfer between the system and the reservoir, so for each component in the reservoir,

$$\mathrm{d}N_i^{\mathrm{R}} = 0, \quad (5.8)$$

and for each component in the vapor–liquid system,

$$\mathrm{d}N_i^{\mathrm{V}} = -\,\mathrm{d}N_i^{\mathrm{L}} - \mathrm{d}N_i^{\mathrm{LV}}. \quad (5.9)$$

There is a movable piston between the system and the reservoir, as illustrated in Figure 5.1(a), which permits changes in volume of each phase and of the reservoir. The final constraint is that the total volume of the system and reservoir together is constant:

$$\mathrm{d}V^{\mathrm{V}} = -\,\mathrm{d}V^{\mathrm{L}} - \mathrm{d}V^{\mathrm{R}}. \quad (5.10)$$

For a spherical liquid drop, the following relationships hold for differential area and volume:

$$\mathrm{d}A^{\mathrm{LV}} = 8\pi r^{\mathrm{L}}\,\mathrm{d}r^{\mathrm{L}} \quad (5.11)$$

$$\mathrm{d}V^{\mathrm{L}} = 4\pi\left(r^{\mathrm{L}}\right)^2\mathrm{d}r^{\mathrm{L}}, \quad (5.12)$$

where r^{L} is the radius of the spherical liquid droplet.

Substituting Equations (5.7)–(5.12) into Equation (5.6) and collecting like terms gives

$$\left(\frac{1}{T^{\mathrm{LV}}}-\frac{1}{T^{\mathrm{V}}}\right)\mathrm{d}U^{\mathrm{LV}}+\left(\frac{1}{T^{\mathrm{L}}}-\frac{1}{T^{\mathrm{V}}}\right)\mathrm{d}U^{\mathrm{L}}+\left(\frac{1}{T^{\mathrm{R}}}-\frac{1}{T^{\mathrm{V}}}\right)\mathrm{d}U^{\mathrm{R}}$$
$$+\left[4\pi\left(r^{\mathrm{L}}\right)^{2}\left(\frac{P^{\mathrm{L}}}{T^{\mathrm{L}}}-\frac{P^{\mathrm{V}}}{T^{\mathrm{V}}}\right)-\frac{\sigma^{\mathrm{LV}}}{T^{\mathrm{LV}}}8\pi r^{\mathrm{L}}\right]\mathrm{d}r^{\mathrm{L}}+\sum_{i=1}^{k}\left(\frac{\mu_i^{\mathrm{V}}}{T^{\mathrm{V}}}-\frac{\mu_i^{\mathrm{L}}}{T^{\mathrm{L}}}\right)\mathrm{d}N_i^{\mathrm{L}}$$
$$+\sum_{i=1}^{k}\left(\frac{\mu_i^{\mathrm{V}}}{T^{\mathrm{V}}}-\frac{\mu_i^{\mathrm{LV}}}{T^{\mathrm{LV}}}\right)\mathrm{d}N_i^{\mathrm{LV}}+\left(\frac{P^{\mathrm{R}}}{T^{\mathrm{R}}}-\frac{P^{\mathrm{V}}}{T^{\mathrm{V}}}\right)\mathrm{d}V^{\mathrm{R}}=0. \quad (5.13)$$

For Equation (5.13) to be satisfied for all possible displacements from equilibrium, each of the coefficients multiplying the differentials must be equal to zero. When these coefficients are set to zero, the following equalities can be derived:

$$T^{\mathrm{V}}=T^{\mathrm{L}}=T^{\mathrm{LV}}=T^{\mathrm{R}} \quad (5.14)$$
$$P^{\mathrm{L}}-P^{\mathrm{V}}=\frac{2\sigma^{\mathrm{LV}}}{r^{\mathrm{L}}} \quad (5.15)$$
$$\mu_i^{\mathrm{V}}=\mu_i^{\mathrm{L}}=\mu_i^{\mathrm{LV}} \quad (5.16)$$
$$P^{\mathrm{R}}=P^{\mathrm{V}}. \quad (5.17)$$

Equations (5.14)–(5.16) are the thermodynamic equations defining the equilibrium conditions for a multicomponent system consisting of a liquid-phase spherical droplet in a vapor phase with temperature and vapor-phase pressure imposed by the surrounding reservoir.

5.2.2 Equilibrium Conditions for a Liquid in a Capillary

Following a procedure similar to the one outlined for a droplet of liquid, the equilibrium conditions for a liquid phase confined in a capillary with a concave hemispherical interface are:

$$T^{\mathrm{V}}=T^{\mathrm{L}}=T^{\mathrm{LV}}=T^{\mathrm{R}} \quad (5.18)$$
$$P^{\mathrm{V}}-P^{\mathrm{L}}=\frac{2\sigma^{\mathrm{LV}}}{r^{\mathrm{V}}} \quad (5.19)$$
$$\mu_i^{\mathrm{L}}=\mu_i^{\mathrm{V}}=\mu_i^{\mathrm{LV}} \quad (5.20)$$
$$P^{\mathrm{R}}=P^{\mathrm{V}}, \quad (5.21)$$

where r^{V} is the radius of curvature in the vapor phase.

5.2.3 Equilibrium Conditions for Two Phases Separated by a Spherical Interface

The thermal and chemical equilibrium conditions are identical for the liquid droplet and for the liquid in a capillary. The only difference between these systems is the sign of the pressure difference (Equation (5.15) *vs*. Equation (5.19)). A common convention is to define a spherical liquid phase as having a positive radius of curvature and a spherical (or hemispherical) vapor phase as having a negative radius of curvature. This convention gives the following equations for equilibrium in the liquid and vapor phases for any multicomponent mixture with a spherical or hemispherical interface between phases:

$$T^{\mathrm{V}} = T^{\mathrm{L}} = T^{\mathrm{LV}} \tag{5.22}$$

$$P^{\mathrm{L}} - P^{\mathrm{V}} = \frac{2\sigma}{r} \tag{5.23}$$

$$\mu_i^{\mathrm{L}} = \mu_i^{\mathrm{V}} = \mu_i^{\mathrm{LV}}. \tag{5.24}$$

The superscript LV on surface tension is dropped for simplicity. The factor $2/r$ in Equation (5.23) is the curvature of a spherical surface [26] which is twice the mean curvature [268, 323].

5.2.4 Governing Equations for Vapor–Liquid Phase Diagrams

5.2.4.1 Curved Interface

From this point forward, the temperature of the system will be denoted by T based on Equation (5.22). The chemical potential for each component i of an ideal-gas vapor phase is [78, 297]

$$\mu_i^{\mathrm{V}}\left(y_i, T, P^{\mathrm{V}}\right) = \mu_i^{\mathrm{V}}\left(T, P_i^{\mathrm{sat}}\right) + RT\ln\left(\frac{y_i P^{\mathrm{V}}}{P_i^{\mathrm{sat}}}\right). \tag{5.25}$$

The chemical potential for each component i of a nonideal, incompressible liquid phase is [78, 223]

$$\mu_i^{\mathrm{L}}\left(x_i, T, P^{\mathrm{L}}\right) = \mu_i^{\mathrm{L}}\left(T, P_i^{\mathrm{sat}}\right) + v_i^{\mathrm{L}}\left(P^{\mathrm{L}} - P_i^{\mathrm{sat}}\right) + RT\ln\left(\gamma_i x_i\right), \tag{5.26}$$

where y_i and x_i are vapor and liquid mole fractions, respectively, R is the universal gas constant, v_i^{L} is the liquid molar volume of pure component i, and γ_i is the activity coefficient for component i. The terms $\mu_i^{\mathrm{V}}\left(T, P_i^{\mathrm{sat}}\right)$ and $\mu_i^{\mathrm{L}}\left(T, P_i^{\mathrm{sat}}\right)$ are the chemical potentials at the reference states, taken to be the chemical potential of the vapor phase and the liquid phase, respectively, at the flat-interface saturation vapor pressure of component i (P_i^{sat}) at a temperature T; at equilibrium, these terms are equal. Equating Equations (5.25) and (5.26) as indicated by Equation (5.24)

gives

$$RT \ln\left(\frac{y_i P^{\mathrm{V}}}{P_i^{\mathrm{sat}}}\right) = v_i^{\mathrm{L}}\left(P^{\mathrm{L}} - P_i^{\mathrm{sat}}\right) + RT\ln\left(\gamma_i x_i\right). \tag{5.27}$$

Rearranging Equation (5.27) gives a modified version of Raoult's Law for a nonideal liquid mixture [266]:

$$y_i P^{\mathrm{V}} = \gamma_i x_i P_i^{\mathrm{sat}} \exp\left[\frac{v_i^{\mathrm{L}}\left(P^{\mathrm{L}} - P_i^{\mathrm{sat}}\right)}{RT}\right]. \tag{5.28}$$

Substituting Equation (5.23) into Equation (5.28) gives [254]

$$y_i P^{\mathrm{V}} = \gamma_i x_i P_i^{\mathrm{sat}} \exp\left[\frac{v_i^{\mathrm{L}}\left(P^{\mathrm{V}} + 2\sigma/r - P_i^{\mathrm{sat}}\right)}{RT}\right]. \tag{5.29}$$

The exponential factor in Equations (5.28) and (5.29) is known as the Poynting factor. Equations for the bubble temperature and dew temperature can be determined by combining Equation (5.29) for each component with $\sum_i y_i = 1$ or $\sum_i x_i = 1$, respectively. For a given overall mole fraction of the mixture (z_i), pressure in the vapor phase, and radius of curvature, the bubble temperature (T_{b}) and dew temperature (T_{d}) can be calculated with the following equations, given that P_i^{sat}, v_i^{L}, and σ are functions of temperature:

$$P^{\mathrm{V}} = \sum_{i=1}^{k} \gamma_i x_i P_i^{\mathrm{sat}}\left(T_{\mathrm{b}}\right) \exp\left[\frac{v_i^{\mathrm{L}}\left(T_{\mathrm{b}}\right)\left(P^{\mathrm{V}} + 2\sigma\left(T_{\mathrm{b}}, x_1, \ldots, x_{k-1}\right)/r - P_i^{\mathrm{sat}}\left(T_{\mathrm{b}}\right)\right)}{RT_{\mathrm{b}}}\right] \tag{5.30}$$

$$P^{\mathrm{V}} = \left(\sum_{i=1}^{k} \frac{y_i}{\gamma_i P_i^{\mathrm{sat}}\left(T_{\mathrm{d}}\right) \exp\left[\frac{v_i^{\mathrm{L}}(T_{\mathrm{d}})\left(P^{\mathrm{V}} + 2\sigma\left(T_{\mathrm{d}}, x_1, \ldots, x_{k-1}\right)/r - P_i^{\mathrm{sat}}(T_{\mathrm{d}})\right)}{RT_{\mathrm{d}}}\right]}\right)^{-1}. \tag{5.31}$$

Equations (5.30) and (5.31) describe the bubble and dew temperatures for a multicomponent system with k components. In this chapter, we consider the phase diagrams of binary mixtures, so the summations in these equations will only contain two terms, one for each component. The surface tension of a binary mixture simplifies to being a function of only temperature and x_1.

To solve for the bubble temperature of a binary mixture, the liquid-phase composition is set to the overall composition ($x_1 = z_1$), and Equation (5.30) is solved for T_{b}. The bubble line of the vapor–liquid phase envelope can be calculated for a given radius of curvature by solving Equation (5.30) for all z_1 between 0 and 1.

Equation (5.31) can be used to solve for the dew temperature by setting the vapor-phase composition to the overall composition ($y_1 = z_1$). Because the liquid-phase activity coefficient and vapor–liquid interfacial tension depend on the liquid-phase composition, another equation is needed to determine this composition. Both sides of Equation (5.29) can be divided by the vapor mole fraction, and then this equation can be written for each component of a binary mixture; the two resulting equations can be equated and then rearranged to give the following expression for liquid phase mole fraction [254]

$$x_1 = \left(\frac{y_2 \gamma_1 P_1^{\mathrm{sat}} \exp\left[v_1^{\mathrm{L}} (P^{\mathrm{V}} + 2\sigma/r - P_1^{\mathrm{sat}})/(RT_{\mathrm{d}}) \right]}{y_1 \gamma_2 P_2^{\mathrm{sat}} \exp\left[v_2^{\mathrm{L}} (P^{\mathrm{V}} + 2\sigma/r - P_2^{\mathrm{sat}})/(RT_{\mathrm{d}}) \right]} + 1 \right)^{-1} . \tag{5.32}$$

Among the possible activity coefficient models for binary mixtures, we select the Margules equations, given by [110, 266]

$$\ln(\gamma_1) = x_2^2 \left[A_{12} + 2(A_{21} - A_{12}) x_1 \right] \tag{5.33}$$

$$\ln(\gamma_2) = x_1^2 \left[A_{21} + 2(A_{12} - A_{21}) x_2 \right], \tag{5.34}$$

where A_{12} and A_{21} are system-dependent empirical constants at a given pressure. The activity coefficients for an ideal system are unity.

5.2.4.2 Composition of the Azeotrope for Curved Interfaces

At the azeotropic composition, the mole fraction in the vapor phase is equal to the mole fraction in the liquid phase. Using this property, the following equation can be used to determine the azeotropic composition for a binary system with a curved interface [254]:

$$\frac{\gamma_1 P_1^{\mathrm{sat}} \exp\left[v_1^{\mathrm{L}} (P^{\mathrm{V}} + 2\sigma/r - P_1^{\mathrm{sat}})/(RT) \right]}{\gamma_2 P_2^{\mathrm{sat}} \exp\left[v_2^{\mathrm{L}} (P^{\mathrm{V}} + 2\sigma/r - P_2^{\mathrm{sat}})/(RT) \right]} = 1. \tag{5.35}$$

An initial estimate of the azeotropic composition can be determined by setting the exponential Poynting correction factor to 1. At the azeotrope, the bubble and dew temperatures are equal, so Equation (5.30) is chosen to solve for temperature, and this temperature can be substituted into Equation (5.35) for the next iteration. This procedure of solving Equation (5.35) followed by solving Equation (5.30) can be repeated until the values of composition and temperature converge.

5.2.4.3 Flat Interface

The governing equations for a system with a flat interface can be derived by using the same Gibbsian composite-system approach that was used for the derivation of bubble and dew temperature equations for a system with curvature. The resulting equations for the flat-interface bubble temperature (T_{bf}) and dew temperature (T_{df}) are outlined in thermodynamics textbooks and are given by, with the addition of the Poynting correction [78]

$$P^{\mathrm{V}} = \sum_{i=1}^{k} \gamma_i x_i P_i^{\mathrm{sat}}(T_{\mathrm{bf}}) \exp\left[\frac{v_i^{\mathrm{L}}(T_{\mathrm{bf}})\left(P^{\mathrm{V}} - P_i^{\mathrm{sat}}(T_{\mathrm{bf}})\right)}{RT_{\mathrm{bf}}}\right] \tag{5.36}$$

$$P^{\mathrm{V}} = \left(\sum_{i=1}^{k} \frac{y_i}{\gamma_i P_i^{\mathrm{sat}}(T_{\mathrm{df}}) \exp\left[\frac{v_i^{\mathrm{L}}(T_{\mathrm{df}})\left(P^{\mathrm{V}} - P_i^{\mathrm{sat}}(T_{\mathrm{df}})\right)}{RT_{\mathrm{df}}}\right]}\right)^{-1}. \tag{5.37}$$

When the Poynting correction is unity, Equation (5.36) simplifies to

$$P^{\mathrm{V}} = \sum_{i=1}^{k} \gamma_i x_i P_i^{\mathrm{sat}}(T_{\mathrm{bf}}), \tag{5.38}$$

and when the activity coefficients are also unity, Equation (5.37) simplifies to

$$P^{\mathrm{V}} = \left(\sum_{i=1}^{k} \frac{y_i}{P_i^{\mathrm{sat}}(T_{\mathrm{df}})}\right)^{-1}. \tag{5.39}$$

When Equations (5.36) and (5.37) are solved using an iterative method, the solutions to Equations (5.38) and (5.39) can be used as the initial estimates of bubble and dew temperatures substituted into the Poynting correction. When solving Equation (5.37), another equation is needed to determine the liquid phase composition for evaluating the activity coefficient. For a binary mixture, an equation for the liquid mole fraction at the dew temperature can be derived by using Equation (5.28) for both components and $P^{\mathrm{L}} = P^{\mathrm{V}}$ for a flat interface, and it is given by

$$x_{1\mathrm{f}} = \left(\frac{y_2 \gamma_1 P_1^{\mathrm{sat}} \exp\left[v_1^{\mathrm{L}}(P^{\mathrm{V}} - P_1^{\mathrm{sat}})/(RT_{\mathrm{df}})\right]}{y_1 \gamma_2 P_2^{\mathrm{sat}} \exp\left[v_2^{\mathrm{L}}(P^{\mathrm{V}} - P_2^{\mathrm{sat}})/(RT_{\mathrm{df}})\right]} + 1\right)^{-1}. \tag{5.40}$$

The flat-interface azeotropic composition can be calculated by setting $2\sigma/r = 0$ in Equation (5.35).

5.2.4.4 Temperature-dependent Properties of Pure Components

One of the challenges of computing isobaric phase diagrams is accurately accounting for the temperature dependence of liquid properties, including flat-interface saturation vapor pressure, liquid molar volume, and surface tension. The saturation vapor pressure of each component with a planar vapor–liquid interface can be calculated as a function of temperature with an extended Antoine equation [71]

$$\ln P_i^{\text{sat}} = A_i + \frac{B_i}{T} + C_i \ln(T) + D_i T^{E_i}, \tag{5.41}$$

where the empirical parameters A_i, B_i, C_i, D_i, and E_i are component-specific. The liquid molar volume of each component can be described by the Rackett equation [169, 225], but because the Rackett equation is not valid for alcohols [225], the following more generalized form can be used instead [315]

$$v_i^{\text{L}} = a_i \times b_i^{\left(1-\frac{T}{c_i}\right)^{n_i}}, \tag{5.42}$$

where a_i, b_i, c_i and n_i are component-specific empirical parameters.

The surface tension of a pure component is also a function of temperature, and for pure components, a multiple linear regression can be performed on experimental data with a polynomial equation:

$$\sigma_i = \sum_{j=0}^{p_i} \theta_{j,i} T^j, \tag{5.43}$$

where p_i is the degree of the polynomial used for component i and $\theta_{j,i}$ are the empirically determined j^{th} order coefficients for component i. Higher order terms can extend the accuracy of the equation to temperatures up to the component's critical point. Another common equation used to describe the surface tension of pure components is of the following form [96, 114, 163]

$$\sigma_i = \alpha_i \left(1 - \frac{T}{T_{\text{cr},i}}\right)^{\beta_i}, \tag{5.44}$$

where α_i and β_i are fitting coefficients and $T_{\text{cr},i}$ is the liquid's critical temperature.

In this chapter, a nitrogen(1) + argon(2) system is first selected to compare dew-point predictions with previously published experimental work. Then, an ideal methanol(1) + ethanol(2) system and a nonideal ethanol(1) + water(2) system are selected and their phase behavior is modelled. The parameters for flat-interface saturation vapor pressure, liquid molar volume, and surface tension are summarized in Tables 5.1 to 5.4 for pure nitrogen, argon, methanol, ethanol, and water. These parameters can be used for temperatures between the listed T_{min} and T_{max} values.

Table 5.1: Extended Antoine equation parameters (Equation (5.41)) for flat-interface vapor pressure [Pa] and the range of validity for all pure components considered in this chapter [71].

	A_i	B_i	C_i	D_i	E_i	$T_{\min}$ [K]	$T_{\max}$ [K]
Nitrogen	58.282	−1084.1	−8.3144	0.044127	1	63.15	126.2
Argon	42.127	−1093.1	−4.1425	5.7254×10^{-5}	2	83.78	150.86
Methanol	82.718	−6904.5	−8.8622	7.4664×10^{-6}	2	175.47	512.50
Ethanol	73.304	−7122.3	−7.1424	2.8853×10^{-6}	2	159.05	514.00
Water	73.649	−7258.2	−7.3037	4.1653×10^{-6}	2	273.16	647.10

Table 5.2: Rackett equation parameters (Equation (5.42)) for liquid molar volume [mL/mol] and the range of validity for all pure components considered in this chapter [315].

	a_i	b_i	c_i	n_i	$T_{\min}$ [K]	$T_{\max}$ [K]
Nitrogen	89.1527	0.2861	126.2	0.2966	63.15	126.20
Argon	75.2038	0.286	150.86	0.2984	83.78	150.86
Methanol	117.802	0.27206	512.58	0.2331	175.47	512.58
Ethanol	166.917	0.27668	516.25	0.2367	159.05	516.25
Water	55.432	0.27	647.13	0.23	290.00	647.13

Table 5.3: Polynomial coefficients (Equation (5.43)) for surface tension [N/m] and the range of validity for pure methanol [71], ethanol [71], and water [315].

	$\theta_{0,i}$	$\theta_{1,i}$	$\theta_{2,i}$	$\theta_{3,i}$	$\theta_{4,i}$	$\theta_{5,i}$	$T_{\min}$ [K]	$T_{\max}$ [K]
Methanol	0.03513	-7.04×10^{-6}	-1.216×10^{-7}	0	0	0	273.10	503.15
Ethanol	0.03764	-2.157×10^{-5}	-1.025×10^{-7}	0	0	0	273.15	503.15
Water	−0.01073	1.299×10^{-3}	-6.544×10^{-6}	1.504×10^{-8}	-1.793×10^{-11}	8.635×10^{-15}	273.16	647.10

Table 5.4: Coefficients (Equation (5.44)) for surface tension [mN/m] and the range of validity for pure nitrogen, argon, and krypton [163].

	α_i	$T_{\text{cr,i}}$ [K]	β_i	$T_{\min}$ [K]	$T_{\max}$ [K]
Nitrogen	29.324108	126.2	1.259	65	120
Argon	37.898063	150.66	1.278	84	145

5.2.4.5 Liquid Mixture Properties

For the nonideal liquid mixture of ethanol(1) + water(2), the constants used in the Margules activity coefficient model are $A_{12} = 1.6252$ and $A_{21} = 0.8610$ for a pressure of 101 325 Pa [110].

In Equations (5.30), (5.31), (5.32), and (5.35), the surface tension is a function of liquid phase composition and temperature. For an ideal liquid mixture, surface tension can be calculated using a linear combination of mole fraction and pure component surface tension [70, 219]:

$$\sigma = \sigma_1 x_1 + \sigma_2 x_2. \tag{5.45}$$

Of interest in this chapter, the methanol + ethanol system has been confirmed to behave ideally from experimental measurements [25], and therefore Equation (5.45) can be used to calculate this mixture's surface tension as a function of composition. Substituting Equation (5.43) into Equation (5.45) for each component gives the following equation that captures the dependence of surface tension on liquid-phase composition and temperature:

$$\sigma = \left(\sum_{j=0}^{p_1} \theta_{j,1} T^j \right) x_1 + \left(\sum_{j=0}^{p_2} \theta_{j,2} T^j \right) x_2. \tag{5.46}$$

The surface tension of a nonideal mixture such as ethanol + water has been described as a function of liquid-phase composition by numerous models, such as those proposed by Shereshefsky [257], Connors and Wright [63], and Li *et al.* [56]. In this chapter, an equation is needed that additionally incorporates the influence of temperature on the nonideal mixture's surface tension. As shown in Chapter 2 [251], an extension of the Connors–Wright model [63] is best for calculating the temperature dependence of surface tension for aqueous binary mixtures. The original Connors–Wright model is given by [63]

$$\sigma = \sigma_2 - \left(1 + \frac{b(1-x_1)}{1-a(1-x_1)} \right) x_1 (\sigma_2 - \sigma_1), \tag{5.47}$$

where a and b are system-specific parameters fit to surface tension data as a function of x_1 at a single temperature, σ_2 is the surface tension of pure water, and σ_1 is the surface tension of the second component.

Substituting the temperature-dependent pure component surface tension (Equation (5.43)) into Equation (5.47) gives the following expression that describes the dependence of surface

tension on composition and temperature [251]:

$$\sigma = \left(\sum_{j=0}^{p_2} \theta_{j,2} T^j \right) - \left(1 + \frac{b(1-x_1)}{1-a(1-x_1)} \right) x_1 \left[\left(\sum_{j=0}^{p_2} \theta_{j,2} T^j \right) - \left(\sum_{j=0}^{p_1} \theta_{j,1} T^j \right) \right]. \quad (5.48)$$

Figure 5.2 compares Equation (5.48) to experimental data for the surface tension of ethanol(1) + water(2) as a function of liquid composition and temperature. For ethanol + water at 293 K, the parameters and 95% confidence intervals for Equation (5.48) are $a = 0.958 \pm 0.002$ and $b = 0.926 \pm 0.009$ for the data reported in Vázquez *et al.* [290] when using Equation (5.43) at 293 K with the coefficients for ethanol and water listed in Table 5.3. When these parameters are used in Equation (5.48) to predict the surface tension at higher temperatures, the average absolute percent error between model values and experimental points is 0.49%, with a maximum percent error of 1.38%. The parameters are not the same as those reported for ethanol + water in Chapter 2 [251], because higher-order polynomials are used in the current chapter to predict surface tension at temperatures greater than previously considered.

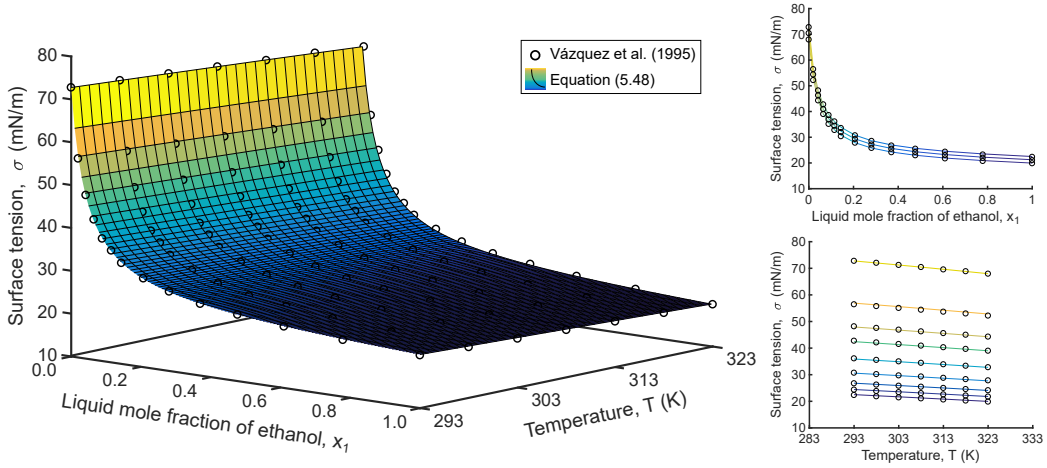

Figure 5.2: Surface tension of ethanol(1) + water(2) as a function of composition and temperature, as measured experimentally by Vázquez *et al.* [290] and as calculated by Equation (5.48).

For nitrogen(1) + argon(2), available surface tension data as a function of concentration is limited to a single temperature. The surface tension equation from Chapter 2 can be used to extrapolate to higher temperatures, since it was shown that the parameters are temperature-independent for the majority of systems previously studied [251]. For nitrogen(1) + argon(2),

Equation (5.44) can be substituted into Equation (5.47) for each pure component to give

$$\begin{aligned}\sigma = \ & \alpha_2 \left(1 - \frac{T}{T_{\mathrm{cr},2}}\right)^{\beta_2} \\ & - \left(1 + \frac{b(1-x_1)}{1-a(1-x_1)}\right) x_1 \left[\alpha_2 \left(1 - \frac{T}{T_{\mathrm{cr},2}}\right)^{\beta_2} - \alpha_1 \left(1 - \frac{T}{T_{\mathrm{cr},1}}\right)^{\beta_1}\right].\end{aligned} \tag{5.49}$$

At 83.82 K, the parameters and 95% confidence intervals for nitrogen + argon in Equation (5.49) are $a = 0.6295 \pm 0.0457$ and $b = 0.3244 \pm 0.0161$ for the data reported in Sprow and Prausnitz [269], and the fit is shown in Figure 5.3.

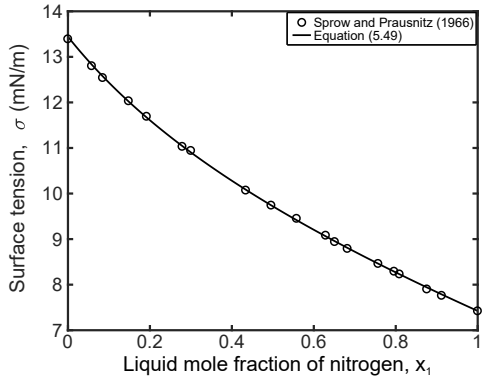

Figure 5.3: Surface tension as a function of composition at 83.82 K for nitrogen(1) + argon(2) measured experimentally by Sprow and Prausnitz [269] and the fit of Equation (5.49).

5.2.5 Numerical Methods

For a given pressure, overall composition, and radius of interfacial curvature, solving Equations (5.30) and (5.31) with Equation (5.32) yields the bubble and dew temperatures. Fixed-point iteration methods are outlined in Figure 5.4 and Figure 5.5 for calculating the bubble temperature and dew temperature, respectively, at a given composition. The tolerance ε for relative error between iteration steps is calculated using [50, 243]

$$\varepsilon = 0.5 \times 10^{-n}, \tag{5.50}$$

where n is the minimum desired number of accurate significant figures. Once the relative error reaches a value less than the tolerance, iteration is stopped. In this chapter, the tolerance for relative error is chosen for accuracy to five significant figures. MATLAB R2016b (Natick, USA) was used for calculations.

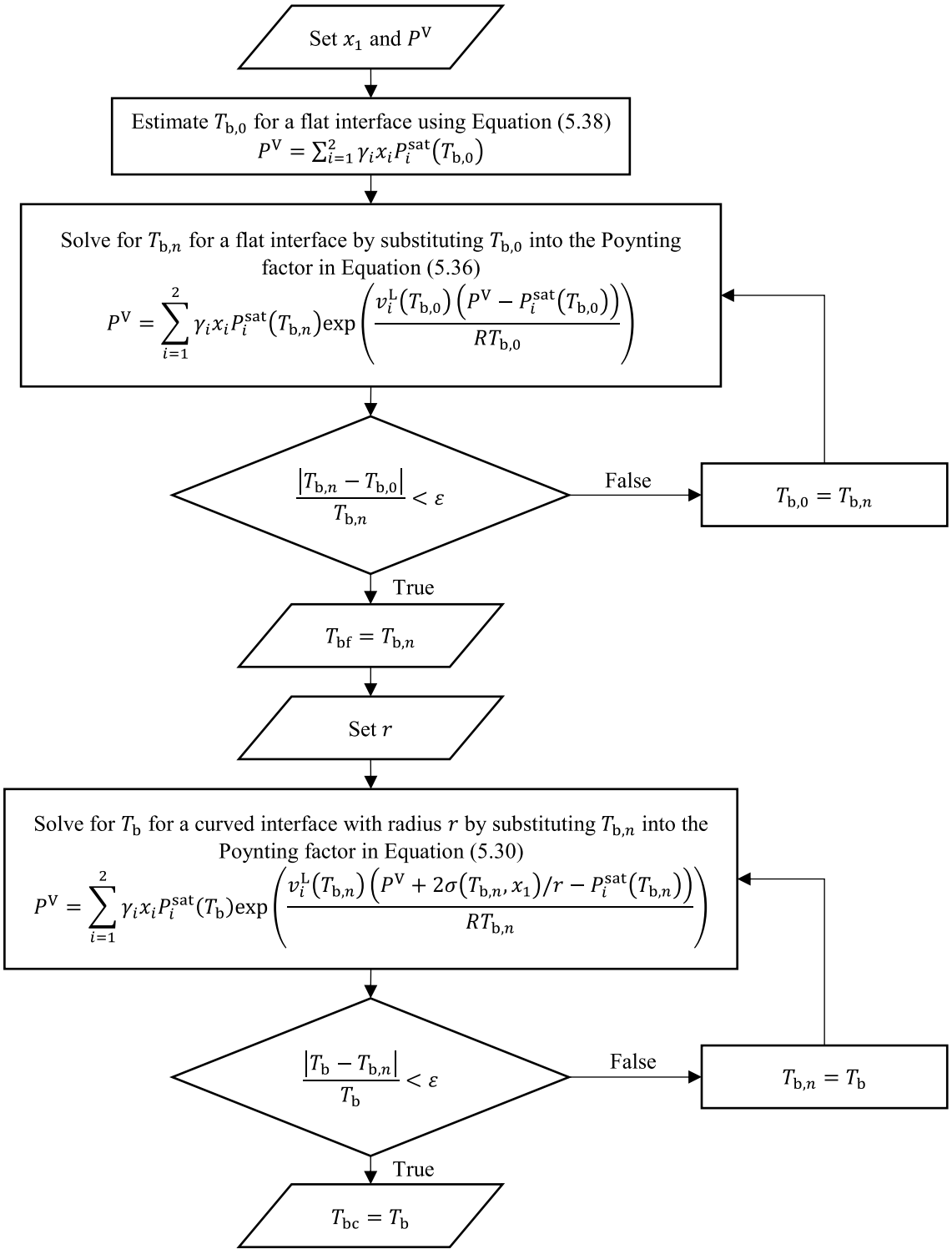

Figure 5.4: Flowchart for calculating the bubble temperature of a binary system with a flat interface and with a curved interface for a given composition in the liquid phase.

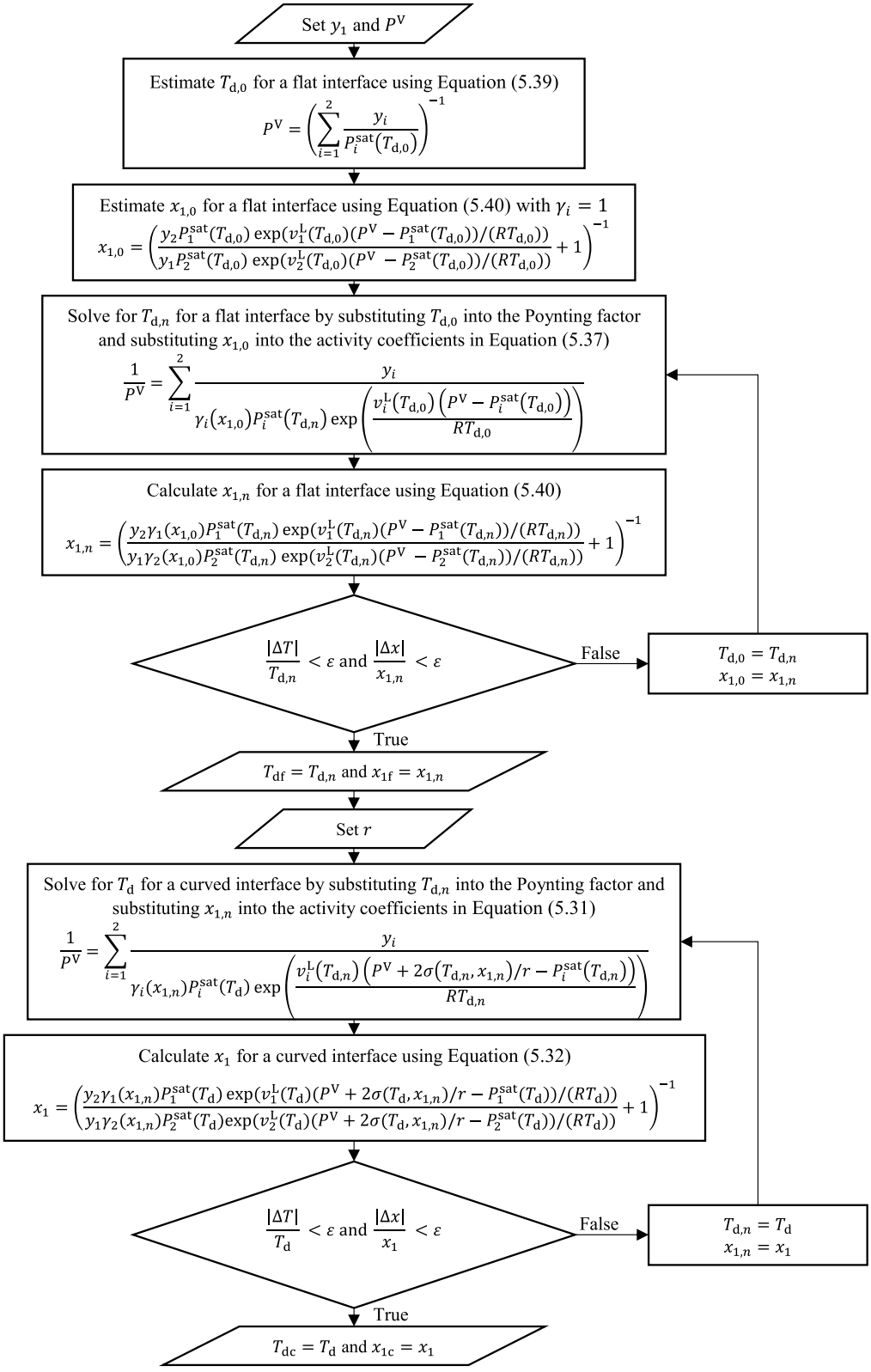

Figure 5.5: Flowchart for calculating the dew temperature of a binary system with a flat interface and with a curved interface for a given composition in the vapor phase.

5.3 Results and Discussion

5.3.1 Comparison with Experimental Data

Alam *et al.* [5] reported experimental results for the temperature at which phase transitions occur during adsorption and desorption for mixtures of nitrogen(1) + argon(2) in Vycor glass with an average cylindrical pore diameter of 4 nm [5, 134] at a constant vapor-phase pressure of 300 kPa, as shown by the symbols in Figure 5.6. The symbols indicate the midpoints of the phase transition and the error bars on each symbol show the start and end of the transition; the values were digitized from the figure published by Alam *et al.* [5]. According to the classical model of adsorption and desorption, only desorption has a geometry resembling the hemispherical interface between the liquid and vapor phases seen in Figure 5.1(b) for a cylindrical pore. Adsorption (and capillary condensation) is hypothesized to occur first on the walls of the cylindrical pore, creating a thin cylindrical layer of liquid. The curvature of an adsorbed cylinder of liquid is equal to half the curvature of a hemisphere in the same pore (curvature is $1/r_\mathrm{p}$ for a cylinder and $2/r_\mathrm{p}$ for a sphere with radius r_p) [26, 60, 112]. That is, r in the governing equations derived herein equals -2 nm for desorption and r equals -4 nm for adsorption. The predictions of dew point using these radii are plotted in Figure 5.6 as a function of nitrogen mole fraction. In the context of the adsorption and desorption experiments, the dew point corresponds to the first appearance of liquid during the adsorption process, and it corresponds to the last disappearance of liquid during the desorption process. The dew point predictions agree closely with the experimental data points (the average absolute percent error between predictions and data is 0.45%), and most importantly, the theoretical predictions are completely independent of the experiments. The governing equations only require the bulk properties of the pure liquids and the pore radius of the experimental porous medium. This is in contrast to the model proposed by Tan and Piri [279] that relies on additional fitting parameters for the behavior of pure nitrogen and pure argon in pores; their fitting parameters are functions of temperature and pore radius.

Jones and Fretwell [134] reported experimental phase-transition temperatures as a function of mole fraction for argon(1) + krypton(2), but the reported trends are not consistent with those reported by Alam *et al.* [5] for nitrogen(1) + argon(2) using the same experimental technique; thus the argon(1) + krypton(2) data cannot be interpreted within the thermodynamic framework proposed in this chapter. That is, the adsorption curve for argon(1) + krypton(2) is concave up and is proposed to correspond to the bubble point [134], whereas the adsorption curve for nitrogen(1) + argon(2) is concave down and corresponds to the dew point for each vapor-phase composition.

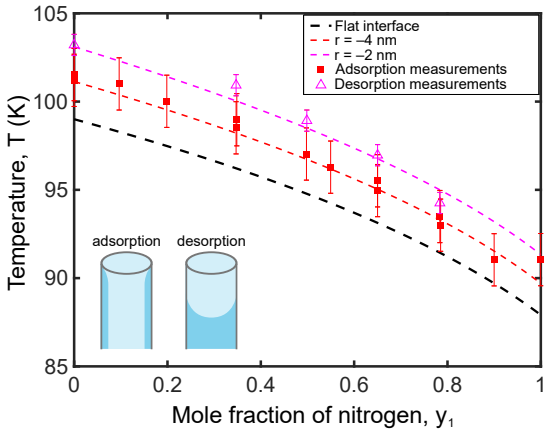

Figure 5.6: Prediction (not a fit) of adsorption and desorption dew temperatures as functions of nitrogen mole fraction for nitrogen(1) + argon(2) in a capillary with a radius of 2 nm and experimental measurements of adsorption and desorption at a vapor-phase pressure of 300 kPa from Alam *et al.* [5]. The schematic of the classical model of adsorption and desorption is adapted from Donohue and Aranovich [76].

5.3.2 Predictions for Methanol(1) + Ethanol(2) and Ethanol(1) + Water(2)

Given the success of Gibbsian composite-system thermodynamics in predicting the phase behavior of nitrogen(1) + argon(2) in porous media, systems of methanol(1) + ethanol(2) and ethanol(1) + water(2) are now considered, and predictions are made for a pressure of 101 325 Pa in the vapor phase. Isobaric phase diagrams and x-y plots are illustrated in Figure 5.7 and Figure 5.8 for these systems, respectively, at various positive and negative radii of curvature. The phase envelope outlined in black is for a system with a flat interface between the liquid and vapor phases. For both systems, the bubble and dew temperatures decrease for positive radii of curvature, whereas for negative radii of curvature, the bubble and dew temperatures increase. As the absolute value of the radius of curvature decreases, the temperatures move farther away from the flat-interface phase envelope. If the flat-interface phase envelope were to be used for phase predictions of systems with significant curvature, it would yield increasingly inaccurate results.

What is the physical meaning behind the shift of the phase envelope in the presence of interfacial curvature? For a given vapor-phase pressure, it is easier to evaporate a liquid droplet (positive radius of curvature) because of the elevated pressure in the liquid phase; a temperature lower than the bubble temperature of a planar liquid interface is therefore needed to evaporate a spherical liquid droplet. Similarly, a temperature lower than the dew temperature for a planar interface is needed to start the condensation of a vapor phase into a spherical liquid droplet because of the higher liquid-phase pressure. The multicomponent vapor phase is supercooled below its

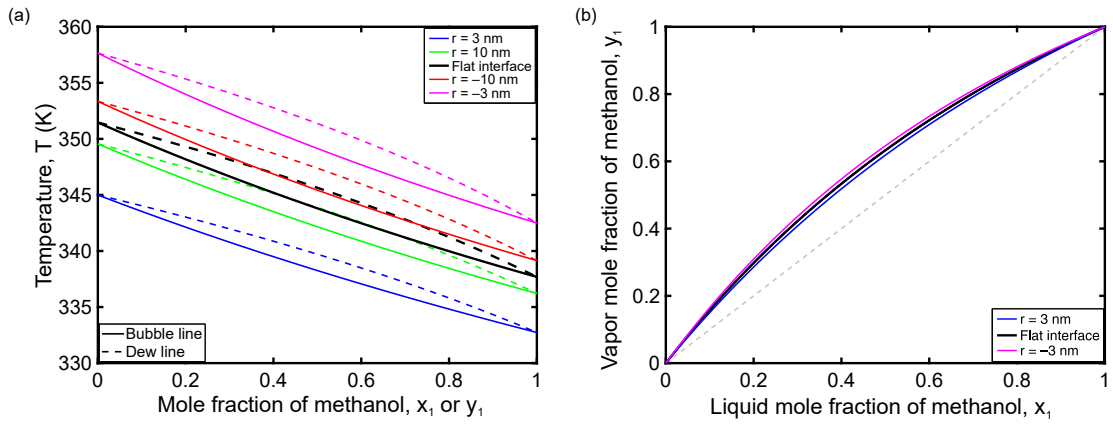

Figure 5.7: Predictions of (a) the phase diagram and (b) the *x*-*y* plot for methanol(1) + ethanol(2) as a function of interfacial radius of curvature for P^{V} = 101 325 Pa.

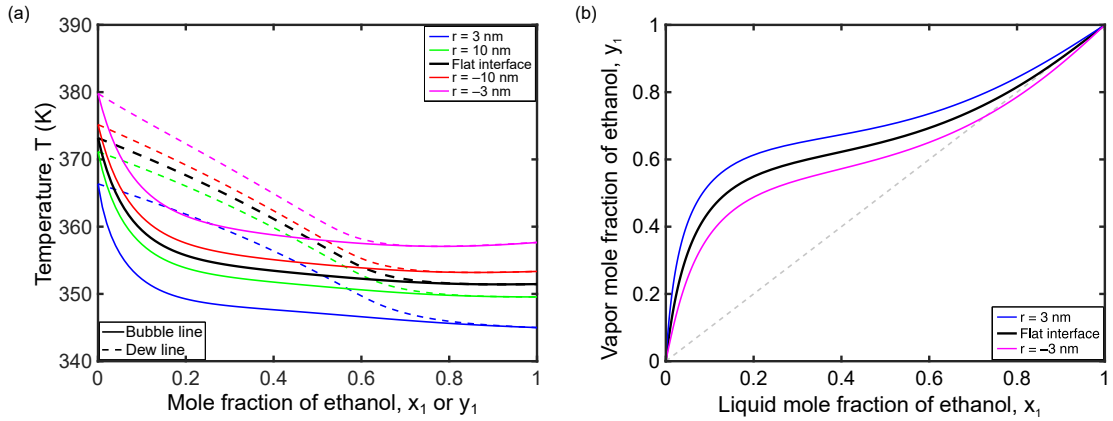

Figure 5.8: Predictions of (a) the phase diagram and (b) the *x*-*y* plot for ethanol(1) + water(2) as a function of interfacial radius of curvature for P^{V} = 101 325 Pa.

planar dew temperature until a phase change occurs to form a highly curved multicomponent liquid phase, as described by Defay and Prigogine for a single component [70].

Considering a negative radius of curvature, a hemispherical vapor phase condenses at a temperature higher than the dew temperature of a planar liquid–vapor interface, because the bubble is at an elevated pressure as compared to the liquid phase in the capillary. For the bubble point of a system with interfacial curvature, a temperature higher than the bubble temperature of a planar interface is needed to evaporate a liquid phase with a hemispherical interface in a capillary, also because of the elevated pressure in the vapor phase. As a result, a bulk liquid can become superheated until a vapor bubble forms [70].

The isobaric *x*-*y* curves show trends as a function of radius of curvature similar to those seen for the isothermal *x*-*y* plots of each system [254]. That is, for methanol(1) + ethanol(2), the curve moves closer to the 45° line for positive radii and away from the line for negative

radii. For ethanol(1) + water(2), the *x*-*y* curve moves farther away from the 45° line for positive radii and closer for negative radii. For a given vapor-phase composition in either system, a positive radius of curvature decreases the equilibrium liquid mole fraction of ethanol compared to the flat-interface value, and a negative radius increases the equilibrium liquid mole fraction of ethanol.

Although the trends are similar, the magnitude of the *x*-*y* curve shift differs between isothermal and isobaric conditions. To compare the magnitude of this shift, the isothermal liquid composition for each vapor mole fraction can be calculated as outlined in Chapter 4 [254] using the equations for flat-interface saturation pressure, liquid molar volume, and surface tension as described in this chapter evaluated at 298 K. Figure 5.9 compares the difference between curved-interface liquid composition and flat-interface liquid composition at the dew point as a function of vapor phase composition for methanol(1) + ethanol(2) and ethanol(1) + water(2) for a radius of curvature of $r = 3$ nm at constant temperature and at constant P^{V}. Under isothermal conditions, the maximum difference in liquid composition relative to the flat-interface liquid composition, $|x_{1\mathrm{c}} - x_{1\mathrm{f}}|$, is 0.02658, while the maximum difference is just 0.01532 under isobaric conditions for methanol(1) + ethanol(2) at the dew point. For ethanol(1) + water(2), the maximum isothermal and isobaric differences are 0.1960 and 0.1886, respectively, for $r = 3$ nm. Therefore, the presence of a nanocurved interface has a greater impact on vapor–liquid equilibrium at a constant temperature of 298 K than it does at a constant P^{V} of 101 325 Pa.

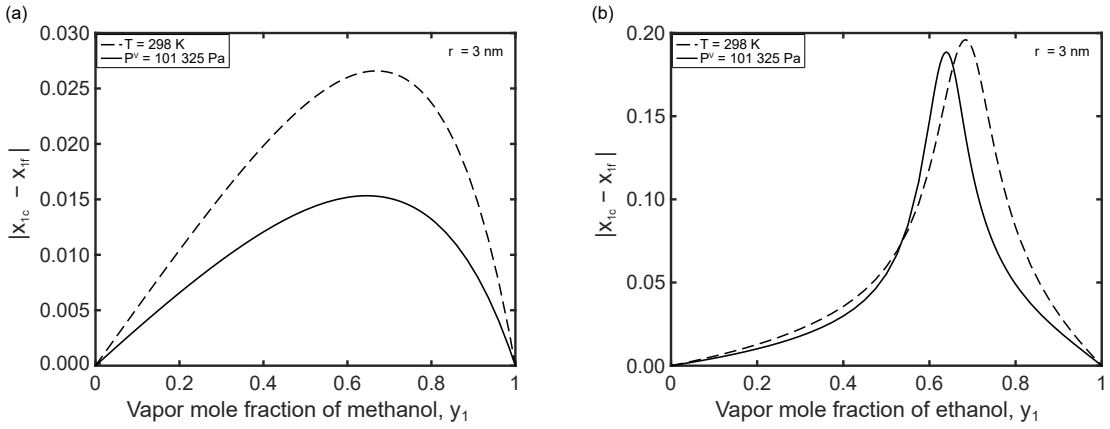

Figure 5.9: Difference between the 3-nm curved-interface liquid-phase composition and the flat-interface liquid-phase composition at the dew point as a function of vapor-phase composition for (a) methanol(1) + ethanol(2) and (b) ethanol(1) + water(2) at a constant P^{V} of 101 325 Pa (solid line) and at a constant temperature of 298 K (dashed line).

For the ethanol(1) + water(2) system, the isobaric azeotropic composition can be calculated as a function of radius of curvature, as illustrated in Figure 5.10; azeotropic composition is plotted as a function of the inverse radius in Figure 5.11. The dashed black line in Figure 5.10

is the azeotropic composition for a system with a flat interface between the vapor and liquid phases. For positive radii of curvature, the azeotrope shifts toward 100 mol% ethanol, whereas for negative radii of curvature, the azeotrope shifts in the opposite direction. Such a trend was also seen under isothermal conditions [254] but, as observed for the *x*-*y* curves, the magnitude of the shift differs under constant vapor-phase pressure conditions. The isobaric (P^{V} = 101 325 Pa) azeotrope vanishes for positive radii of curvature less than 17 nm, while the isothermal (298 K) azeotrope vanishes for positive radii of curvature less than 31 nm. It takes a smaller radius of curvature to remove the azeotrope at a constant vapor-phase pressure of 101 325 Pa than it does at a constant temperature of 298 K.

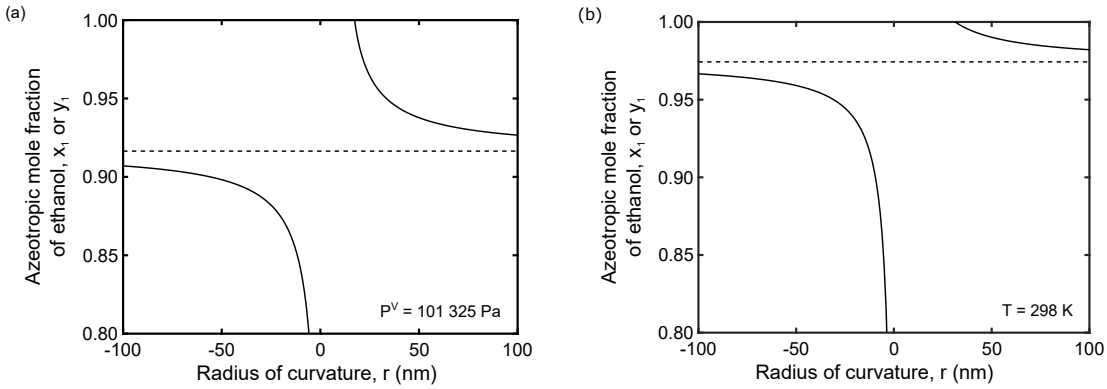

Figure 5.10: Predictions of the azeotropic composition as a function of radius of curvature for ethanol(1) + water(2) (a) at a pressure of 101 325 Pa in the vapor phase and (b) at a temperature of 298 K.

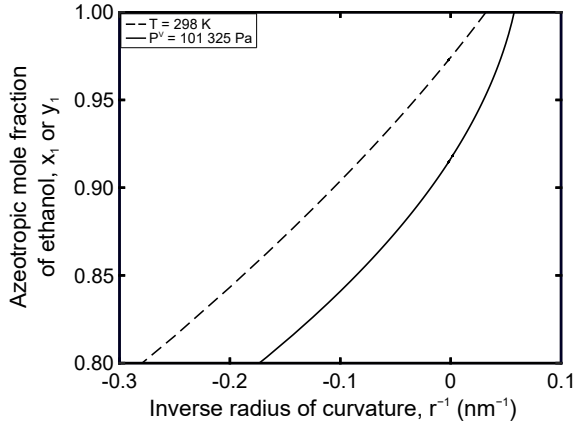

Figure 5.11: Predictions of the azeotropic composition as a function of inverse radius of curvature for ethanol(1) + water(2) at a pressure of 101 325 Pa in the vapor phase (solid line) and at a temperature of 298 K (dashed line).

5.4 Conclusions

From Gibbsian composite-system thermodynamics, the equilibrium conditions for a multicomponent system with interfacial curvature between the vapor and liquid phases were derived. Based on these conditions, the partial phase diagram of nitrogen + argon and the complete phase diagrams of methanol + ethanol and ethanol + water systems were calculated. Predictions of dew point for nitrogen + argon agreed with experimental data of adsorption and desorption reported in the literature with an average percent difference of 0.45%. Over all systems, the phase envelopes shifted to lower bubble and dew temperatures for positive radii of curvature and shifted to higher temperatures for negative radii of curvature, with a greater shift for radii closer to zero. For the nonideal ethanol + water system, the azeotropic composition moved toward 100 mol% ethanol for positive radii, as seen for isothermal conditions, but the magnitude of the change differed.

The outlined thermodynamic approach can be applied to spherical phases within bulk phases and to phases confined in capillaries. While any solid–liquid interactions that would be present in capillaries are neglected in the present analysis, by doing so, the effect of curvature alone is isolated. It is indeed valuable to ascertain the magnitude of the curvature effect in comparison to other forces so that the relative importance of each contribution can be determined, and a more complete understanding of nanoscale phase equilibrium can be reached in applications ranging from hydrocarbon recovery and atmospheric physics to catalysis and drug delivery.

PART III

WETTING

Chapter 6

Gibbsian Thermodynamics of Cassie–Baxter Wetting (Were Cassie and Baxter Wrong? Revisited)[1]

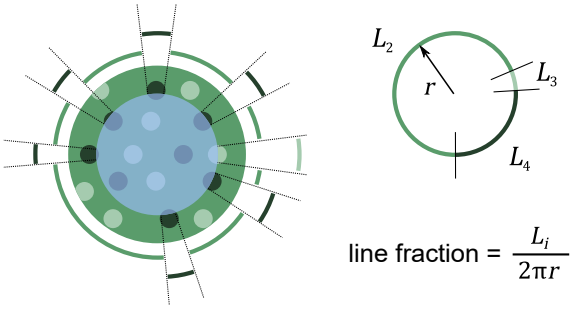

Abstract

Over the past decade, there has been a debate over the correct form of the Cassie–Baxter equation that describes the expected contact angle of a liquid drop on a heterogeneous surface. The original Cassie–Baxter equation uses an area fraction of each solid phase calculated over the entirety of the surface, and its derivation is based on an assumption not all surfaces necessarily satisfy. Herein, we introduce fundamental Gibbsian composite-system thermodynamics as a new approach for deriving the complete set of equilibrium conditions for a liquid drop resting on a heterogeneous multiphase solid substrate. One of the equilibrium conditions is a form of the Cassie–Baxter equation that uses a line fraction determined at the contact line outlining the perimeter of the solid–liquid contact area. We elucidate the practical implications of using the line fraction for common patterns of heterogeneities.

[1]Reproduced, with minor modifications, with permission from N. Shardt and J. A. W. Elliott. "Gibbsian Thermodynamics of Cassie–Baxter Wetting (Were Cassie and Baxter Wrong? Revisited)". *Langmuir* 34.40 (2018), pp. 12191–12198. https://pubs.acs.org/articlesonrequest/AOR-tif5N8X82K2tVuR94pTk Copyright 2018 American Chemical Society. J. A. W. Elliott conceived the original idea. In performing this research, I had valuable discussions with Leila Zargarzadeh, who shared pertinent literature, and the anonymous reviewers brought additional literature to our attention.

6.1 Introduction

The term wetting describes the behavior of a liquid drop when placed on a solid substrate in terms of the equilibrium shape that the drop attains. Understanding wetting behavior is critical in the preparation of food, non-stick and waterproof surfaces, chemical products, and pharmaceutical drugs [26, 62, 106], as well as in the design of nanofluidic technologies [228]. Many natural structures and processes also depend on the ability of the liquid phase to wet or not wet the surface it touches [106, 159], and the roughness of the surface plays an important role in determining the behavior of the liquid.

The term Cassie–Baxter (CB) wetting refers to a wetting state where a liquid drop sits on top of a surface's rough features and traps pockets of gas between these features. The macroscopic angle that the liquid–vapor interface makes with respect to the solid in this state has been described by the CB equation [49]. The CB equation has also been used to predict the contact angle of a liquid on smooth surfaces made up of patches of different components, as given by [188]

$$\cos\theta_{\mathrm{CB}} = \sum_i f_i \cos\theta_i, \tag{6.1}$$

where θ_{CB} is the predicted contact angle, f_i is the area fraction of component i on the solid surface ($A_i/A^{\mathrm{projected}}$) and θ_i is the contact angle of the liquid drop on a smooth homogeneous surface made up of only component i. Considering a drop of water resting on a rough surface, Cassie and Baxter's analysis assumes "that for an increase in area δA of the porous surface–water interface there is formed an area of solid–water interface, $f_1\delta A$, and of water–air interface, $f_2\delta A$, for any infinitesimal value of δA" [49], but this statement is not necessarily satisfied for any arbitrary distribution of rough protrusions or heterogeneities on a surface.

Researchers have questioned the validity of the Cassie–Baxter equation (see a detailed review by Erbil [82]). Extrand [90] and Gao and McCarthy [103] designed heterogeneous surfaces for which Equation (6.1) does not predict the experimentally observed contact angle. However, as explained by McHale [185], these surfaces had single-point defects and did not satisfy the assumption regarding differential areas that was used in the derivation of the Cassie–Baxter equation. The Cassie–Baxter equation should not be expected to accurately predict the contact angles of liquids on such surfaces. Nevertheless, Gao and McCarthy's work motivated the rederivation of the Cassie–Baxter equation, and a local area fraction in the vicinity of the contact line was proposed by McHale [185], Nosonovsky [206], and later by Seo *et al*. [248] to extend the Cassie–Baxter equation to surfaces with single-point defects.

Cubaud and Fermigier [65] and Larsen and Taboryski [158] reported that their experimental measurements of contact angle agreed more closely with predictions when line fractions at the contact line were used in place of area fractions in the Cassie–Baxter equation. The use of a

line fraction was first suggested by Pease in 1945 [212], but it was not adopted by researchers at the time. Later, in 1998, Swain and Lipowsky [275] used a statistical mechanical definition to theoretically justify the use of a line fraction in the Cassie–Baxter equation. Another theoretical justification for using a line fraction was proposed by Xu and Wang [314] using a mathematical technique called homogenization, and they determined that the macroscopic contact angle is the integral average of local contact angles along the contact line. Hey and Kingston [120] minimized the energy of a spherical drop on a heterogeneous surface with the assumptions that the area fraction of the liquid–solid interface changes as a function of drop radius and that the drop volume is constant, and the condition for equilibrium was a line-fraction Cassie–Baxter equation.

To summarize, three versions of the Cassie–Baxter equation are present in the literature. The first uses an area fraction based on the whole solid–liquid interface (a global area fraction), the second uses an area fraction based on the area in the vicinity of the contact line (a local area fraction), and the third uses a line fraction. The line-fraction Cassie–Baxter equation is the most general form, because it is valid for any distribution of heterogeneities in the solid surface, as will be discussed in this chapter.

The goal of this chapter is to introduce Gibbsian composite-system thermodynamics [46, 108] as a new tool for determining the equilibrium contact angle of a liquid drop on a heterogeneous surface. A composite system is one that is not a simple system itself but is made up of simple systems. In general, Gibbsian composite-system thermodynamics is a framework for determining the equilibrium conditions of a composite system by extremizing entropy, subject to the constraints of the system, simultaneously yielding equations for thermal, chemical, and mechanical equilibrium. With such a systematic approach, Gibbsian composite-system thermodynamics can be applied to systems that may be difficult to analyze by other methods, such as systems with a multicomponent liquid phase or those with more complex geometries. Recent work in Gibbsian composite-system thermodynamics has examined the effect of curved interfaces on phase diagrams describing vapor–liquid equilibrium [253, 254] and solid–liquid equilibrium [171]. Past work in Gibbsian composite-system thermodynamics in the field of wetting phenomena has studied smooth, homogeneous surfaces with and without the influence of gravity [79, 87, 298, 299, 323, 324]. Eslami and Elliott derived the equilibrium conditions for a liquid drop on a smooth homogeneous surface that is either rigid or fluid by extremizing entropy subject to system constraints [87], and Zargarzadeh and Elliott derived the equilibrium conditions for a liquid phase located between a sphere and a flat plate [323].

Herein, we outline a new derivation of equilibrium contact angle for a liquid phase in equilibrium with its vapor on smooth heterogeneous surfaces, or rough surfaces, upon which CB wetting is observed. This new theory addresses experimentalists' concerns regarding the

original area-fraction CB equation, and it reinforces the use of the line fraction for the prediction of CB contact angles. Compared to past theoretical work on the line-fraction CB equation, the novelty of this chapter lies in the use of Gibbsian composite-system thermodynamics to simultaneously derive all equations for equilibrium, not solely the one governing the contact angle. Through this derivation, the utility of Gibbsian thermodynamics is highlighted, and it is anticipated that this framework can be extended to derive the equilibrium conditions of more complex systems and modes of wetting.

We emphasize that the present chapter only deals with an equilibrium/static wetting state under no external forces, and therefore the contact angle hysteresis observed between advancing and receding contact lines is not within the scope of our treatment. Interestingly, the original paper by Cassie and Baxter [49] was in fact a model proposed for advancing and receding contact angles, but Equation (6.1) was later shown to describe the equilibrium contact angle instead [133]. The difference between the advancing/receding contact angles and the equilibrium contact angle has been attributed to changes in the local geometry of the contact line [54, 91, 172, 226, 264, 311] and pinning/depinning forces [132, 145, 311].

6.2 Derivation of the Conditions for Equilibrium

Figure 6.1 illustrates the multiphase system of interest. We consider a simplified geometry where the liquid phase is in the shape of a spherical cap and the solid–liquid interface is an undistorted circle. Thus, the final equation derived in this chapter is only valid if the liquid shape satisfies these constraints; physically, this occurs when the sizes of the surface heterogeneities are much smaller than the drop (note that the sizes of heterogeneities have been enlarged in the diagram for illustrative purposes). We also assume that there are no external forces, such as pinning/depinning forces at the three-phase (solid–liquid–vapor) contact line or gravity. The entire solid–liquid–vapor system is contained within a piston–cylinder device that interacts with a surrounding reservoir at temperature T^{R} and pressure P^{R}. Energy can cross the system boundary, and the volume of the system can vary. Following Gibbsian composite-system thermodynamics, a system with an interface is modeled as two homogeneous bulk phases separated by a dividing surface that has no volume but has all other thermodynamic quantities (internal energy, entropy, and moles). The moles attributed to this dividing surface, *i.e.*, "in the interface", are the "excess" moles that account for the gradient in molar concentration in the bulk phases caused by the two phases being in contact, and depending on the location of the interface, the number of excess moles may be positive, zero, or negative. Only component 1 is present in the liquid phase, the vapor phase, the vapor–liquid interface, the vapor–solid interfaces, and the solid–liquid interfaces. There are multiple solid phases (n of them), each

made up of a different component (components 2, 3, . . . , $n+1$).

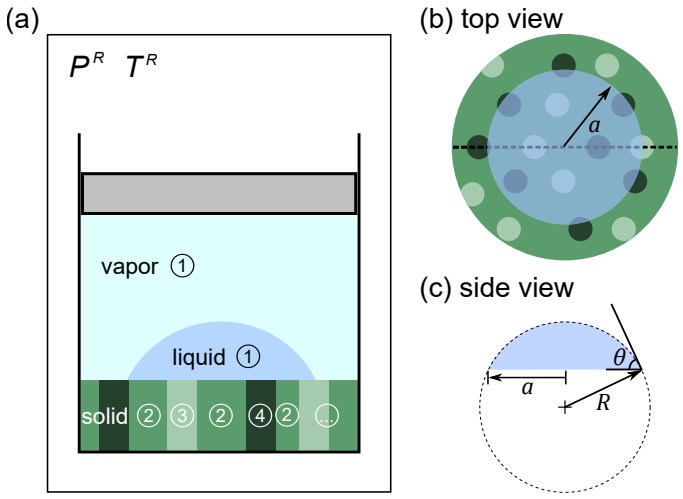

Figure 6.1: System definition and geometry for a drop in the Cassie–Baxter state. (a) Schematic of a piston–cylinder device in a reservoir containing a liquid drop (with only component 1) in equilibrium with its vapor and a multiphase solid surface (with each solid phase containing only one of component 2, 3, . . .). (b) Top view of the liquid drop shape. The dashed line shows the plane across which the illustrated cross-section in (a) is taken. (c) Geometry of the liquid drop in the shape of a spherical cap with contact angle θ, radius of curvature R, and radius of the solid–liquid area a (adapted from Ref. [26]).

The equilibrium conditions of the illustrated system can be derived given that entropy (S) is extremized at equilibrium. At an extremum, the differential of entropy (dS) is equal to zero

$$\mathrm{d}S^{\mathrm{L}} + \mathrm{d}S^{\mathrm{V}} + \sum_{i=2}^{n+1} \mathrm{d}S^{\mathrm{S}_i} + \mathrm{d}S^{\mathrm{LV}} + \sum_{i=2}^{n+1} \mathrm{d}S^{\mathrm{S}_i\mathrm{L}} + \sum_{i=2}^{n+1} \mathrm{d}S^{\mathrm{S}_i\mathrm{V}} + \mathrm{d}S^{\mathrm{R}} = 0, \tag{6.2}$$

where the superscripts L, V, and S denote the liquid, vapor, and solid phases, respectively, LV, S_iL, and S_iV denote the liquid–vapor, solid–liquid, and solid–vapor interfaces, and R denotes the reservoir.

Expressions for the differential entropy of each bulk phase can be written as [46, 108, 129]

$$\mathrm{d}S^{\mathrm{L}} = \frac{1}{T^{\mathrm{L}}}\,\mathrm{d}U^{\mathrm{L}} + \frac{P^{\mathrm{L}}}{T^{\mathrm{L}}}\,\mathrm{d}V^{\mathrm{L}} - \frac{\mu_1^{\mathrm{L}}}{T^{\mathrm{L}}}\,\mathrm{d}N_1^{\mathrm{L}} \tag{6.3}$$

$$\mathrm{d}S^{\mathrm{V}} = \frac{1}{T^{\mathrm{V}}}\,\mathrm{d}U^{\mathrm{V}} + \frac{P^{\mathrm{V}}}{T^{\mathrm{V}}}\,\mathrm{d}V^{\mathrm{V}} - \frac{\mu_1^{\mathrm{V}}}{T^{\mathrm{V}}}\,\mathrm{d}N_1^{\mathrm{V}} \tag{6.4}$$

$$\mathrm{d}S^{\mathrm{S}_i} = \frac{1}{T^{\mathrm{S}_i}}\,\mathrm{d}U^{\mathrm{S}_i} + \frac{P^{\mathrm{S}_i}}{T^{\mathrm{S}_i}}\,\mathrm{d}V^{\mathrm{S}_i} - \frac{\mu_i^{\mathrm{S}_i}}{T^{\mathrm{S}_i}}\,\mathrm{d}N_i^{\mathrm{S}_i}, \tag{6.5}$$

where U is internal energy, T is absolute temperature, P is pressure, V is volume, μ is chemical potential, and N is number of moles.

We use the Gibbs surface of tension approach for the curved liquid–vapor interface [108], which means that component 1 is present in the interface and the surface tension is independent of the radius of curvature. The expression for differential entropy of the liquid–vapor interface is

$$\mathrm{d}S^{\mathrm{LV}} = \frac{1}{T^{\mathrm{LV}}}\,\mathrm{d}U^{\mathrm{LV}} - \frac{\sigma^{\mathrm{LV}}}{T^{\mathrm{LV}}}\,\mathrm{d}A^{\mathrm{LV}} - \frac{\mu_1^{\mathrm{LV}}}{T^{\mathrm{LV}}}\,\mathrm{d}N_1^{\mathrm{LV}}, \tag{6.6}$$

where A is the interfacial area.

We use the Gibbs dividing surface approach for the flat solid–liquid interfaces [108], where the dividing surface is placed such that one of the components is not present in the interfaces. In this case, we choose that the solid-phase component i of solid S_i is not present, leaving only component 1 in the solid–liquid interfaces. The expression for the differential entropy of each solid–liquid interface is

$$\mathrm{d}S^{\mathrm{S}_i\mathrm{L}} = \frac{1}{T^{\mathrm{S}_i\mathrm{L}}}\,\mathrm{d}U^{\mathrm{S}_i\mathrm{L}} - \frac{\sigma^{\mathrm{S}_i\mathrm{L}}}{T^{\mathrm{S}_i\mathrm{L}}}\,\mathrm{d}A^{\mathrm{S}_i\mathrm{L}} - \frac{\mu_1^{\mathrm{S}_i\mathrm{L}}}{T^{\mathrm{S}_i\mathrm{L}}}\,\mathrm{d}N_1^{\mathrm{S}_i\mathrm{L}}. \tag{6.7}$$

Similar to the solid–liquid interfaces, we use the Gibbs dividing surface for the solid–vapor interfaces so that the solid-phase component i is not present in the solid–vapor interfaces. The expression for the differential entropy of each solid–vapor interface is

$$\mathrm{d}S^{\mathrm{S}_i\mathrm{V}} = \frac{1}{T^{\mathrm{S}_i\mathrm{V}}}\,\mathrm{d}U^{\mathrm{S}_i\mathrm{V}} - \frac{\sigma^{\mathrm{S}_i\mathrm{V}}}{T^{\mathrm{S}_i\mathrm{V}}}\,\mathrm{d}A^{\mathrm{S}_i\mathrm{V}} - \frac{\mu_1^{\mathrm{S}_i\mathrm{V}}}{T^{\mathrm{S}_i\mathrm{V}}}\,\mathrm{d}N_1^{\mathrm{S}_i\mathrm{V}}. \tag{6.8}$$

The expression for the differential entropy of the reservoir is

$$\mathrm{d}S^{\mathrm{R}} = \frac{1}{T^{\mathrm{R}}}\,\mathrm{d}U^{\mathrm{R}} + \frac{P^{\mathrm{R}}}{T^{\mathrm{R}}}\,\mathrm{d}V^{\mathrm{R}} - \sum_j \frac{\mu_j^{\mathrm{R}}}{T^{\mathrm{R}}}\,\mathrm{d}N_j^{\mathrm{R}}, \tag{6.9}$$

where the index j covers all components in the reservoir.

Equations (6.3)–(6.9) can be substituted into Equation (6.2), and further simplifications to the resulting expression can be made once certain constraints are defined, including the conservation of mass, the conservation of energy, and geometric constraints.

There is no mass transfer between the piston–cylinder device and the reservoir. The solid phases are non-volatile, and component 1 does not solidify nor absorb/dissolve into the solid phases. Therefore, the following mathematical relationships are true for the components in the

reservoir, for component 1, and for the components in the solid phases, respectively,

$$\mathrm{d}N_j^{\mathrm{R}} = 0 \tag{6.10}$$

$$\mathrm{d}N_1^{\mathrm{V}} = -\,\mathrm{d}N_1^{\mathrm{L}} - \mathrm{d}N_1^{\mathrm{LV}} - \sum_{i=2}^{n+1} \mathrm{d}N_1^{\mathrm{S}_i\mathrm{L}} - \sum_{i=2}^{n+1} \mathrm{d}N_1^{\mathrm{S}_i\mathrm{V}} \tag{6.11}$$

$$\mathrm{d}N_{i\neq 1}^{\mathrm{S}_i} = 0. \tag{6.12}$$

The law of conservation of energy can be applied to the piston–cylinder device within the reservoir (together they make up an isolated system), giving the following relationship between the internal energies of each phase, interface, and reservoir

$$\mathrm{d}U^{V} = -\,\mathrm{d}U^{\mathrm{L}} - \sum_{i=2}^{n+1} \mathrm{d}U^{\mathrm{S}_i} - \mathrm{d}U^{\mathrm{LV}} - \sum_{i=2}^{n+1} \mathrm{d}U^{\mathrm{S}_i\mathrm{L}} - \sum_{i=2}^{n+1} \mathrm{d}U^{\mathrm{S}_i\mathrm{V}} - \mathrm{d}U^{\mathrm{R}}. \tag{6.13}$$

The volume of the piston–cylinder device can change, but the total volume of the piston–cylinder device and the reservoir together remains constant. Given that the solid phases are incompressible ($\mathrm{d}V_i^{\mathrm{S}} = 0$), the volumetric constraint is

$$\mathrm{d}V^{\mathrm{V}} = -\,\mathrm{d}V^{\mathrm{L}} - \mathrm{d}V^{\mathrm{R}}. \tag{6.14}$$

The sum of the solid–liquid interfacial area and the solid–vapor interfacial area is constant for each solid phase, giving the following mathematical relationship for the differential changes in interfacial area

$$\mathrm{d}A^{\mathrm{S}_i\mathrm{V}} = -\,\mathrm{d}A^{\mathrm{S}_i\mathrm{L}}. \tag{6.15}$$

The volume of the spherical cap of liquid illustrated in Figure 6.1 can be written in terms of the radius of curvature, R , and the contact angle, θ [26, 87, 220]

$$V^{\mathrm{L}} = \frac{\pi R^3}{3}\left(2 - 3\cos\theta + \cos^3\theta\right). \tag{6.16}$$

The area of the liquid–vapor curved interface is [26, 87, 220]

$$A^{\mathrm{LV}} = 2\pi R^2\left(1 - \cos\theta\right). \tag{6.17}$$

The solid–liquid interface is in the shape of a circle, as illustrated in Figure 6.1(b) and Figure 6.2(a), and the interfacial area between the liquid and each of the i solid phases can be determined by integrating

$$A^{\mathrm{S}_i\mathrm{L}} = \int_0^a 2\pi r\ \lambda_i(r)\,\mathrm{d}r, \tag{6.18}$$

where $\lambda_i(r)$ is the line fraction of solid i at radius r $[\sum_{i=2}^{n+1} \lambda_i(r) = 1]$ and a is the radius of the solid–liquid contact area ($a = R\sin\theta$). The concept of the line fraction is illustrated in Figure 6.2.

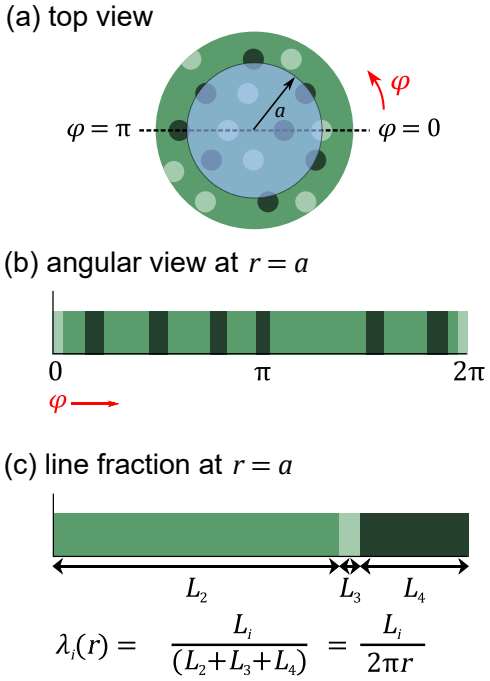

Figure 6.2: Definition of line fraction. (a) Top view of a liquid drop (represented by the transparent blue circle) on a heterogeneous surface. Different shades of green represent different solid phases. (b) Pattern of heterogeneities along the contact line as a function of the angular coordinate. In (c), the pattern shown in (b) is rearranged so that like solids are grouped together. From this rearrangement, the line fraction at a given radius can be defined.

Expressions for differential volume and area are needed for substitution into the equations for differential entropy. The total derivatives of liquid-phase volume (Equation (6.16)) and liquid–vapor interfacial area (Equation (6.17)) are

$$\mathrm{d}V^{\mathrm{L}} = \pi R^2 \left(2 - 3\cos\theta + \cos^3\theta\right) \mathrm{d}R + \pi R^3 \left(\sin\theta - \cos^2\theta \sin\theta\right) \mathrm{d}\theta \tag{6.19}$$

$$\mathrm{d}A^{\mathrm{LV}} = 4\pi R \left(1 - \cos\theta\right) \mathrm{d}R + 2\pi R^2 \sin\theta \, \mathrm{d}\theta. \tag{6.20}$$

The total derivative of each solid–liquid interfacial area (Equation (6.18)) is given by

$$\mathrm{d}A^{\mathrm{S}_i\mathrm{L}} = \left(\frac{\partial A^{\mathrm{S}_i\mathrm{L}}}{\partial R}\right)_{\theta} \mathrm{d}R + \left(\frac{\partial A^{\mathrm{S}_i\mathrm{L}}}{\partial \theta}\right)_{R} \mathrm{d}\theta, \tag{6.21}$$

where the partial derivatives of Equation (6.18) are determined by using the chain rule (or a

simplified form of the Leibniz integral rule—see the next section for details) and are given by

$$\begin{aligned}\left(\frac{\partial A^{\mathrm{S}_i\mathrm{L}}}{\partial R}\right)_{\theta} &= \frac{\partial}{\partial R}\left(\int_0^{R\sin\theta} 2\pi r\lambda_i(r)\,\mathrm{d}r\right)\\ &= \left[\ \lambda_i|_{r=R\sin\theta}\,(2\pi R\sin\theta)\right]\frac{\partial\,(R\sin\theta)}{\partial R}\\ &= \left[\ \lambda_i|_{r=R\sin\theta}\,(2\pi R\sin\theta)\right]\sin\theta\end{aligned} \tag{6.22}$$

$$\begin{aligned}\left(\frac{\partial A^{\mathrm{S}_i\mathrm{L}}}{\partial \theta}\right)_{R} &= \frac{\partial}{\partial \theta}\left(\int_0^{R\sin\theta} 2\pi r\lambda_i(r)\,\mathrm{d}r\right)\\ &= \left[\ \lambda_i|_{r=R\sin\theta}\,(2\pi R\sin\theta)\right]\frac{\partial\,(R\sin\theta)}{\partial \theta}\\ &= \left[\ \lambda_i|_{r=R\sin\theta}\,(2\pi R\sin\theta)\right]R\cos\theta.\end{aligned} \tag{6.23}$$

Substituting Equations (6.22) and (6.23) into Equation (6.21) gives

$$\mathrm{d}A^{\mathrm{S}_i\mathrm{L}} = \left[\ \lambda_i|_{r=R\sin\theta}\left(2\pi R\sin^2\theta\right)\right]\mathrm{d}R + \left[\ \lambda_i|_{r=R\sin\theta}\left(2\pi R^2\sin\theta\cos\theta\right)\right]\mathrm{d}\theta. \tag{6.24}$$

To get the equilibrium conditions for the defined system, Equations (6.3)–(6.9) are substituted into Equation (6.2), and Equations (6.10)–(6.15), (6.19), (6.20), and (6.24) are substituted into

the resulting expression. Like terms are collected, giving the following equation

$$\begin{aligned}
&\left(\frac{1}{T^{\mathrm{L}}}-\frac{1}{T^{\mathrm{V}}}\right)\mathrm{d}U^{\mathrm{L}}+\sum_{i=2}^{n+1}\left(\frac{1}{T^{\mathrm{S}_i}}-\frac{1}{T^{\mathrm{V}}}\right)\mathrm{d}U^{\mathrm{S}_i}+\left(\frac{1}{T^{\mathrm{LV}}}-\frac{1}{T^{\mathrm{V}}}\right)\mathrm{d}U^{\mathrm{LV}}\\
&\quad+\sum_{i=2}^{n+1}\left(\frac{1}{T^{\mathrm{S}_i\mathrm{L}}}-\frac{1}{T^{\mathrm{V}}}\right)\mathrm{d}U^{\mathrm{S}_i\mathrm{L}}+\sum_{i=2}^{n+1}\left(\frac{1}{T^{\mathrm{S}_i\mathrm{V}}}-\frac{1}{T^{\mathrm{V}}}\right)\mathrm{d}U^{\mathrm{S}_i\mathrm{V}}\\
&\quad+\left(\frac{1}{T^{\mathrm{R}}}-\frac{1}{T^{\mathrm{V}}}\right)\mathrm{d}U^{\mathrm{R}}\\
&\quad+\left(\frac{P^{\mathrm{L}}}{T^{\mathrm{L}}}-\frac{P^{\mathrm{V}}}{T^{\mathrm{V}}}\right)\left[\pi R^2\left(2-3\cos\theta+\cos^3\theta\right)\mathrm{d}R\right.\\
&\qquad\left.+\pi R^3\left(\sin\theta-\cos^2\theta\sin\theta\right)\mathrm{d}\theta\right]\\
&\quad+\left(\frac{P^{\mathrm{R}}}{T^{\mathrm{R}}}-\frac{P^{\mathrm{V}}}{T^{\mathrm{V}}}\right)\mathrm{d}V^{\mathrm{R}}+\left(\frac{\mu_1^{\mathrm{V}}}{T^{\mathrm{V}}}-\frac{\mu_1^{\mathrm{L}}}{T^{\mathrm{L}}}\right)\mathrm{d}N_1^{\mathrm{L}}+\left(\frac{\mu_1^{\mathrm{V}}}{T^{\mathrm{V}}}-\frac{\mu_1^{\mathrm{LV}}}{T^{\mathrm{LV}}}\right)\mathrm{d}N_1^{\mathrm{LV}}\\
&\quad+\sum_{i=2}^{n+1}\left(\frac{\mu_1^{\mathrm{V}}}{T^{\mathrm{V}}}-\frac{\mu_1^{\mathrm{S}_i\mathrm{L}}}{T^{\mathrm{S}_i\mathrm{L}}}\right)\mathrm{d}N_1^{\mathrm{S}_i\mathrm{L}}+\sum_{i=2}^{n+1}\left(\frac{\mu_1^{\mathrm{V}}}{T^{\mathrm{V}}}-\frac{\mu_1^{\mathrm{S}_i\mathrm{V}}}{T^{\mathrm{S}_i\mathrm{V}}}\right)\mathrm{d}N_1^{\mathrm{S}_i\mathrm{V}}\\
&\quad-\frac{\sigma^{\mathrm{LV}}}{T^{\mathrm{LV}}}\left[4\pi R\left(1-\cos\theta\right)\mathrm{d}R+2\pi R^2\sin\theta\,\mathrm{d}\theta\right]\\
&\quad+\sum_{i=2}^{n+1}\left(\frac{\sigma^{\mathrm{S}_i\mathrm{V}}}{T^{\mathrm{S}_i\mathrm{V}}}-\frac{\sigma^{\mathrm{S}_i\mathrm{L}}}{T^{\mathrm{S}_i\mathrm{L}}}\right)\left\{\left[\lambda_i|_{r=R\sin\theta}\left(2\pi R\sin^2\theta\right)\right]\mathrm{d}R\right.\\
&\qquad\left.+\left[\lambda_i|_{r=R\sin\theta}\left(2\pi R^2\sin\theta\cos\theta\right)\right]\mathrm{d}\theta\right\}=0.
\end{aligned}\tag{6.25}$$

For dS to equal zero for any arbitrary and independent values of the differentials, the coefficients in front of each differential must be set to zero. Setting the coefficients in front of the differential internal energies, differential moles of component 1, and differential reservoir volume equal to zero yields the following equilibrium conditions

$$T^{\mathrm{L}}=T^{\mathrm{V}}=T^{\mathrm{S}_i}=T^{\mathrm{LV}}=T^{\mathrm{S}_i\mathrm{L}}=T^{\mathrm{S}_i\mathrm{V}}=T^{\mathrm{R}} \tag{6.26}$$

$$\mu_1^{\mathrm{V}}=\mu_1^{\mathrm{L}}=\mu_1^{\mathrm{LV}}=\mu_1^{\mathrm{S}_i\mathrm{L}}=\mu_1^{\mathrm{S}_i\mathrm{V}} \tag{6.27}$$

$$P^{\mathrm{R}}=P^{\mathrm{V}}. \tag{6.28}$$

Two additional equilibrium conditions can be derived from the coefficients in front of dR and dθ in Equation (6.25). Given the equality of temperatures (Equation (6.26)), the coefficients in

front of dR in Equation (6.25) can be collected, set to zero, and simplified to

$$\begin{aligned}\left(P^{\mathrm{L}}-P^{\mathrm{V}}\right)\left[\pi R^2\left(2-3\cos\theta+\cos^3\theta\right)\right]-\sigma^{\mathrm{LV}}\left[4\pi R\left(1-\cos\theta\right)\right]\\ +\sum_{i=2}^{n+1}\left(\sigma^{\mathrm{S}_i\mathrm{V}}-\sigma^{\mathrm{S}_i\mathrm{L}}\right)\left[\ \lambda_i|_{r=R\sin\theta}\left(2\pi R\sin^2\theta\right)\right]=0.\end{aligned} \tag{6.29}$$

The coefficient in front of dθ in Equation (6.25) is set to zero and simplified to

$$\begin{aligned}\left(P^{\mathrm{L}}-P^{\mathrm{V}}\right)\left[\pi R^3\left(\sin\theta-\cos^2\theta\sin\theta\right)\right]-\sigma^{\mathrm{LV}}\left(2\pi R^2\sin\theta\right)\\ +\sum_{i=2}^{n+1}\left(\sigma^{\mathrm{S}_i\mathrm{V}}-\sigma^{\mathrm{S}_i\mathrm{L}}\right)\left[\ \lambda_i|_{r=R\sin\theta}\left(2\pi R^2\sin\theta\cos\theta\right)\right]=0.\end{aligned} \tag{6.30}$$

Rearranging Equation (6.30), substituting it into Equation (6.29), and simplifying yields

$$\sigma^{\mathrm{LV}}\cos\theta=\sum_{i=2}^{n+1}\left(\sigma^{\mathrm{S}_i\mathrm{V}}-\sigma^{\mathrm{S}_i\mathrm{L}}\right)\ \lambda_i|_{r=R\sin\theta}. \tag{6.31}$$

A fourth equilibrium condition can be derived by substituting Equation (6.31) into Equation (6.29) and simplifying to get the Young–Laplace equation

$$P^{\mathrm{L}}-P^{\mathrm{V}}=\frac{2\sigma^{\mathrm{LV}}}{R}. \tag{6.32}$$

For a liquid drop on a solid surface composed of a single component i, the Young equation can be derived from Gibbsian composite system thermodynamics for a liquid drop on a homogeneous substrate [87], and it can be written as

$$\sigma^{\mathrm{S}_i\mathrm{V}}-\sigma^{\mathrm{S}_i\mathrm{L}}=\sigma^{\mathrm{LV}}\cos\theta_i. \tag{6.33}$$

Substituting Equation (6.33) into Equation (6.31) gives the last equilibrium condition that relates the contact angle of a liquid drop on a heterogeneous solid surface to the contact angles of the liquid drop on each homogeneous solid phase

$$\cos\theta=\sum_{i=2}^{n+1}\ \lambda_i|_{r=R\sin\theta}\cos\theta_i. \tag{6.34}$$

Equation (6.34) is the most general form of the CB equation that applies to any surface. Equations (6.26), (6.27), (6.28), (6.32), and (6.34) are a complete set of equilibrium conditions for a liquid drop on a heterogeneous solid surface located in a piston–cylinder device that

interacts with an external reservoir. These equations are valid subject to the assumptions outlined at the outset of our derivation. That is, they are valid when the contact line is undistorted, the shape of the drop is a spherical cap, and there are no external forces present (gravity or pinning).

6.3 Application of the Leibniz Integral Rule

The Leibniz integral rule states [137]

$$\frac{\partial}{\partial t}\int_{a(t)}^{b(t)} f(x,t)\,\mathrm{d}x = \int_{a(t)}^{b(t)} \frac{\partial f(x,t)}{\partial t}\,\mathrm{d}x + f(b(t),t)\frac{\partial b}{\partial t} - f(a(t),t)\frac{\partial a}{\partial t}. \tag{6.35}$$

To find the partial derivative of Equation (6.18) with respect to R, we define

$$\begin{aligned} t &= R \\ a(t) &= 0 \\ b(t) &= b(R) = R\sin\theta \\ x &= r \\ f(x,t) &= f(x) = f(r) = 2\pi r\lambda_i(r). \end{aligned}$$

Substituting these relationships into Equation (6.35) yields:

$$\begin{aligned} &\left(\frac{\partial}{\partial R}\int_0^{R\sin\theta} 2\pi r\lambda_i(r)\,\mathrm{d}r\right)_\theta \\ &\quad= \int_0^{R\sin\theta} \frac{\partial(2\pi r\lambda_i(r))}{\partial R}\,\mathrm{d}r + 2\pi R\sin\theta\ \lambda_i|_{r=R\sin\theta}\frac{\partial(R\sin\theta)}{\partial R} \\ &\qquad - 2\pi(0)\ \lambda_i|_{r=0}\frac{\partial(0)}{\partial R} \\ &\quad= 0 + 2\pi R\sin\theta\ \ \lambda_i|_{r=R\sin\theta}(\sin\theta) - 0. \end{aligned} \tag{6.36}$$

To find the partial derivative with respect to θ, we define

$$\begin{aligned} t &= \theta \\ a(t) &= 0 \\ b(t) &= b(\theta) = R\sin\theta, \end{aligned}$$

and substituting these relationships into Equation (6.35) yields:

$$\begin{aligned}\left(\frac{\partial}{\partial\theta}\int_0^{R\sin\theta} 2\pi r\lambda_i(r)\,\mathrm{d}r\right)_R &= \int_0^{R\sin\theta}\frac{\partial(2\pi r\lambda_i(r)}{\partial\theta}\,\mathrm{d}r + 2\pi R\sin\theta\ \ \lambda_i|_{r=R\sin\theta}\frac{\partial(R\sin\theta)}{\partial\theta} \\ &\quad - 2\pi(0)\ \ \lambda_i|_{r=0}\frac{\partial(0)}{\partial\theta} \\ &= 0 + 2\pi R\sin\theta\ \ \lambda_i|_{r=R\sin\theta}(R\cos\theta) - 0.\end{aligned} \tag{6.37}$$

We note that the Leibniz rule simplifies to an application of the chain rule (as used in the previous section for Equations (6.22) and (6.23)) because the integrand is neither a function of R nor θ.

6.4 Discussion

It is important to emphasize that Equation (6.34) contains a line fraction of each solid component at the perimeter of the circular solid–liquid interfacial area instead of the area fraction in Equation (6.1). This conclusion follows from Equation (6.18), which is one of the most important steps in the derivation. In past derivations, the area fraction of solid i is assumed to be a constant parameter independent of drop radius, which would mean that

$$A^{\mathrm{S}_i\mathrm{L}} = \pi a^2 f_i, \tag{6.38}$$

where f_i is the area fraction of solid phase i. When free energy minimization has been carried out using this assumption, f_i is treated as a constant parameter [28, 33, 248, 304], and this yields the area-fraction Cassie–Baxter equation. In reality, however, the area fraction of solid in contact with the liquid may change when the size of the drop changes, and this fact was also noted by Hey and Kingston [120]. Based on Equation (6.18), Equation (6.34) then arises directly from Equation (6.22) and (6.23)), which is the point in the derivation at which the total derivative of each 2D solid–liquid interfacial area is mathematically transformed to contain a 1D line fraction evaluated at the contact line. This transformation physically means that only interactions at the contact line determine the macroscopic contact angle and interactions over the complete solid–liquid interfacial area are irrelevant. This physical insight is not immediately obvious when the area fraction is assumed to be a constant parameter (Equation (6.38)) and the area-fraction version of the Cassie–Baxter equation (Equation (6.1)) is derived.

In comparison to Equation (6.34), it can be seen that the original CB equation (Equa-

tion (6.1)) is a special case for surfaces where the area fractions and line fractions are equal. The equality of area and line fractions is satisfied when the line fraction is independent of r (*i.e.*, $\lambda_i(r) = \text{const} = f_i$) or equivalently, when the area fraction is independent of r ($f_i(r) = \text{const} = f_i$). Equation (6.1) is valid when $\lambda_i|_{r=R\sin\theta} = f_i$, but this criterion is not necessarily true for all surfaces and all drop sizes. Using the line fraction will yield the most accurate prediction of contact angle, but depending on the spatial distribution of heterogeneities, the local or global area fraction may also be used. As the area considered "local" to the contact line approaches a thickness of zero, the local area fraction model proposed by McHale [185] and Nosonovsky [206] limits to the line fraction model. As the area considered "local" to the contact line increases in thickness, the local area fraction model limits to the global area fraction model. In other words, the contact angle of a liquid on all surfaces can be described by using the line fraction, on a subset of these surfaces by using the local area fraction, and a smaller subset of these surfaces by using the global area fraction.

Figure 6.3 illustrates some common spatial distributions of solid-phase heterogeneities and the applicability of each version of the CB model. The light and dark green areas are two different solid phases; on each of the solid surfaces, a blue liquid drop is placed, and the resulting solid–liquid contact areas are depicted by semi-transparent blue circles. The placement of the drop is important in determining which CB model is valid. For surfaces (i) and (iii), the placement of the drop ensures that the area fraction of the surface and the line fraction at the contact line are equal and independent of liquid drop radius; therefore, all three versions of the CB equation may be used. The validity of the CB equation for surfaces (i) and (iii) is only limited by the scale of the heterogeneities, which must be small enough relative to the size of the liquid drop (see Carmeliet *et al*. [48] for a detailed analysis of surface (iii)). Surface (ii) has the same pattern of heterogeneities as surface (i), and surface (iv) has the same pattern as surface (iii), but the location of the liquid droplet on these patterns differs. With the change in droplet placement, the global area and local area fractions become dependent on drop radius. For surface (v), which has a single heterogeneity in the center, the global area fraction may not be used, but the local area fraction is still valid because it ignores the central heterogeneity. Surface (vi) also has a heterogeneity in the center, but in the surrounding surface, the fraction of each component in the solid–liquid interface changes as a function of drop radius, and the local area fraction model can no longer be used. Surface (vii) is an example of a surface that is "everywhere similar and isotropic" [185], but the local area fraction model cannot be used for the same reason as surface (vi). Only the line-fraction CB equation, Equation (6.34), is valid for describing the equilibrium contact angle of a drop on all surfaces where pinning/depinning forces are negligible and the contact line is circular.

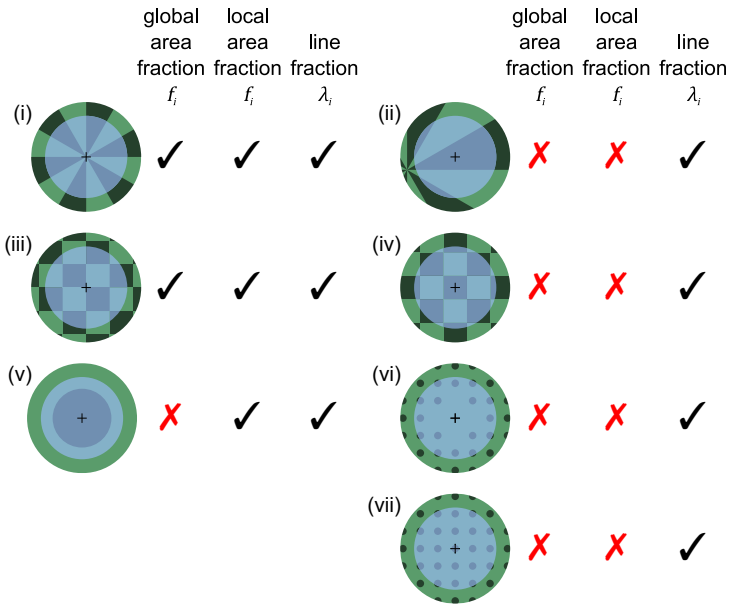

Figure 6.3: Qualitative comparison of spatial distributions of heterogeneities on solid surfaces (top view) and validity of each version of the Cassie–Baxter equation. The light green and dark green areas are two different solid phases, and the semi-transparent blue circles are liquid drops (the locations of the drops with respect to the patterns beneath are very important). The sizes of heterogeneities have been enlarged in the diagram for the purposes of explanation. The equations in this chapter are only valid when the sizes of heterogeneities are much smaller than the drops. Distortions of the contact line shape, although expected for the heterogeneity size in the illustrations, are neither depicted in this diagram nor included in the analysis. The global area fraction label refers to Equation (6.1) where the total liquid–solid area is considered; the local area fraction label refers to the case where only the liquid–solid area in the vicinity of the contact line is considered (Refs. [185] and [206]); and the line fraction label refers to the use of Equation (6.34).

6.5 Summary and Conclusions

Using fundamental Gibbsian composite-system thermodynamics, the equilibrium conditions for a liquid drop on a smooth, multiphase solid surface were derived, two of which were thermal equilibrium and chemical equilibrium. The well-known Young–Laplace equation was found to be a condition for mechanical equilibrium. Finally, a line-fraction CB equation was derived, in agreement with other rigorous theoretical approaches (statistical mechanics [275], homogenization [314], and energy minimization [120]). These equilibrium conditions are also valid for a rough surface where the liquid drop traps gas pockets in between the surface protrusions (CB mode of wetting). For such a rough surface, there would be two line fractions: the fraction of the liquid contact line that is in contact with the solid surface and the fraction that is in contact with the gas phase, where the contact angle of a liquid–air system would be 180°.

The area-fraction CB equation is only valid for surfaces where the area fraction and line fraction are equal (*e.g.*, for a liquid droplet centered on a dartboard pattern (Figure 6.3(i)), whereas the line-fraction CB equation may be used to describe the expected contact angle regardless of the spatial distribution of heterogeneities. Further modifications could be made to the derivation outlined herein to account for: (*i*) any distortions of the contact line that modifies its shape from that of a perfect circle [165, 172, 311] (mathematical expressions for a non-spherical liquid volume and non-circular interfacial areas would be needed) or (*ii*) pinning forces that are encountered experimentally as the contact line advances or recedes across a heterogeneous surface [145–147, 172] (*e.g.*, as proposed in detail by Koch *et al.* [145] an additional term, F/σ^{LV}, may be added to the right-hand side of Equation (6.34), where F is an empirical "pinning" force per unit length of contact line). The success of Gibbsian composite-system thermodynamics in describing wetting on heterogeneous surfaces was illustrated, and applying such a framework to systems under more complicated constraints may uncover new insights into their wetting behavior.

Chapter 7

Gibbsian Thermodynamics of Wenzel Wetting (Was Wenzel Wrong? Revisited)[1]

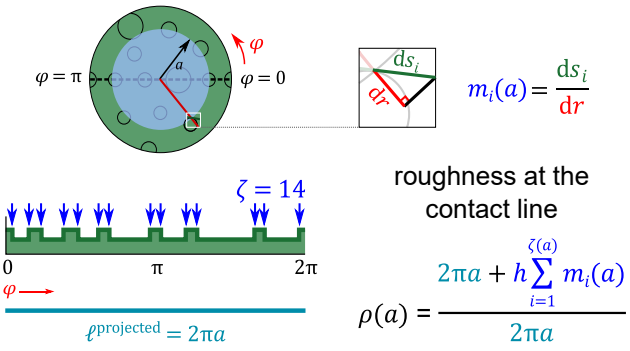

Abstract

When a drop is in contact with a rough surface, it can rest on top of the rough features (the Cassie–Baxter state) or it can completely fill the rough structure (the Wenzel state). The contact angle (θ) of a drop in these states is commonly predicted by the Cassie–Baxter or Wenzel equations, respectively, but the accuracy of these equations has been debated. Previously, we used fundamental Gibbsian composite-system thermodynamics to rigorously derive the Cassie–Baxter equation, and we found that the contact line determined the macroscopic contact angle, not the contact area that was originally proposed. Herein, to address the various perspectives on the Wenzel equation, we apply Gibbsian composite-system thermodynamics to derive the complete set of equilibrium conditions (thermal, chemical, and mechanical) for a liquid drop resting on a homogeneous rough solid substrate in the Wenzel mode of wetting. Through this derivation, we show that the roughness must be evaluated at the contact line, not over the whole interfacial area, and we propose a new Wenzel equation for a surface with pillars of equal height. We define a new dimensionless number $\mathrm{H} = h\left(1-\lambda_{\mathrm{solid}}\right)/R$ to quantify when the

[1]This chapter has been submitted for publication as N. Shardt and J. A. W. Elliott. "Gibbsian Thermodynamics of Wenzel Wetting (Was Wenzel Wrong? Revisited)". In performing this research, I had a valuable discussion with Dr. Orest Shardt on the expression for solid–liquid interfacial area.

drop's radius of curvature (R) is large enough compared to the size of the pillars for the new Wenzel equation to be simplified (h is pillar height; λ_{solid} is the line fraction of the spherical cap's circumference that is on the pillars). Our new line-roughness Wenzel equation can be simplified to $\cos\theta_{\text{W}} = \rho\cos\theta_{\text{Y}}$ when $\text{H} \ll 1$, where ρ is the line roughness. We also perform a thermodynamic free energy analysis to determine the stability of the equilibrium states that are predicted by our new Wenzel equation.

7.1 Introduction

The shape that a liquid drop forms on a substrate depends on the properties of the liquid and solid phases, as well as the geometry of the solid surface. If the solid surface is smooth, the angle that the liquid–vapor interface of the drop forms with respect to the solid surface—the contact angle—is described by the Young equation. If the solid surface is rough, the contact angle may be predicted by the Cassie–Baxter equation [49] when air is trapped under the liquid or by the Wenzel equation [303] when there is no air entrapment. Depending on the application, surfaces can be designed so that a liquid preferentially wets in the Cassie–Baxter state or in the Wenzel state. In dental implants, for example, rough surfaces are used to promote hydrophilicity [231, 238], while food packaging should be hydrophobic so that food does not stick to it [296]. In other applications, the surface needs to be designed so that the Wenzel state is avoided, such as for flow in rough microfluidic channels [95] and for the design of materials with anti-icing or anti-corrosion properties (*e.g.*, concrete [267]).

The Cassie–Baxter equation has been used to predict the contact angle of a liquid drop on (*i*) rough, chemically homogeneous surfaces when air is present in the grooves of the rough pattern and on (*ii*) smooth, chemically heterogeneous surfaces. The original Cassie–Baxter equation [49] considers the area fraction of each heterogeneous portion in contact with the bottom of a liquid drop, but the validity of the area-fraction Cassie–Baxter equation for all patterns of surface heterogeneities has been questioned by experimentalists [90, 103]. A line-fraction Cassie–Baxter equation has been derived rigorously *via* free energy minimization coupled with (*i*) statistical mechanics (Swain and Lipowsky [275]), (*ii*) differential calculus (Hey and Kingston [120]), and (*iii*) homogenization (Xu and Wang [314]). Previously, we used a Gibbsian entropy extremization approach to derive the line-fraction Cassie–Baxter equation, and we showed that the most general form of the equilibrium Cassie–Baxter equation uses line fractions at the contact line in place of area fractions [252]. Area fractions can be used in the Cassie–Baxter equation for certain surfaces where the line fraction at the contact line is independent of drop radius. That is, the area fraction Cassie–Baxter equation is valid when the line fraction is equal to the area fraction [252].

The Wenzel equation has been used to predict the contact angle of a liquid on rough surfaces when there is no air entrapment, and it is given by [303]

$$\cos\theta_{\mathrm{W}} = r_{\mathrm{f}}\cos\theta_{\mathrm{Y}}, \tag{7.1}$$

where θ_{W} is the predicted Wenzel contact angle, r_{f} is the roughness factor of the solid surface (ratio between the solid (S)–liquid (L) interfacial area and the projected area: $A^{\mathrm{SL}}/A^{\mathrm{projected}}$) and θ_{Y} is the contact angle of the liquid drop on a smooth surface made up of the same material (the Young contact angle). As noted by Cassie and Baxter [49], the Wenzel equation is a limiting case of the Cassie–Baxter equation for a single-component solid substrate where the Cassie fraction is equal to the roughness factor. Although the validity of the Wenzel equation has been under question in the same way as the Cassie–Baxter equation (*e.g.*, see Gao and McCarthy [103] and the extensive review by Erbil [82] on this topic), there are fewer rigorous theoretical analyses of Wenzel wetting. Ever since the early studies of wetting on rough surfaces, researchers have noted the importance of drop volume for determining how close the measured contact angle is to the one predicted by the Wenzel equation (Equation (7.1)) [22, 128, 182]. Marmur and Bittoun [181] suggested that insufficiently large drop volumes were studied by Gao and McCarthy [103], and this was the reason why their results disagreed with Equation (7.1).

The Wenzel equation (Equation (7.1)) has commonly been derived using an energy minimization approach [111, 133, 304], but in these derivations, it is assumed that every differential change in projected area yields a proportional change in the actual solid–liquid interfacial area ($\mathrm{d}A^{\mathrm{SL}} = r_{\mathrm{f}}\,\mathrm{d}A^{\mathrm{projected}}$). Such an assumption may not always be satisfied by a real surface, such as one with a central defect [103]. One approach that addresses experimentalists' concerns about the area roughness proposes the use of a local area roughness factor evaluated in the vicinity of the contact line [32, 185, 206, 248], but such an approach still assumes that $\mathrm{d}A^{\mathrm{SL}} = r_{\mathrm{f}}\,\mathrm{d}A^{\mathrm{projected}}$, and this assumption may not necessarily be valid even in the region close to the contact line. The last variant of the Wenzel equation is one that uses a roughness determined at the three-phase contact line. Using mathematical homogenization, Xu and Wang [312, 313] showed that the Wenzel equation is valid solely for certain patterns of roughness that satisfy a specific mathematical constraint. Xu analyzed a surface with a roughness that is orthogonal to the contact line, and instead of an area ratio, suggested that the roughness factor should be a ratio of line lengths: the length of the rough contact line divided by the length of the projected smooth contact line [312]. There are thus three versions of the Wenzel equation (Equation (7.1)): (*i*) where $r_{\mathrm{f}} = A^{\mathrm{SL}}/A^{\mathrm{projected}}$ is evaluated over the whole base of the drop; (*ii*) where $r_{\mathrm{f}} = A^{\mathrm{SL}}/A^{\mathrm{projected}}$ is evaluated in a region close to the contact line, and (*iii*) where $r_{\mathrm{f}} = \ell^{\mathrm{SLV}}/\ell^{\mathrm{projected}}$ is evaluated at the contact line.

To clarify the various perspectives that persist in the literature on the Wenzel equation, we propose the use of Gibbsian composite-system thermodynamics [46, 108]. This framework of thermodynamics has previously been used to examine the behavior of fluids in contact with smooth, homogeneous surfaces, such as: bubble formation [298]; contact angle in the presence of gravity [299]; capillary bridges [79, 323]; fluid behavior on rigid and nonrigid substrates [87]; the behavior of confined liquids [323, 324]; and interfacial nanobubbles [325]. In addition, Gibbsian thermodynamics has been used to calculate the phase diagrams of vapor–liquid [253, 254], and solid–liquid [171] systems with interfacial curvature. In Chapter 6, we applied Gibbsian thermodynamics to Cassie–Baxter wetting, arriving at the line-fraction Cassie–Baxter equation [252].

Herein, we apply the Gibbsian framework to derive all the equilibrium conditions for a liquid drop in equilibrium with its vapor resting in the Wenzel state on a solid, rough, chemically homogeneous solid with pillars. Through our Gibbsian derivation, we find that the roughness ratio must be evaluated at the contact line, and we define an expression for this ratio. This roughness ratio is influenced by two factors: (*i*) how many pillars heights are at the three-phase contact line and (*ii*) the orientation of the solid–liquid interface at the pillar heights with respect to the contact line. We also define a new dimensionless number to quantify how small the surface roughness must be (or how large the liquid drop must be) for a simplified form of the line-roughness Wenzel equation to be valid. For many surfaces, the line-roughness will be a function of drop radius, and the area-roughness ratio should not be used to predict the equilibrium contact angle when Wenzel wetting is observed.

We note that the following analysis only considers the equilibrium state of a liquid drop on a surface, and we do not consider the hysteresis between advancing and receding contact angles. Researchers have proposed that this hysteresis can be due to the geometry of the surface [264], due to pinning forces that distort the local contact angle [91, 102, 132], or a combination of both and perhaps other sources [145, 146, 325].

7.2 Derivation of the Equilibrium Conditions for Wenzel Wetting

The first step for deriving equilibrium conditions is to explicitly define the system—the geometry, phases present, components in each phase, and how the system interacts with the surrounding reservoir. Figure 7.1 illustrates an example of the system of interest: a liquid drop resting on a surface in the Wenzel mode of wetting. Component 1 is present in the bulk liquid and vapor phases as well as in the liquid–vapor interface (according to the Gibbs surface of

tension approach for a curved interface [108]), solid–vapor interface, and solid–liquid interface. Component 2 is only present in the solid phase, and it is not present at the solid–vapor or solid–liquid interfaces according to the Gibbs dividing surface approach [108, 129]. The solid–liquid–vapor system is contained in a piston–cylinder device that imposes the temperature and pressure of a surrounding reservoir on the system, and there is no mass transfer into or out of the piston–cylinder device.

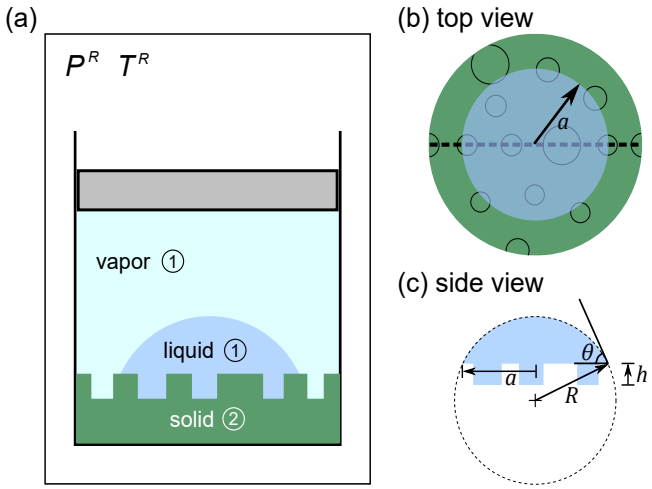

Figure 7.1: Schematic of a liquid drop in equilibrium with its vapor on a rough solid phase in the Wenzel state of wetting. (a) The three-phase system is contained in a piston–cylinder device surrounded by a reservoir with a defined pressure (P^{R}) and temperature (T^{R}). (b) A top view of the liquid drop, where the black circles outline the tops of each pillar and a is the radius of the spherical cap's base. (c) A side view of the liquid phase defining the geometry of the drop and the rough texture, where θ is the contact angle, h is the height of the pillars, and R is the radius of curvature of the spherical cap. The extent of the roughness is exaggerated in the illustration.

The second step for deriving equilibrium conditions is to extremize entropy subject to physical constraints. At equilibrium, the entropy (S) of the system is at a maximum, and this condition is expressed mathematically as:

$$\mathrm{d}S^{\mathrm{L}} + \mathrm{d}S^{\mathrm{V}} + \mathrm{d}S^{\mathrm{S}} + \mathrm{d}S^{\mathrm{LV}} + \mathrm{d}S^{\mathrm{SL}} + \mathrm{d}S^{\mathrm{SV}} + \mathrm{d}S^{\mathrm{R}} = 0, \tag{7.2}$$

where the superscripts L, V, and S denote the bulk liquid, vapor, and solid phases, respectively, the superscripts LV, SL, and SV denote the liquid–vapor, solid–liquid, and solid–vapor interfaces, respectively, and R denotes the reservoir.

For bulk phases, differential changes in entropy are related to differential changes in internal energy (U), volume (V), and number of moles (N). For the liquid and vapor phases that contain

only component 1, the following equations apply, respectively:

$$\mathrm{d}S^{\mathrm{L}} = \frac{1}{T^{\mathrm{L}}}\,\mathrm{d}U^{\mathrm{L}} + \frac{P^{\mathrm{L}}}{T^{\mathrm{L}}}\,\mathrm{d}V^{\mathrm{L}} - \frac{\mu_1^{\mathrm{L}}}{T^{\mathrm{L}}}\,\mathrm{d}N_1^{\mathrm{L}} \tag{7.3}$$

$$\mathrm{d}S^{\mathrm{V}} = \frac{1}{T^{\mathrm{V}}}\,\mathrm{d}U^{\mathrm{V}} + \frac{P^{\mathrm{V}}}{T^{\mathrm{V}}}\,\mathrm{d}V^{\mathrm{V}} - \frac{\mu_1^{\mathrm{V}}}{T^{\mathrm{V}}}\,\mathrm{d}N_1^{\mathrm{V}}, \tag{7.4}$$

where T is absolute temperature, P is pressure, and μ_1 is the chemical potential of component 1. For the solid phase containing component 2, the following is true:

$$\mathrm{d}S^{\mathrm{S}} = \frac{1}{T^{\mathrm{S}}}\,\mathrm{d}U^{\mathrm{S}} + \frac{P^{\mathrm{S}}}{T^{\mathrm{S}}}\,\mathrm{d}V^{\mathrm{S}} - \frac{\mu_2^{\mathrm{S}}}{T^{\mathrm{S}}}\,\mathrm{d}N_2^{\mathrm{S}}. \tag{7.5}$$

Differential changes in the reservoir's entropy are described by

$$\mathrm{d}S^{\mathrm{R}} = \frac{1}{T^{\mathrm{R}}}\,\mathrm{d}U^{\mathrm{R}} + \frac{P^{\mathrm{R}}}{T^{\mathrm{R}}}\,\mathrm{d}V^{\mathrm{R}} - \sum_j \frac{\mu_j^{\mathrm{R}}}{T^{\mathrm{R}}}\,\mathrm{d}N_j^{\mathrm{R}}, \tag{7.6}$$

where the summation index j covers all components present in the reservoir.

For the interfaces present in the system, differential changes in entropy are related to internal energy and mole number as they are for bulk phases, but the term containing differential volume is replaced by one with differential area (A). For each of the liquid–vapor, solid–liquid, and solid–vapor interfaces, differential changes in entropy are governed by the following equations, respectively:

$$\mathrm{d}S^{\mathrm{LV}} = \frac{1}{T^{\mathrm{LV}}}\,\mathrm{d}U^{\mathrm{LV}} - \frac{\sigma^{\mathrm{LV}}}{T^{\mathrm{LV}}}\,\mathrm{d}A^{\mathrm{LV}} - \frac{\mu_1^{\mathrm{LV}}}{T^{\mathrm{LV}}}\,\mathrm{d}N_1^{\mathrm{LV}} \tag{7.7}$$

$$\mathrm{d}S^{\mathrm{SL}} = \frac{1}{T^{\mathrm{SL}}}\,\mathrm{d}U^{\mathrm{SL}} - \frac{\sigma^{\mathrm{SL}}}{T^{\mathrm{SL}}}\,\mathrm{d}A^{\mathrm{SL}} - \frac{\mu_1^{\mathrm{SL}}}{T^{\mathrm{SL}}}\,\mathrm{d}N_1^{\mathrm{SL}} \tag{7.8}$$

$$\mathrm{d}S^{\mathrm{SV}} = \frac{1}{T^{\mathrm{SV}}}\,\mathrm{d}U^{\mathrm{SV}} - \frac{\sigma^{\mathrm{SV}}}{T^{\mathrm{SV}}}\,\mathrm{d}A^{\mathrm{SV}} - \frac{\mu_1^{\mathrm{SV}}}{T^{\mathrm{SV}}}\,\mathrm{d}N_1^{\mathrm{SV}}, \tag{7.9}$$

where σ is interfacial tension.

7.2.1 System Constraints

Not all differential quantities in Equations (7.3)–(7.9) vary independently of each other, while other variables never vary. The constraints on the system are defined as follows. The numbers of moles of each component in the reservoir do not change:

$$\mathrm{d}N_j^{\mathrm{R}} = 0. \tag{7.10}$$

The conservation of mass states that the total number of moles of component 1 must be constant, giving the following relationship between the moles present in the vapor phase, liquid phase, liquid–vapor interface, solid–liquid interface, and solid–vapor interface:

$$\mathrm{d}N_1^{\mathrm{V}} = -\mathrm{d}N_1^{\mathrm{L}} - \mathrm{d}N_1^{\mathrm{LV}} - \mathrm{d}N_1^{\mathrm{SL}} - \mathrm{d}N_1^{\mathrm{SV}}. \tag{7.11}$$

Component 2 in the solid phase is non-volatile:

$$\mathrm{d}N_2^{\mathrm{S}} = 0. \tag{7.12}$$

The conservation of energy is applied to the system and reservoir together:

$$\mathrm{d}U^{\mathrm{V}} = -\mathrm{d}U^{\mathrm{L}} - \mathrm{d}U^{\mathrm{S}} - \mathrm{d}U^{\mathrm{LV}} - \mathrm{d}U^{\mathrm{SL}} - \mathrm{d}U^{\mathrm{SV}} - \mathrm{d}U^{\mathrm{R}}. \tag{7.13}$$

The solid phase is considered to be incompressible ($\mathrm{d}V^{\mathrm{S}} = 0$), so that the volumetric constraint on the system is:

$$\mathrm{d}V^{\mathrm{V}} = -\mathrm{d}V^{\mathrm{L}} - \mathrm{d}V^{\mathrm{R}}. \tag{7.14}$$

Any increase/decrease in the solid–vapor interfacial area yields a corresponding decrease/increase in the solid–liquid interfacial area:

$$\mathrm{d}A^{\mathrm{SV}} = -\mathrm{d}A^{\mathrm{SL}}. \tag{7.15}$$

To determine further expressions for the differential quantities of volume and area, we first derive equations for liquid volume and all interfacial areas. The volume of the liquid phase is split into two parts: the volume of the spherical cap and the volume of a partially-filled cylinder within the surface asperities, as illustrated in Figure 7.2. The total volume can be calculated by:

$$V^{\mathrm{L}} = \frac{\pi R^3}{3}\left(2 - 3\cos\theta + \cos^3\theta\right) + h\int_0^a 2\pi r \lambda_{\mathrm{liquid}}(r)\,\mathrm{d}r, \tag{7.16}$$

where a is the radius of the spherical cap's base ($a = R\sin\theta$ where R is the radius of curvature of the spherical cap) and $\lambda_{\mathrm{liquid}}$ pertains to the liquid cylinder within the surface asperities, defined as the fraction of the spherical cap's circumference at radius r that is liquid ($\lambda_{\mathrm{liquid}} + \lambda_{\mathrm{solid}} = 1$; see Figure 7.3(c)). The first term of Equation (7.16) is the volume of the spherical cap [26, 87, 220], and the second term is the volume of the partially-filled cylinder.

The surface area of the liquid–vapor interface is equal to the top of the spherical cap along

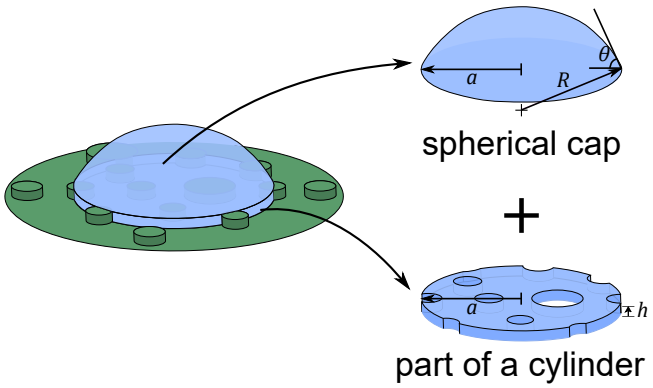

Figure 7.2: Illustration of a liquid drop in the Wenzel state and how its volume is divided into two parts: a spherical cap and a cylinder of liquid with holes missing (the holes are filled by the solid pillars).

with a contribution from the side of the partially-filled cylinder:

$$A^{\mathrm{LV}} = 2\pi R^2 (1 - \cos\theta) + h \left(2\pi a \, \lambda_{\mathrm{liquid}}\big|_{r=a} \right). \tag{7.17}$$

The following expression can be used to calculate the solid–liquid interfacial area

$$A^{\mathrm{SL}} = \pi a^2 + h \int_0^a \left[\sum_{i=1}^{\zeta(r)} \frac{\mathrm{d}s_i}{\mathrm{d}r} \right] \mathrm{d}r, \tag{7.18}$$

where the first term is the projected area of the liquid drop's bottom surface. The second term contains an integral over all radii that determines the total perimeter of all pillars, and when this perimeter is multiplied by the height of each pillar, the additional solid–liquid area from contact with the sides of the cylindrical pillars is obtained. In the second term, $\zeta(r)$ is the integral number of pillar sides with height h that are located along the contact line at a radius of r. Each pillar side has a unique orientation with respect to the drop radius that is captured by the value of $\mathrm{d}s_i/\mathrm{d}r$, where $\mathrm{d}s_i$ is the differential arc length on the side of the pillar at the ith intersection (described in more geometric detail later in this section). Defining $m_i(r) = \mathrm{d}s_i/\mathrm{d}r$ and $m(r) = \sum_{i=1}^{\zeta(r)} m_i(r)$ yields

$$A^{\mathrm{SL}} = \pi a^2 + h \int_0^a m(r) \, \mathrm{d}r. \tag{7.19}$$

To illustrate the physical meanings of $\lambda_{\mathrm{liquid}}$ and ζ, we show a sample surface with pillars of equal height in Figure 7.3. For a liquid drop on such a surface in the Wenzel state with $r = a$, there are 14 intersections with pillar edges at a radius of a; that is, $\zeta(a) = 14$ (Figure 7.3(b)). In Figure 7.3(c), we show the line fraction of liquid at the base of the spherical cap along the

radius $r = a$. Each of the 14 intersections in Figure 7.3 has a corresponding orientation factor m_i, an expression for which can be derived geometrically.

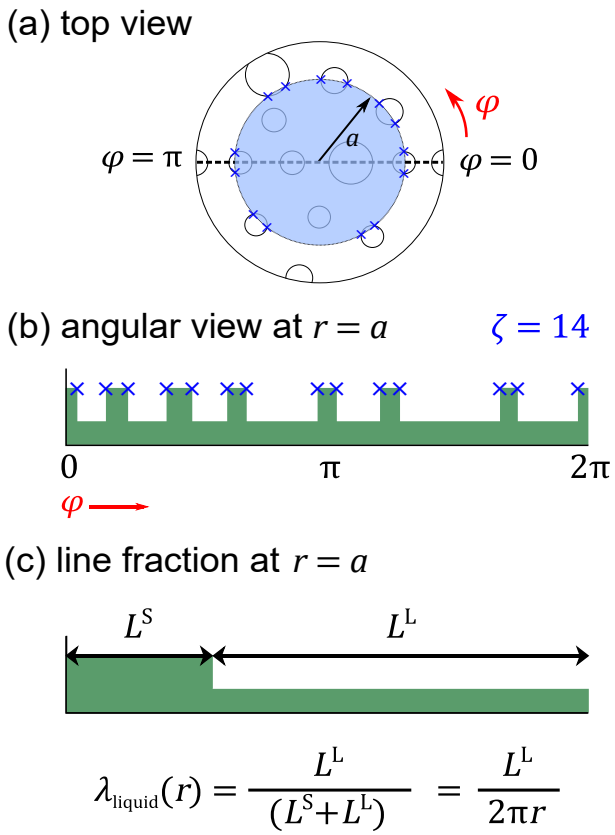

Figure 7.3: An example of a surface with pillars and how to determine the values of ζ and λ_{liquid}. (a) A top view of a liquid drop on the surface; (b) a profile of the rough surface features along the contact line (at $r = a = R\sin\theta$) as a function of the angular coordinate; and (c) a rearrangement of the pillars in (b) for the calculation of the defined line fraction of liquid at the spherical cap's circumference, where L^{L} is the length of the contact line that is liquid at the spherical cap's base and L^{S} is the length of the contact line that is touching the tops of the pillars.

As illustrated in Figure 7.4(a), for a given intersection between the edge of a liquid drop and the edge of a pillar, two characteristic angles for that intersection can be defined. Using the polar coordinate system, the intersection point is on the edge of the liquid drop at an angle of φ_i relative to the x-axis. When a tangent line to the solid is drawn at the intersection point, it makes an angle of ψ_i relative to the x-axis. In Figure 7.4(b), a differential increase in r is shown, yielding a corresponding increase in solid–liquid arc length of $\mathrm{d}s_i$. A relationship between these differential quantities can be derived based on the angle between them, which is equal to $\psi_i - \varphi_i$ (Figure 7.4(c)). As shown in Figure 7.4(d), the orientation factor is given by the following

expression

$$m_i(r) = \frac{\mathrm{d}s_i}{\mathrm{d}r} = \frac{1}{\cos(\psi_i - \varphi_i)}. \tag{7.20}$$

By examining Equation (7.20), we see that $\mathrm{d}s_i/\mathrm{d}r = 1$ when $\psi_i = \varphi_i$, which is when the tangent line at pillar side i goes through the origin and is coincident with the ray going from the origin to the intersection point.

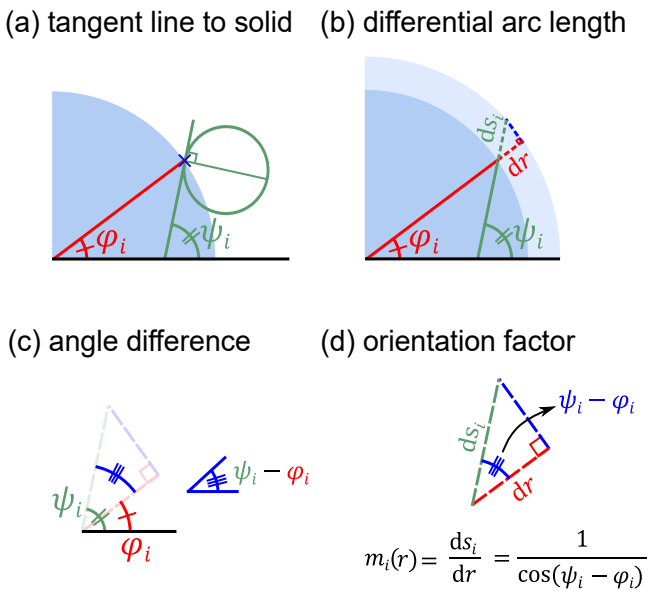

Figure 7.4: Derivation of the orientation factor m_i for each intersection with the side of a pillar. (a) An example of an intersection between the edge of a liquid drop (shaded in blue with center at the origin) and the edge of a pillar (circle outlined in green). A ray from the origin to the intersection point makes an angle of φ_i with respect to the x-axis, and the line tangent to the solid pillar makes an angle of ψ_i. (b) The result of a differential increase in radius ($\mathrm{d}r$), yielding a corresponding $\mathrm{d}s_i$, where s is the perimeter of the pillar. (c) How to obtain the angle between $\mathrm{d}s_i$ and $\mathrm{d}r$. (d) Definition of the orientation factor m_i.

Having found equations for the volume and interfacial areas, we now find the total derivatives of these equations. The total derivative of any function f dependent on R and θ is given by

$$\mathrm{d}f = \left(\frac{\partial f}{\partial R}\right)_\theta \mathrm{d}R + \left(\frac{\partial f}{\partial \theta}\right)_R \mathrm{d}\theta. \tag{7.21}$$

The partial derivatives of Equation (7.16) for the liquid volume are, using the Leibniz integral

rule [137, 252]:

$$\begin{aligned}
&\frac{\partial}{\partial R}\left[\frac{\pi R^3}{3}\left(2-3\cos\theta+\cos^3\theta\right)+h\int_0^{R\sin\theta}2\pi r\lambda_{\text{liquid}}(r)\,\mathrm{d}r\right] \\
&\quad=\pi R^2(2-3\cos\theta+\cos^3\theta)+2\pi h(R\sin\theta)\left(\lambda_{\text{liquid}}\big|_{r=R\sin\theta}\right)\frac{\partial(R\sin\theta)}{\partial R} \\
&\quad=\pi R^2(2-3\cos\theta+\cos^3\theta)+2\pi h(R\sin^2\theta)\left(\lambda_{\text{liquid}}\big|_{r=R\sin\theta}\right)
\end{aligned} \tag{7.22}$$

$$\begin{aligned}
&\frac{\partial}{\partial\theta}\left[\frac{\pi R^3}{3}\left(2-3\cos\theta+\cos^3\theta\right)+h\int_0^{R\sin\theta}2\pi r\lambda_{\text{liquid}}(r)\,\mathrm{d}r\right] \\
&\quad=\pi R^3\left(\sin\theta-\cos^2\theta\sin\theta\right)+2\pi h\left(R\sin\theta\right)\left(\lambda_{\text{liquid}}\big|_{r=R\sin\theta}\right)\frac{\partial(R\sin\theta)}{\partial\theta} \\
&\quad=\pi R^3\left(\sin\theta-\cos^2\theta\sin\theta\right)+2\pi h\left(R^2\sin\theta\cos\theta\right)\left(\lambda_{\text{liquid}}\big|_{r=R\sin\theta}\right).
\end{aligned} \tag{7.23}$$

Substituting Equations (7.22) and (7.23) into Equation (7.21), the total derivative of liquid volume (Equation (7.16)) is

$$\begin{aligned}
\mathrm{d}V^{\mathrm{L}} &= \left[\pi R^2(2-3\cos\theta+\cos^3\theta)+2\pi h(R\sin^2\theta)\left(\lambda_{\text{liquid}}\big|_{r=R\sin\theta}\right)\right]\mathrm{d}R \\
&\quad+\left[\pi R^3(\sin\theta-\cos^2\theta\sin\theta)+2\pi h\left(R^2\sin\theta\cos\theta\right)\left(\lambda_{\text{liquid}}\big|_{r=R\sin\theta}\right)\right]\mathrm{d}\theta.
\end{aligned} \tag{7.24}$$

The partial derivatives of the liquid–vapor interfacial area (Equation (7.17)) are:

$$\begin{aligned}
&\frac{\partial}{\partial R}\left[2\pi R^2(1-\cos\theta)+2\pi Rh\sin\theta\;\lambda_{\text{liquid}}\big|_{r=R\sin\theta}\right] \\
&\quad=4\pi R(1-\cos\theta)+2\pi Rh\sin\theta\;\left.\frac{\partial\left(\lambda_{\text{liquid}}\right)}{\partial a}\right|_{r=R\sin\theta}\frac{\partial a}{\partial R} \\
&\qquad+2\pi h\sin\theta\;\lambda_{\text{liquid}}\big|_{r=R\sin\theta}
\end{aligned} \tag{7.25}$$

$$\begin{aligned}
&\frac{\partial}{\partial\theta}\left[2\pi R^2(1-\cos\theta)+2\pi Rh\sin\theta\;\lambda_{\text{liquid}}\big|_{r=R\sin\theta}\right] \\
&\quad=2\pi R^2(\sin\theta)+2\pi Rh\sin\theta\;\left.\frac{\partial\left(\lambda_{\text{liquid}}\right)}{\partial a}\right|_{r=R\sin\theta}\frac{\partial a}{\partial\theta} \\
&\qquad+2\pi Rh\cos\theta\;\lambda_{\text{liquid}}\big|_{r=R\sin\theta},
\end{aligned} \tag{7.26}$$

and the total derivative of Equation (7.17) is

$$\begin{aligned} \mathrm{d}A^{\mathrm{LV}} = &\left[4\pi R(1-\cos\theta) + 2\pi Rh\sin^2\theta \left.\frac{\partial\left(\lambda_{\mathrm{liquid}}\right)}{\partial a}\right|_{r=R\sin\theta} \right. \\ &\left. + 2\pi h\sin\theta\, \lambda_{\mathrm{liquid}}\big|_{r=R\sin\theta} \right] \mathrm{d}R \\ &+ \left[2\pi R^2(\sin\theta) + 2\pi R^2 h\sin\theta\cos\theta \left.\frac{\partial(\lambda_{\mathrm{liquid}})}{\partial a}\right|_{r=R\sin\theta} \right. \\ &\left. + 2\pi Rh\cos\theta\, \lambda_{\mathrm{liquid}}\big|_{r=R\sin\theta} \right] \mathrm{d}\theta. \end{aligned} \tag{7.27}$$

The partial derivatives of the solid–liquid interfacial area (Equation (7.19)) are

$$\begin{aligned} &\frac{\partial}{\partial R}\left[\pi(R\sin\theta)^2 + h\int_0^{R\sin\theta} m(r)\,\mathrm{d}r\right] \\ &\qquad = 2\pi R\sin^2\theta + h\left(m|_{r=R\sin\theta}\right)\frac{\partial\left(R\sin\theta\right)}{\partial R} \\ &\qquad = 2\pi R\sin^2\theta + h\left(m|_{r=R\sin\theta}\right)\sin\theta \end{aligned} \tag{7.28}$$

$$\begin{aligned} &\frac{\partial}{\partial\theta}\left[\pi(R\sin\theta)^2 + h\int_0^{R\sin\theta} m(r)\,\mathrm{d}r\right] \\ &\qquad = 2\pi R^2\sin\theta\cos\theta + h\left(m|_{r=R\sin\theta}\right)\frac{\partial\left(R\sin\theta\right)}{\partial\theta} \\ &\qquad = 2\pi R^2\sin\theta\cos\theta + h\left(m|_{r=R\sin\theta}\right)R\cos\theta, \end{aligned} \tag{7.29}$$

and the total derivative of Equation (7.19) is

$$\begin{aligned} \mathrm{d}A^{\mathrm{SL}} = &\left[2\pi R\sin^2\theta + h\left(m|_{r=R\sin\theta}\right)\sin\theta\right]\mathrm{d}R \\ &+ \left[2\pi R^2\sin\theta\cos\theta + h\left(m|_{r=R\sin\theta}\right)R\cos\theta\right]\mathrm{d}\theta. \end{aligned} \tag{7.30}$$

7.2.2 Equilibrium Conditions

Equations (7.3)–(7.9) are substituted into Equation (7.2), and the constraints given by Equations (7.10)–(7.15), (7.24), (7.27), and (7.30) are substituted into the resulting expression to give,

after collection of some like terms:

$$
\begin{aligned}
&\left(\frac{1}{T^{\mathrm{L}}}-\frac{1}{T^{\mathrm{V}}}\right)\mathrm{d}U^{\mathrm{L}}+\left(\frac{1}{T^{\mathrm{S}}}-\frac{1}{T^{\mathrm{V}}}\right)\mathrm{d}U^{\mathrm{S}}+\left(\frac{1}{T^{\mathrm{LV}}}-\frac{1}{T^{\mathrm{V}}}\right)\mathrm{d}U^{\mathrm{LV}}\\
&\quad+\left(\frac{1}{T^{\mathrm{SL}}}-\frac{1}{T^{\mathrm{V}}}\right)\mathrm{d}U^{\mathrm{SL}}+\left(\frac{1}{T^{\mathrm{SV}}}-\frac{1}{T^{\mathrm{V}}}\right)\mathrm{d}U^{\mathrm{SV}}+\left(\frac{1}{T^{\mathrm{R}}}-\frac{1}{T^{\mathrm{V}}}\right)\mathrm{d}U^{\mathrm{R}}\\
&\quad+\left(\frac{P^{\mathrm{L}}}{T^{\mathrm{L}}}-\frac{P^{\mathrm{V}}}{T^{\mathrm{V}}}\right)\left\{\left[\pi R^2(2-3\cos\theta+\cos^3\theta)+2\pi h(R\sin^2\theta)\left(\lambda_{\mathrm{liquid}}\big|_{r=R\sin\theta}\right)\right]\mathrm{d}R\right.\\
&\qquad\qquad\left.+\left[\pi R^3(\sin\theta-\cos^2\theta\sin\theta)+2\pi h(R^2\sin\theta\cos\theta)\left(\lambda_{\mathrm{liquid}}\big|_{r=R\sin\theta}\right)\right]\mathrm{d}\theta\right\}\\
&\quad+\left(\frac{P^{\mathrm{R}}}{T^{\mathrm{R}}}-\frac{P^{\mathrm{V}}}{T^{\mathrm{V}}}\right)\mathrm{d}V^{\mathrm{R}}+\left(\frac{\mu_1^{\mathrm{V}}}{T^{\mathrm{V}}}-\frac{\mu_1^{\mathrm{L}}}{T^{\mathrm{L}}}\right)\mathrm{d}N_1^{\mathrm{L}}+\left(\frac{\mu_1^{\mathrm{V}}}{T^{\mathrm{V}}}-\frac{\mu_1^{\mathrm{LV}}}{T^{\mathrm{LV}}}\right)\mathrm{d}N_1^{\mathrm{LV}}\\
&\quad+\left(\frac{\mu_1^{\mathrm{V}}}{T^{\mathrm{V}}}-\frac{\mu_1^{\mathrm{SL}}}{T^{\mathrm{SL}}}\right)\mathrm{d}N_1^{\mathrm{SL}}+\left(\frac{\mu_1^{\mathrm{V}}}{T^{\mathrm{V}}}-\frac{\mu_1^{\mathrm{SV}}}{T^{\mathrm{SV}}}\right)\mathrm{d}N_1^{\mathrm{SV}}\\
&\quad-\frac{\sigma^{\mathrm{LV}}}{T^{\mathrm{LV}}}\left\{\left[4\pi R(1-\cos\theta)+2\pi Rh\sin^2\theta\ \left.\frac{\partial\left(\lambda_{\mathrm{liquid}}\right)}{\partial a}\right|_{r=R\sin\theta}\right.\right.\\
&\qquad\qquad\left.+2\pi h\sin\theta\ \lambda_{\mathrm{liquid}}\big|_{r=R\sin\theta}\right]\mathrm{d}R\\
&\quad+\left[2\pi R^2(\sin\theta)+2\pi R^2h\sin\theta\cos\theta\ \left.\frac{\partial\left(\lambda_{\mathrm{liquid}}\right)}{\partial a}\right|_{r=R\sin\theta}\right.\\
&\qquad\qquad\left.\left.+2\pi Rh\cos\theta\ \lambda_{\mathrm{liquid}}\big|_{r=R\sin\theta}\right]d\theta\right\}\\
&\quad+\left(\frac{\sigma^{\mathrm{SV}}}{T^{\mathrm{SV}}}-\frac{\sigma^{\mathrm{SL}}}{T^{\mathrm{SL}}}\right)\left\{\left[2\pi R\sin^2\theta+h\left(m|_{r=R\sin\theta}\right)\sin\theta\right]\mathrm{d}R\right.\\
&\qquad\qquad\left.+\left[2\pi R^2\sin\theta\cos\theta+h\left(m|_{r=R\sin\theta}\right)R\cos\theta\right]\mathrm{d}\theta\right\}=0.
\end{aligned}
\tag{7.31}
$$

To solve Equation (7.31) for any arbitrary values of the differential quantities, each coefficient in front of the differentials (made independent by use of all constraints) must be set to zero. Setting all coefficients of differential internal energies, moles of component 1, and reservoir

volume to zero yields the following three equilibrium conditions:

$$T^{\mathrm{L}} = T^{\mathrm{V}} = T^{\mathrm{S}} = T^{\mathrm{LV}} = T^{\mathrm{SL}} = T^{\mathrm{SV}} = T^{\mathrm{R}} \tag{7.32}$$

$$\mu_1^{\mathrm{V}} = \mu_1^{\mathrm{L}} = \mu_1^{\mathrm{LV}} = \mu_1^{\mathrm{SL}} = \mu_1^{\mathrm{SV}} \tag{7.33}$$

$$P^{\mathrm{R}} = P^{\mathrm{V}}. \tag{7.34}$$

Using the equality of temperatures (Equation (7.32)), the coefficients in front of dR in Equation (7.31) are collected and set to zero, giving

$$\begin{aligned}
&\left(P^{\mathrm{L}} - P^{\mathrm{V}}\right)\left[\pi R^2\left(2 - 3\cos\theta + \cos^3\theta\right) + 2\pi h\left(R\sin^2\theta\right)\left(\lambda_{\mathrm{liquid}}\big|_{r=R\sin\theta}\right)\right] \\
&\quad - \sigma^{\mathrm{LV}}\left[4\pi R\left(1-\cos\theta\right) + 2\pi R h\sin^2\theta\left.\frac{\partial\left(\lambda_{\mathrm{liquid}}\right)}{\partial a}\right|_{r=R\sin\theta} + 2\pi h\sin\theta\ \lambda_{\mathrm{liquid}}\big|_{r=R\sin\theta}\right] \\
&\quad + \left(\sigma^{\mathrm{SV}} - \sigma^{\mathrm{SL}}\right)\left(2\pi R\sin^2\theta + h\left(m|_{r=R\sin\theta}\right)\sin\theta\right) = 0.
\end{aligned} \tag{7.35}$$

The coefficients in front of dθ are collected and set to zero, giving

$$\begin{aligned}
&\left(P^{\mathrm{L}} - P^{\mathrm{V}}\right)\left[\pi R^3\left(\sin\theta - \cos^2\theta\sin\theta\right) + 2\pi h\left(R^2\sin\theta\cos\theta\right)\left(\lambda_{\mathrm{liquid}}\big|_{r=R\sin\theta}\right)\right] \\
&\quad - \sigma^{\mathrm{LV}}\left[2\pi R^2\left(\sin\theta\right) + 2\pi R^2 h\sin\theta\cos\theta\left.\frac{\partial\left(\lambda_{\mathrm{liquid}}\right)}{\partial a}\right|_{r=R\sin\theta} + 2\pi R h\cos\theta\ \lambda_{\mathrm{liquid}}\big|_{r=R\sin\theta}\right] \\
&\quad + \left(\sigma^{\mathrm{SV}} - \sigma^{\mathrm{SL}}\right)\left(2\pi R^2\sin\theta\cos\theta + h\left(m|_{r=R\sin\theta}\right)R\cos\theta\right) = 0.
\end{aligned} \tag{7.36}$$

Equation (7.35) can be rearranged to form an expression for $\left(P^{\mathrm{L}} - P^{\mathrm{V}}\right)$ and substituted into Equation (7.36) to give the fourth equilibrium condition (when a common factor of $\sin\theta\left(1-\cos\theta\right)^2$ is removed from every term of the equation):

$$\begin{aligned}
\cos\theta - \frac{2h\ \lambda_{\mathrm{liquid}}\big|_{r=R\sin\theta}}{R} + \frac{h\ \lambda_{\mathrm{liquid}}\big|_{r=R\sin\theta}}{R\sin\theta} + h\left.\frac{\partial\left(\lambda_{\mathrm{liquid}}\right)}{\partial a}\right|_{r=R\sin\theta} \\
= \left(1 + \frac{h\left(m|_{r=R\sin\theta}\right)}{2\pi R\sin\theta}\right)\frac{\left(\sigma^{\mathrm{SV}} - \sigma^{\mathrm{SL}}\right)}{\sigma^{\mathrm{LV}}}.
\end{aligned} \tag{7.37}$$

Substituting Equation (7.37) into Equation (7.35) and simplifying gives the Young–Laplace equation as the last equilibrium condition:

$$P^{\mathrm{L}} - P^{\mathrm{V}} = \frac{2\sigma^{\mathrm{LV}}}{R} \ . \tag{7.38}$$

The Young equation for the contact angle of a liquid drop on a smooth surface can be derived by minimizing energy [26, 304] or maximizing entropy subject to constraints [87], and it is given by

$$\sigma^{\mathrm{SV}} - \sigma^{\mathrm{SL}} = \sigma^{\mathrm{LV}} \cos\theta_{\mathrm{Y}} \ . \tag{7.39}$$

The Young equation (Equation (7.39)) can be substituted into Equation (7.37) to give a simplified form of the equilibrium condition for contact angle:

$$\begin{aligned} \cos\theta - \frac{2h\,\lambda_{\mathrm{liquid}}\big|_{r=R\sin\theta}}{R} + \frac{h\,\lambda_{\mathrm{liquid}}\big|_{r=R\sin\theta}}{R\sin\theta} + h\ \left.\frac{\partial\left(\lambda_{\mathrm{liquid}}\right)}{\partial a}\right|_{r=R\sin\theta} \\ = \left(1 + \frac{h\left(m|_{r=R\sin\theta}\right)}{2\pi R\sin\theta}\right)\cos\theta_{\mathrm{Y}} \ . \end{aligned} \tag{7.40}$$

Defining a line roughness ρ at the contact line as

$$\rho|_{r=R\sin\theta} = 1 + \frac{h\left(m|_{r=R\sin\theta}\right)}{2\pi R\sin\theta} \tag{7.41}$$

further simplifies Equation (7.40) to

$$\cos\theta - \frac{2h\,\lambda_{\mathrm{liquid}}\big|_{r=R\sin\theta}}{R} + \frac{h\,\lambda_{\mathrm{liquid}}\big|_{r=R\sin\theta}}{R\sin\theta} + h\ \left.\frac{\partial\left(\lambda_{\mathrm{liquid}}\right)}{\partial a}\right|_{r=R\sin\theta} = \rho|_{r=R\sin\theta}\cos\theta_{\mathrm{Y}}, \tag{7.42}$$

which is our newly-derived version of the Wenzel equation.

7.3 Discussion of Equilibrium Conditions

Comparing our new equation (Equation (7.42)) to the area-roughness Wenzel equation (Equation (7.1)) and the orthogonal line-roughness Wenzel equation derived by Xu [312], we note two differences: (*i*) three additional terms on the left-hand side of Equation (7.42) and (*ii*) the prefactor to $\cos\theta_{\mathrm{Y}}$. In the sections that follow, we investigate the additional terms, perform a thermodynamic free energy analysis, and discuss what conditions must be met for the prefactor to limit to the orthogonal line-roughness and area-roughness Wenzel equations.

7.3.1 On the Magnitudes of the Terms in Equation (7.42)

What are the magnitudes of the three additional terms on the left-hand side of Equation (7.42), and under what conditions are they, if ever, negligible? By negligible, we mean that these terms should be orders of magnitude smaller than $\cos\theta$. We first isolate the three terms of interest in Equation (7.42):

$$k = -\frac{2h\,\lambda_{\text{liquid}}\big|_{r=R\sin\theta}}{R} + \frac{h\,\lambda_{\text{liquid}}\big|_{r=R\sin\theta}}{R\sin\theta} + h\,\left.\frac{\partial\left(\lambda_{\text{liquid}}\right)}{\partial a}\right|_{r=R\sin\theta}. \tag{7.43}$$

The first term in Equation (7.43) arises from the differential of liquid volume within the pillars (Equation (7.24)), while the last two terms originate from the differential of liquid–vapor interfacial area that is between the pillars at the contact line (Equation (7.27)). Therefore, the contribution of these terms becomes negligible when the volume of liquid between the pillars is insignificant compared to the volume of liquid that forms the spherical cap. Next, we develop a quantitative criterion to describe how much smaller the liquid volume and area between the pillars need to be.

For the purpose of further exploring when these terms can or cannot be neglected, if we assume that a surface has a constant liquid line fraction ($\partial\lambda_{\text{liquid}}/\partial a\big|_{r=R\sin\theta} = 0$), Equation (7.43) simplifies to, after factoring,

$$k = \frac{h\,\lambda_{\text{liquid}}\big|_{r=R\sin\theta}}{R}\left(\frac{1}{\sin\theta} - 2\right). \tag{7.44}$$

The factor $\frac{1}{\sin\theta} - 2$ varies from -1 at $\theta = 90^\circ$ to approaching infinity as θ approaches 0° or 180°. Thus, by inspection, a ratio $h\lambda_{\text{liquid}}/R \ll 1$ is required for k to be considered negligible, and how much less than unity this ratio has to be is dependent on contact angle. We define this dimensionless quantity as H and use the relationship between λ_{liquid} and the solid line fraction at the contact line (λ_{solid}, the line fraction of the spherical cap's circumference that is on the pillars) to replace the liquid fraction ($\lambda_{\text{liquid}}\big|_{r=R\sin\theta} = 1 - \lambda_{\text{solid}}$) to give the following criterion:

$$\text{H} = \frac{h\,\lambda_{\text{liquid}}\big|_{r=R\sin\theta}}{R} = \frac{h(1-\lambda_{\text{solid}})}{R} \ll 1. \tag{7.45}$$

Using this definition of H, assuming λ_{liquid} is constant, and substituting Equation (7.44) into Equation (7.42) yields

$$\cos\theta + \text{H}\left(\frac{1}{\sin\theta} - 2\right) = \rho\cos\theta_{\text{Y}}, \tag{7.46}$$

where ρ is evaluated at the three-phase contact line ($r = R\sin\theta$). To determine the effect of H on the equilibrium contact angle, we solve Equation (7.46) for $\cos\theta$ at various values of H for

all $\rho\cos\theta_Y$ between -1 and 1.

Figure 7.5 illustrates the contact angles calculated using Equation (7.46) for H values ranging over several orders of magnitude, showing that the number and magnitude of equilibrium contact angles varies with H and $\rho\cos\theta_Y$. From Figure 7.5(a), it can be seen that for $H > 0.5$, there are two equilibrium contact angles for a given value of $\rho\cos\theta_Y$ for all $\rho\cos\theta_Y$ that satisfy $-1 \leq \rho\cos\theta_Y \leq 1$. For $H = 0.5$, there is one equilibrium contact angle for $\rho\cos\theta_Y = -1$, and there are two equilibrium contact angles for $-1 < \rho\cos\theta_Y \leq 1$. For H between 0.5 and 0.144, there are two equilibrium contact angles for a given value of $\rho\cos\theta_Y$ when $\rho\cos\theta_Y$ is between some threshold value and 1, one equilibrium contact angle at the threshold value, and no equilibrium contact angles for $\rho\cos\theta_Y$ between -1 and the threshold value. The size of the no-equilibrium-contact-angle region grows as H decreases below 0.5, reaching a maximum size at $H = 0.144$ where there is no equilibrium contact angle for $-1 \leq \rho\cos\theta_Y < -\sqrt{3}/2$ (equivalently, for $\text{acos}(\rho\cos\theta_Y)$ between 150° and 180°, as seen in Figure 7.5(b)). When H decreases below 0.144, there continues to be two equilibrium contact angles for a given value of $\rho\cos\theta_Y$ when $\rho\cos\theta_Y$ is between some threshold value and 1, one equilibrium contact angle at the threshold value, and no equilibrium contact angles for $\rho\cos\theta_Y$ between -1 and the threshold value. However, for $H < 0.144$, the size of the no-equilibrium region shrinks as H approaches 0 (*vs.* when H decreased from 0.5 to 0.144, the no-equilibrium region grew). Overall, the number of equilibrium contact angles for a given value of $\rho\cos\theta_Y$ depends on both H and $\rho\cos\theta_Y$. For a given $\rho\cos\theta_Y$, what effect does H have on the value(s) of the equilibrium contact angle(s)? When there are two equilibrium contact angles at a given $\rho\cos\theta_Y$, the smaller equilibrium contact angle approaches the 45° line in Figure 7.5 (where $\cos\theta = \rho\cos\theta_Y$) as H approaches 0. At the same time, the larger equilibrium contact angle approaches 180° when H decreases past 0.144 and approaches 0.

Often in applications, the dimensionless variable H is much smaller than 1 (*e.g.*, for a drop with a radius of curvature $R = 2.5$ mm on a surface with $\lambda_{\text{solid}} = 0.5$ and $h = 5$ μm, $h(1-\lambda_{\text{solid}})/R = 0.001$). When $H \ll 1$ and $\rho\cos\theta_Y$ is not near -1 or 1, Equation (7.46) simplifies to

$$\cos\theta = \rho\cos\theta_Y. \tag{7.47}$$

For a liquid drop in the Wenzel state, Equation (7.47) predicts that a hydrophobic smooth surface ($\theta_Y > 90^\circ$) will become more hydrophobic when it is rough ($\theta > \theta_Y$), and a hydrophilic smooth surface ($\theta_Y < 90^\circ$) will become more hydrophilic when it is rough ($\theta < \theta_Y$). This enhancement of hydrophobicity/hydrophilicity is also predicted by the area-roughness Wenzel equation [303], but Equation (7.47) reveals that only the roughness at the three-phase contact line affects the macroscopic contact angle. Therefore, for experimental systems where the line roughness varies significantly over the solid–liquid contact area (*e.g.*, for a drop on a surface with a central island

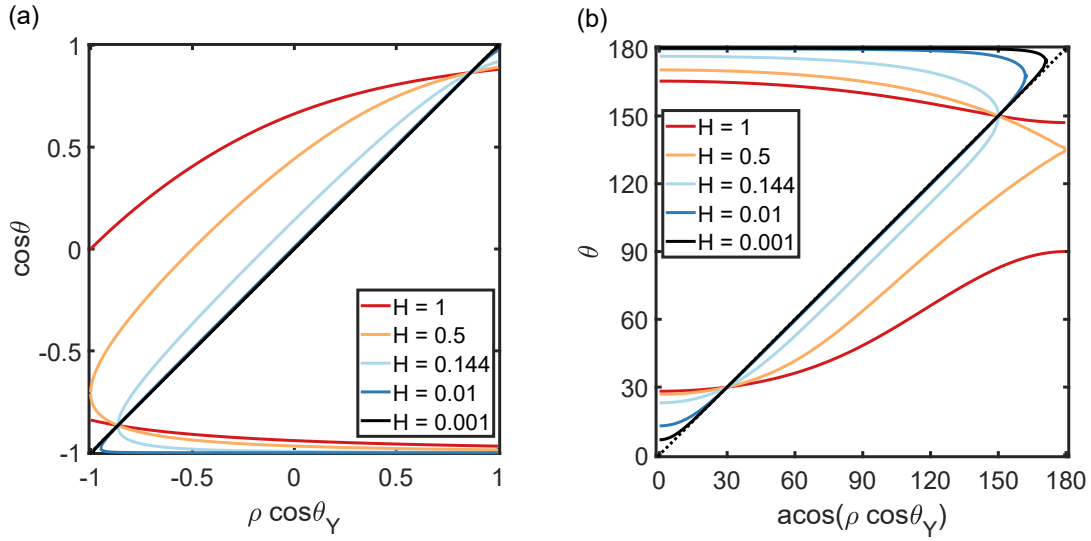

Figure 7.5: Effect of the dimensionless variable $\mathrm{H} = h(1-\lambda_{\mathrm{solid}})/R$ on (a) the cosine of the contact angle as a function of $\rho\cos\theta_{\mathrm{Y}}$ and (b) the contact angle as a function of $\mathrm{acos}\left(\rho\cos\theta_{\mathrm{Y}}\right)$ as determined by Equation (7.46), where ρ is line roughness and θ_{Y} is the Young contact angle. From panel (b), it can be seen that where there are two equilibrium contact angles for a given value of $\rho\cos\theta_{\mathrm{Y}}$, as H decreases below 0.144, the smaller equilibrium contact angle that is a solution to Equation (7.46) approaches the 45° line where $\theta = \mathrm{acos}(\rho\cos\theta_{\mathrm{Y}})$. Simultaneously, the larger equilibrium contact angle approaches 180° as H approaches zero. This trend can also be seen in panel (a), where the cosine of the smaller equilibrium contact angle approaches the 45° line where $\cos\theta = \rho\cos\theta_{\mathrm{Y}}$ and the cosine of the larger equilibrium contact angle approaches -1.

of one material surrounded by rough features [103]), the area-roughness Wenzel equation will be incorrect. In fact, if a drop is in contact with a rough surface that has varying degrees of roughness at the contact line as the drop spreads (*e.g.*, a surface with pillars arranged in a square or hexagonal array), the equilibrium contact angle will change according to the local roughness at the three-phase line.

7.3.2 Thermodynamic Free Energy Analysis

To understand the thermodynamic stability of the equilibrium contact angles obtained from Equation (7.46), we perform a free energy analysis next. The free energy (B) of a liquid drop in equilibrium with its vapor and in contact with an incompressible solid surface where the temperature and vapor-phase pressure are imposed by a reservoir is [79, 87, 323]

$$B = \left(P^{\mathrm{V}} - P^{\mathrm{L}}\right)V^{\mathrm{L}} - \left(\sigma^{\mathrm{SV}} - \sigma^{\mathrm{SL}}\right)A^{\mathrm{SL}} + \sigma^{\mathrm{LV}}A^{\mathrm{LV}} + \sum_j \mu^j N^j. \tag{7.48}$$

For calculating the free energy of a given equilibrium state, we choose a reference equilibrium state with free energy B_0 where there is no liquid phase ($V^{\mathrm{L}} = 0$, $A^{\mathrm{LV}} = 0$, and $A^{\mathrm{SL}} = 0$) to give

$$B_0 = \sum_j \mu^j N^j. \tag{7.49}$$

Because both the state of interest and the reference state are equilibrium states, Equation (7.33) for chemical potential applies, so that subtracting Equation (7.49) from (7.48) yields:

$$B - B_0 = \left(P^{\mathrm{V}} - P^{\mathrm{L}}\right) V^{\mathrm{L}} - \left(\sigma^{\mathrm{SV}} - \sigma^{\mathrm{SL}}\right) A^{\mathrm{SL}} + \sigma^{\mathrm{LV}} A^{\mathrm{LV}}. \tag{7.50}$$

Because we are interested in the free energy of equilibrium states, the equilibrium conditions dictated by Equations (7.38) and (7.46) apply to each equilibrium state. At every equilibrium state, the Young–Laplace equation (Equation (7.38)) has the following form

$$P^{\mathrm{L}} - P^{\mathrm{V}} = \frac{2\sigma^{\mathrm{LV}}}{R_{\mathrm{eq}}}, \tag{7.51}$$

where R_{eq} is the equilibrium radius of curvature of the liquid phase, the numerical value of which is dictated by the equality of chemical potential of the compound in the liquid phase and the vapor phase at equilibrium combined with the Young–Laplace equation [79, 87, 323].

We proceed as we did when examining the magnitude of H and consider a drop on a solid surface with $\lambda_{\mathrm{liquid}}$ and line roughness (ρ) that are constant with the drop's spherical cap bottom radius. Substituting (7.39) into (7.46) gives (after rearranging for ($\sigma^{\mathrm{SV}} - \sigma^{\mathrm{SL}}$)):

$$\sigma^{\mathrm{SV}} - \sigma^{\mathrm{SL}} = \frac{\sigma^{\mathrm{LV}}}{\rho}\left[\cos\theta_{\mathrm{eq}} + \frac{h\lambda_{\mathrm{liquid}}}{R_{\mathrm{eq}}}\left(\frac{1}{\sin\theta_{\mathrm{eq}}} - 2\right)\right], \tag{7.52}$$

where θ_{eq} is the contact angle at equilibrium. We substitute the equilibrium conditions as stated by Equations (7.51) and (7.52) into Equation (7.50) to yield

$$B - B_0 = -\frac{2\sigma^{\mathrm{LV}}}{R_{\mathrm{eq}}} V^{\mathrm{L}} - \left(\frac{\sigma^{\mathrm{LV}}}{\rho}\left[\cos\theta_{\mathrm{eq}} + \frac{h\lambda_{\mathrm{liquid}}}{R_{\mathrm{eq}}}\left(\frac{1}{\sin\theta_{\mathrm{eq}}} - 2\right)\right]\right) A^{\mathrm{SL}} + \sigma^{\mathrm{LV}} A^{\mathrm{LV}}. \tag{7.53}$$

Substituting Equation (7.16) for V^{L}, Equation (7.17) for A^{LV}, and Equation (7.19) for A^{SL} (assuming $m(r) = Cr$, which is true when line roughness is constant; see Equation (7.62) below)

into Equation (7.53) yields

$$\begin{aligned} B - B_0 = &-\frac{2\sigma^{\mathrm{LV}}}{R_{\mathrm{eq}}}\left[\frac{\pi R^3}{3}\left(2 - 3\cos\theta + \cos^3\theta + 3\frac{h\lambda_{\mathrm{liquid}}}{R}\sin^2\theta\right)\right] \\ &- \sigma^{\mathrm{LV}}\left[\cos\theta_{\mathrm{eq}} + \frac{h\lambda_{\mathrm{liquid}}}{R_{\mathrm{eq}}}\left(\frac{1}{\sin\theta_{\mathrm{eq}}} - 2\right)\right]\left(\pi R^2\sin^2\theta\right) \\ &+ \sigma^{\mathrm{LV}}\left[2\pi R^2(1-\cos\theta) + 2\pi\frac{h\lambda_{\mathrm{liquid}}}{R}R^2\sin\theta\right]. \end{aligned} \tag{7.54}$$

Note that a geometric radius of curvature and a geometric contact angle are used in the substituted expressions governing the geometric volume and areas, and not the equilibrium radius of curvature or equilibrium contact angle. To evaluate Equation (7.54), we consider a system where water is component 1 (in the liquid phase and in the vapor phase). We choose a temperature and a vapor-phase pressure such that $\sigma^{\mathrm{LV}} = 0.072$ N/m and $R_{\mathrm{eq}} = 5 \times 10^{-8}$ m [87]. We also choose three representative values for $\mathrm{H_{eq}} = h\lambda_{\mathrm{liquid}}/R_{\mathrm{eq}}$ of 0.5, 0.1, and 0 and a representative value for $\rho\cos\theta_{\mathrm{Y}} = -0.5$, which means that in the second term of Equation (7.54),

$$\left[\cos\theta_{\mathrm{eq}} + \frac{h\lambda_{\mathrm{liquid}}}{R_{\mathrm{eq}}}\left(\frac{1}{\sin\theta_{\mathrm{eq}}} - 2\right)\right] = \rho\cos\theta_{\mathrm{Y}} = -0.5, \tag{7.55}$$

as dictated by the equilibrium condition of Equation (7.46). Thus, the number and magnitude of equilibrium contact angles (θ_{eq}) will change according to Equation (7.55) when $\mathrm{H_{eq}}$ changes, while $\rho\cos\theta_{\mathrm{Y}}$ remains constant. Using Equation (7.55) and evaluating Equation (7.54) as a function of geometric radius of curvature R and geometric contact angle θ yields the 3D free energy surfaces in Figure 7.6 for each considered $\mathrm{H_{eq}}$. For each free energy surface, we trace the trend in free energy as a function of geometric contact angle at $R = R_{\mathrm{eq}}$, shown with a solid black curve on each surface. We also trace the trend in free energy as a function of geometric radius of curvature at each equilibrium contact angle $\theta = \theta_{\mathrm{eq}}$ that is a solution to Equation (7.55) for every value of $\mathrm{H_{eq}}$, as shown with yellow curves.

Thermodynamically, an equilibrium state at a global minimum in free energy is stable; an equilibrium state at a local minimum in free energy is metastable; and an equilibrium state at a maximum or inflection point in free energy is unstable [79, 87, 300, 323]. The presence of a local maximum also indicates that a free energy barrier needs to be overcome to pass through this equilibrium state. For the free energy surface illustrated in Figure 7.6(a) for $\mathrm{H_{eq}} = 0.5$, the smaller equilibrium contact angle is at 90° (from Equation (7.55)), and this equilibrium state is at an inflection point in free energy with respect to geometric contact angle and at a maximum in

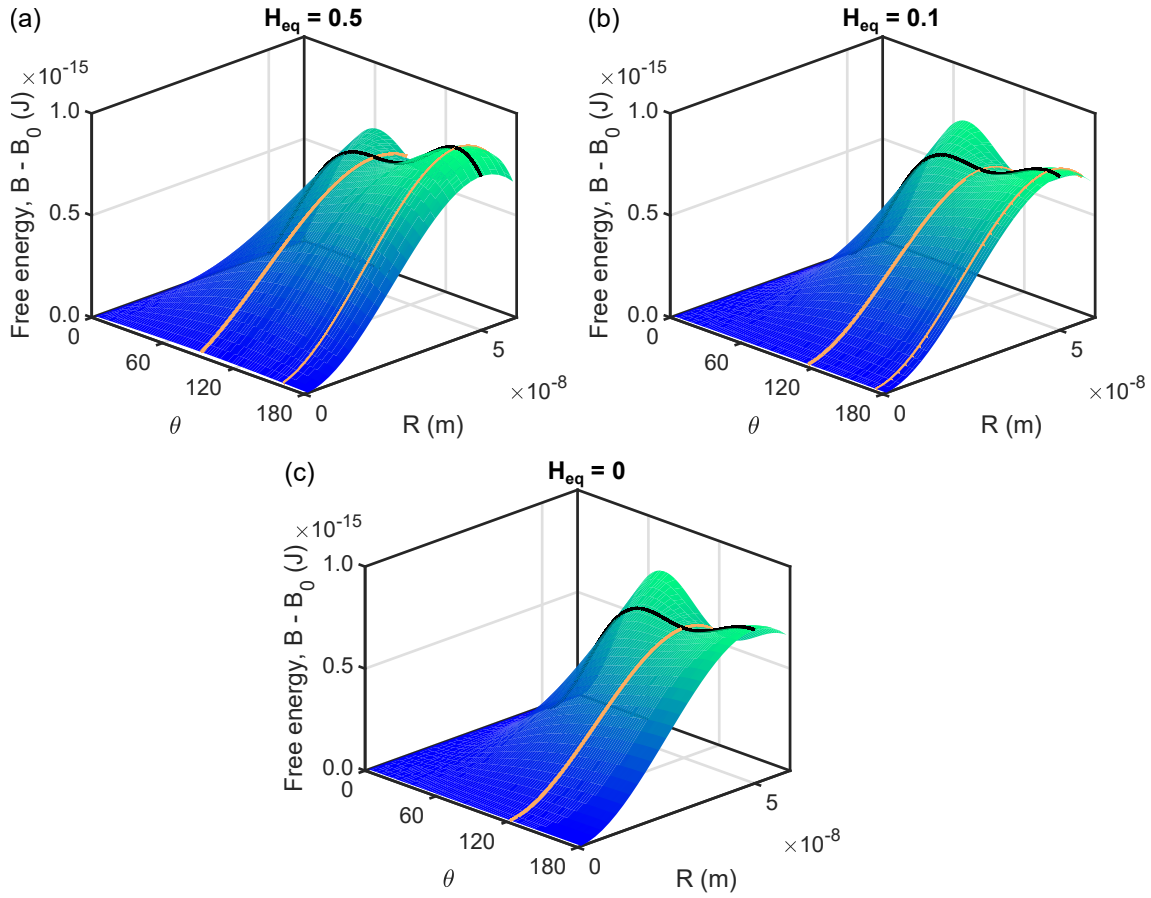

Figure 7.6: Free energy surfaces calculated using Equation (7.54) as a function of geometric radius of curvature R and geometric contact angle θ with $\sigma^{\mathrm{LV}} = 0.072$ N/m, $R_{\mathrm{eq}} = 5 \times 10^{-8}$ m, and $\rho \cos\theta_{\mathrm{Y}} = -0.5$. Free energy surface for (a) $\mathrm{H_{eq}} = 0.5$, (b) $\mathrm{H_{eq}} = 0.1$, and (c) $\mathrm{H_{eq}} = 0$. In each plot, yellow curves trace the trend in free energy at each $\theta = \theta_{\mathrm{eq}}$ as governed by Equation (7.55), and one black curve traces the free energy at $R = R_{\mathrm{eq}}$.

free energy with respect to geometric radius of curvature—it is therefore an unstable equilibrium state. The larger equilibrium contact angle is at 160° with a free energy that is at a maximum with respect to both changes in geometric contact angle and radius of curvature, so it is also an unstable equilibrium state. The same conclusion about stability of the equilibrium states is reached in Figure 7.6(b) for $\mathrm{H_{eq}} = 0.1$: the smaller equilibrium contact angle is at a local minimum in free energy with respect to changes in geometric contact angle, but at a maximum with respect to changes in geometric radius of curvature; the larger equilibrium contact angle is at a maximum in free energy with respect to both geometric variables. Figure 7.6(c) shows the free energy surface for $\mathrm{H_{eq}} = 0$, where there is one equilibrium state (at $\theta = \theta_{\mathrm{eq}} = 120°$ and $R = R_{\mathrm{eq}} = 5 \times 10^{-8}$ m) that is unstable because it is a maximum with respect to changes in geometric radius of curvature.

The instability of the equilibrium state for a single-component liquid drop in equilibrium

with its vapor where the vapor-phase pressure is held constant was also previously seen when the liquid was on a smooth, homogeneous solid phase [87]. More generally, as Gibbs stated, for the case where a two-phase system contains a single component with a curved interface between phases (*e.g.*, a liquid drop in a vapor), there is an unstable equilibrium state when a pressure is imposed on the system, and this unstable equilibrium state is at a radius of curvature that is dictated by the equality of chemical potential [108, p. 406]. The number and stability of equilibrium states have been shown to change when the constraints of the system change (*e.g.*, geometry or chemical composition). For example, if the liquid and vapor phases contain two components (*e.g.*, water with carbon dioxide), there may be zero or more equilibrium states that can be unstable, stable, or metastable—depending on the imposition of constraints such as constant system volume, degree of saturation in the liquid phase, or number of bubbles present [298, 325].

As a result, we emphasize that the trends in free energy illustrated in Figure 7.6 are for a single-component system where the liquid drop is in thermodynamic equilibrium (that is, it is in mechanical, chemical, and thermal equilibrium) with the vapor phase, and the vapor phase has its pressure imposed. For such a system where the liquid phase is a single component that is in equilibrium with its vapor, the mechanical equilibrium condition dictated by Young–Laplace equation determines the equilibrium radius of curvature of the liquid drop and is also a component of the free energy of the system. This assumption of vapor–liquid equilibrium is in contrast to the free energy used by Johnson and Dettre [133] to investigate the thermodynamic stability of the area-roughness Wenzel equation, where they analyzed a liquid drop under the constraint of constant volume. Johnson and Dettre [133] showed that there is one global minimum in energy (a stable equilibrium state) at a contact angle of θ_{W} when (*i*) $V^{\mathrm{L}} = \text{const}$, (*ii*) the liquid–vapor interfacial area is approximately that of a spherical cap: $A^{\mathrm{LV}} \approx A^{\mathrm{cap}} = 2\pi R^2(1-\cos\theta)$, and (*iii*) Equation (7.1) ($\cos\theta_{\mathrm{W}} = r_{\mathrm{f}}\cos\theta_{\mathrm{Y}}$) describes the equilibrium contact angle. Under the constraint of constant volume, the liquid drop will not need to satisfy the Young–Laplace equation, and together with assuming that $A^{\mathrm{LV}} = A^{\mathrm{cap}}$, the trend in free energy and the stability of the equilibrium state obtained by Johnson and Dettre [133] is different from the trends shown in Figure 7.6.

If we were to assume that liquid drop volume were constant within the framework of Gibbsian composite-system thermodynamics, then the equilibrium conditions would be obtained by substituting the constraint $\mathrm{d}V^{\mathrm{L}} = 0$ into Equation (7.3) and (7.14) and accounting for the fact that $\mathrm{d}R$ and $\mathrm{d}\theta$ are no longer independent (Equation (7.24) governs their dependent relationship). After applying these constraints to the expression obtained once Equations (7.3)–(7.13), (7.15), (7.27) and (7.30) are substituted into Equation (7.2), the resulting equilibrium conditions are Equations (7.32), (7.33), (7.34), and (7.42). Importantly, the Young–Laplace equation is not an

equilibrium condition for a liquid drop with a constant volume. The free energy of a drop under constant volume is [133]

$$B - B_0 = \sigma^{\mathrm{LV}} \left(A^{\mathrm{LV}} - \frac{\sigma^{\mathrm{SV}} - \sigma^{\mathrm{SL}}}{\sigma^{\mathrm{LV}}} A^{\mathrm{SL}} - 4\pi R_0^2 \right), \tag{7.56}$$

where we choose a reference state of a liquid drop in the shape of a sphere with radius R_0. Using our specified geometry for each interfacial area shown in Figure 7.2 and assuming $\lambda_{\mathrm{liquid}}$ and ρ are constant with drop radius, we substitute Equation (7.17) for A^{LV}, Equation (7.19) for A^{SL}, and Equation (7.52) for $\left(\sigma^{\mathrm{SV}} - \sigma^{\mathrm{SL}}\right)$ into Equation (7.56) to yield:

$$\begin{aligned} B - B_0 = \sigma^{\mathrm{LV}} \Bigg\{ & 2\pi R^2 (1 - \cos\theta) + 2\pi h \lambda_{\mathrm{liquid}} R \sin\theta \\ & - \left[\cos\theta_{\mathrm{eq}} + \frac{h\lambda_{\mathrm{liquid}}}{R_{\mathrm{eq}}} \left(\frac{1}{\sin\theta_{\mathrm{eq}}} - 2 \right) \right] \pi R^2 \sin^2\theta - 4\pi R_0^2 \Bigg\}. \end{aligned} \tag{7.57}$$

Here, in contrast to setting a value for R_{eq} that is dictated by combining the Young–Laplace equation with the equality of chemical potential of a pure component in the liquid and vapor phases, the values of R_{eq} and R are both governed by the constraint of constant volume (Equation (7.16)) and are a function of V^{L}, $h\lambda_{\mathrm{liquid}}$, and θ. The value of R_{eq} also needs to satisfy the equilibrium condition in Equation (7.46). Therefore, when calculating free energy with Equation (7.57) we set a value for V^{L} and $h\lambda_{\mathrm{liquid}}$ instead of H_{eq} as we did previously because R_{eq} varies with $h\lambda_{\mathrm{liquid}}$ and $\rho\cos\theta_{\mathrm{Y}}$. Next, we set a representative value for $\rho\cos\theta_{\mathrm{Y}} = -0.5$ for our analysis, which can be substituted into Equation (7.57) using the relationship in Equation (7.55).

After setting values for V^{L} and $h\lambda_{\mathrm{liquid}}$, the drop's radius of curvature R is calculated *via* Equation (7.16) at each θ. Then, Equation (7.57) is evaluated as a function of θ to calculate the free energy, as shown in Figure 7.7 when $\rho\cos\theta_{\mathrm{Y}} = -0.5$, $\sigma^{\mathrm{LV}} = 0.072$ N/m, and $V^{\mathrm{L}} = 1 \times 10^{-12}$ m^3 for two values of $h\lambda_{\mathrm{liquid}} = 1 \times 10^{-5}$ m and $h\lambda_{\mathrm{liquid}} = 0$ m. Under the constraint of constant liquid volume and $h\lambda_{\mathrm{liquid}} = 1 \times 10^{-5}$ m, one equilibrium contact angle is at a maximum in free energy (an unstable equilibrium state with $\theta_{\mathrm{eq}} = 168^\circ$, $R_{\mathrm{eq}} = 6.2 \times 10^{-5}$ m, and $\mathrm{H}_{\mathrm{eq}} = 0.16$) and another equilibrium contact angle is at a global minimum in free energy (a stable equilibrium state with $\theta_{\mathrm{eq}} = 111^\circ$, $R_{\mathrm{eq}} = 6.5 \times 10^{-5}$ m, and $\mathrm{H}_{\mathrm{eq}} = 0.15$), where the values of these equilibrium contact angles are dictated by Equation (7.55). The maximum in free energy at the larger equilibrium contact angle is an energy barrier that the liquid drop must overcome to reach the stable equilibrium state at the smaller contact angle. When $h\lambda_{\mathrm{liquid}} = 0$ m so that $A^{\mathrm{LV}} = A^{\mathrm{cap}}$, there is only one equilibrium contact angle where $\cos\theta = \rho\cos\theta_{\mathrm{Y}}$ that

corresponds to a stable equilibrium state, in agreement with the results presented by Johnson and Dettre [133].

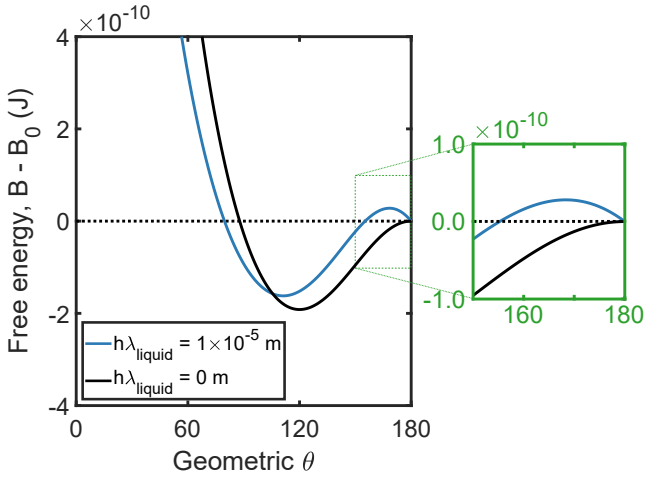

Figure 7.7: Free energy with respect to the chosen reference state (the liquid in a spherical shape) as a function of geometric contact angle calculated using Equation (7.57) for $\sigma^{\mathrm{LV}} = 0.072$ N/m, $V^{\mathrm{L}} = 1 \times 10^{-12}$ m^3 and $\rho \cos\theta_{\mathrm{Y}} = -0.5$ for two values of $h\lambda_{\mathrm{liquid}} = 1 \times 10^{-5}$ m and $h\lambda_{\mathrm{liquid}} = 0$ m. This free energy was obtained assuming that the liquid phase has a constant volume. The graph on the right-hand side is a magnification of the region where $150^\circ < \theta < 180^\circ$.

7.3.3 On the Prefactor to $\cos\theta_{\mathrm{Y}}$

The original area-roughness Wenzel equation is restricted to surfaces where every change in projected area yields a proportional change in the solid–liquid interfacial area. This condition is explicitly stated by Johnson and Dettre [133] in their derivation of the Wenzel equation ($\mathrm{d}A^{\mathrm{SL}} = r_{\mathrm{f}}\ \mathrm{d}A^{\mathrm{projected}}$). In the derivation of the Wenzel equation presented by Xu [312], the surface roughness was assumed to be orthogonal to the contact line, and the resulting macroscopic contact angle was found to be a function of the roughness at the contact line, which was a ratio between the actual contact line length and the projected contact line length ($\ell^{\mathrm{SLV}}/2\pi a$).

The version of the Wenzel equation derived in this chapter has neither the restriction that $\mathrm{d}A^{\mathrm{SL}} = r_{\mathrm{f}}\ \mathrm{d}A^{\mathrm{projected}}$ nor that the roughness must be orthogonal to the contact line. Our derived equation (Equation (7.42), or Equation (7.47) if $\mathrm{H} \ll 1$ and $\rho \cos\theta_{\mathrm{Y}}$ is not approaching -1 or 1) can be applied to any surface as long as (*i*) the shape of the drop can be separated into a spherical cap and a partially-filled cylinder and (*ii*) Equation (7.18) describes the solid–liquid interfacial area (that is, for a surface with flat-topped, vertical pillars of equal height). Starting from Equation (7.47) (which requires $\mathrm{H} \ll 1$ and $\rho \cos\theta_{\mathrm{Y}}$ not be approaching -1 or 1), each of the Xu [312] and Johnson and Dettre [133] results can be obtained when their respective assumptions are applied.

First, in the case where the roughness is orthogonal to the contact line, each intersection point at the edge of the liquid drop will have an orientation factor m_i equal to 1:

$$m\,|_{r=R\sin\theta} = \sum_{i=1}^{\zeta(r)} 1 = \zeta\,|_{r=R\sin\theta}\,, \tag{7.58}$$

which gives a line roughness from Equation (7.41) of

$$\rho|_{r=R\sin\theta} = 1 + \frac{h\left(\zeta|_{r=R\sin\theta}\right)}{2\pi R\sin\theta}. \tag{7.59}$$

Physically, Equation (7.59) is equal to the total length of the three-phase contact line divided by the circumference of the liquid drop's spherical cap ($\ell^{\mathrm{SLV}}/2\pi a$), which is the result obtained by Xu [312].

If the line roughness in Equation (7.47) does not change with radius r, then the assumption $\mathrm{d}A^{\mathrm{SL}} = r_{\mathrm{f}}\ \mathrm{d}A^{\mathrm{projected}}$ made by Johnson and Dettre [133] will be satisfied. Mathematically, a constant line roughness means that the derivative of line roughness with respect to radius must equal zero. For a surface with vertical pillars of uniform height, setting the derivative of Equation (7.41) with respect to radius equal to zero yields

$$\frac{\mathrm{d}\rho}{\mathrm{d}r} = \frac{\mathrm{d}}{\mathrm{d}r}\left(1 + \frac{hm(r)}{2\pi r}\right) = \frac{h}{2\pi r}\frac{\mathrm{d}m}{\mathrm{d}r} - m\frac{h}{2\pi r^2} = 0. \tag{7.60}$$

Rearranging Equation (7.60) gives

$$\frac{\mathrm{d}m}{\mathrm{d}r} = \frac{m}{r}. \tag{7.61}$$

Rearranging, integrating, and raising each side to an exponent with base e gives the following solution to this differential equation

$$m = Cr, \tag{7.62}$$

where C is a proportionality factor. When m increases proportionally with radius, the line roughness defined by Equation (7.41) becomes

$$\begin{aligned} \rho &= 1 + \frac{hm}{2\pi r} \\ &= 1 + \frac{hC}{2\pi}. \end{aligned} \tag{7.63}$$

Substituting Equation (7.62) into the expression for A^{SL} in Equation (7.19) yields

$$\begin{aligned} A^{\mathrm{SL}} &= \pi a^2 + h\int_0^a Cr\,\mathrm{d}r \\ &= \left(1+\frac{hC}{2\pi}\right)\pi a^2. \end{aligned} \tag{7.64}$$

Substituting Equation (7.63) into (7.64) and using $A^{\mathrm{projected}} = \pi a^2$ gives, after rearranging,

$$\rho = \frac{A^{\mathrm{SL}}}{A^{\mathrm{projected}}} \equiv r_{\mathrm{f}}, \tag{7.65}$$

which means that $\rho = r_{\mathrm{f}}$ when the line roughness is constant with radius r and therefore, $\mathrm{d}A^{\mathrm{SL}} = r_{\mathrm{f}}\ \mathrm{d}A^{\mathrm{projected}}$ so that $\cos\theta = r_{\mathrm{f}}\cos\theta_{\mathrm{Y}}$.

7.4 Conclusions

Herein, we approached the derivation of the Wenzel equation with a rigorous entropy extremization subject to constraints from the framework of Gibbsian composite-system thermodynamics. We derived a Wenzel equation (Equation (7.42)) that uses a roughness factor evaluated at the contact line instead of the original ratio of areas ($r_{\mathrm{f}} = A^{\mathrm{SL}}/A^{\mathrm{projected}}$), together with additional terms that arise from the volume and liquid–vapor interfacial area within the surface asperities. Our roughness factor is a function of two variables: (*i*) the number of pillar heights at the three-phase contact line and (*ii*) the orientation of these pillar heights with respect to the contact line. Supposing there are no forces due to gravity or pinning, our line-roughness Wenzel equation may be used for a drop whose shape can be divided into a spherical cap and a partially-filled cylinder on a surface with vertical pillars of equal height. If there are any changes to the physical geometry of the liquid drop from that assumed in this chapter, the principal conclusion that the three-phase line dictates the contact angle will remain. This is due to the Leibniz rule being applied to any integral expression that calculates the surface area of the solid–liquid interface during the entropy extremization.

We highlight that our Gibbsian thermodynamic approach ensures that all equilibrium conditions are derived given explicitly defined constraints. For example, when vapor–liquid equilibrium is imposed on the system, the Young–Laplace equation and the line-roughness Wenzel equations need to both be satisfied for mechanical equilibrium. On the other hand, when the liquid volume is constrained to be constant, the Young–Laplace equation is not an equilibrium condition, but the line-roughness Wenzel equation is. To gain an understanding of the thermodynamic stability of systems satisfying our new Wenzel equation, we also performed

a free energy analysis. Under the constraint of satisfying the equality of chemical potential and the Young–Laplace equation for the considered single-component system (*i.e.*, in a state of vapor–liquid equilibrium) with a pressure imposed on the vapor phase, the obtained equilibrium state is unstable for each equilibrium contact angle. Under the constraint of constant liquid-phase volume, one stable and one unstable equilibrium state are obtained when $h\lambda_{\text{liquid}} > 0$, and one stable equilibrium state is obtained when $h\lambda_{\text{liquid}} = 0$. Physically, a constant liquid volume may arise, for example, when the liquid is non-volatile.

In our analysis, we also explicitly defined the assumptions required for our line-roughness Wenzel equation to limit to other forms of the Wenzel equation in the literature. When the contribution of the liquid between surface asperities is negligible (quantified by the dimensionless quantity $\mathrm{H} = h(1-\lambda_{\text{solid}})/R \ll 1$ and $\rho\cos\theta_{\mathrm{Y}}$ not approaching -1 or 1), our equation has the form $\cos\theta = \rho\,|_{r=R\cos\theta}\cos\theta_{\mathrm{Y}}$. When the roughness is orthogonal at all intersection points along the contact line, our equation limits to the line-ratio Wenzel equation derived by Xu [312]. When $\rho = r_{\mathrm{f}} = A^{\mathrm{SL}}/A^{\text{projected}}$, the original area-roughness Wenzel equation is obtained. Thus, the equation derived herein is the most general form of the Wenzel equation for the equilibrium contact angle of a three-phase system, where one of the phases is rough, rigid, and inert (a rough solid), subject to the defined constraints.

The derived line-roughness Wenzel equation has significant consequences for understanding natural substrates and for designing surfaces with desirable wetting properties, illustrating in a rigorous manner that properties at the three-phase contact line (orientation and number of pillar intersections) determine the contact angle instead of the solid–liquid interfacial area. The importance of the properties at the contact line is in agreement with our derived line-fraction Cassie–Baxter equation (Chapter 6), where we emphasized that an area mathematically transforms to a line when a differential change in area is considered under the extremization of entropy subject to defined constraints. Thus, in the limiting case that the line-fraction Cassie–Baxter equation is applied to a drop on a single-component solid phase and the line fraction is replaced by the line roughness, the line-roughness Wenzel equation is obtained (the same connection that was observed by Cassie and Baxter for the area versions of the equations). To design surfaces that will preferentially wet in either the Cassie–Baxter or Wenzel states, therefore, the properties at the contact line must be quantified and used in predicting the equilibrium contact angle.

Chapter 8

Conclusions

This work developed mathematical tools for predicting and controlling a broad range of multicomponent systems with interfacial curvature. More specifically, Part I proposed a new semi-empirical equation for calculating the surface tension of mixtures as a function of both composition and temperature. To implement this new equation, three steps were needed:

i. fitting coefficients were obtained to describe each pure component's surface tension as a function of temperature, whether retrieved from a database or determined by a fit to available experimental data;

ii. the critical composition of the mixture was calculated (a method for this calculation was developed using the Peng–Robinson equation of state); and

iii. semi-empirical parameters were obtained by fitting to experimental data of surface tension as a function of composition at one temperature.

The parameters obtained in step (*iii*) could be considered composition- and temperature-independent, and the predictions obtained using the proposed equation were compared to experimental measurements of surface tension for 31 systems, including subcritical aqueous mixtures, subcritical organic mixtures, and supercritical hydrocarbon mixtures (containing methane or carbon dioxide). Importantly, the predictions for the studied aqueous mixtures were the best out of five tested models over a wide range of compositions and temperatures, and the predictions for supercritical hydrocarbon mixtures had an accuracy comparable to those reported for computationally-intensive models based on statistical mechanics. The proposed model was also able to accurately predict the surface tension of a ternary mixture (methanol(1) + ethanol(2) + water(3) using only pure component data and coefficients obtained from binary mixtures each at a single temperature—no coefficients needed to be obtained from ternary data), illustrating its applicability to systems with more than two components.

Part II presented an activity-coefficient model for predicting the bubble and dew points of multicomponent systems with interfacial curvature for two cases: (*i*) given an imposed temperature and (*ii*) given an imposed vapor-phase pressure. Both ideal (methanol + ethanol) and nonideal (ethanol + water) mixtures were studied, and phase diagrams were calculated as a function of composition and radius of curvature. To produce substantial deviation in phase behavior, the radius of curvature needed to approach the nanoscale. When the curvature was toward the vapor phase (a bubble in a bulk liquid), bubble and dew pressures decreased, while bubble and dew temperatures increased. The opposite trend was observed when the curvature was toward the liquid phase (a droplet in a bulk vapor): the bubble and dew pressures increased, while bubble and dew temperatures decreased. In addition, a shift in liquid- and vapor-phase compositions was observed for both ideal and nonideal mixtures. In fact, in the studied nonideal mixture (ethanol + water), the composition of the azeotrope shifted with a change in interfacial curvature, and the azeotrope was predicted to no longer be present at high curvatures (a radius of curvature on the order of 10 nm for $T = 298$ K or $P^{\mathrm{V}} = 101$ kPa). In investigating case (*ii*), the surface tension model in Part I was used for calculating the surface tension of nitrogen + argon mixtures at temperatures beyond those available experimentally. The resulting vapor–liquid equilibrium calculations of dew temperature in pores with 2-nm radii were in agreement with independent experimental measurements when the geometries of adsorption and desorption in pores were accounted for and the surface tension model in Part I was used. These predictions for nitrogen + argon mixtures were made without any fitting parameters to pure-component vapor–liquid behavior in pores, and the accuracy of the predictions was sensitive to the magnitude of surface tension as a function of both composition and temperature.

In Part III, the wetting of liquids on rough or heterogeneous surfaces was investigated using Gibbsian composite-system thermodynamics. Equilibrium conditions for both the Cassie–Baxter and Wenzel states were derived by extremizing entropy while explicitly defining all physical and geometric constraints. By mathematically allowing the properties of the solid–liquid interface to vary, the derived mechanical equilibrium conditions for contact angle contained information from the contact line (due to the application of the Leibniz rule for differentiating integrals whose limits vary during the entropy extremization). This result is in contrast to previous derivations of the Cassie–Baxter and Wenzel equations that assume the properties at the solid–liquid–vapor contact line are the same as the properties of the whole solid–liquid interfacial area, and as a result, these area-based equations cannot be applied to drops on surfaces that do not satisfy this assumption. Part III of this thesis showed that a line-fraction Cassie–Baxter equation and a line-roughness Wenzel equation avoid the need for such an assumption, and these line-based equations should instead be used to describe equilibrium contact angles. Additionally, for the line-roughness Wenzel equation, a dimensionless parameter was proposed to quantify how large

a liquid drop must be compared to the liquid imbibed between asperities for the equilibrium equation that governs contact angle to be simplified.

The intertwining of the studied parts was demonstrated in a preliminary manner when the surface tension model developed in Part I was incorporated into phase diagram calculations in Part II. In many applications, all three parts would be relevant. For example, vapor–liquid equilibrium predictions of a system containing a nonideal multicomponent mixture in the presence of a porous medium with chemical heterogeneities or physical roughness may be needed for the design of nano- or microfluidic technologies. For making such predictions, the theoretical model might incorporate: the surface tension model from Part I, the interfacial-curvature activity coefficient model from Part II, and either the line-Wenzel or line-Cassie–Baxter equations from Part III. Taken together, the three parts presented in this thesis provided fundamental theoretical understanding of phenomena at the intersection of multicomponent, multiphase thermodynamics and interfacial thermodynamics.

References

[1] F. A. Abu Al-Rub, F. A. Banat, and R. Jumah. "Vapor–Liquid Equilibrium of Ethanol–Water System in the Presence of Molecular Sieves". *Separation Science and Technology* 34.12 (1999), pp. 2355–2368 (cited on p. 72).

[2] J. P. Acker, J. A. W. Elliott, and L. E. McGann. "Intercellular Ice Propagation: Experimental Evidence for Ice Growth Through Membrane Pores". *Biophysical Journal* 81.3 (2001), pp. 1389–97 (cited on p. 71).

[3] J. Ahlers and J. Gmehling. "Development of an Universal Group Contribution Equation of State: I. Prediction of Liquid Densities for Pure Compounds with a Volume Translated Peng–Robinson Equation of State". *Fluid Phase Equilibria* 191.1–2 (2001), pp. 177–188 (cited on pp. xx, 44).

[4] W. S. Ahn, M. S. Jhon, H. Pak, and S. Chang. "Surface Tension of Curved Surfaces". *Journal of Colloid and Interface Science* 38 (1972), pp. 605–608 (cited on p. 63).

[5] M. A. Alam, A. P. Clarke, and J. A. Duffy. "Capillary Condensation and Desorption of Binary Mixtures of N_2–Ar Confined in a Mesoporous Medium". *Langmuir* 16.20 (2000), pp. 7551–7553 (cited on pp. 38, 51, 88, 89).

[6] N. S. Alharthy, T. W. W. Teklu, T. N. Nguyen, H. Kazemi, and R. M. Graves. "Nanopore Compositional Modeling in Unconventional Shale Reservoirs". *SPE Reservoir Evaluation & Engineering* 19.3 (2016), pp. 415–428 (cited on p. 70).

[7] J. K. Ali. "Prediction of Parachors of Petroleum Cuts and Pseudocomponents". *Fluid Phase Equilibria* 95 (1994), pp. 383–398 (cited on pp. 12, 37).

[8] J. Ally, S. Molla, and F. Mostowfi. "Condensation in Nanoporous Packed Beds". *Langmuir* 32.18 (2016), pp. 4494–4499 (cited on p. 70).

[9] E. Álvarez, G. Vázquez, M. Sánchez-Vilas, B. Sanjurjo, and J. M. Navaza. "Surface Tension of Organic Acids + Water Binary Mixtures from 20 °C to 50 °C". *Journal of Chemical & Engineering Data* 42.5 (1997), pp. 957–960 (cited on pp. 19, 24, 26).

[10] E. Álvarez, Á. Cancela, R. Maceiras, J. M. Navaza, and R. Táboas. "Surface Tension of Aqueous Binary Mixtures of 1-Amino-2-propanol and 3-Amino-1-propanol, and Aqueous Ternary Mixtures of these Amines with Diethanolamine, Triethanolamine, and 2-Amino-2-methyl-1-propanol from (298.15 to 323.15) K". *Journal of Chemical & Engineering Data* 48.1 (2003), pp. 32–35 (cited on pp. 24, 26).

[11] E. Álvarez, R. Rendo, B. Sanjurjo, M. Sanchez-Vilas, and J. M. Navaza. "Surface Tension of Binary Mixtures of Water + *N*-Methyldiethanolamine and Ternary Mixtures of This Amine and Water with Monoethanolamine, Diethanolamine, and 2-Amino-2-methyl-1-propanol from 25 to 50 °C". *Journal of Chemical & Engineering Data* 43.6 (1998), pp. 1027–1029 (cited on pp. 19, 24, 26).

[12] R. Amin and T. N. Smith. "Interfacial Tension and Spreading Coefficient under Reservoir Conditions". *Fluid Phase Equilibria* 142 (1998), pp. 231–241 (cited on pp. 43, 45, 46, 48, 49).

[13] J. Aracil, G. Luengo, B. S. Almeida, M. M. Telo da Gama, R. G. Rubio, and M. Diaz Pena. "Surface Properties of Mixtures of Molecular Fluids: An Experimental and Theoretical Study of Carbon Disulfide + Dichloromethane and Carbon Disulfide + Carbon Tetrachloride". *The Journal of Physical Chemistry* 93 (1989), pp. 3210–3218 (cited on pp. 42, 43, 46, 48).

[14] M. Argyle and C. Bartholomew. "Heterogeneous Catalyst Deactivation and Regeneration: A Review". *Catalysts* 5.1 (2015), pp. 145–269 (cited on p. 3).

[15] A. Arzhavitina and H. Steckel. "Surface Active Drugs Significantly Alter the Drug Output Rate from Medical Nebulizers". *International Journal of Pharmaceutics* 384.1–2 (2010), pp. 128–136 (cited on p. 36).

[16] P. N. Aukett, N. Quirke, S. Riddiford, and S. R. Tennison. "Methane Adsorption on Microporous Carbons—A Comparison of Experiment, Theory, and Simulation". *Carbon* 30.6 (1992), pp. 913–924 (cited on p. 72).

[17] E. Aumann, L. M. Hildemann, and A. Tabazadeh. "Measuring and Modeling the Composition and Temperature-Dependence of Surface Tension for Organic Solutions". *Atmospheric Environment* 44.3 (2010), pp. 329–337 (cited on pp. 19, 36).

[18] A. Bagheri and K. Alizadeh. "How Do Temperature and Chemical Structure Affect Surface Properties of Aqueous Solutions of Carboxylic Acids?" *Colloids and Surfaces A: Physicochemical and Engineering Aspects* 467 (2015), pp. 78–88 (cited on pp. 21, 22, 31).

[19] V. G. Baidakov, A. M. Kaverin, and M. N. Khotienkova. “Surface Tension of Ethane–Methane Solutions: 1. Experiment and Thermodynamic Analysis of the Results”. *Fluid Phase Equilibria* 356 (2013), pp. 90–95 (cited on pp. 43, 45–47).

[20] V. G. Baidakov, A. M. Kaverin, and A. S. Pankov. “Nucleation in Liquid Ethane with Small Additions of Methane”. *Journal of Physical Chemistry C* 116.38 (2012), pp. 20458–20464 (cited on p. 36).

[21] E. Barsotti, S. P. Tan, S. Saraji, M. Piri, and J. H. Chen. “A Review on Capillary Condensation in Nanoporous Media: Implications for Hydrocarbon Recovery from Tight Reservoirs”. *Fuel* 184 (2016), pp. 344–361 (cited on pp. 70, 71).

[22] F. E. Bartell and J. W. Shepard. “Surface Roughness as Related to Hysteresis of Contact Angles. II. The Systems Paraffin-3 Molar Calcium Chloride Solution–Air and Paraffin–Glycerol–Air”. *The Journal of Physical Chemistry* 57.4 (1953), pp. 455–458 (cited on p. 113).

[23] D. Bastakoti, H. Zhang, D. Li, W. Cai, and F. Li. “An Overview on the Developing Trend of Pulsating Heat Pipe and its Performance”. *Applied Thermal Engineering* 141 (2018), pp. 305–332 (cited on p. 36).

[24] E. R. Becker and C. J. Pereira. *Computer-Aided Design of Catalysts*. Marcel Dekker, 1993 (cited on pp. 2, 3, 56, 71).

[25] G. C. Benson and V. T. Lam. “Surface Tensions of Binary Liquid Systems. II. Mixtures of Alcohols”. *Journal of Colloid and Interface Science* 38.2 (1972), pp. 294–301 (cited on p. 83).

[26] J. C. Berg. *An Introduction to Interfaces & Colloids: The Bridge to Nanoscience*. New Jersey: World Scientific, 2010, pp. 6, 50, 111 (cited on pp. 10, 67, 77, 88, 96, 99, 101, 117, 125).

[27] J. C. Berg. “Emulsions and Foams”. In: *An Introduction to Interfaces and Colloids: The Bridge to Nanoscience*. World Scientific Publishing, 2010, pp. 643–694 (cited on p. 19).

[28] J. Bico, U. Thiele, and D. Quéré. “Wetting of Textured Surfaces”. *Colloids and Surfaces A: Physicochemical and Engineering Aspects* 206.1–3 (2002), pp. 41–46 (cited on p. 107).

[29] M. Binggeli and C. M. Mate. “Influence of Capillary Condensation of Water on Nanotribology Studied by Force Microscopy”. *Applied Physics Letters* 65.4 (1994), pp. 415–417 (cited on pp. 3, 71).

[30] M. Blander, D. Hengstenberg, and J. L. Katz. "Bubble Nucleation in *n*-Pentane, *n*-Hexane, *n*-Pentane + Hexadecane Mixtures, and Water". *The Journal of Physical Chemistry* 75.23 (1971), pp. 3613–3619 (cited on p. 36).

[31] W. S. Bonnell, L. Byman, and D. B. Keyes. "Surface Tension of Ethyl Alcohol–Water Mixtures". *Industrial & Engineering Chemistry* 32 (1940), pp. 532–534 (cited on p. 64).

[32] E. Bormashenko. "A Variational Approach to Wetting of Composite Surfaces: Is Wetting of Composite Surfaces a One-Dimensional or Two-Dimensional Phenomenon?" *Langmuir* 25.18 (2009), pp. 10451–10454 (cited on pp. 15, 113).

[33] E. Bormashenko. "Why Does the Cassie–Baxter Equation Apply?" *Colloids and Surfaces A: Physicochemical and Engineering Aspects* 324.1–3 (2008), pp. 47–50 (cited on p. 107).

[34] H. C. Boyer and C. S. Dutcher. "Atmospheric Aqueous Aerosol Surface Tensions: Isotherm-Based Modeling and Biphasic Microfluidic Measurements". *Journal of Physical Chemistry A* 121.25 (2017), pp. 4733–4742 (cited on p. 36).

[35] B. Breure and C. J. Peters. "Modeling of the Surface Tension of Pure Components and Mixtures Using the Density Gradient Theory Combined with a Theoretically Derived Influence Parameter Correlation". *Fluid Phase Equilibria* 334 (2012), pp. 189–196 (cited on pp. 12, 36).

[36] J. R. Brock and R. B. Bird. "Surface Tension and the Principle of Corresponding States". *AIChE Journal* 1.2 (1955), pp. 174–177 (cited on p. 36).

[37] J. L. Brown. "Vapour–Liquid Equilibria within Nanoporous Media". PhD thesis. University of Cambridge, 2018 (cited on pp. 13, 36).

[38] F. P. Buff. "The Spherical Interface. I. Thermodynamics". *The Journal of Chemical Physics* 19 (1951), pp. 1591–1594 (cited on p. 56).

[39] N. M. Bukhavtsova and N. M. Ostrovskii. "Catalytic Reaction Accompanied by Capillary Condensation, 3. Influence on Reaction Kinetics and Dynamics". *Reaction Kinetics and Catalysis Letters* 65.2 (1998), pp. 321–329 (cited on pp. 3, 71).

[40] N. M. Bukhavtsova and N. M. Ostrovskii. "Kinetics of Catalyst Poisoning During Capillary Condensation of Reactants". *Kinetics and Catalysis* 43.1 (2002), pp. 81–88 (cited on pp. 3, 71).

[41] C. G. V. Burgess, D. H. Everett, and S. Nuttall. "Adsorption Hysteresis in Porous Materials". *Pure and Applied Chemistry* 61 (1989), pp. 1845–1852 (cited on p. 56).

[42] H.-J. Butt and M. Kappl. “Normal Capillary Forces”. *Advances in Colloid and Interface Science* 146 (2009), pp. 48–60 (cited on p. 56).

[43] H.-J. Butt, K. Graf, and M. Kappl. *Physics and Chemistry of Interfaces*. John Wiley & Sons, 2013 (cited on p. 11).

[44] J. T. Cabral and S. D. Hudson. “Microfluidic Approach for Rapid Multicomponent Interfacial Tensiometry”. *Lab on a Chip* 6.3 (2006), pp. 427–436 (cited on p. 71).

[45] J. W. Cahn and J. E. Hilliard. “Free Energy of a Nonuniform System. I. Interfacial Free Energy”. *The Journal of Chemical Physics* 28.2 (1958), pp. 258–267 (cited on p. 36).

[46] H. B. Callen. *Thermodynamics and an Introduction to Thermostatistics*. 2nd ed. John Wiley & Sons, Inc., 1985 (cited on pp. 4–6, 56, 74, 97, 99, 114).

[47] H. Cárdenas and A. Mejía. “Phase Behaviour and Interfacial Properties of Ternary System CO_2 + *n*-Butane + *n*-Decane: Coarse-Grained Theoretical Modelling and Molecular Simulations”. *Molecular Physics* 114.18 (2016), pp. 2627–2640 (cited on p. 36).

[48] J. Carmeliet, L. Chen, Q. Kang, and D. Derome. “Beyond-Cassie Mode of Wetting and Local Contact Angles of Droplets on Checkboard-Patterned Surfaces”. *Langmuir* 33.24 (2017), pp. 6192–6200 (cited on p. 108).

[49] A. B. D. Cassie and S. Baxter. “Wettability of Porous Surfaces”. *Transactions of the Faraday Society* 40 (1944), pp. 546–551 (cited on pp. 14, 96, 98, 112, 113).

[50] S. C. Chapra and R. P. Canale. “Approximations and Round-Off Errors”. In: *Numerical Methods for Engineers*. 6th ed. McGraw-Hill, 2010. Chap. 3, p. 58 (cited on p. 85).

[51] J.-H. Chen, A. Mehmani, B. Li, D. Georgi, and G. Jin. “Estimation of Total Hydrocarbon in the Presence of Capillary Condensation for Unconventional Shale Reservoirs”. In: *SPE Middle East Oil and Gas Show and Conference*. Society of Petroleum Engineers, 2013, pp. 1–10 (cited on p. 71).

[52] W. J. Cheong and P. W. Carr. “The Surface Tension of Mixtures of Methanol, Acetonitrile, Tetrahydrofuran, Isopropanol, Tertiary Butanol and Dimethyl Sulfoxide with Water at 25 °C”. *Journal of Liquid Chromatography* 10.4 (1987), pp. 561–581 (cited on p. 19).

[53] H. Cho, M. H. Bartl, and M. Deo. “Bubble Point Measurements of Hydrocarbon Mixtures in Mesoporous Media”. *Energy & Fuels* 31.4 (2017), pp. 3436–3444 (cited on p. 71).

[54] W. Choi, A. Tuteja, J. M. Mabry, R. E. Cohen, and G. H. McKinley. “A Modified Cassie–Baxter Relationship to Explain Contact Angle Hysteresis and Anisotropy on Non-wetting Textured Surfaces”. *Journal of Colloid and Interface Science* 339.1 (2009), pp. 208–216 (cited on p. 98).

[55] H. K. Christenson. “Capillary Condensation in Systems of Immiscible Liquids”. *Journal of Colloid and Interface Science* 104 (1985), pp. 234–249 (cited on p. 56).

[56] L. Chunxi, W. Wenchuan, and W. Zihao. “A Surface Tension Model for Liquid Mixtures Based on the Wilson Equation”. *Fluid Phase Equilibria* 175 (2000), pp. 185–196 (cited on pp. xx, xxi, xxv, 19–21, 28, 36, 37, 40, 83).

[57] C. L. Cipolla, E. P. Lolon, J. C. Erdle, and B. Rubin. “Reservoir Modeling in Shale Gas Reservoirs”. *SPE Reservoir Evaluation & Engineering* 13.4 (2010), pp. 638–653 (cited on p. 70).

[58] B. Coasne, J. Czwartos, M. Sliwinska-Bartkowiak, and K. E. Gubbins. “Effect of Pressure on the Freezing of Pure Fluids and Mixtures Confined in Nanopores”. *Journal of Physical Chemistry B* 113.42 (2009), pp. 13874–13881 (cited on p. 72).

[59] B. Coasne, J. Czwartos, K. E. Gubbins, F. R. Hung, and M. Sliwinska-Bartkowiak. “Freezing of Mixtures Confined in a Slit Nanopore”. *Adsorption* 11 (2005), pp. 301–306 (cited on p. 72).

[60] L. H. Cohan. “Sorption Hysteresis and the Vapor Pressure of Concave Surfaces”. *Journal of the American Chemical Society* 60 (1938), pp. 433–435 (cited on pp. 56, 88).

[61] N. L. Coleburn and J. L. Shereshefsky. “Liquid–Vapor Equilibrium in Microscopic Capillaries”. *Journal of Colloid and Interface Science* 38 (1972), pp. 84–90 (cited on p. 56).

[62] K. A. Connors and S. Mecozzi. “Surfaces and Interfaces”. In: *Thermodynamics of Pharmaceutical Systems: An Introduction to Theory and Applications*. 2nd ed. John Wiley & Sons, 2010. Chap. 11, pp. 201–208 (cited on pp. 19, 36, 96).

[63] K. A. Connors and J. L. Wright. “Dependence of Surface Tension on Composition of Binary Aqueous–Organic Solutions”. *Analytical Chemistry* 61.3 (1989), pp. 194–198 (cited on pp. xxii, 12, 19, 21, 36, 37, 40, 83).

[64] P. M. W. Cornelisse, C. J. Peters, and J. de Swaan Arons. “Application of the Peng–Robinson Equation of State to Calculate Interfacial Tensions and Profiles at Vapour–Liquid Interfaces”. *Fluid Phase Equilibria* 82.1 (1993), pp. 119–129 (cited on pp. 12, 36).

[65] T. Cubaud and M. Fermigier. “Advancing Contact Lines on Chemically Patterned Surfaces”. *Journal of Colloid and Interface Science* 269.1 (2004), pp. 171–177 (cited on pp. 15, 96).

[66] C. Cumicheo, M. Cartes, E. A. Müller, and A. Mejía. “Experimental Measurements and Theoretical Modeling of High-Pressure Mass Densities and Interfacial Tensions of Carbon Dioxide + *n*-Heptane + Toluene and its Carbon Dioxide Binary Systems”. *Fuel* 228.April (2018), pp. 92–102 (cited on pp. 12, 36).

[67] J. E. Curry and H. K. Christenson. “Adsorption, Wetting, and Capillary Condensation of Nonpolar Fluids in Mica Slits”. *Langmuir* 12 (1996), pp. 5729–5735 (cited on p. 56).

[68] J. Czwartos, B. Coasne, K. E. Gubbins, F. R. Hung, and M. Sliwinska-Bartkowiak. “Freezing and Melting of Azeotropic Mixtures Confined in Nanopores: Experiment and Molecular Simulation”. *Molecular Physics* 103.21–23 (2005), pp. 3103–3113 (cited on p. 72).

[69] J. Daehwan, K. Dongjo, and M. Jooho. “Influence of Fluid Physical Properties on Ink-Jet Printability”. *Langmuir* 25.14 (2009), pp. 2629–2635 (cited on p. 36).

[70] R. Defay, I. Prigogine, and A. Bellemans. *Surface Tension and Adsorption*. Trans. by D. H. Everett. London: Longmans, 1966, pp. 168, 280 (cited on pp. 2, 12, 63, 68, 71, 72, 83, 90).

[71] Design Institute for Physical Properties, Sponsored by AIChE. “DIPPR Project 801 - Full Version” (2016) (cited on pp. 81, 82).

[72] Design Institute for Physical Properties, Sponsored by AIChE. “DIPPR Project 801 - Full Version” (2019) (cited on pp. 44, 52).

[73] D. Devegowda, K. Sapmanee, F. Civan, and R. Sigal. “Phase Behavior of Gas Condensates in Shales Due to Pore Proximity Effects: Implications for Transport, Reserves and Well Productivity”. In: *SPE Annual Technical Conference and Exhibition*. Society of Petroleum Engineers, 2012, pp. 1–22 (cited on p. 70).

[74] C. Diddens, H. Tan, P. Lv, M. Versluis, J. G. M. Kuerten, X. Zhang, and D. Lohse. “Evaporating Pure, Binary and Ternary Droplets: Thermal Effects and Axial Symmetry Breaking”. *Journal of Fluid Mechanics* 823 (2017), pp. 470–497 (cited on p. 36).

[75] A. Dinsmore, M. F. Hsu, M. Nikolaides, M. Marquez, A. Bausch, and D. Weitz. “Colloidosomes: Selectively Permeable Capsules Composed of Colloidal Particles”. *Science* 298.5595 (2002), pp. 1006–1009 (cited on p. 3).

[76] M. D. Donohue and G. L. Aranovich. “Adsorption Hysteresis in Porous Solids”. *Journal of Colloid and Interface Science* 205 (1998), pp. 121–30 (cited on p. 89).

[77] J. A. W. Elliott. “On the Complete Kelvin Equation”. *Chemical Engineering Education* 35 (2001), pp. 274–278 (cited on pp. 10, 56).

[78] J. R. Elliott and C. T. Lira. *Introductory Chemical Engineering Thermodynamics*. Upper Saddle River: Prentice-Hall Inc., 2012, pp. 350, 373, 401, 403, 425 (cited on pp. 9, 58, 59, 73, 77, 80).

[79] J. A. W. Elliott and O. Voitcu. “On the Thermodynamic Stability of Liquid Capillary Bridges”. *The Canadian Journal of Chemical Engineering* 85.5 (2007), pp. 692–700 (cited on pp. 56, 97, 114, 128–130).

[80] S. Enders and H. Kahl. “Interfacial Properties of Water + Alcohol Mixtures”. *Fluid Phase Equilibria* 263 (2008), pp. 160–167 (cited on p. 36).

[81] R. Eötvös. “Ueber den Zusammenhang der Oberflächenspannung der Flüssigkeiten mit ihrem Molecularvolumen”. *Annalen der Physik* 263.3 (1886), pp. 448–459 (cited on pp. 19, 36).

[82] H. Y. Erbil. “The Debate on the Dependence of Apparent Contact Angles on Drop Contact Area or Three-Phase Contact Line: A Review”. *Surface Science Reports* 69.4 (2014), pp. 325–365 (cited on pp. 15, 96, 113).

[83] J. Escobedo and G. A. Mansoori. “Surface-Tension Prediction for Liquid Mixtures”. *AIChE Journal* 44.10 (1998), pp. 2324–2332 (cited on p. 37).

[84] F. Eslami and J. A. W. Elliott. “Design of Microdrop Concentrating Processes”. *Journal of Physical Chemistry B* 117.7 (2013), pp. 2205–2214 (cited on pp. 19, 36, 56).

[85] F. Eslami and J. A. W. Elliott. “Role of Precipitating Solute Curvature on Microdrops and Nanodrops During Concentrating Processes: The Nonideal Ostwald–Freundlich Equation”. *Journal of Physical Chemistry B* 118.50 (2014), pp. 14675–14686 (cited on pp. 19, 36, 56).

[86] F. Eslami and J. A. W. Elliott. “Stability Analysis of Microdrops During Concentrating Processes”. *Journal of Physical Chemistry B* 118.13 (2014), pp. 3630–3641 (cited on pp. 19, 36, 56).

[87] F. Eslami and J. A. W. Elliott. “Thermodynamic Investigation of the Barrier for Heterogeneous Nucleation on a Fluid Surface in Comparison with a Rigid Surface”. *Journal of Physical Chemistry B* 115.36 (2011), pp. 10646–10653 (cited on pp. 10, 11, 19, 56, 71, 74, 97, 101, 105, 114, 117, 125, 128–130, 132).

[88] R. O. Espósito, F. W. Tavares, and M. Castier. “Phase Equilibrium Calculations for Confined Fluids, Including Surface Tension Prediction Models”. *Brazilian Journal of Chemical Engineering* 22 (2005), pp. 93–104 (cited on pp. 2, 3, 56).

[89] R. Evans. “Fluids Adsorbed in Narrow Pores: Phase Equilibria and Structure”. *Journal of Physics: Condensed Matter* 2.46 (1990), pp. 8989–9007 (cited on p. 72).

[90] C. W. Extrand. “Contact Angles and Hysteresis on Surfaces with Chemically Heterogeneous Islands”. *Langmuir* 19.9 (2003), pp. 3793–3796 (cited on pp. 15, 96, 112).

[91] C. W. Extrand. “Model for Contact Angles and Hysteresis on Rough and Ultraphobic Surfaces”. *Langmuir* 18.21 (2002), pp. 7991–7999 (cited on pp. 98, 114).

[92] M. H. Factorovich, V. Molinero, and D. A. Scherlis. “Vapor Pressure of Water Nanodroplets”. *Journal of the American Chemical Society* 136.12 (2014), pp. 4508–4514 (cited on p. 71).

[93] K. I. Falk, B. A. Coasne, and R. J.-M. Pellenq. “Effect of Temperature on Adsorption of Mixtures in Porous Materials”. *Molecular Simulation* 40 (2014), pp. 45–51 (cited on p. 72).

[94] J. R. Fanchi. “Calculation of Parachors for Compositional Simulation: An Update”. *SPE Reservoir Engineering* 5.3 (2007), pp. 433–436 (cited on p. 36).

[95] G. Fang, W. Li, X. Wang, and G. Qiao. “Droplet Motion on Designed Microtextured Superhydrophobic Surfaces with Tunable Wettability”. *Langmuir* 24.20 (2008), pp. 11651–11660 (cited on p. 112).

[96] A. Ferguson. “Relations Between Thermo-Physical Properties”. *Proceedings of the Physical Society* 52 (1940), pp. 759–763 (cited on p. 81).

[97] T. Firincioglu. “Bubble Point Suppression in Unconventional Liquids Rich Reservoirs and its Impact on Oil Production”. PhD thesis. Colorado School of Mines, 2013 (cited on pp. 2, 3, 56, 70).

[98] A. Firoozabadi. *Thermodynamics and Applications in Hydrocarbon Energy Production*. McGraw-Hill Education, 2016 (cited on pp. 36, 39).

[99] L. R. Fisher, R. A. Gamble, and J. Middlehurst. “The Kelvin Equation and the Capillary Condensation of Water”. *Nature* 290 (1981), pp. 575–576 (cited on pp. 11, 56).

[100] L. R. Fisher and J. N. Israelachvili. “Direct Experimental Verification of the Kelvin Equation for Capillary Condensation”. *Nature* 277 (1979), pp. 548–549 (cited on p. 56).

[101] L. R. Fisher and J. N. Israelachvili. “Experimental Studies on the Applicability of the Kelvin Equation to Highly Curved Concave Menisci”. *Journal of Colloid and Interface Science* 80 (1981), pp. 528–541 (cited on pp. 11, 56).

[102] P. S. Forsberg, C. Priest, M. Brinkmann, R. Sedev, and J. Ralston. "Contact Line Pinning on Microstructured Surfaces for Liquids in the Wenzel State". *Langmuir* 26.2 (2010), pp. 860–865 (cited on p. 114).

[103] L. Gao and T. J. McCarthy. "How Wenzel and Cassie Were Wrong". *Langmuir* 23.7 (2007), pp. 3762–3765 (cited on pp. 15, 96, 112, 113, 128).

[104] J. M. Garrido and I. Polishuk. "Toward Development of a Universal CP-PC-SAFT-Based Modeling Framework for Predicting Thermophysical Properties at Reservoir Conditions: Inclusion of Surface Tensions". *Industrial & Engineering Chemistry Research* 57.26 (2018), pp. 8819–8831 (cited on p. 36).

[105] L. D. Gelb, K. E. Gubbins, R. Radhakrishnan, and M. Sliwinska-Bartkowiak. "Phase Separation in Confined Systems". *Reports on Progress in Physics* 62 (1999), pp. 1573–1659 (cited on pp. 71, 72).

[106] P.-G. de Gennes, F. Brochard-Wyart, and D. Quéré. *Capillarity and Wetting Phenomena: Drops, Bubbles, Pearls, Waves*. Springer Science & Business Media, 2004 (cited on pp. 19, 96).

[107] H. Ghahremani, A. Moradi, J. Abedini-Torghabeh, and S. M. Hassani. "Measuring Surface Tension of Binary Mixtures of Water + Alcohols from the Diffraction Pattern of Surface Ripples". *Der Chemica Sinica* 2 (2011), pp. 212–221 (cited on p. 64).

[108] J. W. Gibbs. "On the Equilibrium of Heterogeneous Substances. *Trans. Conn. Acad. 3* (1876), pp. 108–248 and (1878), pp. 343–524." In: *The Scientific Papers of J. Willard Gibbs*. Ox Bow Press, 1993, pp. 55–353 (cited on pp. 1, 4, 10, 56, 63, 74, 97, 99, 100, 114, 115, 132).

[109] G. J. Gloor, G. Jackson, F. J. Blas, E. Martín Del Río, and E. De Miguel. "Prediction of the Vapor–Liquid Interfacial Tension of Nonassociating and Associating Fluids with the SAFT-VR Density Functional Theory". *Journal of Physical Chemistry C* 111.43 (2007), pp. 15513–15522 (cited on p. 36).

[110] J. Gmehling, U. Onken, and W. Arlt. *Vapor–Liquid Equilibrium Data Collection: Aqueous–Organic Systems (Supplement 1)*. Frankfurt: DECHEMA, 1981 (cited on pp. 64, 79, 83).

[111] R. J. Good. "A Thermodynamic Derivation of Wenzel's Modification of Young's Equation for Contact Angles; Together with a Theory of Hysteresis". *Journal of the American Chemical Society* 74.20 (1952), pp. 5041–5042 (cited on p. 113).

[112] S. J. Gregg and K. S. W. Sing. *Adsorption, Surface Area and Porosity*. 2nd ed. Academic Press, 1982 (cited on p. 88).

[113] N. Gudris and L. Kulikova. “Die Verdampfung kleiner Wassertropfen”. *Zeitschrift für Physik* 25 (1924), pp. 121–132 (cited on p. 56).

[114] E. A. Guggenheim. “The Principle of Corresponding States”. *The Journal of Chemical Physics* 13.7 (1945), pp. 253–261 (cited on pp. 19, 36, 81).

[115] R. Gupta, J. Shea, C. Scafe, A. Shurlygina, and N. Rapoport. “Polymeric Micelles and Nanoemulsions as Drug Carriers: Therapeutic Efficacy, Toxicity, and Drug Resistance”. *Journal of Controlled Release* 212 (2015), pp. 70–77 (cited on p. 71).

[116] L. Haar, J. S. Gallagher, and G. S. Kell. *NBS/NRC Steam Tables: Thermodynamic and Transport Properties and Computer Programs for Vapor and Liquid States of Water in SI Units*. Washington: Hemisphere, 1984 (cited on p. 64).

[117] J. Haneveld, N. R. Tas, N. Brunets, H. V. Jansen, and M. Elwenspoek. “Capillary Filling of Sub-10nm Nanochannels”. *Journal of Applied Physics* 104.1 (2008), p. 014309 (cited on p. 71).

[118] G. S. Heffelfinger, Z. Tan, K. E. Gubbins, U. M. B. Marconi, and F. V. Swol. “Lennard–Jones Mixtures in a Cylindrical Pore. A Comparison of Simulation and Density Functional Theory”. *Molecular Simulation* 2.4–6 (1989), pp. 393–411 (cited on p. 72).

[119] L. Herrmann. “Untersuchung von Struktur und Grenzflächeneigenschaften binärer Systeme”. PhD thesis. Martin-Luther-Universität Halle-Wittenberg, 1994 (cited on pp. 42, 43, 46).

[120] M. J. Hey and J. G. Kingston. “The Apparent Contact Angle for a Nearly Spherical Drop on a Heterogeneous Surface”. *Chemical Physics Letters* 447.1–3 (2007), pp. 44–48 (cited on pp. 15, 97, 107, 109, 112).

[121] T. L. Hill. *An Introduction to Statistical Thermodynamics*. New York: Dover Publications, Inc., 1986, pp. 49–51, 169 (cited on p. 5).

[122] B. C. Hoke and E. F. Patton. “Surface Tensions of Propylene Glycol + Water”. *Journal of Chemical & Engineering Data* 37.3 (1992), pp. 331–333 (cited on pp. 19, 23, 24, 26).

[123] B. C. Hoke and J. C. Chen. “Binary Aqueous–Organic Surface Tension Temperature Dependence”. *Journal of Chemical & Engineering Data* 36.5 (1991), pp. 322–326 (cited on p. 19).

[124] S. Honary and F. Zahir. “Effect of Zeta Potential on the Properties of Nano-Drug Delivery Systems—A Review (Part 1)”. *Tropical Journal of Pharmaceutical Research* 12.2 (2013), pp. 255–264 (cited on p. 71).

[125] J. Hong, J. B. Edel, and A. J. Demello. “Micro- and Nanofluidic Systems for High-Throughput Biological Screening”. *Drug Discovery Today* 14.3-4 (2009), pp. 134–146 (cited on p. 3).

[126] T. Horikawa, D. D. Do, and D. Nicholson. “Capillary Condensation of Adsorbates in Porous Materials”. *Advances in Colloid and Interface Science* 169 (2011), pp. 40–58 (cited on pp. 56, 71).

[127] J. J.-C. Hsu, N. Nagarajan, and R. L. Robinson. “Equilibrium Phase Compositions, Phase Densities, and Interfacial Tensions for CO_2 + Hydrocarbon Systems. 1. CO_2 + *n*-Butane”. *Journal of Chemical & Engineering Data* 30 (1985), pp. 485–491 (cited on pp. 43, 44, 46, 47).

[128] C. Huh and S. G. Mason. “Effects of Surface Roughness on Wetting (Theoretical)”. *Journal of Colloid and Interface Science* 60.1 (1977), pp. 11–38 (cited on p. 113).

[129] R. J. Hunter. “Thermodynamics of Surfaces”. In: *Introduction to Modern Colloid Science*. Oxford University Press, 2002. Chap. 5, p. 140 (cited on pp. 99, 115).

[130] P. T. Jaeger, M. B. Alotaibi, and H. A. Nasr-El-Din. “Influence of Compressed Carbon Dioxide on the Capillarity of the Gas–Crude Oil–Reservoir Water System”. *Journal of Chemical & Engineering Data* 55.11 (2010), pp. 5246–5251 (cited on pp. 44, 46).

[131] Z. Jin and A. Firoozabadi. “Thermodynamic Modeling of Phase Behavior in Shale Media”. *SPE Journal* (2016), pp. 190–207 (cited on p. 36).

[132] J. F. Joanny and P. G. de Gennes. “A Model for Contact Angle Hysteresis”. *The Journal of Chemical Physics* 81.1 (1984), pp. 552–562 (cited on pp. 98, 114).

[133] R. E. Johnson and R. H. Dettre. “Contact Angle Hysteresis. III. Study of an Idealized Heterogeneous Surface”. *The Journal of Physical Chemistry* 68.7 (1964), pp. 1744–1750 (cited on pp. 14, 98, 113, 132–135).

[134] D. G. Jones and H. M. Fretwell. “Condensation and Freezing of a Binary Gas Mixture Adsorbed in Mesoporous Vycor Glass”. *Langmuir* 19.21 (2003), pp. 9018–9022 (cited on p. 88).

[135] F. Jufu, L. Buqiang, and W. Zihao. “Estimation of Fluid–Fluid Interfacial Tensions of Multicomponent Mixtures”. *Chemical Engineering Science* 41.10 (1986), pp. 2673–2679 (cited on pp. 36, 37).

[136] A. S. Kabalnov, A. V. Pertzov, and E. D. Shchukin. “Ostwald Ripening in Two-Component Disperse Phase Systems: Application to Emulsion Stability”. *Colloids and Surfaces* 24 (1987), pp. 19–32 (cited on p. 56).

[137] W. Kaplan. “Integral Calculus of Functions of Several Variables”. In: *Advanced Calculus*. 4th ed. Addison-Wesley, 1991. Chap. 4, p. 267 (cited on pp. 106, 121).

[138] G. Kaptay. “The Gibbs Equation versus the Kelvin and the Gibbs–Thomson Equations to Describe Nucleation and Equilibrium of Nano-materials”. *Journal of Nanoscience and Nanotechnology* 12 (2012), pp. 1–9 (cited on p. 56).

[139] T. Karbowiak, F. Debeaufort, and A. Voilley. “Importance of Surface Tension Characterization for Food, Pharmaceutical and Packaging Products: A Review”. *Critical Reviews in Food Science and Nutrition* 46.5 (2006), pp. 391–407 (cited on p. 36).

[140] S. E. Kharin, A. A. Kniga, and G. S. Sorokina. “Surface Tension of Water–Ethanol–Methanol Solutions”. *Izvestiya Vysshikh Uchebnykh Zavedenii Khimiya i Khimicheskaya Tekhnologiya* 12 (1968), pp. 1341–1344 (cited on pp. iv, 35, 49, 50).

[141] I. S. Khattab, F. Bandarkar, M. A. A. Fakhree, and A. Jouyban. “Density, Viscosity, and Surface Tension of Water + Ethanol Mixtures from 293 to 323 K”. *Korean Journal of Chemical Engineering* 29 (2012), pp. 812–817 (cited on p. 64).

[142] H. Kim and H. A. Stone. “Direct Measurement of Selective Evaporation of Binary Mixture Droplets by Dissolving Materials”. *Journal of Fluid Mechanics* 850 (2018), pp. 769–783 (cited on p. 36).

[143] H. Kister. *Distillation Design*. New York: McGraw-Hill Education, 1992 (cited on p. 56).

[144] C. Klink, B. Planková, and J. Gross. “Density Functional Theory for Liquid–Liquid Interfaces of Mixtures Using the Perturbed-Chain Polar Statistical Associating Fluid Theory Equation of State”. *Industrial & Engineering Chemistry Research* 54.16 (2015), pp. 4633–4642 (cited on pp. 12, 36, 41, 48).

[145] B. M. L. Koch, A. Amirfazli, and J. A. W. Elliott. “Modeling and Measurement of Contact Angle Hysteresis on Textured High-Contact-Angle Surfaces”. *Journal of Physical Chemistry C* 118.32 (2014), pp. 18554–18563 (cited on pp. 19, 98, 110, 114).

[146] B. M. L. Koch, A. Amirfazli, and J. A. W. Elliott. “Wetting of Rough Surfaces by a Low Surface Tension Liquid”. *Journal of Physical Chemistry C* 118.41 (2014), pp. 23777–23782 (cited on pp. 19, 110, 114).

[147] B. M. L. Koch, J. A. W. Elliott, and A. Amirfazli. “Study of Model Superoleophobic Surfaces Fabricated with a Modified Bosch Etch Method”. *Langmuir* 30.46 (2014), pp. 14039–14047 (cited on pp. 19, 110).

[148] K. Koch, B. Dew, T. E. Corcoran, T. M. Przybycien, R. D. Tilton, and S. Garoff. "Surface Tension Gradient Driven Spreading on Aqueous Mucin Solutions: A Possible Route to Enhanced Pulmonary Drug Delivery". *Molecular Pharmaceutics* 8.2 (2011), pp. 387–394 (cited on p. 36).

[149] M. M. Kohonen, N. Maeda, and H. K. Christenson. "Kinetics of Capillary Condensation in a Nanoscale Pore". *Physical Review Letters* 82.23 (1999), pp. 4667–4670 (cited on pp. 3, 71).

[150] M. M. Kohonen and H. K. Christenson. "Capillary Condensation from Vapors of *n*-Hexane/Perfluoro-*n*-hexane Mixtures". *Journal of Physical Chemistry B* 106 (2002), pp. 6685–6695 (cited on p. 56).

[151] B. Konobeev and V. Lyapin. "Density, Viscosity, and Surface Tension of Some Binary Systems". *Zhurnal Prikladnoi Khimii* 43.4 (1970), p. 803 (cited on p. 46).

[152] M. Kruk, M. Jaroniec, and A. Sayari. "Application of Large Pore MCM-41 Molecular Sieves to Improve Pore Size Analysis Using Nitrogen Adsorption Measurements". *Langmuir* 13.23 (1997), pp. 6267–6273 (cited on p. 71).

[153] A. E. Kuchma and A. K. Shchekin. "Multicomponent Condensation on the Nucleation Stage". *The Journal of Chemical Physics* 150.5 (2019) (cited on p. 36).

[154] V. K. La Mer and R. Gruen. "A Direct Test of Kelvin's Equation Connecting Vapour Pressure and Radius of Curvature". *Transactions of the Faraday Society* 48 (1952), pp. 410–415 (cited on pp. 11, 56).

[155] M. Lago, R. Martin, and M. Araujo. "Liquid–Vapor Isotherm in a Closed Single-Component System with Curved Interfaces". *Journal of Colloid and Interface Science* 267 (2003), pp. 429–444 (cited on pp. 56, 71).

[156] V. T. Lam and G. C. Benson. "Surface Tension of Binary Liquid Systems I. Mixtures of Nonelectrolytes". *Canadian Journal of Chemistry* 48.24 (1970), pp. 3773–3781 (cited on p. 46).

[157] P. M. Larsen, B. Maribo-Mogensen, and G. M. Kontogeorgis. "A Collocation Method for Surface Tension Calculations with the Density Gradient Theory". *Fluid Phase Equilibria* 408 (2016), pp. 170–179 (cited on pp. 12, 37).

[158] S. T. Larsen and R. Taboryski. "A Cassie-like Law Using Triple Phase Boundary Line Fractions for Faceted Droplets on Chemically Heterogeneous Surfaces". *Langmuir* 25.3 (2009), pp. 1282–1284 (cited on pp. 15, 96).

[159] M. Lazaridis, Ø. Hov, and K. Eleftheriadis. “Heterogeneous Nucleation on Rough Surfaces: Implications to Atmospheric Aerosols”. *Atmospheric Research* 55 (2000), pp. 103–113 (cited on p. 96).

[160] P. P. H. Le Brun, A. H. de Boer, H. G. M. Heijerman, and H. W. Frijlink. “A Review of the Technical Aspects of Drug Nebulization”. *Pharmacy World & Science* 22.3 (2000), pp. 75–81 (cited on p. 36).

[161] H. H. Lee, K. S. Chou, and K. C. Huang. “Inkjet Printing of Nanosized Silver Colloids”. *Nanotechnology* 16.10 (2005), pp. 2436–2441 (cited on p. 36).

[162] W. G. Lee, Y.-G. Kim, B. G. Chung, U. Demirci, and A. Khademhosseini. “Nano/Microfluidics for Diagnosis of Infectious Diseases in Developing Countries”. *Advanced Drug Delivery Reviews* 62.4-5 (2010), pp. 449–457 (cited on p. 3).

[163] E. W. Lemmon and S. G. Penoncello. “The Surface Tension of Air and Air Component Mixtures”. *Advances in Cryogenic Engineering* 39 (1994), pp. 1927–1934 (cited on pp. 81, 82).

[164] E. R. Lewis. “The Effect of Surface Tension (Kelvin Effect) on the Equilibrium Radius of a Hygroscopic Aqueous Aerosol Particle”. *Journal of Aerosol Science* 37 (2006), pp. 1605–1617 (cited on pp. 2, 56).

[165] D. Li, F. Y. Lin, and A. W. Neumann. “Effect of Corrugations of the Three-Phase Line on the Drop Size Dependence of Contact Angles”. *Journal of Colloid and Interface Science* 142.1 (1991), pp. 224–231 (cited on p. 110).

[166] Y. F. Li, Y. X. Yu, Y. X. Zheng, and J. D. Li. “Shift of the Azeotropic Point of Binary Lennard–Jones Mixtures Confined in a Slit-like Pore”. *Fluid Phase Equilibria* 292.1–2 (2010), pp. 110–116 (cited on p. 72).

[167] Z. Li and A. Firoozabadi. “Interfacial Tension of Nonassociating Pure Substances and Binary Mixtures by Density Functional Theory Combined with Peng–Robinson Equation of State”. *The Journal of Chemical Physics* 130 (2009), p. 154108 (cited on pp. 12, 36, 48).

[168] X. Liang, M. L. Michelsen, and G. M. Kontogeorgis. “A Density Gradient Theory Based Method for Surface Tension Calculations”. *Fluid Phase Equilibria* 428 (2016), pp. 153–163 (cited on p. 36).

[169] D. R. Lide and H. V. Kehiaian. *CRC Handbook of Thermophysical and Thermochemical Data*. Boca Raton: CRC Press, 1994 (cited on pp. 64, 81).

[170] H. Lin, Y. Y. Duan, and J. T. Zhang. “Simplified Gradient Theory Modeling of the Surface Tension for Binary Mixtures”. *International Journal of Thermophysics* 29.1 (2008), pp. 423–433 (cited on pp. 12, 36, 37, 41, 48).

[171] F. Liu, L. Zargarzadeh, H.-J. Chung, and J. A. W. Elliott. “Thermodynamic Investigation of the Effect of Interface Curvature on Solid–Liquid Equilibrium and Eutectic Point of Binary Mixtures”. *Journal of Physical Chemistry B* 121 (2017), pp. 9452–9462 (cited on pp. 71, 97, 114).

[172] T. L. Liu, Z. Chen, and C.-J. Kim. “A Dynamic Cassie–Baxter model”. *Soft Matter* 11.8 (2015), pp. 1589–1596 (cited on pp. 98, 110).

[173] X. Liu, L. Wang, Y. Qiao, X. Sun, S. Ma, X. Cheng, W. Qi, W. Huang, and Y. Li. “Adhesion of Liquid Food to Packaging Surfaces: Mechanisms, Test Methods, Influencing Factors and Anti-adhesion Methods”. *Journal of Food Engineering* 228 (2018), pp. 102–117 (cited on p. 36).

[174] Y. Liu, H. A. Li, and R. Okuno. “Phase Behavior of Fluid Mixtures in a Partially Confined Space”. In: *SPE Annual Technical Conference and Exhibition*. 2016, pp. 1–26 (cited on p. 70).

[175] F. Llovell, A. Galindo, F. J. Blas, and G. Jackson. “Classical Density Functional Theory for the Prediction of the Surface Tension and Interfacial Properties of Fluids Mixtures of Chain Molecules Based on the Statistical Associating Fluid Theory for Potentials of Variable Range”. *The Journal of Chemical Physics* 133.2 (2010), p. 024704 (cited on pp. 12, 36).

[176] G. Luengo, J. Aracil, R. G. Rubio, and M. Diaz Pena. “Bulk and Surface Thermodynamic Properties in Mixtures of Small Rigid Molecules: The Carbon Tetrachloride + Carbon Disulfide System”. *The Journal of Physical Chemistry* 92 (1988), pp. 228–234 (cited on pp. 42, 43, 46).

[177] S. Luo, J. L. Lutkenhaus, and H. Nasrabadi. “Confinement-Induced Supercriticality and Phase Equilibria of Hydrocarbons in Nanopores”. *Langmuir* 32.44 (2016), pp. 11506–11513 (cited on p. 70).

[178] S. Luo, H. Nasrabadi, and J. L. Lutkenhaus. “Effect of Confinement on the Bubble Points of Hydrocarbons in Nanoporous Media”. *AIChE Journal* 62.5 (2016), pp. 1772–1780 (cited on p. 3).

[179] D. B. Macleod. “On a Relation Between Surface Tension and Density”. *Transactions of the Faraday Society* 19 (1923), pp. 38–41 (cited on p. 36).

[180] Y. Maham and A. E. Mather. “Surface Thermodynamics of Aqueous Solutions of Alkyl-ethanolamines”. *Fluid Phase Equilibria* 182.1–2 (2001), pp. 325–336 (cited on p. 19).

[181] A. Marmur and E. Bittoun. “When Wenzel and Cassie are Right”. *Langmuir* 25 (2009), pp. 1277–1281 (cited on p. 113).

[182] A. Marmur and G. Wolansky. “Apparent Contact Angles on Rough Surfaces: The Wenzel Equation Revisited”. *Colloids and Surfaces A: Physicochemical and Engineering Aspects* 156.1–3 (1999), pp. 381–388 (cited on p. 113).

[183] R. Massoudi and A. D. King. “Effect of Pressure on the Surface Tension of *n*-Hexane. Adsorption of Low Molecular Weight Gases on *n*-Hexane at 25 °”. *The Journal of Physical Chemistry* 79.16 (1975), pp. 1676–1679 (cited on pp. 43, 45).

[184] G. McFiggans, P. Artaxo, U. Baltensperger, H. Coe, M. C. Facchini, G. Feingold, S. Fuzzi, M. Gysel, A. Laaksonen, U. Lohmann, and et al. “The Effect of Physical and Chemical Aerosol Properties on Warm Cloud Droplet Activation”. *Atmospheric Chemistry and Physics* 6.9 (2006), pp. 2593–2649 (cited on p. 19).

[185] G. McHale. “Cassie and Wenzel: Were They Really so Wrong?” *Langmuir* 23.15 (2007), pp. 8200–8205 (cited on pp. 15, 96, 108, 109, 113).

[186] J. C. Melrose. “Model Calculations for Capillary Condensation”. *AIChE Journal* 12 (1966), pp. 986–994 (cited on p. 56).

[187] J. C. Melrose. “Thermodynamic Aspects of Capillarity”. *Industrial & Engineering Chemistry* 60 (1968), pp. 53–70 (cited on p. 71).

[188] A. J. Milne and A. Amirfazli. “The Cassie Equation: How It Is Meant to Be Used”. *Advances in Colloid and Interface Science* 170 (2012), pp. 48–55 (cited on pp. 14, 96).

[189] C. Miqueu, B. Mendiboure, C. Graciaa, and J. Lachaise. “Modelling of the Surface Tension of Binary and Ternary Mixtures with the Gradient Theory of Fluid Interfaces”. *Fluid Phase Equilibria* 218.2 (2004), pp. 189–203 (cited on p. 36).

[190] C. Miqueu, B. Mendiboure, A. Graciaa, and J. Lachaise. “Modeling of the Surface Tension of Multicomponent Mixtures with the Gradient Theory of Fluid Interfaces”. *Industrial & Engineering Chemistry Research* (2005), pp. 3321–3329 (cited on p. 36).

[191] C. Miqueu, B. Mendiboure, A. Graciaa, and J. Lachaise. “Petroleum Mixtures: An Efficient Predictive Method for Surface Tension Estimations at Reservoir Conditions”. *Fuel* 87.6 (2008), pp. 612–621 (cited on pp. 12, 37).

[192] C. Miqueu, J. M. Míguez, M. M. Piñeiro, T. Lafitte, and B. Mendiboure. "Simultaneous Application of the Gradient Theory and Monte Carlo Molecular Simulation for the Investigation of Methane/Water Interfacial Properties". *Journal of Physical Chemistry B* 115.31 (2011), pp. 9618–9625 (cited on p. 36).

[193] A. C. Mitropoulos. "The Kelvin Equation". *Journal of Colloid and Interface Science* 317 (2008), pp. 643–648 (cited on p. 56).

[194] W. J. Moore. *Physical Chemistry*. Englewood Cliffs: Prentice-Hall, Inc., 1972, pp. 475–519 (cited on pp. 57, 64).

[195] S. Mozaffari, P. Tchoukov, A. Mozaffari, J. Atias, J. Czarnecki, and N. Nazemifard. "Capillary Driven Flow in Nanochannels—Application to Heavy Oil Rheology Studies". *Colloids and Surfaces A: Physicochemical and Engineering Aspects* 513 (2017), pp. 178–187 (cited on pp. 19, 71).

[196] A. Mulero, I. Cachadiña, and M. I. Parra. "Recommended Correlations for the Surface Tension of Common Fluids". *Journal of Physical and Chemical Reference Data* 41.4 (2012), p. 043105 (cited on pp. xxiii, 41, 44, 48).

[197] N. Nagarajan, M. Honarpour, and F. Arasteh. "Critical Role of Rock and Fluid—Impact on Reservoir Performance on Unconventional Shale Reservoirs". In: *Unconventional Resources Technology Conference*. 2013, pp. 1–20 (cited on p. 70).

[198] N. Nagarajan, K. A. Gasem, and R. L. Robinson. "Equilibrium Phase Compositions, Phase Densities, and Interfacial Tensions for CO_2 + Hydrocarbon Systems. 6. CO_2 + *n*-Butane + *n*-Decane". *Journal of Chemical & Engineering Data* 35.3 (1990), pp. 228–231 (cited on p. 49).

[199] S. Nagy and J. Siemek. "Confined Phase Envelope of Gas–Condensate Systems in Shale Rocks". *Archives of Mining Sciences* 59.4 (2014), pp. 1005–1022 (cited on p. 70).

[200] J. C. Neyt, A. Wender, V. Lachet, A. Ghoufi, and P. Malfreyt. "Molecular Modeling of the Liquid–Vapor Interfaces of a Multi-component Mixture: Prediction of the Coexisting Densities and Surface Tensions at Different Pressures and Gas Compositions". *The Journal of Chemical Physics* 139.2 (2013), p. 024701 (cited on p. 36).

[201] H. N. Nilssen. *Calculation of Interfacial Tension of Methane + n-Butane Mixture with Gradient Theory near Critical Conditions*. Report prepared for KP8108 Advanced Thermodynamics. Norwegian University of Science and Technology, 2008 (cited on pp. 43, 45, 46).

[202] O. G. Niño Amézquita, S. Enders, P. T. Jaeger, and R. Eggers. “Interfacial Properties of Mixtures Containing Supercritical Gases”. *Journal of Supercritical Fluids* 55.2 (2010), pp. 724–734 (cited on pp. 36, 43, 44, 46).

[203] O. G. Niño Amézquita, S. Enders, P. T. Jaeger, and R. Eggers. “Measurement and Prediction of Interfacial Tension of Binary Mixtures”. *Industrial & Engineering Chemistry Research* 49.2 (2010), pp. 592–601 (cited on pp. 45, 46).

[204] B. Nojabaei, R. T. Johns, and L. Chu. “Effect of Capillary Pressure on Phase Behavior in Tight Rocks and Shales”. *SPE Reservoir Evaluation & Engineering* 16.3 (2013), pp. 281–289 (cited on pp. 12, 70).

[205] M. Noppel, H. Vehkamäki, P. M. Winkler, M. Kulmala, and P. E. Wagner. “Heterogeneous Nucleation in Multi-component Vapor on a Partially Wettable Charged Conducting Particle. II. The Generalized Laplace, Gibbs–Kelvin, and Young Equations and Application to Nucleation”. *The Journal of Chemical Physics* 139 (2013), p. 134108 (cited on p. 56).

[206] M. Nosonovsky. “On the Range of Applicability of the Wenzel and Cassie Equations”. *Langmuir* 23.19 (2007), pp. 9919–9920 (cited on pp. 15, 96, 108, 109, 113).

[207] M. Nosonovsky and B. Bhushan. “Phase Behavior of Capillary Bridges: Towards Nanoscale Water Phase Diagram”. *Physical Chemistry Chemical Physics* 10.16 (2008), pp. 2137–2144 (cited on p. 71).

[208] S. Ohe. *Vapor–Liquid Equilibrium Data, Physical Sciences Data 37*. Vol. 37. Tokyo: Elsevier, 1989, pp. 206–216 (cited on pp. 7, 8).

[209] N. M. Ostrovskii and J. Wood. “Reaction and Capillary Condensation in Dispersed Porous Particles”. In: *Finely Dispersed Particles: Micro-, Nano-, and Atto-Engineering*. Ed. by J. Hsu and A. M. Spasic. Boca Raton: CRC Press, 2005 (cited on pp. 2, 3, 56).

[210] T. Ozturk and H. Y. Erbil. “Evaporation of Water–Ethanol Binary Sessile Drop on Fluoropolymer Surfaces: Influence of Relative Humidity”. *Colloids and Surfaces A: Physicochemical and Engineering Aspects* 553 (2018), pp. 327–336 (cited on p. 36).

[211] K. Park. “Facing the Truth About Nanotechnology in Drug Delivery”. *ACS Nano* 7.9 (2013), pp. 7442–7447 (cited on p. 71).

[212] D. C. Pease. “The Significance of the Contact Angle in Relation to the Solid Surface”. *The Journal of Physical Chemistry* 49.2 (1945), pp. 107–110 (cited on pp. 15, 97).

[213] D.-Y. Peng and D. B. Robinson. “A New Two-Constant Equation of State”. *Industrial & Engineering Chemistry Fundamentals* 15.1 (1976), pp. 59–64 (cited on p. 39).

[214] D.-Y. Peng and D. B. Robinson. “A Rigorous Method for Predicting the Critical Properties of Multicomponent Systems from an Equation of State”. *AIChE Journal* 23.2 (1977), pp. 137–144 (cited on p. 39).

[215] B. Pennington and E. Hough. “Interfacial Tension of the Methane–normal Butane System”. *Producers Monthly* 29 (1965), p. 4 (cited on pp. 43, 45, 46).

[216] L. M. Pereira, A. Chapoy, R. Burgass, and B. Tohidi. “Measurement and Modelling of High Pressure Density and Interfacial Tension of (Gas + *n*-Alkane) Binary Mixtures”. *The Journal of Chemical Thermodynamics* 97 (2016), pp. 55–69 (cited on pp. 12, 36, 37, 45, 46, 48).

[217] T. Pitakbunkate, P. B. Balbuena, G. J. Moridis, and T. A. Blasingame. “Effect of Confinement on Pressure/Volume/Temperature Properties of Hydrocarbons in Shale”. *SPE Journal* 21.2 (2016), pp. 621–634 (cited on pp. 70, 72).

[218] A. Pockels. “Surface Tension”. *Nature* 43.1115 (1891), pp. 437–439 (cited on p. 1).

[219] B. E. Poling, J. M. Prausnitz, and J. P. O’Connell. *The Properties of Gases and Liquids*. 5th ed. New York: McGraw-Hill, 2001, pp. 12.12–12.20, 12.23 (cited on pp. 63, 83).

[220] A. D. Polyanin and A. V. Manzhirov. *Handbook of Mathematics for Engineers and Scientists*. Chapman & Hall/CRC, 2007, p. 69 (cited on pp. 101, 117).

[221] S. Pouralhosseini, F. Eslami, J. A. W. Elliott, and J. M. Shaw. “Modeling the Phase Behavior of Asphaltene + Toluene + Polystyrene Mixtures—A Depletion Flocculation Approach”. *Energy & Fuels* 30 (2016), pp. 904–914 (cited on p. 71).

[222] J. H. Poynting. “Change of State: Solid–Liquid”. *Proceedings of the Physical Society of London* 4 (1880), pp. 271–288 (cited on pp. 9, 58).

[223] J. M. Prausnitz, R. N. Lichtenthaler, and E. G. de Azevedo. “Classical Thermodynamics of Phase Equilibria”. In: *Molecular Thermodynamics of Fluid-Phase Equilibria*. 3rd ed. Prentice Hall, 1999. Chap. 2, pp. 19–20 (cited on p. 77).

[224] Y. Qiu and V. Molinero. “Morphology of Liquid–Liquid Phase Separated Aerosols”. *Journal of the American Chemical Society* 137 (2015), pp. 10642–10651 (cited on p. 19).

[225] H. G. Rackett. “Equation of State for Saturated Liquids”. *Journal of Chemical & Engineering Data* 15 (1970), pp. 514–517 (cited on p. 81).

[226] R. Raj, R. Enright, Y. Zhu, S. Adera, and E. N. Wang. “Unified Model for Contact Angle Hysteresis on Heterogeneous and Superhydrophobic Surfaces”. *Langmuir* 28.45 (2012), pp. 15777–15788 (cited on p. 98).

[227] W. J. Randel and F. Wu. “The Polar Summer Tropopause Inversion Layer”. *Journal of the Atmospheric Sciences* 67.8 (2010), pp. 2572–2581 (cited on p. 70).

[228] M. Rauscher and S. Dietrich. “Wetting Phenomena in Nanofluidics”. *Annual Review of Materials Research* 38 (2008), pp. 143–172 (cited on p. 96).

[229] A. V. Rayer, K. Z. Sumon, A. Henni, and P. Tontiwachwuthikul. “Physicochemical Properties of 1-Methyl Piperazine(1) + Water(2) System at T = (298.15 to 343.15) K and Atmospheric Pressure”. *The Journal of Chemical Thermodynamics* 43.12 (2011), pp. 1897–1905 (cited on p. 19).

[230] D. Robinson and D. Peng. *Research Report 28: The Characterization of the Heptanes and Heavier Fractions for the GPA Peng–Robinson Programs*. Gas Processors Association, 1978 (cited on p. 39).

[231] J. I. Rosales-Leal, M. A. Rodríguez-Valverde, G. Mazzaglia, P. J. Ramón-Torregrosa, L. Díaz-Rodríguez, O. García-Martínez, M. Vallecillo-Capilla, C. Ruiz, and M. A. Cabrerizo-Vílchez. “Effect of Roughness, Wettability and Morphology of Engineered Titanium Surfaces on Osteoblast-like Cell Adhesion”. *Colloids and Surfaces A: Physicochemical and Engineering Aspects* 365.1–3 (2010), pp. 222–229 (cited on p. 112).

[232] J. Rouquerol, D. Avnir, C. Fairbridge, D. Everett, J. Haynes, N. Pernicone, J. Ramsay, K. Sing, and K. Unger. “Recommendations for the Characterization of Porous Solids (Technical Report)”. *Pure and Applied Chemistry* 66.8 (1994), pp. 1739–1758 (cited on p. 3).

[233] F. A. A. Al-Rub. “Distillation in Capillary Porous Media for Separation of Biomass Ethanol–Water Mixtures”. PhD thesis. University of Iowa, 1994 (cited on p. 56).

[234] F. A. A. Al-Rub, J. Akili, and R. Datta. “Distillation of Binary Mixtures with Capillary Porous Plates”. *Separation Science and Technology* 33 (1998), pp. 1529–1550 (cited on pp. 56, 72).

[235] F. A. A. Al-Rub and R. Datta. “Isothermal Vapor–Liquid Equilibrium of Ethanol–Water Mixtures + Acetone–Ethanol Mixtures Inside Capillary Porous Plates”. *Separation Science and Technology* 35 (2000), pp. 2203–2225 (cited on p. 56).

[236] F. A. A. Al-Rub and R. Datta. “Theoretical Study of Vapor Pressure of Pure Liquids in Porous Media”. *Fluid Phase Equilibria* 147 (1998), pp. 65–83 (cited on pp. 56, 72).

[237] F. A. A. Al-Rub and R. Datta. “Theoretical Study of Vapor–Liquid Equilibrium Inside Capillary Porous Plates”. *Fluid Phase Equilibria* 162 (1999), pp. 83–96 (cited on p. 56).

[238] F. Rupp, R. A. Gittens, L. Scheideler, A. Marmur, B. D. Boyan, Z. Schwartz, and J. Geis-Gerstorfer. “A Review on the Wettability of Dental Implant Surfaces I: Theoretical and Experimental Aspects”. *Acta Biomaterialia* 10.7 (2014), pp. 2894–2906 (cited on p. 112).

[239] M. Sahimi and B. N. Taylor. “Surface Tension of Binary Liquid–Vapor Mixtures: A Comparison of Mean-Field and Scaling Theories”. *The Journal of Chemical Physics* 95.9 (1991), pp. 6749–6761 (cited on p. 36).

[240] D. R. Sandoval, W. Yan, M. L. Michelsen, and E. H. Stenby. “The Phase Envelope of Multicomponent Mixtures in the Presence of a Capillary Pressure Difference”. *Industrial & Engineering Chemistry Research* 55.22 (2016), pp. 6530–6538 (cited on pp. 36, 70, 71).

[241] B. M. S. Santos, A. G. M. Ferreira, and I. M. A. Fonseca. “Surface and Interfacial Tensions of the Systems Water + *n*-Butyl Acetate + Methanol and Water + *n*-Pentyl Acetate + Methanol at 303.15 K”. *Fluid Phase Equilibria* 208 (2003), pp. 1–21 (cited on p. 21).

[242] S. Sarman, H. Greberg, J. Satherley, R. Penfold, and S. Nordholm. “Effective Potential Approach to Bulk Thermodynamic Properties and Surface Tension of Molecular Fluids. II. Binary Mixtures of *n*-Alkanes and Miscible Gas”. *Fluid Phase Equilibria* 172.2 (2000), pp. 145–167 (cited on p. 36).

[243] J. B. Scarborough. “The Accuracy of Approximate Calculations”. In: *Numerical Mathematical Analysis*. 5th ed. The Johns Hopkins Press, 1962. Chap. 1, p. 8 (cited on p. 85).

[244] D. Schechter and B. Guo. “Parachors Based on Modern Physics and Their Uses in IFT Prediction of Reservoir Fluids”. *SPE Reservoir Evaluation & Engineering* 1.3 (2007), pp. 207–217 (cited on pp. 36, 37).

[245] R. L. Schmidt, J. C. Randall, and H. Lawrence Clever. “The Surface Tension and Density of Binary Hydrocarbon Mixtures: Benzene–*n*-Hexane and Benzene–*n*-Dodecane”. *The Journal of Physical Chemistry* 70.12 (1966), pp. 3912–3916 (cited on pp. 42, 43, 46, 48).

[246] J. H. Seinfeld and S. N. Pandis. *Atmospheric Chemistry and Physics: From Air Pollution to Climate Change*. John Wiley & Sons, Inc., 2006, pp. 434–486 (cited on pp. 2, 56, 70, 71).

[247] K. N. Seneviratne, T. J. Hughes, M. L. Johns, K. N. Marsh, and E. F. May. "Surface Tension and Critical Point Measurements of Methane + Propane Mixtures". *The Journal of Chemical Thermodynamics* 111 (2017), pp. 173–184 (cited on pp. 45, 46).

[248] K. Seo, M. Kim, and D. H. Kim. "Validity of the Equations for the Contact Angle on Real Surfaces". *Korea–Australia Rheology Journal* 25.3 (2013), pp. 175–180 (cited on pp. 15, 96, 107, 113).

[249] A. A. Shapiro and E. H. Stenby. "Kelvin Equation for a Non-ideal Multicomponent Mixture". *Fluid Phase Equilibria* 134 (1997), pp. 87–101 (cited on pp. 56, 71).

[250] A. A. Shapiro and E. H. Stenby. "Thermodynamics of the Multicomponent Vapor–Liquid Equilibrium under Capillary Pressure Difference". *Fluid Phase Equilibria* 178 (2001), pp. 17–32 (cited on pp. 56, 71).

[251] N. Shardt and J. A. W. Elliott. "A Model for the Surface Tension of Dilute and Concentrated Binary Aqueous Mixtures as a Function of Composition and Temperature". *Langmuir* 33 (2017), pp. 11077–11085 (cited on pp. 37, 38, 40, 49, 50, 83, 84).

[252] N. Shardt and J. A. W. Elliott. "Gibbsian Thermodynamics of Cassie–Baxter Wetting (Were Cassie and Baxter Wrong? Revisited)". *Langmuir* 34.40 (2018), pp. 12191–12198 (cited on pp. 112, 114, 121).

[253] N. Shardt and J. A. W. Elliott. "Isobaric Vapor–Liquid Phase Diagrams for Multicomponent Systems with Nanoscale Radii of Curvature". *Journal of Physical Chemistry B* 122.8 (2018), pp. 2434–2447 (cited on pp. 36, 38, 51, 52, 97, 114).

[254] N. Shardt and J. A. W. Elliott. "Thermodynamic Study of the Role of Interface Curvature on Multicomponent Vapor–Liquid Phase Equilibrium". *Journal of Physical Chemistry A* 120.14 (2016), pp. 2194–2200 (cited on pp. 19, 36, 52, 72, 78, 79, 90–92, 97, 114).

[255] Y. A. W. Shardt. "Regression". In: *Statistics for Chemical and Process Engineers*. Springer, 2015. Chap. 3, p. 102 (cited on p. 21).

[256] M. Sherafati and K. Jessen. "Stability Analysis for Multicomponent Mixtures Including Capillary Pressure". *Fluid Phase Equilibria* 433 (2017), pp. 56–66 (cited on p. 36).

[257] J. L. Shereshefsky. "A Theory of Surface Tension of Binary Solutions". *Journal of Colloid and Interface Science* 24.3 (1967), pp. 317–322 (cited on pp. xxi, xxv, 12, 19, 20, 36, 37, 83).

[258] J. L. Shereshefsky. "A Study of Vapor Pressures in Small Capillaries. Part I. Water Vapor. (A). Soft Glass Capillaries". *Journal of the American Chemical Society* 50 (1928), pp. 2966–2980 (cited on p. 56).

[259] J. Shi, A. R. Votruba, O. C. Farokhzad, and R. Langer. “Nanotechnology in Drug Delivery and Tissue Engineering: From Discovery to Applications”. *Nano Letters* 10.9 (2010), pp. 3223–3230 (cited on p. 71).

[260] J.-U. Shim, G. Cristobal, D. R. Link, T. Thorsen, Y. Jia, K. Piattelli, and S. Fraden. “Control and Measurement of the Phase Behavior of Aqueous Solutions Using Microfluidics”. *Journal of the American Chemical Society* 129.28 (2007), pp. 8825–35 (cited on p. 36).

[261] S. Shin, O. Shardt, P. B. Warren, and H. A. Stone. “Membraneless Water Filtration Using CO_2”. *Nature Communications* 8 (2017), p. 15181 (cited on p. 3).

[262] Y.-O. Shin and J. Simandl. “Reply to ‘Comment on “Vapor–Liquid Equilibria in Porous Media”’”. *Fluid Phase Equilibria* 175 (2000), p. 325 (cited on p. 56).

[263] Y.-O. Shin and J. Simandl. “Vapor and Liquid Equilibria in Porous Media”. *Fluid Phase Equilibria* 166 (1999), pp. 79–90 (cited on p. 56).

[264] R. Shuttleworth and G. L. J. Bailey. “Spreading of a Liquid over a Rough Solid”. *Discussions of the Faraday Society* 3 (1948), pp. 16–22 (cited on pp. 98, 114).

[265] L. M. Skinner and J. R. Sambles. “The Kelvin Equation—A Review”. *Journal of Aerosol Science* 2 (1972), pp. 199–210 (cited on p. 56).

[266] J. M. Smith, H. C. Van Ness, and M. M. Abbott. *Introduction to Chemical Engineering Thermodynamics*. New York: McGraw-Hill, 2005, pp. 430–482 (cited on pp. 9, 10, 58, 59, 78, 79).

[267] J. Song, D. Zhao, Z. Han, W. Xu, Y. Lu, X. Liu, B. Liu, C. J. Carmalt, X. Deng, and I. P. Parkin. “Super-Robust Superhydrophobic Concrete”. *Journal of Materials Chemistry A* 5.28 (2017), pp. 14542–14550 (cited on pp. 2, 112).

[268] M. Spivak. “Elements of the Theory of Surfaces in $\mathbb{R}^3$”. In: *A Comprehensive Introduction to Differential Geometry*. Publish or Perish, Inc., 1979. Chap. 2, p. 69 (cited on p. 77).

[269] F. B. Sprow and J. M. Prausnitz. “Surface Tensions of Simple Liquid Mixtures”. *Transactions of the Faraday Society* 62 (1966), pp. 1105–1111 (cited on p. 85).

[270] H. J. J. Staat, A. van der Bos, M. van den Berg, H. Reinten, H. Wijshoff, M. Versluis, and D. Lohse. “Ultrafast Imaging Method to Measure Surface Tension and Viscosity of Inkjet-Printed Droplets in Flight”. *Experiments in Fluids* 58.1 (2017), pp. 1–8 (cited on p. 19).

[271] G. L. Stegemeier, B. F. Pennington, E. B. Brauer, and E. W. Hough. “Interfacial Tension of the Methane–normal Decane System”. *SPE Journal* 2.3 (1962), pp. 257–260 (cited on pp. 43, 45, 46).

[272] B. Stevens and G. Feingold. “Untangling Aerosol Effects on Clouds and Precipitation in a Buffered System”. *Nature* 461.7264 (2009), p. 607 (cited on p. 71).

[273] B. C. Stimpson and M. A. Barrufet. “Thermodynamic Modeling of Pure Components Including the Effects of Capillarity”. *Journal of Chemical & Engineering Data* 61.8 (2016), pp. 2844–2850 (cited on p. 71).

[274] B. A. Stradi, J. F. Brennecke, J. P. Kohn, and M. A. Stadtherr. “Reliable Computation of Mixture Critical Points”. *AIChE Journal* 47.1 (2001), pp. 212–221 (cited on p. 39).

[275] P. S. Swain and R. Lipowsky. “Contact Angles on Heterogeneous Surfaces: A New Look at Cassie’s and Wenzel’s Laws”. *Langmuir* 14.23 (1998), pp. 6772–6780 (cited on pp. 15, 97, 109, 112).

[276] R. Tahery, H. Modarress, and J. Satherley. “Surface Tension Prediction and Thermodynamic Analysis of the Surface for Binary Solutions”. *Chemical Engineering Science* 60.17 (2005), pp. 4935–4952 (cited on pp. 20, 22).

[277] M. Talreja, I. Kusaka, and D. L. Tomasko. “Analyzing Surface Tension in Higher Alkanes and Their CO_2 Mixtures”. *Fluid Phase Equilibria* 319 (2012), pp. 67–76 (cited on p. 36).

[278] S. P. Tan and M. Piri. “Equation-of-State Modeling of Associating-Fluids Phase Equilibria in Nanopores”. *Fluid Phase Equilibria* 405 (2015), pp. 157–166 (cited on pp. 12, 19, 36, 72).

[279] S. P. Tan and M. Piri. “Equation-of-State Modeling of Confined-Fluid Phase Equilibria in Nanopores”. *Fluid Phase Equilibria* 393 (2015), pp. 48–63 (cited on pp. 12, 19, 36, 72, 88).

[280] X. Tang and J. Gross. “Density Functional Theory for Calculating Surface Tensions with a Simple Renormalization Formalism for the Critical Point”. *Journal of Supercritical Fluids* 55.2 (2010), pp. 735–742 (cited on p. 36).

[281] P. I. C. Teixeira, B. S. Almeida, M. M. Telo da Gama, J. A. Rueda, and R. G. Rubio. “Interfacial Properties of Mixtures of Molecular Fluids: Comparison Between Theory and Experiment; Methyl Iodide + Carbon Tetrachloride and Acetonitrile + Carbon Tetrachloride”. *The Journal of Physical Chemistry* 96.21 (1992), pp. 8488–8497 (cited on pp. 42, 43, 46).

[282] M. Thomä. “Über die an gekrümmten Flüssigkeitsoberflächen auftretenden Dampfdruckänderungen”. *Zeitschrift für Physik* 64 (1930), pp. 224–236 (cited on p. 56).

[283] W. Thomson. “On the Equilibrium of Vapour at a Curved Surface of Liquid”. *Proceedings of the Royal Society of Edinburgh* 7 (1872), pp. 63–68 (cited on pp. 10, 56).

[284] R. C. Tolman. “The Effect of Droplet Size on Surface Tension”. *The Journal of Chemical Physics* 17 (1949), pp. 333–337 (cited on p. 63).

[285] L. Travalloni, M. Castier, and F. W. Tavares. “Phase Equilibrium of Fluids Confined in Porous Media from an Extended Peng–Robinson Equation of State”. *Fluid Phase Equilibria* 362 (2014), pp. 335–341 (cited on p. 13).

[286] K. S. Udell. “The Thermodynamics of Evaporation and Condensation in Porous Media”. In: *SPE California Regional Meeting*. Society of Petroleum Engineers, 1982 (cited on p. 71).

[287] J. D. Van der Waals. “The Thermodynamic Theory of Capillarity Under the Hypothesis of a Continuous Variation of Density. *Verhandel. Konink. Akad. Weten. Amsterdam* 1.8 (1893)”. Trans. by J. S. Rowlinson. *Journal of Statistical Physics* 20.2 (1979), pp. 197–200 (cited on p. 36).

[288] J. Vanhanen, A.-P. Hyvärinen, T. Anttila, T. Raatikainen, Y. Viisanen, and H. Lihavainen. “Ternary Solution of Sodium Chloride, Succinic Acid and Water; Surface Tension and its Influence on Cloud Droplet Activation”. *Atmospheric Chemistry and Physics* 8 (2008), pp. 4595–4604 (cited on p. 19).

[289] G. Vázquez, E. Álvarez, J. M. Navaza, R. Rendo, and E. Romero. “Surface Tension of Binary Mixtures of Water + Monoethanolamine and Water + 2-Amino-2-methyl-1-propanol and Tertiary Mixtures of these Amines with Water from 25 °C to 50 °C”. *Journal of Chemical & Engineering Data* 42.1 (1997), pp. 57–59 (cited on pp. 19, 23, 24, 26).

[290] G. Vázquez, E. Álvarez, and J. M. Navaza. “Surface Tension of Alcohol + Water from 20 to 50 °C”. *Journal of Chemical & Engineering Data* 40.3 (1995), pp. 611–614 (cited on pp. 19, 23, 24, 26, 64, 84).

[291] G. Vázquez, E. Álvarez, R. Rendo, E. Romero, and J. M. Navaza. “Surface Tension of Aqueous Solutions of Diethanolamine and Triethanolamine from 25 °C to 50 °C”. *Journal of Chemical & Engineering Data* 41.4 (1996), pp. 806–808 (cited on pp. 19, 24, 26).

[292] H. Vehkamäki. *Classical Nucleation Theory in Multicomponent Systems*. Springer, 2006 (cited on pp. 12, 56, 71, 74).

[293] H. L. Vörtler and W. R. Smith. “Computer Simulation Studies of a Square-Well Fluid in a Slit Pore. Spreading Pressure and Vapor–Liquid Phase Equilibria Using the Virtual-Parameter-Variation Method”. *The Journal of Chemical Physics* 112.11 (2000), pp. 5168–5174 (cited on p. 72).

[294] J. P. R. B. Walton and N. Quirke. “Capillary Condensation: A Molecular Simulation Study”. *Molecular Simulation* 2.4–6 (1989), pp. 361–391 (cited on p. 72).

[295] L. Wang, E. Parsa, Y. Gao, J. T. Ok, K. Neeves, X. Yin, and E. Ozkan. “Experimental Study and Modeling of the Effect of Nanoconfinement on Hydrocarbon Phase Behavior in Unconventional Reservoirs”. In: *SPE Western North American and Rocky Mountain Joint Meeting*. Society of Petroleum Engineers, 2014 (cited on pp. 2, 3, 36, 70).

[296] W. Wang, K. Lockwood, L. M. Boyd, M. D. Davidson, S. Movafaghi, H. Vahabi, S. R. Khetani, and A. K. Kota. “Superhydrophobic Coatings with Edible Materials”. *ACS Applied Materials and Interfaces* 8.29 (2016), pp. 18664–18668 (cited on pp. 2, 112).

[297] C. A. Ward, A. Balakrishnan, and F. C. Hooper. “On the Thermodynamics of Nucleation in Weak Gas–Liquid Solutions”. *Journal of Basic Engineering* 92.4 (1970), pp. 695–701 (cited on pp. 36, 56, 71, 77).

[298] C. A. Ward and E. Levart. “Conditions for Stability of Bubble Nuclei in Solid Surfaces Contacting a Liquid–Gas Solution”. *Journal of Applied Physics* 56 (1984), pp. 491–500 (cited on pp. 58, 97, 114, 132).

[299] C. A. Ward and M. R. Sasges. “Effect of Gravity on Contact Angle: A Theoretical Investigation”. *The Journal of Chemical Physics* 109.9 (1998), pp. 3651–3660 (cited on pp. 97, 114).

[300] C. Ward, W. Johnson, R. Venter, S. Ho, T. Forest, and W. Fraser. “Heterogeneous Bubble Nucleation and Conditions for Growth in a Liquid–Gas System of Constant Mass and Volume”. *Journal of Applied Physics* 54.4 (1983), pp. 1833–1843 (cited on p. 130).

[301] H. G. Warren and E. W. Hough. “Interfacial Tension of the Methane–normal Heptane System”. *SPE Journal* 10.4 (1970), p. 327 (cited on pp. 45, 46).

[302] C. F. Weinaug and D. L. Katz. “Surface Tensions of Methane–Propane Mixtures”. *Industrial & Engineering Chemistry* 35 (1943), pp. 239–246 (cited on pp. 12, 36, 43–47).

[303] R. N. Wenzel. “Resistance of Solid Surfaces to Wetting by Water”. *Industrial & Engineering Chemistry* 28.8 (1936), pp. 988–994 (cited on pp. 14, 112, 113, 127).

[304] G. Whyman, E. Bormashenko, and T. Stein. “The Rigorous Derivation of Young, Cassie–Baxter and Wenzel Equations and the Analysis of the Contact Angle Hysteresis Phenomenon”. *Chemical Physics Letters* 450.4–6 (2008), pp. 355–359 (cited on pp. 107, 113, 125).

[305] J. Wisniak. “Historical Development of the Vapor Pressure Equation from Dalton to Antoine”. *Journal of Phase Equilibria* 22 (2001), pp. 622–630 (cited on pp. 9, 58).

[306] C. Wohlfarth and B. Wohlfarth. “Binary Mixtures: Data”. In: *Surface Tension of Pure Liquids and Binary Liquid Mixtures*. Ed. by M. D. Lechner. Springer, 1997 (cited on pp. 42, 43, 46, 52).

[307] N. S. J. Wong. “The Effects of Capillary Plates on Vapour–Liquid Equilibrium in Aqueous Alcohol Systems”. MSc thesis. McGill University, 1997 (cited on p. 56).

[308] J. Wood and L. F. Gladden. “Modelling Diffusion and Reaction Accompanied by Capillary Condensation Using Three-Dimensional Pore Networks. Part 1. Fickian Diffusion and Pseudo-First-Order Reaction Kinetics”. *Chemical Engineering Science* 57 (2002), pp. 3033–3045 (cited on pp. 2, 3, 56, 71).

[309] R. C. Wootton, R. Fortt, and A. J. de Mello. “A Microfabricated Nanoreactor for Safe, Continuous Generation and Use of Singlet Oxygen”. *Organic Process Research & Development* 6.2 (2002), pp. 187–189 (cited on p. 3).

[310] T. Wu, K. Hirata, H. Suzuki, R. Xiang, Z. Tang, and T. Yomo. “Shrunk to Femtolitre: Tuning High-Throughput Monodisperse Water-in-Oil Droplet Arrays for Ultra-small Micro-reactors”. *Applied Physics Letters* 101.7 (2012), pp. 2–6 (cited on p. 36).

[311] W. Xu and C.-H. Choi. “From Sticky to Slippery Droplets: Dynamics of Contact Line Depinning on Superhydrophobic Surfaces”. *Physical Review Letters* 109.2 (2012), pp. 1–5 (cited on pp. 98, 110).

[312] X. Xu. “Analysis for Wetting on Rough Surfaces by a Three-dimensional Phase Field Model”. *Discrete and Continuous Dynamical Systems - Series B* 21.8 (2016), pp. 2839–2850 (cited on pp. 15, 113, 125, 134, 135, 137).

[313] X. Xu and X. Wang. “Derivation of the Wenzel and Cassie Equations from a Phase Field Model for Two Phase Flow on Rough Surface”. *SIAM Journal on Applied Mathematics* 70.8 (2010), pp. 2929–2941 (cited on pp. 15, 113).

[314] X. Xu and X. Wang. “The Modified Cassie’s Equation and Contact Angle Hysteresis”. *Colloid and Polymer Science* 291.2 (2013), pp. 299–306 (cited on pp. 15, 97, 109, 112).

[315] C. L. Yaws. *Yaws’ Critical Property Data for Chemical Engineers and Chemists*. Knovel, 2014 (cited on pp. 81, 82).

[316] B. V. Yeh, G. C. Yeh, M. S. Yeh, S. T. Schmidt, A. M. McCarthy, and W. J. Celenza. "Vapor–Liquid Equilibrium in Capillary Distillation". *Desalination* 81.1 (1991), pp. 161–187 (cited on p. 72).

[317] G. C. Yeh, M. S. Shah, and B. V. Yeh. "Vapor–Liquid Equilibria of Nonelectrolyte Solutions in Small Capillaries. 1. Experimental Determination of Equilibrium Composition". *Langmuir* 2.1 (1986), pp. 90–96 (cited on p. 72).

[318] G. C. Yeh, B. V. Yeh, B. J. Ratigan, S. J. Correnti, M. S. Yeh, D. W. Pitakowski, W. Fleming, D. B. Ritz, and J. A. Lariviere. "Separation of Liquid Mixtures by Capillary Distillation". *Desalination* 81 (1991), pp. 129–160 (cited on pp. 56, 72).

[319] G. C. Yeh, B. V. Yeh, S. T. Schmidt, M. S. Yeh, A. M. McCarthy, and W. J. Celenza. "Vapor–Liquid Equilibrium in Capillary Distillation". *Desalination* 81 (1991), pp. 161–187 (cited on p. 56).

[320] Y. C. Yortsos and A. K. Stubos. "Phase Change in Porous Media". *Current Opinion in Colloid & Interface Science* 6.3 (2001), pp. 208–216 (cited on p. 71).

[321] T. Young. "III. An Essay on the Cohesion of Fluids". *Philosophical Transactions of the Royal Society of London* 95 (1805), pp. 65–87 (cited on pp. 1, 11).

[322] Y. S. Yu, L. Sun, X. Huang, and J. Z. Zhou. "Evaporation of Ethanol/Water Mixture Droplets on a Pillar-like PDMS Surface". *Colloids and Surfaces A: Physicochemical and Engineering Aspects* 574 (2019), pp. 215–220 (cited on p. 36).

[323] L. Zargarzadeh and J. A. W. Elliott. "Comparative Surface Thermodynamic Analysis of New Fluid Phase Formation Between a Sphere and a Flat Plate". *Langmuir* 29.11 (2013), pp. 3610–3627 (cited on pp. 19, 56, 71, 74, 77, 97, 114, 128–130).

[324] L. Zargarzadeh and J. A. W. Elliott. "Surface Thermodynamic Analysis of Fluid Confined in a Cone and Comparison with the Sphere–Plate and Plate–Plate Geometries". *Langmuir* 29.42 (2013), pp. 12950–12958 (cited on pp. 19, 56, 71, 97, 114).

[325] L. Zargarzadeh and J. A. W. Elliott. "Thermodynamics of Surface Nanobubbles". *Langmuir* 32.43 (2016), pp. 11309–11320 (cited on pp. 114, 132).

[326] R. Zhang, A. Khalizov, L. Wang, M. Hu, and W. Xu. "Nucleation and Growth of Nanoparticles in the Atmosphere". *Chemical Reviews* 112.3 (2012), pp. 1957–2011 (cited on p. 71).

[327] J. Y. Zhu, Y. Y. Duan, Z. Yang, and H. Lin. "Factors Influencing the Surface Tension of Binary Hydrocarbon Mixtures". *Fuel* 116 (2014), pp. 116–122 (cited on pp. 36, 37, 41, 48).

[328] Y.-X. Zuo and E. H. Stenby. “Prediction of Interfacial Tensions of Reservoir Crude Oil and Gas Condensate Systems”. *SPE Journal* (1998), pp. 134–145 (cited on p. 36).

Appendix A

Supplementary Information for Chapter 3

A.1 Governing Equations for Vapor–Liquid Equilibrium (VLE) and Molar Volume

We use the Peng–Robinson equation of state (PR-EOS) with volume translation for all calculations of vapor–liquid equilibrium and molar volume. The volume-translated Peng–Robinson equation of state is [1, 41]

$$P = \frac{RT}{v^{\mathrm{PR}} + c - b^{\mathrm{PR}}} - \frac{a^{\mathrm{PR}}(T)}{\left(v^{\mathrm{PR}} + c\right)\left(v^{\mathrm{PR}} + c + b^{\mathrm{PR}}\right) + b^{\mathrm{PR}}\left(v^{\mathrm{PR}} + c - b^{\mathrm{PR}}\right)}, \tag{A.1}$$

where P is pressure, R is the universal gas constant, T is absolute temperature, and v^{PR} is molar volume that is corrected by a shift of c. A cubic polynomial can be obtained by rearranging Equation (A.1) in terms of the compressibility factor Z [41]:

$$Z^3 - (1-B)Z^2 + \left(A - 3B^2 - 2B\right)Z - \left(AB - B^2 - B^3\right) = 0, \tag{A.2}$$

and defining the following quantities [41, 51]:

$$A = \frac{a^{\mathrm{PR}}P}{R^2T^2} \tag{A.3}$$

$$B = \frac{b^{\mathrm{PR}}P}{RT} \tag{A.4}$$

$$Z = \frac{P(v^{\mathrm{PR}} + c)}{RT}, \tag{A.5}$$

where a^{PR} depends on temperature through the following expressions

$$a^{\mathrm{PR}}(T) = 0.45724\frac{R^2T_{\mathrm{cr}}^2}{P_{\mathrm{cr}}}\left[1 + \kappa\left(1 - \sqrt{T/T_{\mathrm{cr}}}\right)\right]^2 \tag{A.6}$$

$$\kappa = \begin{cases} 0.37464 + 1.54226\omega - 0.26992\omega^2 & \text{for } \omega < 0.5 \\ 0.3796 + 1.4850\omega - 0.1644\omega^2 + 0.01667\omega^3 & \text{for } \omega > 0.5 \end{cases} \tag{A.7}$$

and b^{PR} is calculated by

$$b^{\mathrm{PR}} = 0.07780\frac{RT_{\mathrm{cr}}}{P_{\mathrm{cr}}}. \tag{A.8}$$

In the above equations, T_{cr} is the critical temperature, P_{cr} is the critical pressure, and ω is the acentric factor.

For mixtures, the coefficients are obtained via mixing rules:

$$a^{\mathrm{PR}} = \sum_i \sum_j x_i x_j a_{ij}^{\mathrm{PR}} \tag{A.9}$$

$$a_{ij}^{\mathrm{PR}} = \left(1 - k_{ij}\right) \sqrt{a_i^{\mathrm{PR}}} \sqrt{a_j^{\mathrm{PR}}} \tag{A.10}$$

$$b^{\mathrm{PR}} = \sum_i x_i b_i^{\mathrm{PR}}, \tag{A.11}$$

where a_i^{PR} and b_i^{PR} are calculated using Equations (A.6) and (A.8) for each pure component and x_i can denote the mole fraction of either the liquid or vapor phase. The binary interaction parameter k_{ij} is specific to each pair of compounds i and j.

At a state of vapor–liquid equilibrium (VLE), the fugacity of the liquid phase is equal to the fugacity of the vapor phase, where the fugacity of each phase is calculated with [41]

$$\begin{aligned} \ln \phi_i &= \ln \frac{f_i}{x_i P} \\ &= \frac{b_i^{\mathrm{PR}}}{b^{\mathrm{PR}}} (Z-1) - \ln (Z-B) - \frac{A}{2\sqrt{2}B} \left(\frac{2\sum_k x_k a_{ki}^{\mathrm{PR}}}{a^{\mathrm{PR}}} - \frac{b_i^{\mathrm{PR}}}{b^{\mathrm{PR}}} \right) \ln \left(\frac{Z + 2.414B}{Z - 0.414B} \right), \end{aligned} \tag{A.12}$$

where f_i is the fugacity of component i and a fugacity coefficient is defined as $\phi_i = f_i / x_i P$. To perform a flash calculation of a mixture with overall composition z_i at a pressure P, we use the Wilson correlation [12, 68] for an initial guess of the equilibrium ratio $K_i = y_i / x_i$, where y_i is the vapor mole fraction and x_i is the liquid mole fraction:

$$K_i = \frac{P_{\mathrm{cr},i}}{P} \exp \left[5.37 \left(1 + \omega_i\right) \left(1 - \frac{T_{\mathrm{cr},i}}{T} \right) \right]. \tag{A.13}$$

Then we use the Rachford–Rice equation [12, 46]:

$$\sum_i \frac{\left(K_i - 1\right) z_i}{1 + \beta \left(K_i - 1\right)} = 0 \tag{A.14}$$

to iterate for the vapor fraction β using the Newton method [12] and updating the equilibrium ratio with Equation (A.12) where $K_i = \phi_i^L / \phi_i^V$. Following the convergence of β and K_i, the liquid composition is computed with [12]:

$$x_i = \frac{z_i}{1 + \beta \left(K_i - 1\right)}. \tag{A.15}$$

To calculate the bubble point of a mixture given its liquid-phase composition, we evaluate

Equation (A.12) for the liquid and vapor phases at two initial guesses of pressure and use the bisection method to converge to the bubble pressure, where the sum of mole fractions in the vapor phase sum to unity.

Once phase equilibrium is calculated via a flash or bubble point calculation, volume translation is applied to the molar volume of each phase calculated via the PR-EOS to obtain the molar volume v, and it is defined by [1, 39]

$$v = v^{\mathrm{PR}} + c, \tag{A.16}$$

where for a pure component, c can be calculated using the correlation developed by Ahlers and Gmehling [1]

$$c = 0.252 \frac{RT_{\mathrm{cr}}}{P_{\mathrm{cr}}} \left(\chi - Z_{\mathrm{cr}}\right), \tag{A.17}$$

where χ is an empirical parameter obtained from fitting and Z_{cr} is the compressibility factor at the critical point, or more generally by

$$c = 0.252 \frac{RT_{\mathrm{cr}}}{P_{\mathrm{cr}}} \left(1.5448 Z_{\mathrm{cr}} - 0.4024\right), \tag{A.18}$$

and for a mixture [39],

$$c = \sum_i x_i c_i. \tag{A.19}$$

We use Equation (A.17) for all supercritical mixtures for which χ has been reported by Ahlers and Gmehling [1], while we use Equation (A.18) for all subcritical mixture compounds.

A.1.1 Pure Component Properties Used for Calculations of VLE and Molar Volume

Table A.1 lists critical properties of each pure component considered in our study (temperature, pressure, and compressibility), along with acentric factor, a parameter χ for volume translation used in Ahlers and Gmehling [1], and molar mass. Critical temperatures, pressures, acentric factor, and molar mass are all obtained from Perry's Handbook [16]; only the acentric factor for methyl iodide was calculated based on its vapor pressure at a reduced temperature of 0.7 from NIST [28] according to the equation developed by Pitzer *et al.* [45]. Values for critical compressibility and χ are taken from Ahlers and Gmehling [1] for the listed alkanes and carbon dioxide. The remaining critical compressibility values are obtained from Perry's Handbook [16].

Table A.1: Critical temperature T_{cr}, critical pressure P_{cr}, critical compressibility factor Z_{cr}, acentric factor ω, volume translation parameter χ, and molar weight MW [g/mol] for each pure component.

Component	T_{cr} [K]	P_{cr} [MPa]	Z_{cr}	ω	χ	MW [g/mol]
methane	190.564	4.599	0.2874	0.0115	0.336	16.042
ethane	305.32	4.872	0.2847	0.0995	0.3195	30.069
propane	369.83	4.248	0.2803	0.1523	0.306	44.096
n-butane	425.12	3.796	0.2741	0.2002	0.2945	58.122
n-pentane	469.7	3.37	0.2623	0.2515	0.274	72.149
n-hexane	507.6	3.025	0.2644	0.3013	0.2667	86.175
n-heptane	540.2	2.74	0.2629	0.3495	0.2606	100.202
n-octane	568.7	2.49	0.2595	0.3996	0.2525	114.229
n-nonane	594.6	2.29	0.2527	0.4435	0.2378	128.255
n-decane	617.7	2.11	0.2462	0.4923	0.2275	142.282
n-dodecane	658	1.82	0.2356	0.5764	0.205	
carbon dioxide	304.21	7.383	0.2741	0.2236	0.2921	
benzene	562.05	4.895	0.268	0.2103		
cyclohexane	553.8	4.08	0.273	0.2081		
carbon tetrachloride	556.35	4.56	0.272	0.1926		
methyl iodide	527.8	6.35	0.2648	0.1577		
acetonitrile	545.5	4.83	0.184	0.3379		
carbon disulfide	552	7.9	0.275	0.1107		
dichloromethane	510	6.08	0.265	0.1986		

A.1.2 Validating VLE Calculations against Experimental Data

Using the governing equations outlined above for the PR-EOS, we calculate the pressure *vs.* composition diagrams for those mixtures with one supercritical compound (*i.e.*, containing methane or carbon dioxide) for comparison to experimental data. For all subcritical mixtures, we use a binary interaction parameter of zero (this choice is supported by the correlation developed by Gao *et al.* [13] for the PR-EOS, which is a function of the critical temperature and compressibility factor of each component—when the critical temperatures of two components are similar (as seen in Table A.1, this is true for all subcritical compounds), the binary interaction parameter is very close to zero).

A.1.2.1 Methane(1) + *n*-Alkane(2) Systems

For the binary interaction coefficients of methane(1) + *n*-alkane(2) systems, we use the correlation given by Arbabi and Firoozabadi [5, 12]

$$k_{ij} = 0.0289 + 1.633 \times 10^{-4}\text{MW}, \tag{A.20}$$

where MW is the molar weight of the second component in units of g/mol. We compare our VLE calculations to the experimentally-measured phase diagrams of each system containing methane listed in Table A.2, as illustrated in Figure A.1.

Table A.2: Literature sources for experimental measurements of vapor–liquid equilibrium compositions for methane(1) + *n*-alkane (2) systems with corresponding ranges of temperature and pressure.

methane(1) +	Temperatures [K]	Pressures [MPa]	Data Reference
ethane(2)	130.37–199.92	0.19–5.10	Wichterle and Kobayashi [67]
	260.00–280.00	1.80–6.60	Gupta *et al.* [17]
propane(2)	277.59–344.26	0.69–10.00	Reamer *et al.* [49]
n-butane(2)	294.26–327.59	0.28–13.10	Sage *et al.* [52]
n-pentane(2)	310.89–410.97	0.69–16.10	Reiff *et al.* [50]
n-hexane(2)	298.15–348.15	1.01–10.1	Shim and Kohn [57]
n-heptane(2)	310.93–444.26	1.38–24.88	Reamer *et al.* [48]
n-octane(2)	248.15–323.15	1.01–7.09	Kohn and Bradish [23]
n-nonane(2)	223.15–298.15	1.01–32.32	Shipman and Kohn [58]
n-decane(2)	310.90–377.60	1.08–8.52	Srivastan *et al.* [59]
	423.15	3.04–7.09	Lin *et al.* [27]

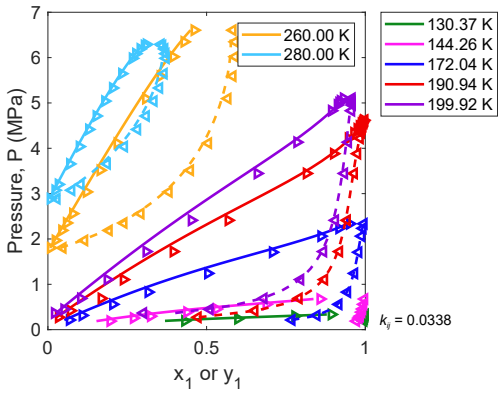

(a) Methane(1) + ethane(2); predictions use $k_{ij} = 0.0338$; experimental measurements are from Wichterle and Kobayashi [67] (outer legend) and Gupta *et al.* [17] (inner legend).

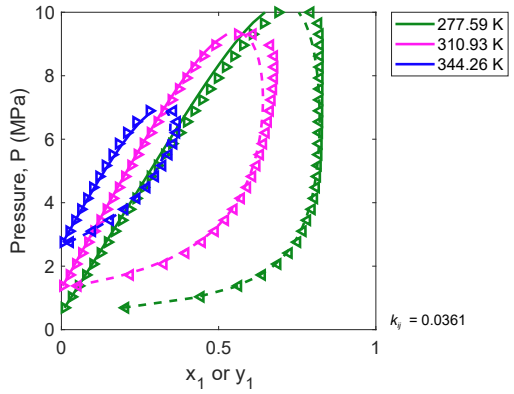

(b) Methane(1) + propane(2); predictions use $k_{ij} = 0.0361$; experimental measurements are from Reamer *et al.* [49].

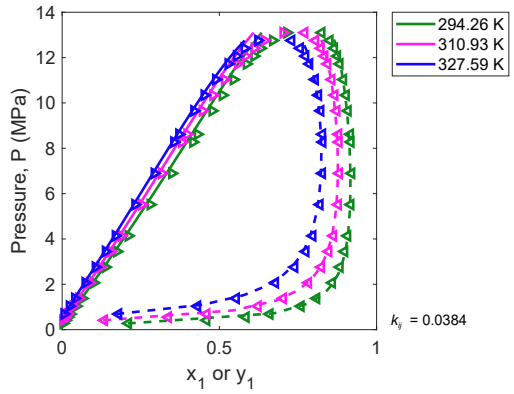

(c) Methane(1) + *n*-butane (2); predictions use $k_{ij} = 0.0384$; experimental measurements are from Sage *et al.* [52].

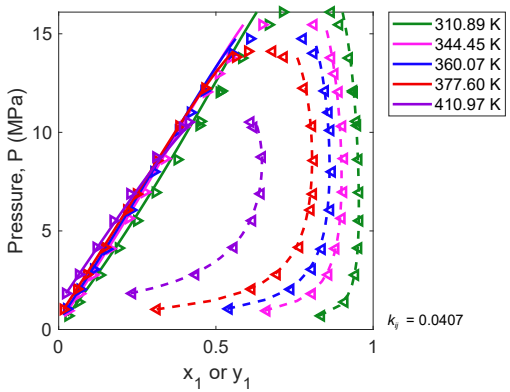

(d) Methane(1) + *n*-pentane (2); predictions use $k_{ij} = 0.0407$; experimental measurements are from Reiff *et al.* [50].

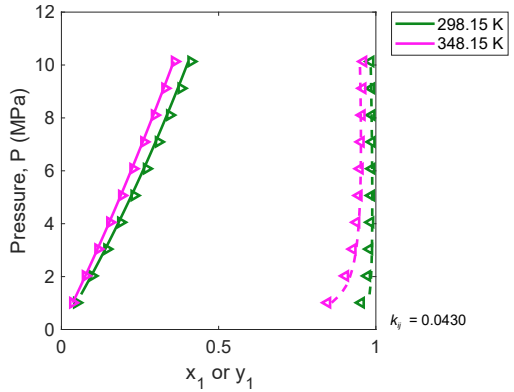

(e) Methane(1) + *n*-hexane(2); predictions use $k_{ij} = 0.0430$; experimental measurements are from Shim and Kohn [57].

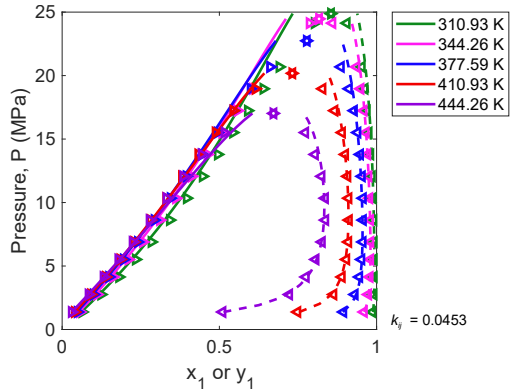

(f) Methane(1) + *n*-heptane(2); predictions use $k_{ij} = 0.0453$; experimental measurements are from Reamer *et al.* [48].

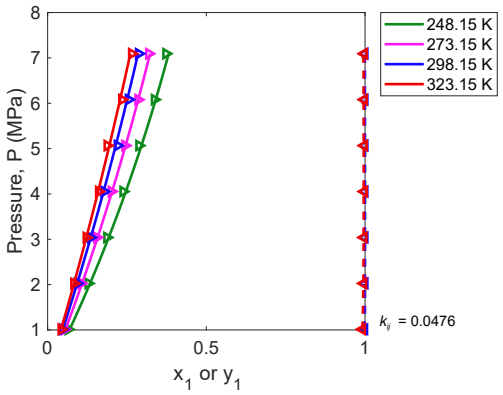

(g) Methane(1) + *n*-octane(2); predictions use $k_{ij} = 0.0476$; experimental measurements are from Kohn and Bradish [23].

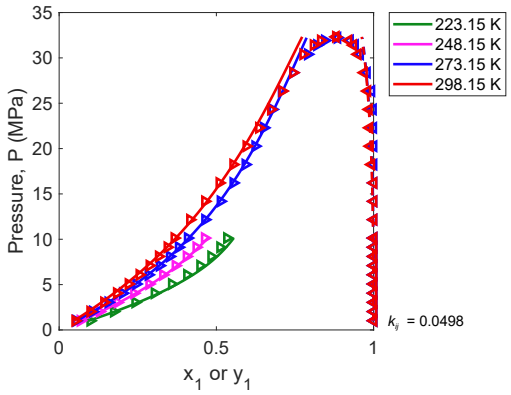

(h) Methane(1) + *n*-nonane(2); predictions use $k_{ij} = 0.0498$; experimental measurements are from Shipman and Kohn [58].

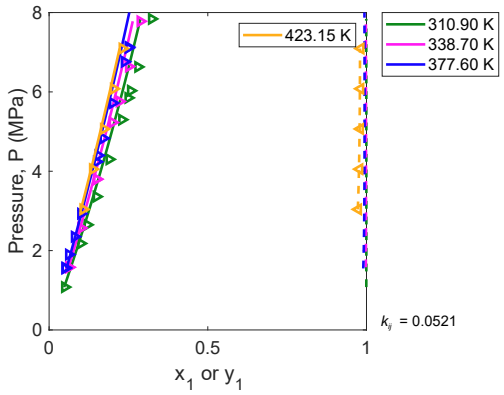

(i) Methane(1) + *n*-decane(2); predictions use $k_{ij} = 0.0521$; experimental measurements are from Srivastan *et al.* [59] (outer legend) and Lin *et al.* [27] (inner legend).

Figure A.1: Pressure–composition diagrams for methane(1) + *n*-alkane(2) systems, as calculated with the Peng–Robinson equation of state (Equations (A.2)–(A.12), where solid lines are for liquid-phase compositions and dashed lines are for vapor-phase compositions) and as measured experimentally (symbols).

A.1.2.2 Carbon Dioxide(1) + *n*-Alkane(2) Systems

For the binary interaction coefficients of carbon dioxide(1) + *n*-alkane(2) systems, we use values reported in Vitu *et al.* [64]:

- $k_{ij} = 0.12$ for carbon dioxide(1) + *n*-butane(2)
- $k_{ij} = 0.11$ for carbon dioxide(1) + *n*-heptane(2)
- $k_{ij} = 0.10$ for carbon dioxide(1) + *n*-decane(2)

We compare our VLE calculations to the experimentally-measured phase diagrams of each system listed in Table A.3, as illustrated in Figure A.2.

Table A.3: Literature sources for experimental measurements of vapor–liquid equilibrium compositions for carbon dioxide(1) + *n*-alkane (2) systems with corresponding ranges of temperature and pressure.

carbon dioxide(1) +	Temperatures (K)	Pressures (MPa)	Data Reference
n-butane(2)	319.30–377.60	2.18–8.08	Hsu *et al.* [19]
n-heptane(2)	310.65–394.26	0.42–13.31	Kalra *et al.* [21]
n-decane(2)	277.59–444.26	0.34–17.24	Reamer and Sage [47]

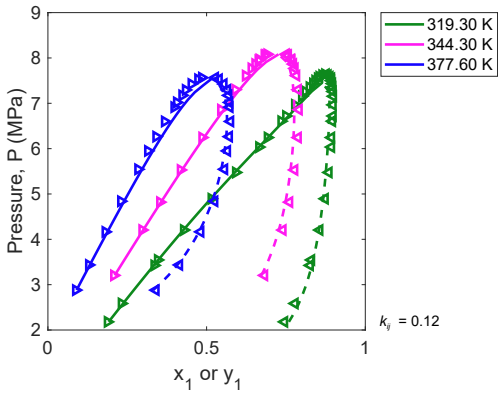

(a) Carbon dioxide(1) + *n*-butane(2); predictions use $k_{ij} = 0.12$; experimental measurements are from Hsu *et al.* [19].

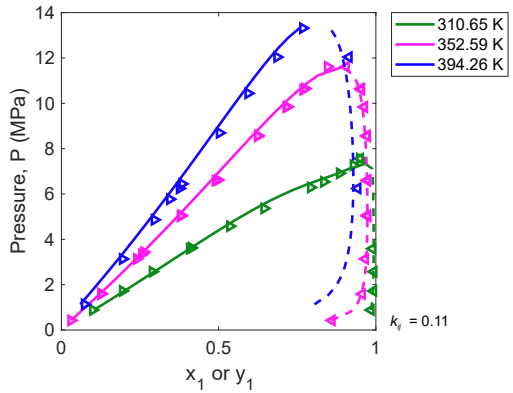

(b) Carbon dioxide(1) + *n*-heptane(2); predictions use $k_{ij} = 0.11$; experimental measurements are from Kalra *et al.* [21].

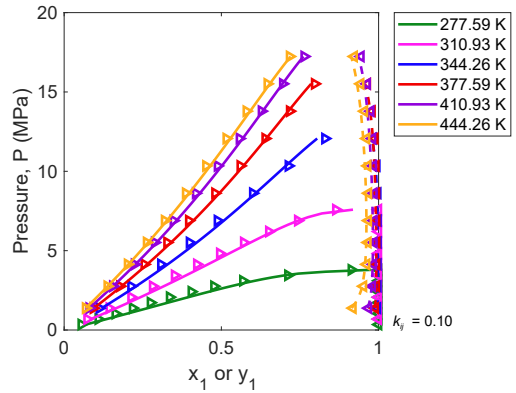

(c) Carbon dioxide(1) + *n*-decane(2); predictions use $k_{ij} = 0.10$; experimental measurements are from Reamer and Sage [47].

Figure A.2: Pressure–composition diagrams for carbon dioxide(1) + *n*-alkane(2) systems, as calculated with the Peng–Robinson equation of state (Equations (A.2)–(A.12), where solid lines are for liquid-phase compositions and dashed lines are for vapor-phase compositions) and as measured experimentally (symbols).

A.2 Numerical Method for Calculating the Critical Composition

We develop a method for calculating the critical composition of methane or carbon dioxide in a mixture, as outlined in the schematic in Figure A.3 and the flowchart in Figure A.4. It is a numerical iteration scheme that, given an initial guess for liquid composition, calculates the pressure and vapor-phase composition of the bubble point at progressively increasing liquid compositions until the critical composition is reached (that is, the maximum liquid-phase composition where vapor–liquid equilibrium is possible). Each bubble point is determined by iterating on pressure using the bisection method until (*i*) each component's fugacity in the liquid phase equals its fugacity in the vapor phase (Equation (A.12)) and (*ii*) the sum of vapor-phase mole fractions equals unity. Critical compositions were calculated for all mixtures at the temperatures reported in each literature source, as summarized in Table 3.3 and Table 3.4 in Chapter 3, as well as in Tables A.10 to A.13.

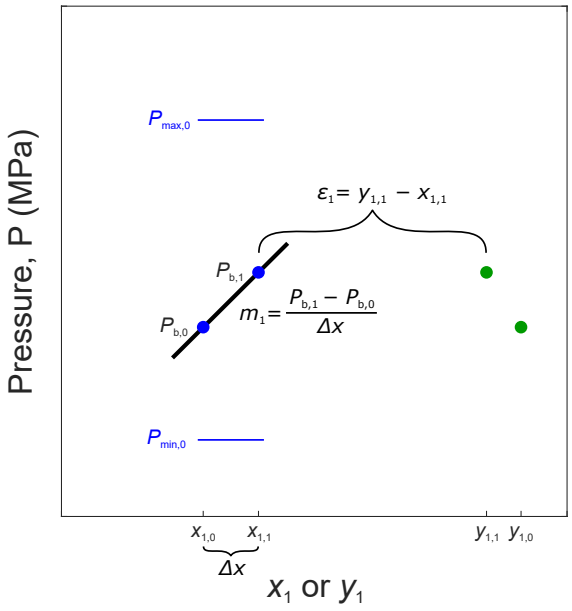

Figure A.3: Graphical illustration of the initialization of our numerical method used to calculate the critical composition at a given temperature, as described by the boxes outlined in blue at the top of Figure A.4.

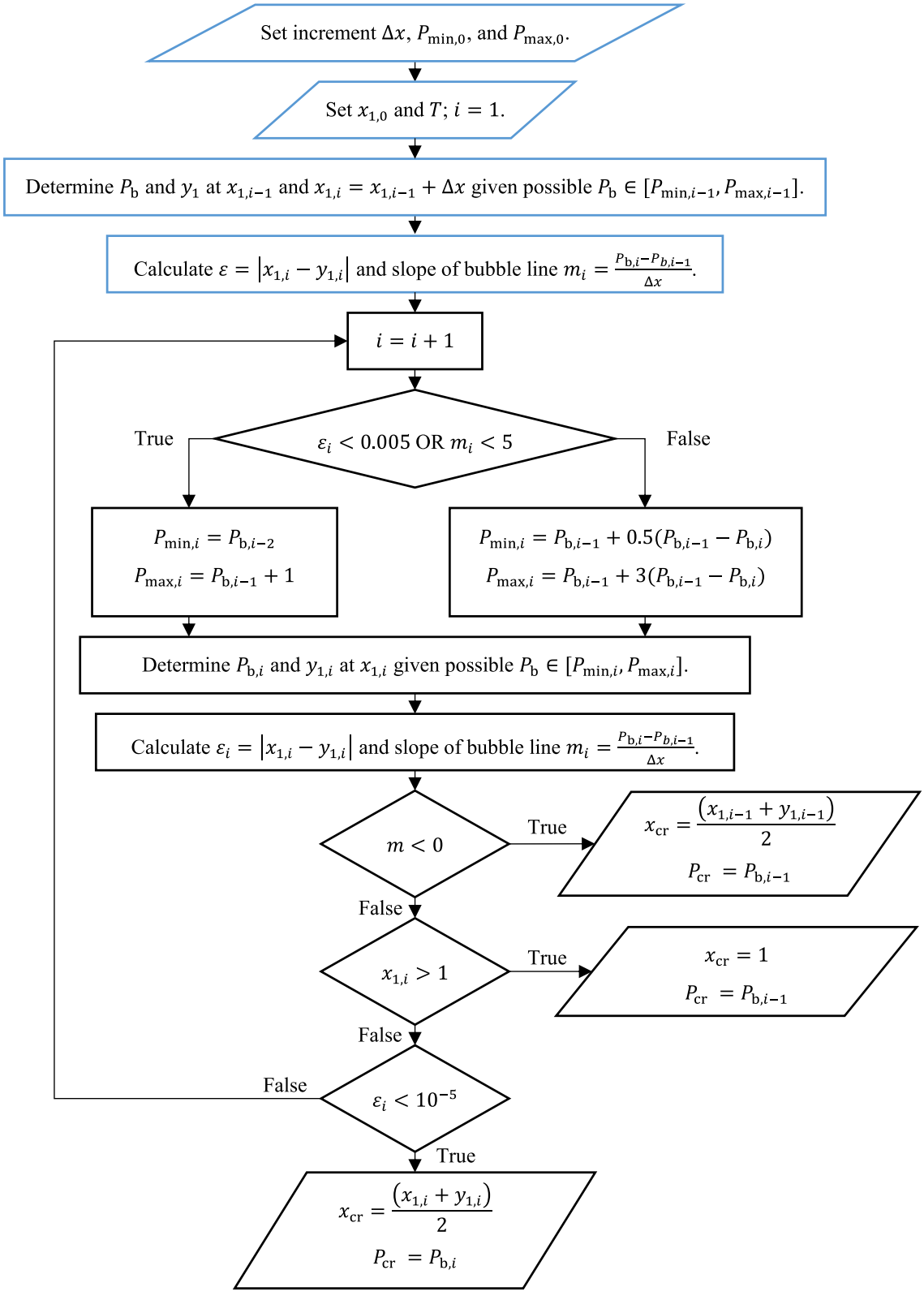

Figure A.4: Flowchart for calculating the critical composition of a mixture at a temperature T.

A.3 Our Model for Surface Tension

All equations and data needed for the implementation of our new model of surface tension as a function of composition and temperature are given in Chapter 3, except for the coefficients for the Mulero *et al.* [33] correlation used for pure-species surface tension as a function of temperature for supercritical mixtures. These coefficients previously published by Mulero *et al.* [33] are given below.

A.3.1 Pure Component Surface Tension

For all mixtures containing methane or carbon dioxide, we use the Mulero *et al.* [33] correlation to calculate pure component surface tension, which uses the coefficients in Table A.4 substituted into Equation (3.6) in Chapter 3.

Table A.4: Coefficients from Mulero *et al.* [33] for use in Equation (3.6) in Chapter 3 $\left[\sigma_i = \sum_{j=0}^{m_i} \sigma_{j,i} \left(1 - \frac{T}{T_{\mathrm{cr},i}}\right)^{p_{j,i}}\right]$ for pure components.

Component	Temperatures [K]	σ_0	p_0	σ_1	p_1	σ_2	p_2
methane	90.67–188.84	0.03825	1.191	−0.00602	5.422	−0.00071	0.6161
ethane	89.87–304.93	0.07602	1.32	−0.02912	1.676		
propane	193.15–366.48	0.05334	1.235	−0.01748	4.404		
n-butane	134.84–420.00	0.05138	1.209				
n-pentane	144.18–469.67	0.08015	1.408	0.004384	1.031	−0.03437	1.818
n-hexane	173.15–507.39	0.210952	1.0962	−0.15849	1.05893		
n-heptane	183.00–540.08	0.07765	1.319	−0.02599	1.6		
n-octane	218.00–568.56	0.34338	1.6607	−0.50634	1.9632	0.2238	2.3547
n-nonane	223.00–393.15	0.05388	1.262				
n-decane	243.00–443.15	0.05473	1.29				
carbon dioxide	216.55–304.11	0.07863	1.254				

A.4 Parachor Model for Surface Tension

For comparison with our work, we also calculated surface tension using the previously available and commonly used parachor model. In this section, we outline the governing equations for this model, and we summarize the coefficients that we use when making calculations with this model for both pure components and mixtures.

A.4.1 Pure Component Surface Tension

The parachor model for a pure compound is given by [30, 61]:

$$\sigma_i = \left[\mathscr{P}_i \left(\frac{1}{v^{\mathrm{L}}} - \frac{1}{v^{\mathrm{V}}} \right) \right]^4, \tag{A.21}$$

where liquid and vapor molar volumes (v^{L} and v^{V}, respectively) are calculated using the Peng–Robinson equation of state with volume translation at the condition where the chemical potential of the liquid phase equals the chemical potential of the vapor phase.

For mixtures containing methane or carbon dioxide, we fit the parachor model to experimental data of surface tension as a function of temperature retrieved from the DIPPR database [9], with fitting results for the parachor, $\mathscr{P}_i$, summarized in Table A.5. For mixtures containing both compounds below their critical points, the parachor model is fit separately to data from each literature source, yielding the coefficients listed in Table A.6. Note that some compounds appear more than once because of overlap between binary mixtures; the parachor values for any individual compound are statistically the same based on the listed 95% confidence intervals.

Table A.5: Parachor values with 95% confidence intervals determined from a fit of Equation (A.21) to experimental data of surface tension *vs.* temperature from the DIPPR database [9] for each pure component making up mixtures containing either methane or carbon dioxide, where molar volumes are determined using the PR-EOS with volume shift. The number of data points used in the fit (n), the temperature range of the experimental data, and the standard deviation (SD) are also listed.

Component	n	Temperatures [K]	Parachor $\mathscr{P}_i$ [(mN·m^{-1})$^{1/4}$ cm^3·mol^{-1}]	SD [mN/m]
methane	16	93.15–173.15	72.9 ± 0.5	0.646
ethane	27	117.8–296.1	112.8 ± 0.3	0.524
propane	19	193.15–360.93	151.7 ± 1.4	0.662
n-butane	22	203.15–313.15	191.4 ± 0.4	0.321
n-pentane	11	253.15–313.15	231.4 ± 0.4	0.194
n-hexane	29	273.15–493.15	269.7 ± 0.6	0.304
n-heptane	31	283.15–503.15	311.1 ± 0.9	0.427
n-octane	43	233.15–503.15	355.2 ± 1.2	0.728
n-nonane	12	283.15–393.15	391.8 ± 2.3	0.689
n-decane	12	283.15–393.15	435.3 ± 2.8	0.811
carbon dioxide	70	216.55–301.06	77.6 ± 0.5	0.650

Table A.6: Parachor values with 95% confidence intervals determined from a fit of Equation (A.21) to experimental data of surface tension *vs.* temperature for each pure component in mixtures at states below both components' critical point obtained from the listed references, where molar volumes are determined using the PR-EOS with volume shift. The number of data points used in the fit (n), the temperature range of the experimental data, the standard deviation (SD), and the literature source are also listed.

Component	n	Temperatures [K]	Parachor $\mathscr{P}_i$ $[(\mathrm{mN{\cdot}m^{-1}})^{1/4}\ \mathrm{cm^3{\cdot}mol^{-1}}]$	SD [mN/m]	Data Reference
dodecane(1)	4	298–313	519.0 ± 1.4	0.160	Schmidt *et al.*
benzene(2)	4		207.2 ± 0.5	0.152	[53]
n-hexane(1)	4	298–313	269.8 ± 0.5	0.077	Schmidt *et al.*
benzene(2)	4		207.2 ± 0.5	0.152	[53]
cyclohexane(1)	4	293–313	242.3 ± 0.6	0.156	Herrmann
benzene(2)	4		207.2 ± 0.4	0.121	[18, 69]
carbon tetrachloride(1)	5	288–308	221.6 ± 0.6	0.229	Teixiera *et al.*
methyl iodide(2)	5		155.4 ± 0.3	0.192	[63]
carbon tetrachloride(1)	5	298–318	221.0 ± 0.6	0.156	Teixiera *et al.*
acetonitrile(2)	5		133.1 ± 0.6	0.121	[63]
carbon tetrachloride(1)	6	293–318	221.6 ± 0.3	0.229	Luengo *et al.*
carbon disulfide(2)	6		136.5 ± 0.1	0.192	[29]
dichloromethane(1)	4	293–308	153.8 ± 0.2	0.223	Aracil *et al.*
carbon disulfide(2)	4		136.4 ± 0.1	0.366	[4]

A.4.2 Mixture Surface Tension

The parachor model for mixtures is, for a binary mixture, [66]

$$\sigma_{\text{mix}} = \left[\mathscr{P}_1 \left(\frac{x_1}{v^{\text{L}}} - \frac{y_1}{v^{\text{V}}} \right) + \mathscr{P}_2 \left(\frac{x_2}{v^{\text{L}}} - \frac{y_2}{v^{\text{V}}} \right) \right]^4 . \tag{A.22}$$

For making predictions using Equation (A.22), we use parachor values taken from Table A.5 or Table A.6, vapor and liquid mole fractions from vapor–liquid equilibrium calculations using the PR-EOS, and molar volumes of the vapor and liquid phases also from the PR-EOS with volume translation for the mixture. For supercritical mixtures, vapor and liquid mole fractions are determined via flash calculations given the experimental pressure and an overall composition z_1 that is inputted as an initial guess to the algorithm. For subcritical mixtures, the compositions reported in the literature are assumed to be liquid-phase compositions, and bubble-point calculations are carried out using the PR-EOS to determine the vapor-phase composition that is in equilibrium with the liquid phase for substitution into Equation (A.22).

A.5 Mixture Surface Tension *vs.* Composition and Temperature

In this section, we first provide an overview of the experimental literature available for binary mixtures. Then, we show all predictions of surface tension for all mixtures.

A.5.1 Overview of Experimental Data

Tables A.7 and Table A.8 list all experimental datasets containing methane or carbon dioxide that were assessed for agreement with other datasets and fitting suitability. Only those manuscripts with more than one temperature are considered so that the predictive ability of our model can be tested at higher temperatures (one exception is methane(1) + *n*-hexane(2) where fitting was done to data in Massoudi and King [31] and predictions were made for data in Niño–Amézquita *et al.* [38], because there were insufficient data points for fitting to the lowest temperature in Niño–Amézquita *et al.* [38]).

The primary reason for excluding a dataset for mixtures containing methane or carbon dioxide was a discrepancy between references in the low-pressure limit (*i.e.*, as the mole fraction of the more volatile component approaches zero). The second reason for exclusion was that the available data yielded very large fitting confidence intervals on coefficients (> 10, reaching 10^8 for, *e.g.*, carbon dioxide(1) + *n*-decane(2) from Pereira *et al.* [44]).

Table A.7: Compilation of available experimental data of surface tension for methane(1) + *n*-alkane(2) mixtures with more than one temperature reported (partially from the compilation in Pereira [43]). An asterisk in the column "Included in Chapter 3?" indicates that data from that reference was used for fitting; fitting coefficients thus obtained were then used to make predictions for all listed references of that system.

methane(1) +	Data Reference	Included in Chapter 3?	Reason for exclusion or other notes
ethane(2)	Baidakov *et al.* [6]	✓*	Note that data at 93.15 K were not included because there are no mixture data reported at this temperature—only pure component data.
propane(2)	Weinaug and Katz [66]	✓*	Note that the liquid compositions reported in Ref. [66] were not measured by the authors, but rather, interpolated or extrapolated from phase equilibrium data from another source.
	Seneviratne *et al.* [54]	✓	Note that 363.15 K only has one data point for pure propane; no mixture data.
n-butane(2)	Pennington and Hough [36, 42]	✓*	Note that this dataset has a limited range of experimental compositions for fitting (only six values of x_1 ranging from 0.40 to 0.48).
n-pentane(2)	Amin and Smith [3]	✗	Excluded because surface tension data for reported temperatures above 311 K are much too high, as noted previously by other researchers [26]; see Section A.6.1 for further discussion.
n-hexane(2)	Massoudi and King [31]	✓*	Note that this dataset was used for fitting at 298.15 K. Also note that this data was digitized from a figure, and the point at the lowest pressure of ∼0.02 MPa was excluded because it was obscured by another data point.
	Niño–Amézquita *et al.* [38]	✓	Note that fitting at 300 K gave very large coefficients, so this dataset was predicted at 300 K and 350 K based on the fit to data in Massoudi and King [31].
n-heptane(2)	Warren and Hough [65]	✓	Note that the reported data is smoothed.
	Amin and Smith [3]	✓*	
n-octane(2)	Peng *et al.* [40]	✗	Excluded because the limiting value of surface tension for pure *n*-octane does not agree with the Mulero correlation [33] (see Equation (3.6) in Chapter 3), and this leads to extreme values for fitting coefficients. See Section A.6.2 for further discussion of this dataset.
n-nonane(2)	Deam and Maddox [8]	✗	Excluded because this dataset has very few experimental compositions for fitting (only four values of x_1 ranging from 0.08 to 0.41) that, when fit to, yield large confidence intervals. See Section A.6.3 for further discussion.

Table A.7 – continued from previous page

methane(1) +	Data Reference	Included in Chapter 3?	Reason for exclusion or other notes
n-decane(2)	Stegemeier *et al.* [60]	✓*	
	Amin and Smith [3]	✓	Note that the low-pressure data is higher than expected, an observation also noted by Li and Firoozabadi [26] and Pereira *et al.* [44].
	Pereira *et al.* [44]	✓	Note that the limit of surface tension for pure *n*-decane is slightly lower than the Mulero correlation [33] (see Equation (3.6)).

Table A.8: Compilation of available experimental data of surface tension for carbon dioxide(1) + *n*-alkane(2) mixtures with more than one temperature reported (partially from the compilation in Pereira [43]). An asterisk in the column "Included in Chapter 3?" indicates that data from that reference was used for fitting; fitting coefficients thus obtained were then used to make predictions for all listed references of that system.

carbon dioxide(1) +	Data Reference	Included in Chapter 3?	Reason for exclusion or other notes
n-butane(2)	Hsu *et al.* [19]	✓*	
n-heptane(2)	Niño-Amézquita *et al.* [37]	✓*	
	Jaeger *et al.* [20]	✓	
	Zolghadr *et al.* [70]	✗	Excluded because the limiting value of surface tension for pure *n*-heptane is up to 2 mN/m lower than the Mulero correlation [33] (see Equation (3.6) in Chapter 3), and data at 353 K is consistently lower than reported in Niño-Amézquita *et al.* [37] and Jaeger *et al.* [20] for this system. See Section A.6.4 for further discussion of this dataset.
n-decane(2)	Nagarajan and Robinson [34]	✗	Excluded because the available datasets yielded very large fitting coefficients. See Section A.6.5 for further discussion of these datasets.
	Georgiadis *et al.* [15]	✗	
	Pereira *et al.* [44]	✗	

Table A.9 summarizes all considered subcritical mixtures with notes on agreement with other datasets, details on fitting, and a corrected data point.

Table A.9: Compilation of available experimental data of surface tension for subcritical mixtures with more than one temperature reported (partially from a compilation by Escobedo and Mansoori [11]). An asterisk in the column "Included in Chapter 3?" indicates that data from that reference was used for fitting; fitting coefficients thus obtained were then used to make predictions for all listed references of that system.

(1)	(2)	Data Reference	Included in Chapter 3?	Reason for exclusion or other notes
dodecane	benzene	Schmidt *et al.* [53]	✓*	
n-hexane	benzene	Schmidt *et al.* [53]	✓*	
cyclohexane	benzene	Suri and Ramakrishna [62]	✗	Excluded because data at 303.15 K are too high when compared to both Lam and Benson [25] and Herrmann [18, 69] at the same temperature. See Section A.6.6 for further discussion of this dataset.
		Lam and Benson [25]	✓	
		Konobeev and Lyapin [24, 69]	✓	
		Herrmann [18, 69]	✓*	Note that fitting coefficients for both pure components and the mixture were obtained with data from this reference.
carbon tetrachloride	methyl iodide	Teixeira *et al.* [63]	✓*	
carbon tetrachloride	acetonitrile	Teixeira *et al.* [63]	✓*	Note that Table II in this paper lists a value of 24.45 mN/m at $x_{CH_3CN} = 0.5204$ but Figure 2 therein shows a surface tension of 25.45 mN/m when digitized; we use 25.45 mN/m as the experimental value.
carbon tetrachloride	carbon disulfide	Luengo *et al.* [29]	✓*	
dichloromethane	carbon disulfide	Aracil *et al.* [4]	✓*	

A.5.2 Predictions

For the nonaqueous binary mixtures included in Chapter 3, we plot predicted surface tension *vs.* experimental surface tension for predictions from our model and for predictions from the parachor model in Figure A.5. These plots highlight the closer agreement of our model along the identity line ($y = x$) compared to the parachor model. In addition to a generally closer agreement over all studied systems, our model does not require the use of an equation of state to determine molar volumes at all temperatures of interest for prediction.

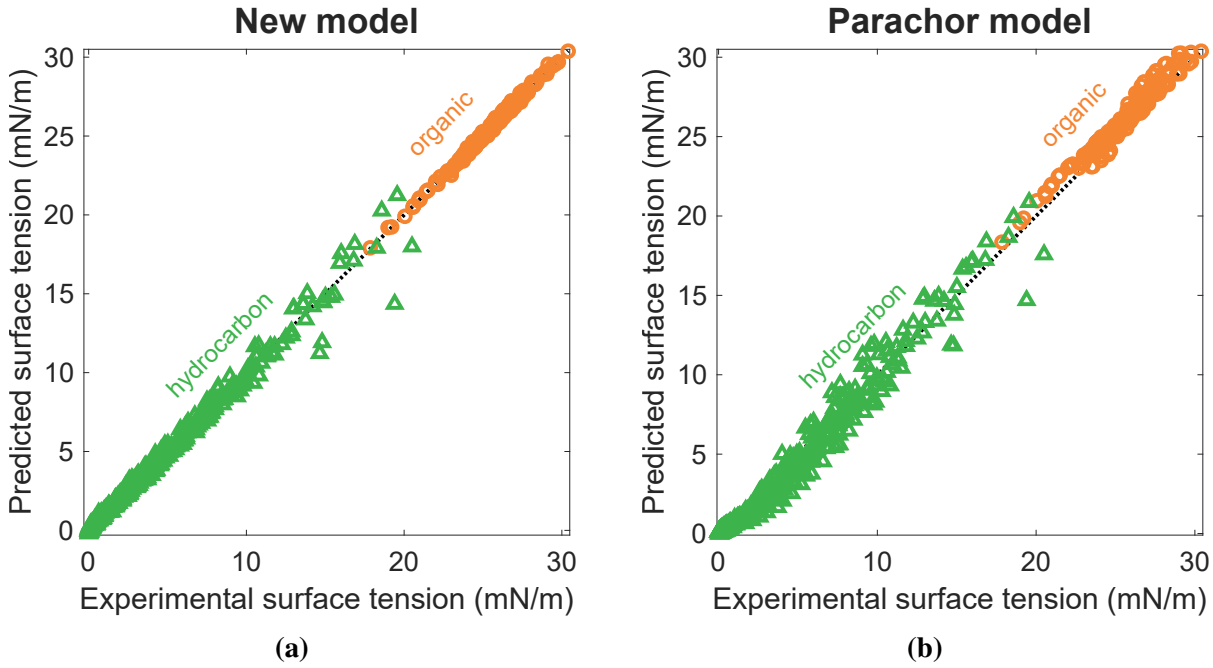

Figure A.5: Predicted surface tension *vs.* experimental surface tension for mixtures containing methane or carbon dioxide (△) and for other organic mixtures (○) using (a) our new model (Equation (3.2) in Chapter 3) and (b) the parachor model for mixtures (Equation (A.22)).

In the subsequent subsections, vapor–liquid equilibrium calculations and surface tension fits/predictions are illustrated for all mixtures listed in Table A.7 to Table A.9. Vapor–liquid equilibrium calculations for all mixtures are performed using the Peng–Robinson equation of state (Equations (A.2)–(A.12)). When illustrating surface tension as a function of composition or pressure, plots with lines labeled "New model fit" are obtained using Equation (3.2) in Chapter 3 as a function of composition, as fit to the experimental surface tension data depicted by black open circles. For all subcritical mixtures, surface tension is only plotted as a function of liquid-phase composition (and not as a function of pressure), because the properties of subcritical mixtures with components that are both relatively non-volatile are generally independent of pressure. Lines labeled "New model prediction" are calculated using Equation (3.2) in Chapter 3 as a function of composition and temperature. Equation (3.2) in Chapter 3 uses

fitting coefficients *a* and *b*, as summarized in Table 3.2 in Chapter 3, and the pure component parameters listed in Table 3.1 in Chapter 3 and Table A.4. Dotted lines labeled "Parachor prediction" are calculated using Equation (A.22) with the pure-component parachor values listed in Table A.5 and Table A.6.

A.5.2.1 Methane(1) + Ethane(2)

Figure A.6(a) shows the calculated phase envelopes of methane(1) + ethane(2) at the temperatures reported in Baidakov *et al.* [6]. At the pressures reported in Baidakov *et al.* [6], we depict our calculated liquid-phase compositions and vapor-phase compositions with + and $\times$ symbols, respectively. Using the algorithm presented in Figure A.4, the critical composition of the binary mixture is calculated at each temperature, as shown by the $\square$ symbols. In Figures A.6(b) and (c), surface tension calculated using Equation (3.2) in Chapter 3 is compared to experimental measurements from Baidakov *et al.* [6] as a function of liquid-phase composition and pressure, respectively. Figures A.6(d) and (e) show the difference between predicted surface tension and surface tension measured experimentally by Baidakov *et al.* [6] when using our new model (Equation (3.2) in Chapter 3) and the parachor model (Equation (A.22)), respectively.

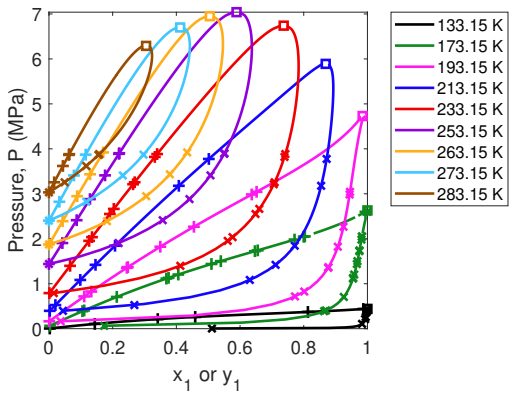

(a) Calculated liquid (+) and vapor (×) compositions at the temperatures and pressures in Baidakov *et al.* [6] and the calculated critical compositions (□) obtained using the algorithm in Figure A.4.

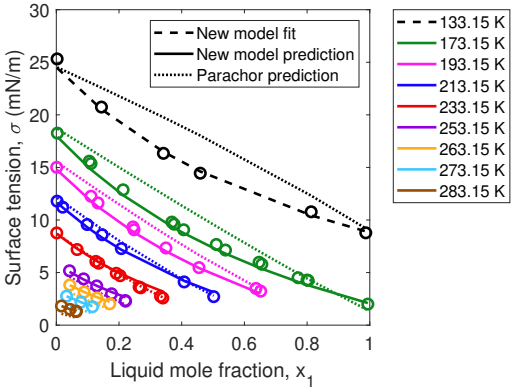

(b) Surface tension fit (black dashed line) and predictions (solid lines) *vs.* liquid composition at elevated temperatures using our new model. Parachor predictions are shown by dotted lines.

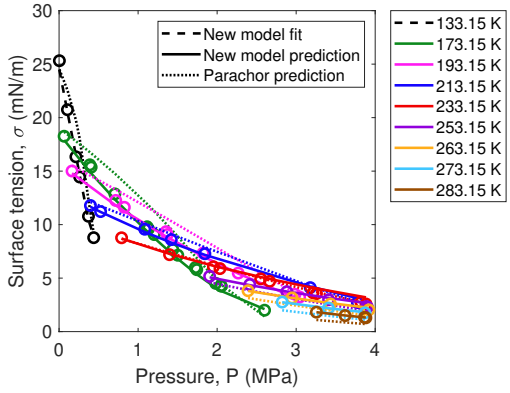

(c) Same as (b), but *vs.* pressure.

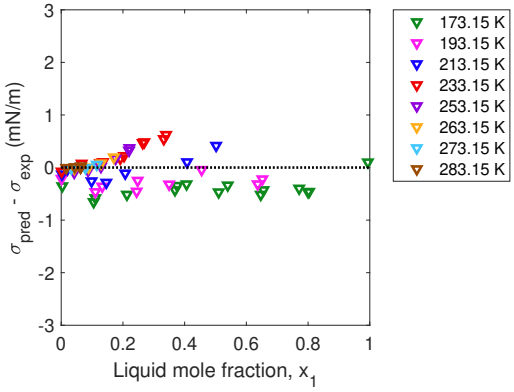

(d) Difference between predicted and experimental surface tension as a function of composition using our new model (▽).

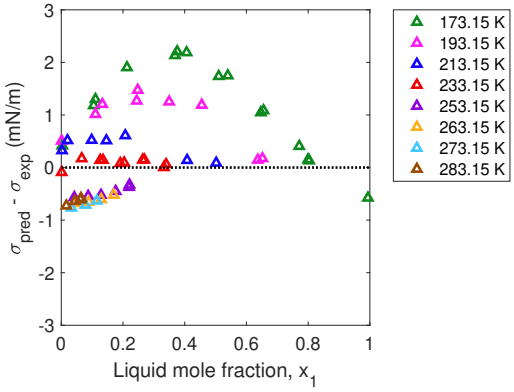

(e) Difference between predicted and experimental surface tension as a function of composition using the parachor model (△).

Figure A.6: Results for methane(1) + ethane(2) with data (○) from Baidakov *et al.* [6].

A.5.2.2 Methane(1) + Propane(2)

Figure A.7(a) shows the calculated phase envelopes of methane(1) + propane(2) at the temperatures reported in Weinaug and Katz [66]. At the pressures reported in Weinaug and Katz [66], we depict our calculated liquid-phase compositions and vapor-phase compositions with + and $\times$ symbols, respectively. Using the algorithm presented in Figure A.4, the critical composition of the binary mixture is calculated at each temperature, as shown by the $\square$ symbols. In Figures A.7(b) and (c), surface tension calculated using Equation (3.2) in Chapter 3 is compared to experimental measurements from Weinaug and Katz [66] as a function of liquid-phase composition and pressure, respectively. Figures A.7(d) and (e) show the difference between predicted surface tension and surface tension measured experimentally by Weinaug and Katz [66] when using our new model (Equation (3.2) in Chapter 3) and the parachor model (Equation (A.22)), respectively.

Figure A.8(a) shows the calculated phase envelopes of methane(1) + propane(2) at the temperatures reported in Seneviratne *et al.* [54]. At the pressures reported in Seneviratne *et al.* [54], we depict our calculated liquid-phase compositions and vapor-phase compositions with + and $\times$ symbols, respectively. Using the algorithm presented in Figure A.4, the critical composition of the binary mixture is calculated at each temperature, as shown by the $\square$ symbols. In Figures A.8(b) and (c), surface tension calculated using Equation (3.2) in Chapter 3 with fitting coefficients obtained from data in Weinaug and Katz [66] is compared to experimental measurements from Seneviratne *et al.* [54] as a function of liquid-phase composition and pressure, respectively. Figures A.8(d) and (e) show the difference between predicted surface tension and surface tension measured experimentally by Seneviratne *et al.* [54] when using our new model (Equation (3.2) in Chapter 3) and the parachor model (Equation (A.22)), respectively.

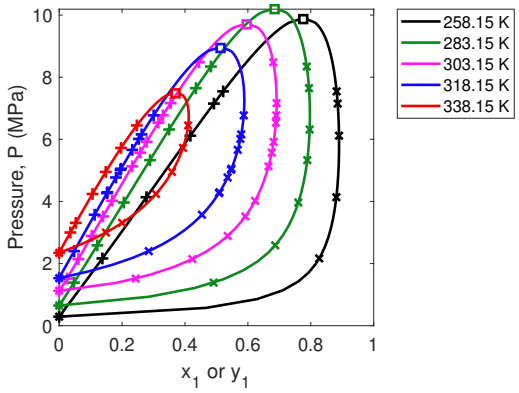

(a) Calculated liquid (+) and vapor (×) compositions at the temperatures and pressures in Weinaug and Katz [66] and the calculated critical compositions (□) obtained using the algorithm in Figure A.4.

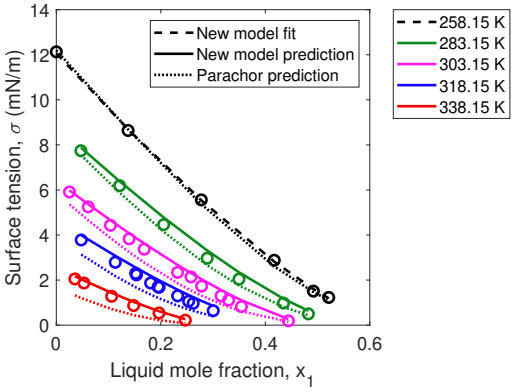

(b) Surface tension fit (black dashed line) and predictions (solid lines) *vs.* liquid composition at elevated temperatures using our new model. Parachor predictions are shown by dotted lines.

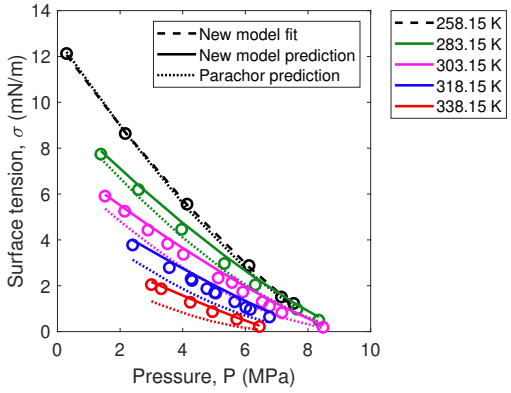

(c) Same as (b), but *vs.* pressure.

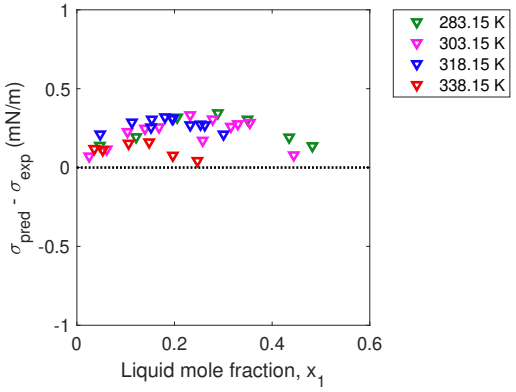

(d) Difference between predicted and experimental surface tension as a function of composition using our new model (▽).

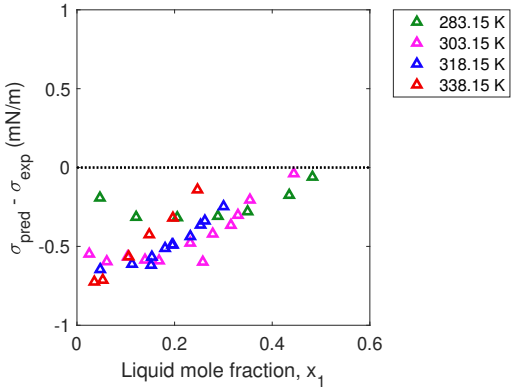

(e) Difference between predicted and experimental surface tension as a function of composition using the parachor model (△).

Figure A.7: Results for methane(1) + propane(2) with data (○) from Weinaug and Katz [66].

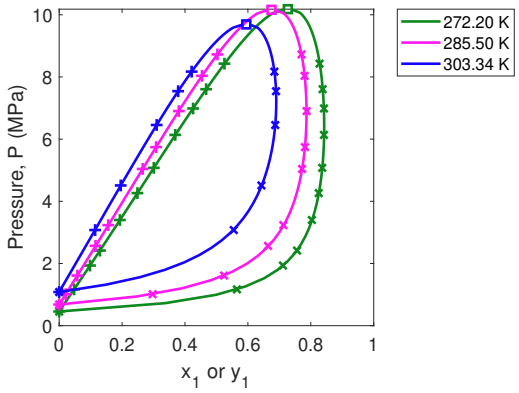

(a) Calculated liquid (+) and vapor (×) compositions at the temperatures and pressures in Seneviratne *et al.* [54] and the calculated critical compositions (□) obtained using the algorithm in Figure A.4.

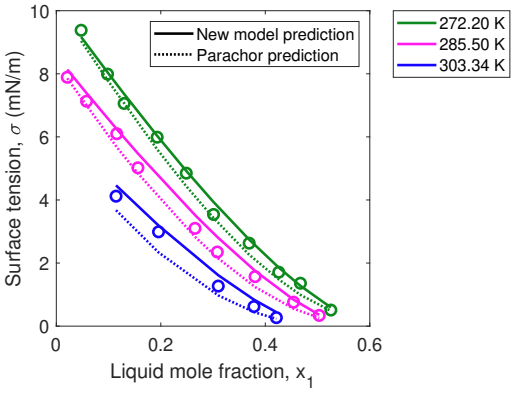

(b) Surface tension predictions using our new model (solid lines) *vs.* liquid composition at elevated temperatures. Parachor predictions are shown by dotted lines.

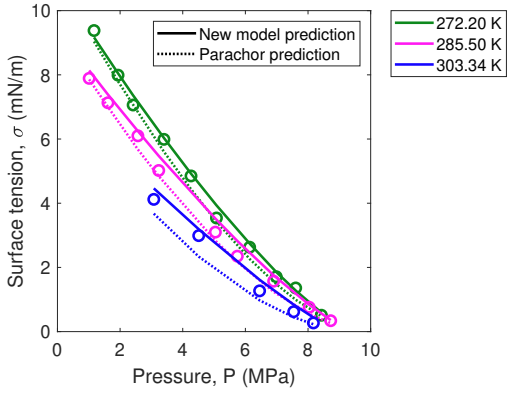

(c) Same as (b), but *vs.* pressure.

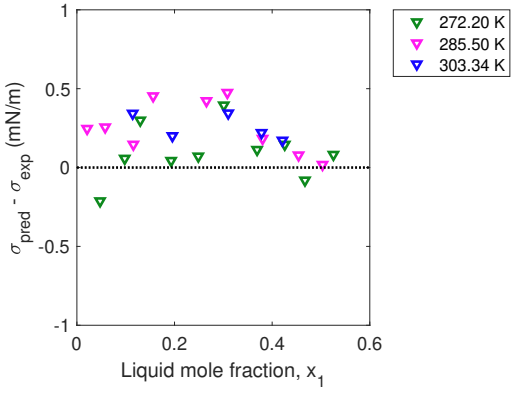

(d) Difference between predicted and experimental surface tension as a function of composition using our new model (▽).

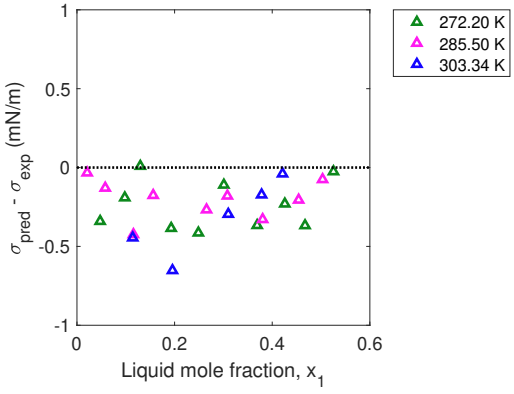

(e) Difference between predicted and experimental surface tension as a function of composition using the parachor model (△).

Figure A.8: Results for methane(1) + propane(2) with data (○) from Seneviratne *et al.* [54].

A.5.2.3 Methane(1) + *n*-Butane(2)

Figure A.9(a) shows the calculated phase envelopes of methane(1) + *n*-butane(2) at the temperatures reported by Pennington and Hough, as digitized from Nilssen [36, 42]. At the pressures reported in Nilssen [36, 42], we depict our calculated liquid-phase compositions and vapor-phase compositions with + and $\times$ symbols, respectively. Using the algorithm presented in Figure A.4, the critical composition of the binary mixture is calculated at each temperature, as shown by the $\square$ symbols. In Figures A.9(b) and (c), surface tension calculated using Equation (3.2) in Chapter 3 is compared to experimental measurements from Nilssen [36, 42] as a function of liquid-phase composition and pressure, respectively. Figures A.9(d) and (e) show the difference between predicted surface tension and surface tension measured experimentally by Nilssen [36, 42] when using our new model (Equation (3.2) in Chapter 3) and the parachor model (Equation (A.22)), respectively.

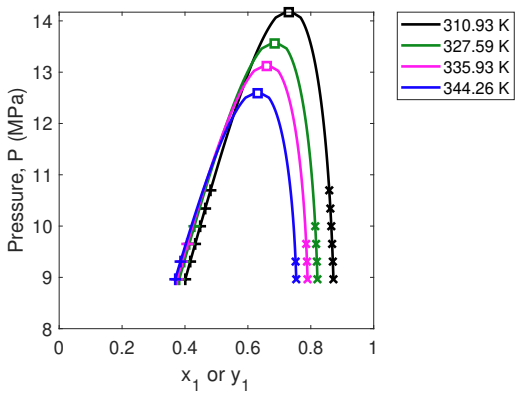

(a) Calculated liquid (+) and vapor (×) compositions at the temperatures and pressures in Nilssen [36, 42] and the calculated critical compositions (□) obtained using the algorithm in Figure A.4.

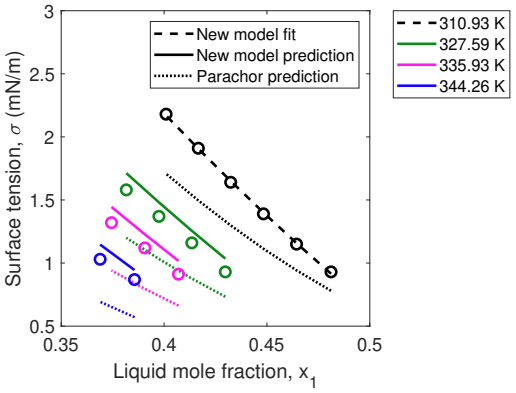

(b) Surface tension fit (black dashed line) and predictions (solid lines) *vs.* liquid composition at elevated temperatures using our new model. Parachor predictions are shown by dotted lines.

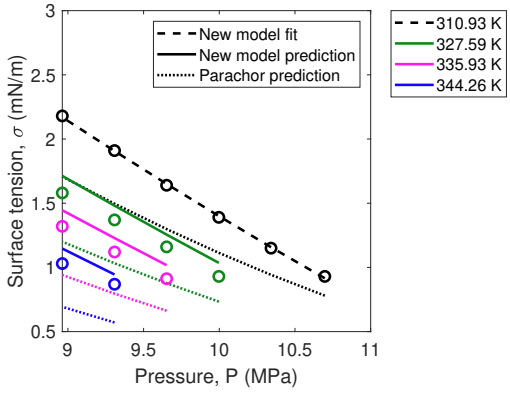

(c) Same as (b), but *vs.* pressure.

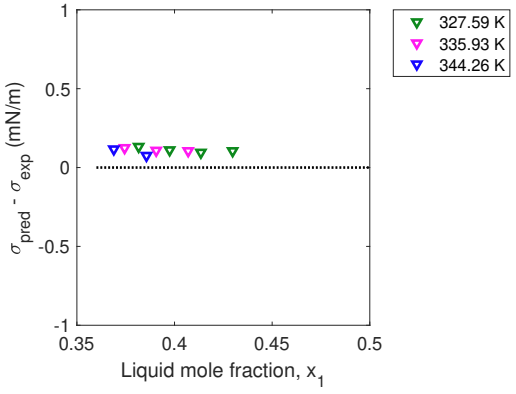

(d) Difference between predicted and experimental surface tension as a function of composition using our new model (▽).

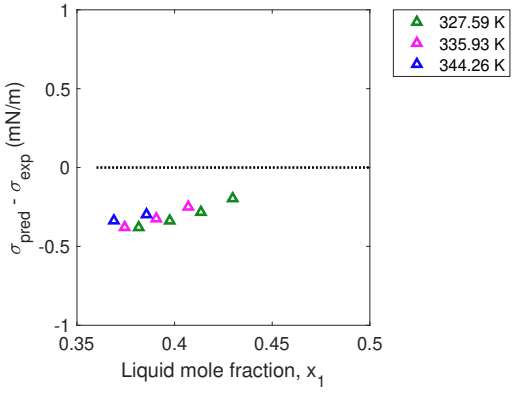

(e) Difference between predicted and experimental surface tension as a function of composition using the parachor model (△).

Figure A.9: Results for methane(1) + *n*-butane(2) with data (○) from Nilssen [36, 42].

A.5.2.4 Methane(1) + *n*-Hexane(2)

Figure A.10(a) shows the calculated phase envelope of methane(1) + *n*-hexane(2) at the temperature reported in Massoudi and King [31]. At the pressures reported in Massoudi and King [31], we depict our calculated liquid-phase compositions and vapor-phase compositions with + and × symbols, respectively. Using the algorithm presented in Figure A.4, the critical composition of the binary mixture is calculated at the relevant temperature, as shown by the □ symbol. In Figures A.10(b) and (c), surface tension fit using Equation (3.2) in Chapter 3 is compared to experimental measurements from Massoudi and King [31] as a function of liquid-phase composition and pressure, respectively.

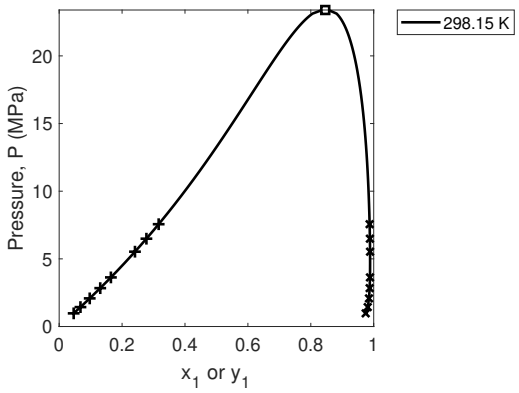

(a) Calculated liquid (+) and vapor (×) compositions at the temperature and pressures in Massoudi and King [31] and the calculated critical composition (□) obtained using the algorithm in Figure A.4.

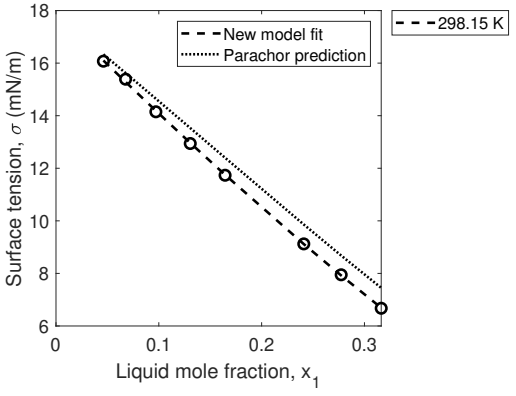

(b) Surface tension fit (black dashed line) *vs.* liquid composition using our new model. Parachor predictions are shown by a dotted line.

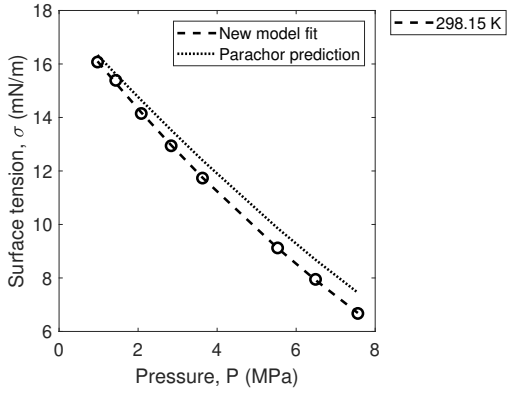

(c) Same as (b), but *vs.* pressure.

Figure A.10: Results for methane(1) + *n*-hexane(2) with data (○) from Massoudi and King [31].

Figure A.11(a) shows the calculated phase envelopes of methane(1) + *n*-hexane(2) at the temperatures reported in Niño–Amézquita *et al.* [38]. At the pressures reported in Niño–Amézquita *et al.* [38], we depict our calculated liquid-phase compositions and vapor-phase compositions with + and $\times$ symbols, respectively. Using the algorithm presented in Figure A.4, the critical composition of the binary mixture is calculated at each temperature, as shown by the $\square$ symbols. In Figures A.11(b) and (c), surface tension calculated using Equation (3.2) in Chapter 3 with fitting coefficients obtained from data in Massoudi and King [31] is compared to experimental measurements from [38] as a function of liquid-phase composition and pressure, respectively. Figures A.11(d) and (e) show the difference between predicted surface tension and surface tension measured experimentally by Niño–Amézquita *et al.* [38] when using our new model (Equation (3.2) in Chapter 3) and the parachor model (Equation (A.22)), respectively.

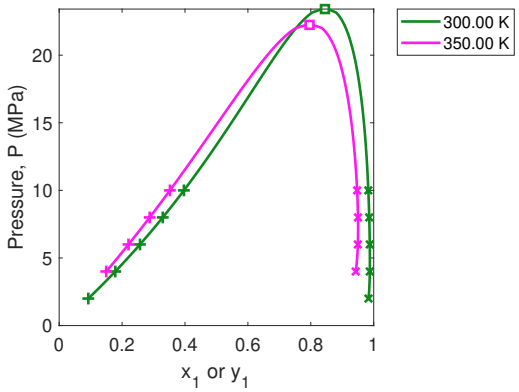

(a) Calculated liquid (+) and vapor (×) compositions at the temperatures and pressures in Niño–Amézquita *et al.* [38] and the calculated critical compositions (□) obtained using the algorithm in Figure A.4.

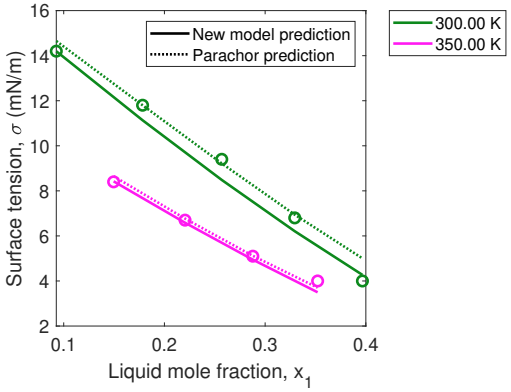

(b) Surface tension predictions using our new model (solid lines) *vs.* liquid composition at elevated temperatures. Parachor predictions are shown by dotted lines.

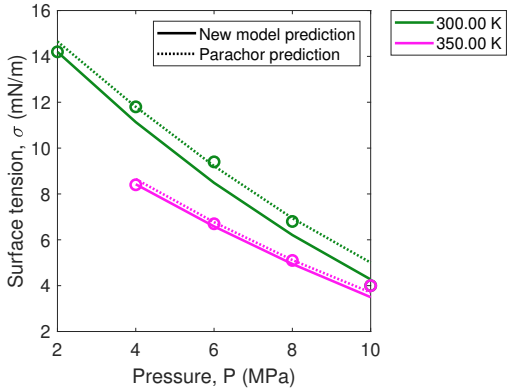

(c) Same as (b), but *vs.* pressure.

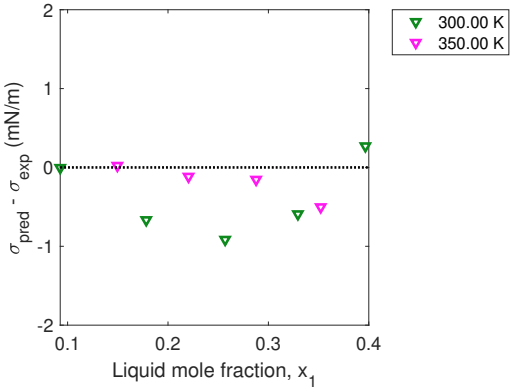

(d) Difference between predicted and experimental surface tension as a function of composition using our new model (▽).

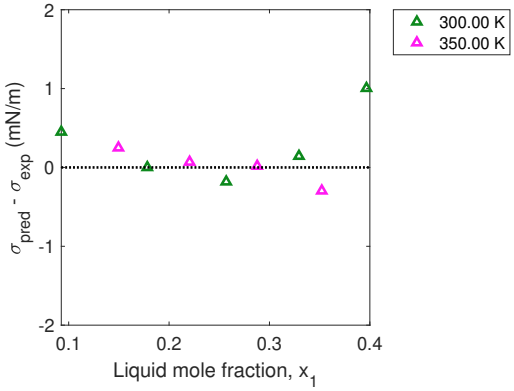

(e) Difference between predicted and experimental surface tension as a function of composition using the parachor model (△).

Figure A.11: Results for methane(1) + *n*-hexane(2) with data (○) from Niño–Amézquita *et al.* [38].

A.5.2.5 Methane(1) + *n*-Heptane(2)

Figure A.12(a) shows the calculated phase envelopes of methane(1) + *n*-heptane(2) at the temperatures reported in Warren and Hough [65]. At the pressures reported in Warren and Hough [65], we depict our calculated liquid-phase compositions and vapor-phase compositions with + and $\times$ symbols, respectively. Using the algorithm presented in Figure A.4, the critical composition of the binary mixture is calculated at each temperature, as shown by the $\square$ symbols. In Figures A.12(b) and (c), surface tension calculated using Equation (3.2) in Chapter 3 with fitting coefficients obtained from data in Amin and Smith [3] is compared to experimental measurements from Warren and Hough [65] as a function of liquid-phase composition and pressure, respectively. Figures A.12(d) and (e) show the difference between predicted surface tension and surface tension measured experimentally by Warren and Hough [65] when using our new model (Equation (3.2) in Chapter 3) and the parachor model (Equation (A.22)), respectively.

Figure A.13(a) shows the calculated phase envelopes of methane(1) + *n*-heptane(2) at the temperatures reported in Amin and Smith [3]. At the pressures reported in Amin and Smith [3], we depict our calculated liquid-phase compositions and vapor-phase compositions with + and $\times$ symbols, respectively. Using the algorithm presented in Figure A.4, the critical composition of the binary mixture is calculated at each temperature, as shown by the $\square$ symbols. In Figure A.13(b) and (c), surface tension calculated using Equation (3.2) in Chapter 3 is compared to experimental measurements from Amin and Smith [3] as a function of liquid-phase composition and pressure, respectively. Figures A.13(d) and (e) show the difference between predicted surface tension and surface tension measured experimentally by Amin and Smith [3] when using our new model (Equation (3.2) in Chapter 3) and the parachor model (Equation (A.22)), respectively.

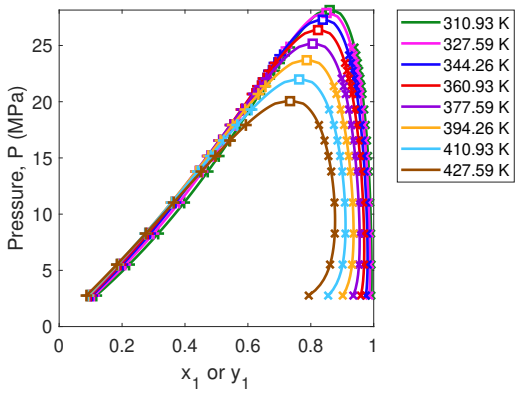

(a) Calculated liquid (+) and vapor (×) compositions at the temperatures and pressures in Warren and Hough [65] and the calculated critical compositions (□) obtained using the algorithm in Figure A.4.

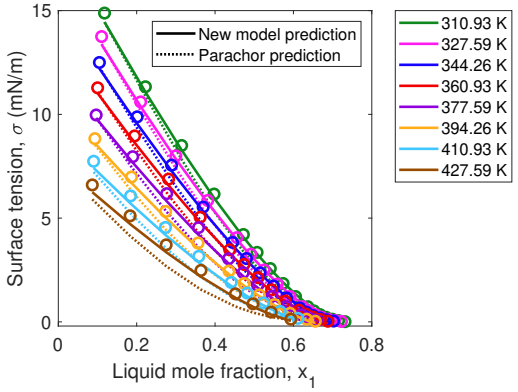

(b) Surface tension predictions (solid lines) *vs.* liquid composition at elevated temperatures using our new model. Parachor predictions are shown by dotted lines.

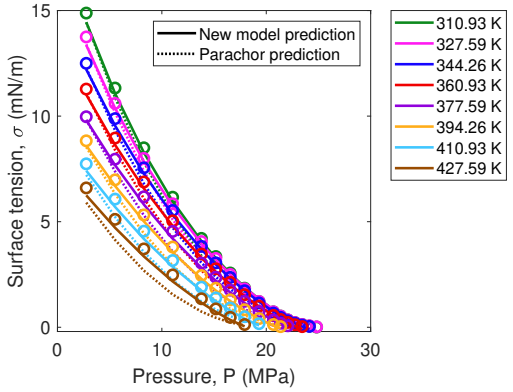

(c) Same as (b), but *vs.* pressure.

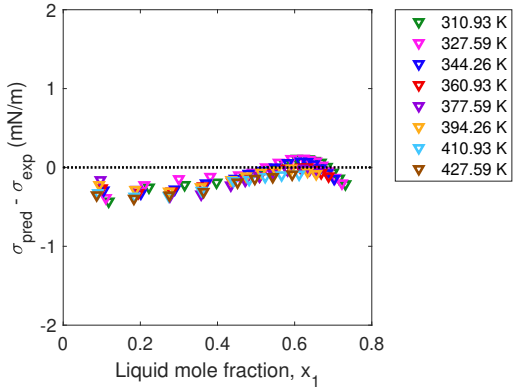

(d) Difference between predicted and experimental surface tension as a function of composition using our new model (▽).

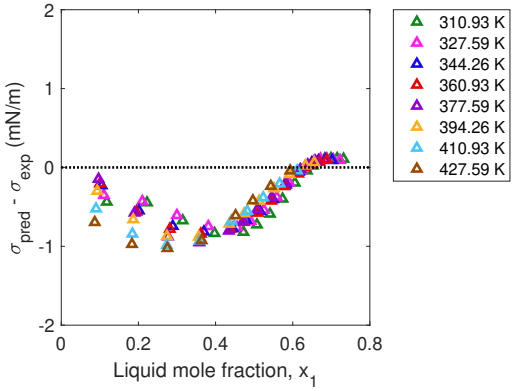

(e) Difference between predicted and experimental surface tension as a function of composition using the parachor model (△).

Figure A.12: Results for methane(1) + *n*-heptane(2) with data (○) from Warren and Hough [65].

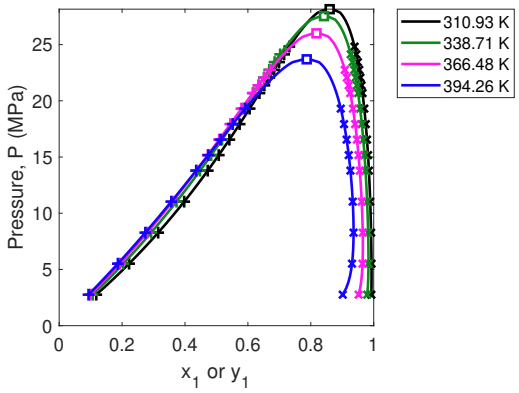

(a) Calculated liquid (+) and vapor (×) compositions at the temperatures and pressures in Amin and Smith [3] and the calculated critical compositions (□) obtained using the algorithm in Figure A.4.

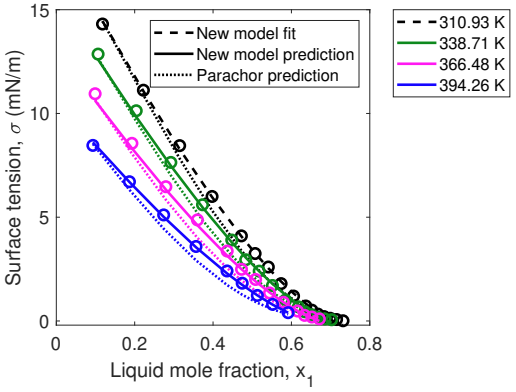

(b) Surface tension fit (black dashed line) and predictions (solid lines) *vs.* liquid composition at elevated temperatures using our new model. Parachor predictions are shown by dotted lines.

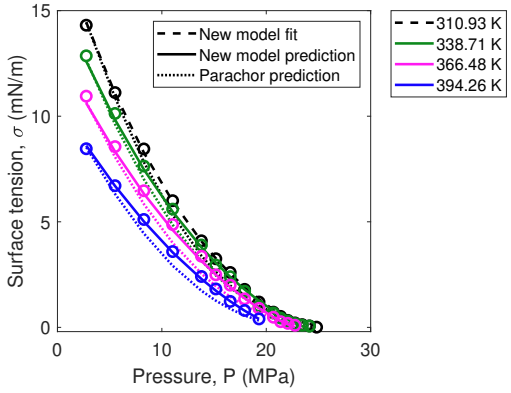

(c) Same as (b), but *vs.* pressure.

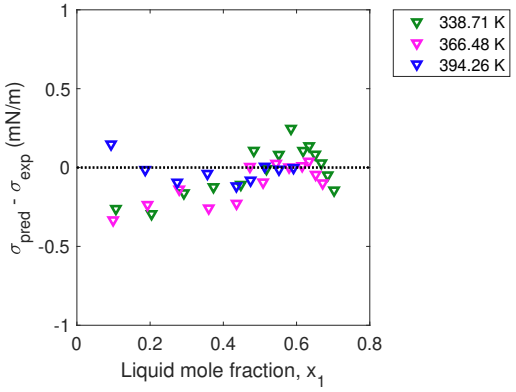

(d) Difference between predicted and experimental surface tension as a function of composition using our new model (▽).

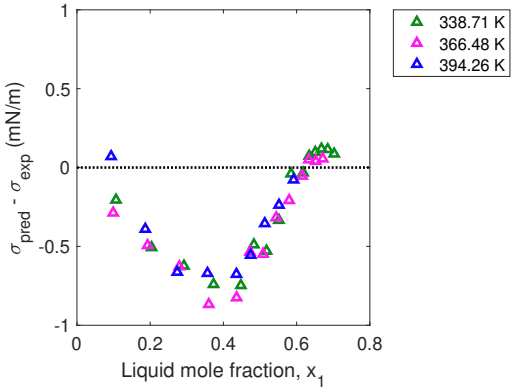

(e) Difference between predicted and experimental surface tension as a function of composition using the parachor model (△).

Figure A.13: Results for methane(1) + *n*-heptane(2) with data (○) from Amin and Smith [3].

A.5.2.6 Methane(1) + *n*-Decane(2)

Figure A.14(a) shows the calculated phase envelopes of methane(1) + *n*-decane(2) at the temperatures reported in Stegemeier *et al.* [60]. At the pressures reported in Stegemeier *et al.* [60], we depict our calculated liquid-phase compositions and vapor-phase compositions with + and $\times$ symbols, respectively. Using the algorithm presented in Figure A.4, the critical composition of the binary mixture is calculated at each temperature, as shown by the $\square$ symbols. In Figures A.14(b) and (c), surface tension calculated using Equation (3.2) in Chapter 3 is compared to experimental measurements from Stegemeier *et al.* [60] as a function of liquid-phase composition and pressure, respectively. Figures A.14(d) and (e) show the difference between predicted surface tension and surface tension measured experimentally by Stegemeier *et al.* [60] when using our new model (Equation (3.2) in Chapter 3) and the parachor model (Equation (A.22)), respectively.

Figure A.15(a) shows the calculated phase envelopes of methane(1) + *n*-decane(2) at the temperatures reported in Amin and Smith [3]. At the pressures reported in Amin and Smith [3], we depict our calculated liquid-phase compositions and vapor-phase compositions with + and $\times$ symbols, respectively. Using the algorithm presented in Figure A.4, the critical composition of the binary mixture is calculated at each temperature, as shown by the $\square$ symbols. In Figures A.15(b) and (c), surface tension calculated using Equation (3.2) in Chapter 3 with fitting coefficients obtained from data in Stegemeier *et al.* [60] is compared to experimental measurements from Amin and Smith [3] as a function of liquid-phase composition and pressure, respectively. Figures A.15(d) and (e) show the difference between predicted surface tension and surface tension measured experimentally by Amin and Smith [3] when using our new model (Equation (3.2) in Chapter 3) and the parachor model (Equation (A.22)), respectively.

Figure A.16(a) shows the calculated phase envelopes of methane(1) + *n*-decane(2) at the temperatures reported in Pereira *et al.* [44]. At the pressures reported in Pereira *et al.* [44], we depict our calculated liquid-phase compositions and vapor-phase compositions with + and $\times$ symbols, respectively. Using the algorithm presented in Figure A.4, the critical composition of the binary mixture is calculated at each temperature, as shown by the $\square$ symbols. In Figures A.16(b) and (c), surface tension calculated using Equation (3.2) in Chapter 3 with fitting coefficients obtained from data in Stegemeier *et al.* [60] is compared to experimental measurements from Pereira *et al.* [44] as a function of liquid-phase composition and pressure, respectively. Figures A.16(d) and (e) show the difference between predicted surface tension and surface tension measured experimentally by Pereira *et al.* [44] when using our new model (Equation (3.2) in Chapter 3) and the parachor model (Equation (A.22)), respectively.

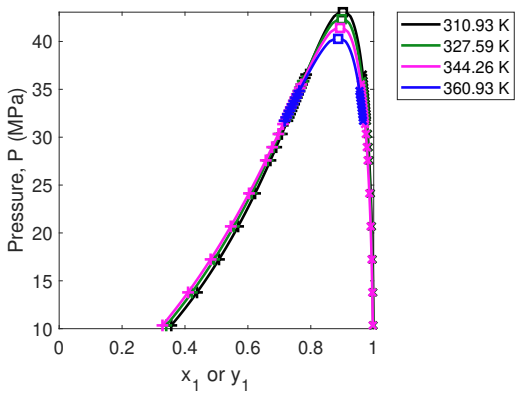

(a) Calculated liquid (+) and vapor (×) compositions at the temperatures and pressures in Stegemeier *et al.* [60] and the calculated critical compositions (□) obtained using the algorithm in Figure A.4.

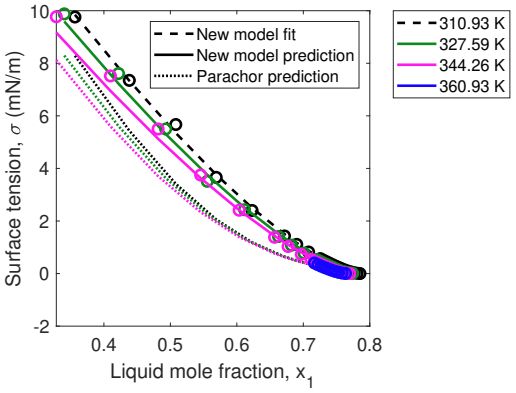

(b) Surface tension fit (black dashed line) and predictions (solid lines) *vs.* liquid composition at elevated temperatures using our new model. Parachor predictions are shown by dotted lines.

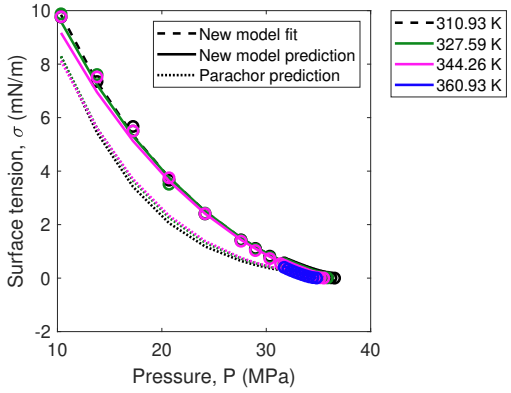

(c) Same as (b), but *vs.* pressure.

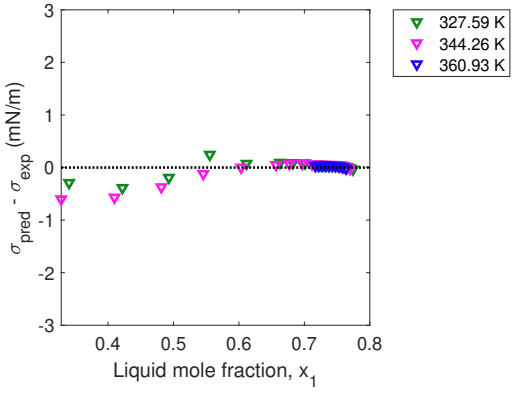

(d) Difference between predicted and experimental surface tension as a function of composition using our new model (▽).

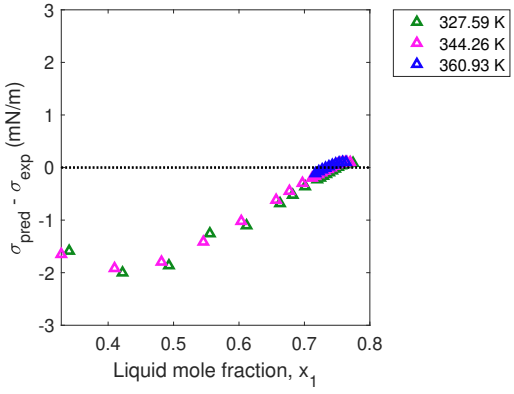

(e) Difference between predicted and experimental surface tension as a function of composition using the parachor model (△).

Figure A.14: Results for methane(1) + *n*-decane(2) with data (○) from Stegemeier *et al.* [60].

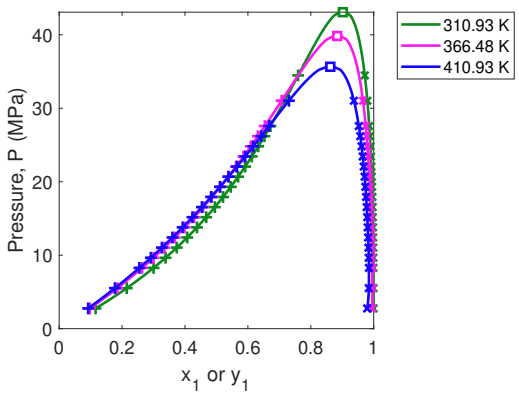

(a) Calculated liquid (+) and vapor (×) compositions at the temperatures and pressures in Amin and Smith [3] and the calculated critical compositions (□) obtained using the algorithm in Figure A.4.

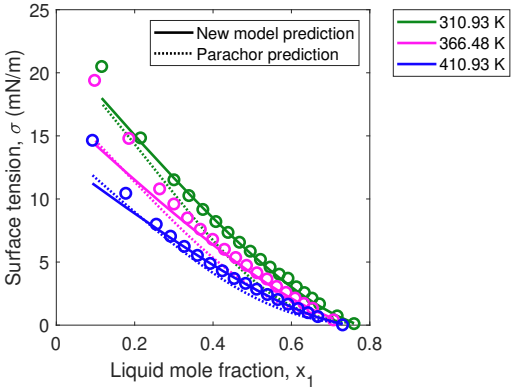

(b) Surface tension predictions (solid lines) *vs.* liquid composition at elevated temperatures using our new model. Parachor predictions are shown by dotted lines.

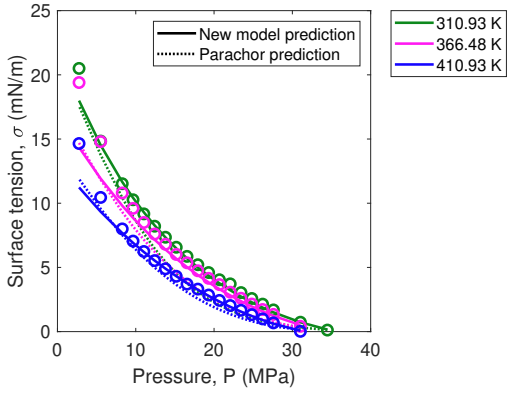

(c) Same as (b), but *vs.* pressure.

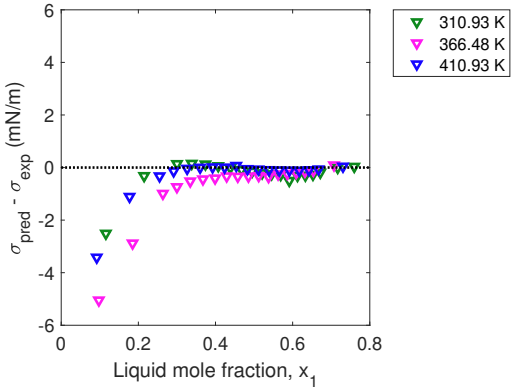

(d) Difference between predicted and experimental surface tension as a function of composition using our new model (▽).

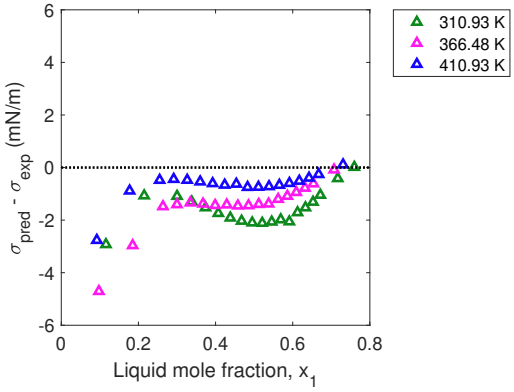

(e) Difference between predicted and experimental surface tension as a function of composition using the parachor model (△).

Figure A.15: Results for methane(1) + *n*-decane(2) with data (○) from Amin and Smith [3].

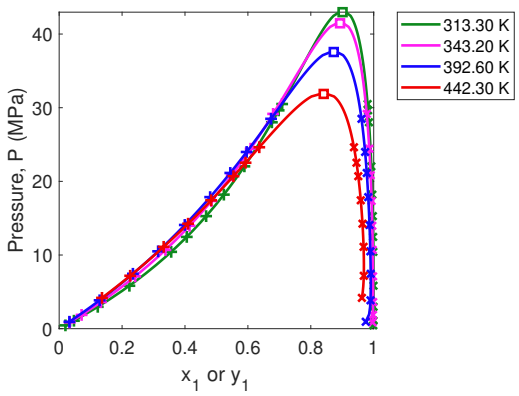

(a) Calculated liquid (+) and vapor (×) compositions at the temperatures and pressures in Pereira *et al.* [44] and the calculated critical compositions (□) obtained using the algorithm in Figure A.4.

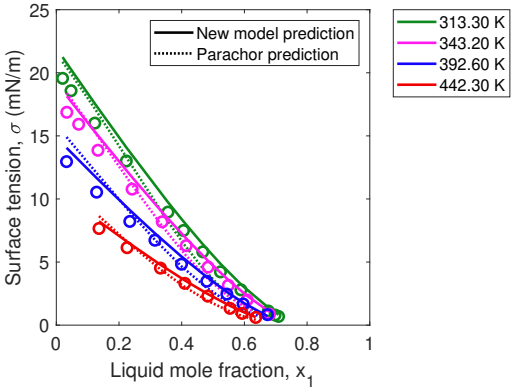

(b) Surface tension predictions (solid lines) *vs.* liquid composition at elevated temperatures using our new model. Parachor predictions are shown by dotted lines.

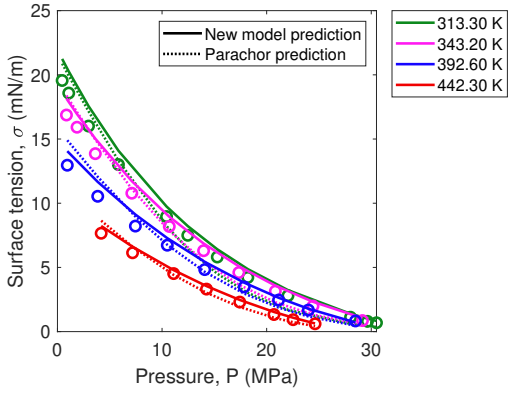

(c) Same as (b), but *vs.* pressure.

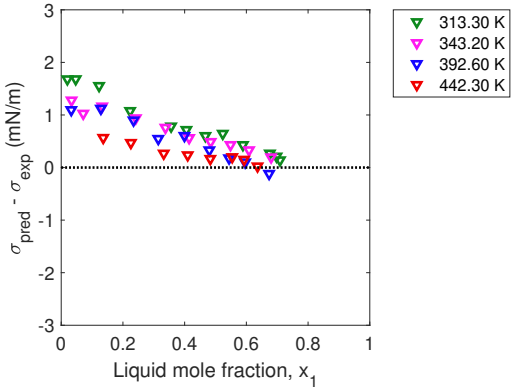

(d) Difference between predicted and experimental surface tension as a function of composition using our new model (▽).

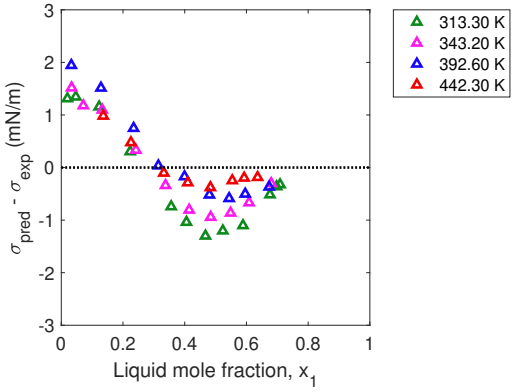

(e) Difference between predicted and experimental surface tension as a function of composition using the parachor model (△).

Figure A.16: Results for methane(1) + *n*-decane(2) with data (○) from Pereira *et al.* [44].

A.5.2.7 Carbon Dioxide(1) + *n*-Butane(2)

Figure A.17(a) shows the calculated phase envelopes of carbon dioxide(1) + *n*-butane(2) at the temperatures reported in Hsu *et al.* [19]. At the pressures reported in Hsu *et al.* [19], we depict our calculated liquid-phase compositions and vapor-phase compositions with + and $\times$ symbols, respectively. Using the algorithm presented in Figure A.4, the critical composition of the binary mixture is calculated at each temperature, as shown by the $\square$ symbols. In Figures A.17(b) and (c), surface tension calculated using Equation (3.2) in Chapter 3 is compared to experimental measurements from Hsu *et al.* [19] as a function of liquid-phase composition and pressure, respectively. Figures A.17(d) and (e) show the difference between predicted surface tension and surface tension measured experimentally by Hsu *et al.* [19] when using our new model (Equation (3.2) in Chapter 3) and the parachor model (Equation (A.22)).

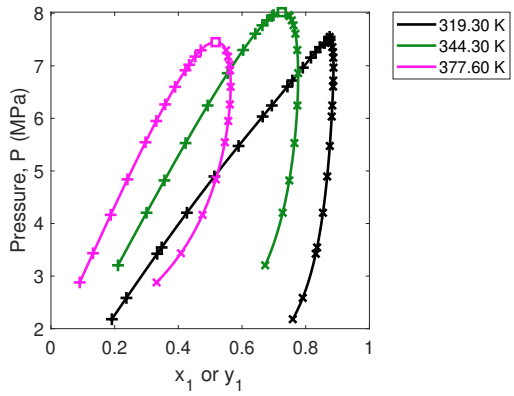

(a) Calculated liquid (+) and vapor (×) compositions at the temperatures and pressures in Hsu *et al.* [19] and the calculated critical compositions (□) obtained using the algorithm in Figure A.4.

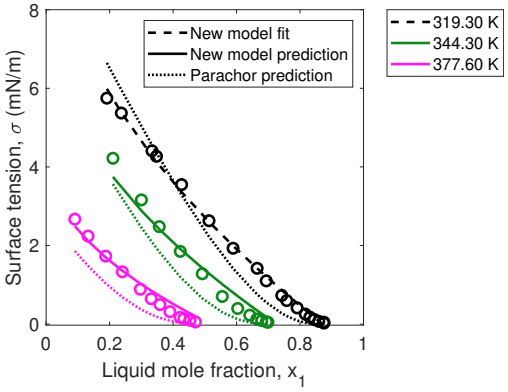

(b) Surface tension fit (black dashed line) and predictions (solid lines) *vs.* liquid composition at elevated temperatures using our new model. Parachor predictions are shown by dotted lines.

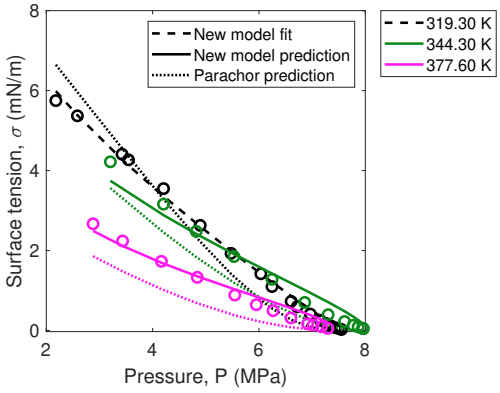

(c) Same as (b), but *vs.* pressure.

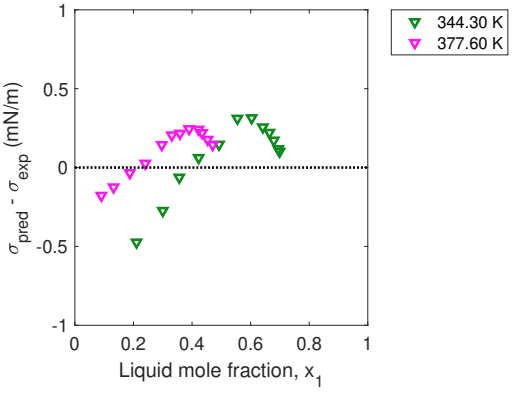

(d) Difference between predicted and experimental surface tension as a function of composition using our new model (▽).

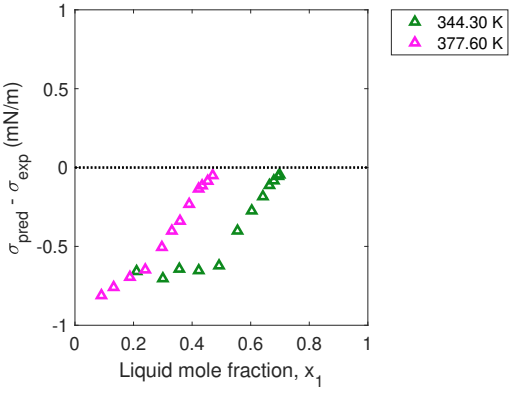

(e) Difference between predicted and experimental surface tension as a function of composition using the parachor model (△).

Figure A.17: Results for carbon dioxide(1) + *n*-butane(2) with data (○) from Hsu *et al.* [19].

A.5.2.8 Carbon Dioxide(1) + *n*-Heptane(2)

Figure A.18(a) shows the calculated phase envelopes of carbon dioxide(1) + *n*-heptane(2) at the temperatures reported in Niño-Amézquita *et al.* [37]. At the pressures reported in Niño-Amézquita *et al.* [37], we depict our calculated liquid-phase compositions and vapor-phase compositions with + and $\times$ symbols, respectively. Using the algorithm presented in Figure A.4, the critical composition of the binary mixture is calculated at each temperature, as shown by the $\square$ symbols. In Figures A.18(b) and (c), surface tension calculated using Equation (3.2) in Chapter 3 is compared to experimental measurements from Niño-Amézquita *et al.* [37] as a function of liquid-phase composition and pressure. Figures A.18(d) and (e) show the difference between predicted surface tension and surface tension measured experimentally by Niño-Amézquita *et al.* [37] when using our new model (Equation (3.2) in Chapter 3) and the parachor model (Equation (A.22)), respectively.

Figure A.19(a) shows the calculated phase envelopes of carbon dioxide(1) + *n*-heptane(2) at the temperatures reported in Jaeger *et al.* [20]. At the pressures reported in Jaeger *et al.* [20], we depict our calculated liquid-phase compositions and vapor-phase compositions with + and $\times$ symbols, respectively. Using the algorithm presented in Figure A.4, the critical composition of the binary mixture is calculated at each temperature, as shown by the $\square$ symbols. In Figures A.19(b) and (c), surface tension calculated using Equation (3.2) in Chapter 3 with fitting coefficients obtained from data in Niño-Amézquita *et al.* [37] is compared to experimental measurements from Jaeger *et al.* [20] as a function of liquid-phase composition and pressure, respectively. Figures A.19(d) and (e) show the difference between predicted surface tension and surface tension measured experimentally by Jaeger *et al.* [20] when using our new model (Equation (3.2) in Chapter 3) and the parachor model (Equation (A.22)), respectively.

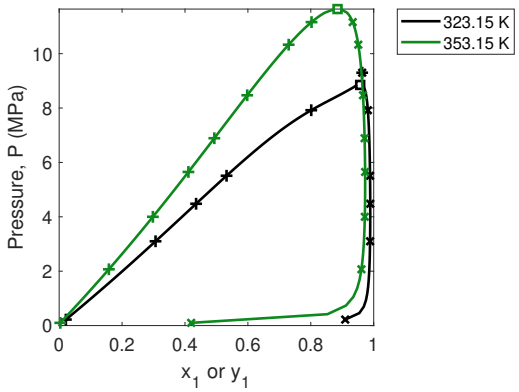

(a) Calculated liquid (+) and vapor (×) compositions at the temperatures and pressures in Niño-Amézquita *et al.* [37] and the calculated critical compositions (□) obtained using the algorithm in Figure A.4.

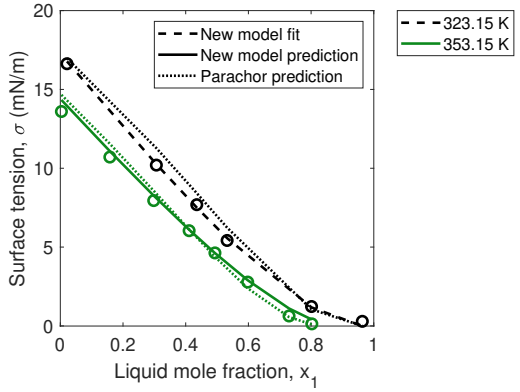

(b) Surface tension fit (black dashed line) and predictions (solid line) *vs.* liquid composition at an elevated temperature using our new model. Parachor predictions are shown by dotted lines.

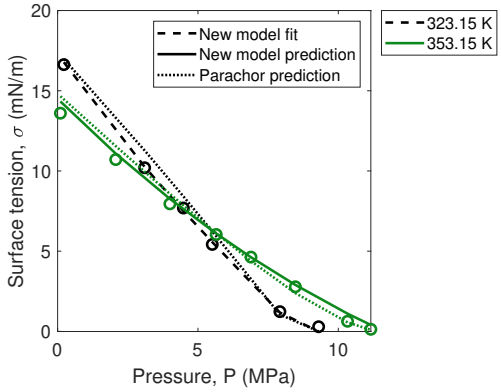

(c) Same as (b), but *vs.* pressure.

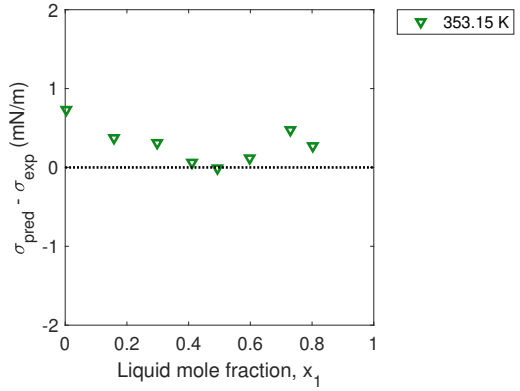

(d) Difference between predicted and experimental surface tension as a function of composition using our new model (▽).

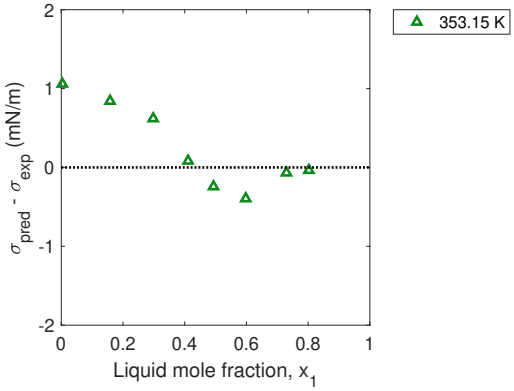

(e) Difference between predicted and experimental surface tension as a function of composition using the parachor model (△).

Figure A.18: Results for carbon dioxide(1) + *n*-heptane(2) with data (○) from Niño-Amézquita *et al.* [37].

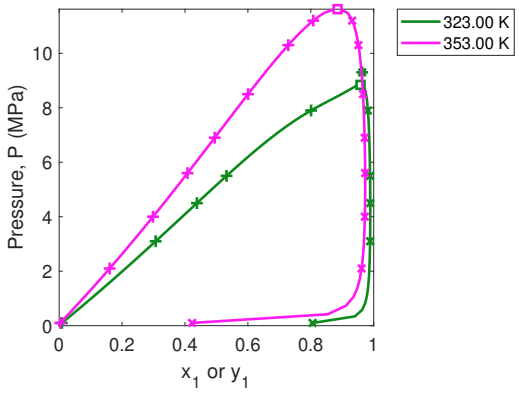

(a) Calculated liquid (+) and vapor (×) compositions at the temperatures and pressures in Jaeger *et al.* [20] and the calculated critical compositions (□) obtained using the algorithm in Figure A.4.

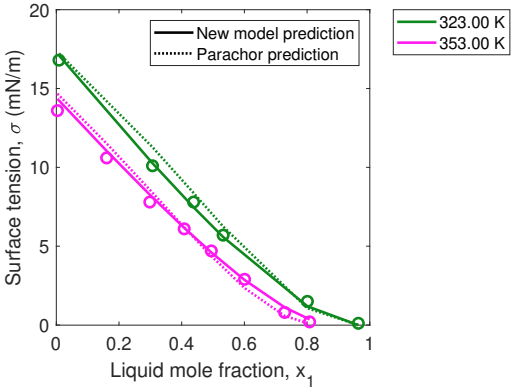

(b) Surface tension predictions using our new model (solid lines) *vs.* liquid composition at elevated temperatures. Parachor predictions are shown by dotted lines.

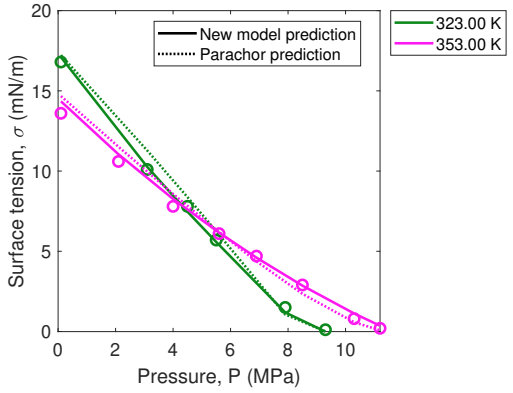

(c) Same as (b), but *vs.* pressure.

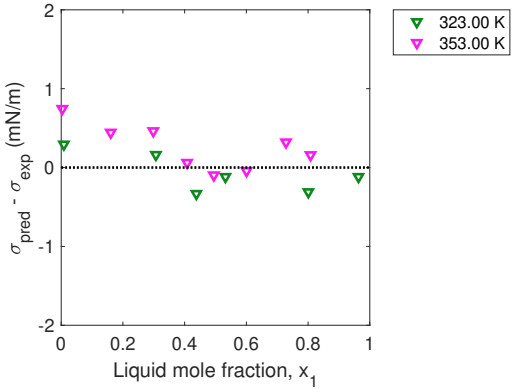

(d) Difference between predicted and experimental surface tension as a function of composition using our new model (▽).

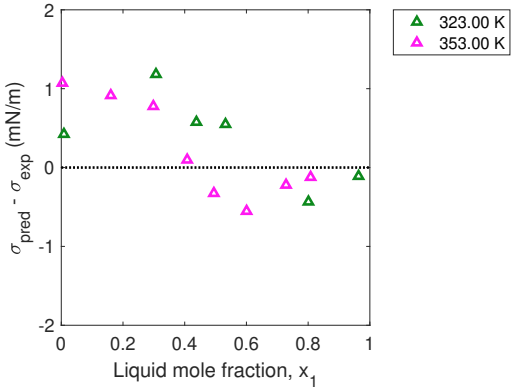

(e) Difference between predicted and experimental surface tension as a function of composition using the parachor model (△).

Figure A.19: Results for carbon dioxide(1) + *n*-heptane(2) with data (○) from Jaeger *et al.* [20].

A.5.2.9 Dodecane(1) + Benzene(2)

Figure A.20(a) shows the calculated phase envelopes of dodecane(1) + benzene(2) at the temperatures reported in Schmidt *et al.* [53]. At the liquid compositions reported in Schmidt *et al.* [53], we depict our calculated bubble pressures and vapor-phase compositions with + and $\times$ symbols, respectively. In Figure A.20(b), surface tension calculated using Equation (3.2) in Chapter 3 is compared to experimental measurements from Schmidt *et al.* [53] as a function of liquid-phase composition. Figures A.20(c) and (d) show the difference between predicted surface tension and surface tension measured experimentally by Schmidt *et al.* [53] when using our new model (Equation (3.2) in Chapter 3) and the parachor model (Equation (A.22)), respectively.

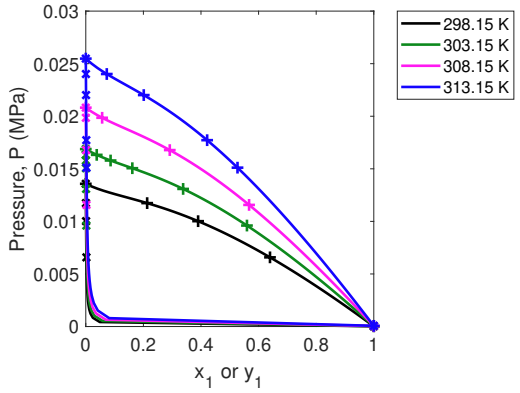

(a) Calculated bubble pressures (+) and vapor ($\times$) compositions at the temperatures and liquid compositions in Schmidt *et al.* [53].

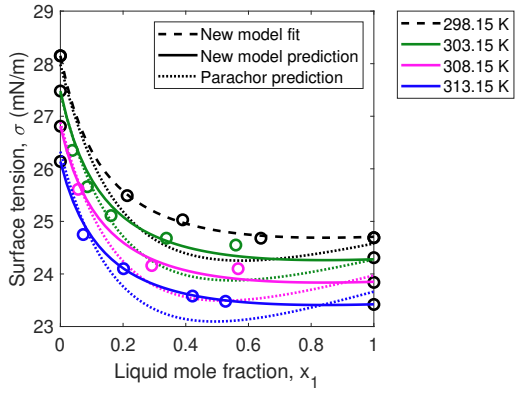

(b) Surface tension fit (black dashed line) and predictions (solid lines) *vs.* liquid composition at elevated temperatures using our new model. Parachor predictions are shown by dotted lines.

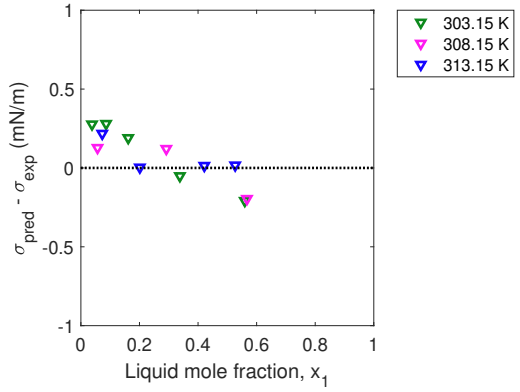

(c) Difference between predicted and experimental surface tension as a function of composition using our new model ($\bigtriangledown$).

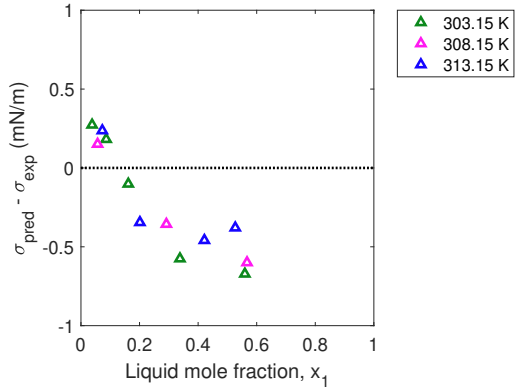

(d) Difference between predicted and experimental surface tension as a function of composition using the parachor model ($\bigtriangleup$).

Figure A.20: Results for dodecane(1) + benzene(2) with data ($\circ$) from Schmidt *et al.* [53].

A.5.2.10 *n*-Hexane(1) + Benzene(2)

Figure A.21(a) shows the calculated phase envelopes of *n*-hexane(1) + benzene(2) at the temperatures reported in Schmidt *et al.* [53]. At the liquid compositions reported in Schmidt *et al.* [53], we depict our calculated bubble pressures and vapor-phase compositions with + and $\times$ symbols, respectively. In Figure A.21(b), surface tension calculated using Equation (3.2) in Chapter 3 is compared to experimental measurements from Schmidt *et al.* [53] as a function of liquid-phase composition. Figures A.21(c) and (d) show the difference between predicted surface tension and surface tension measured experimentally by Schmidt *et al.* [53] when using our new model (Equation (3.2) in Chapter 3) and the parachor model (Equation (A.22)), respectively.

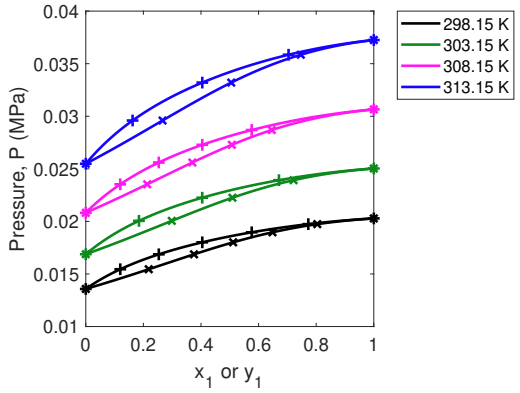

(a) Calculated bubble pressures (+) and vapor ($\times$) compositions at the temperatures and liquid compositions in Schmidt *et al.* [53].

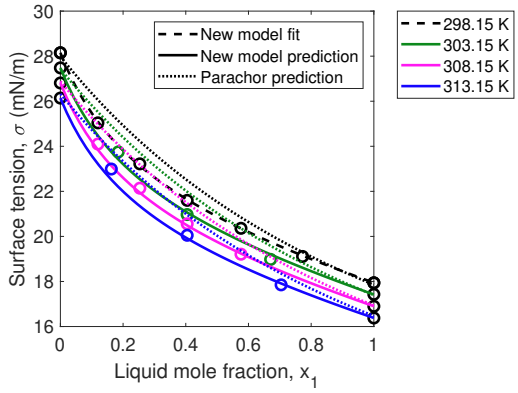

(b) Surface tension fit (black dashed line) and predictions (solid lines) *vs.* liquid composition at elevated temperatures using our new model. Parachor predictions are shown by dotted lines.

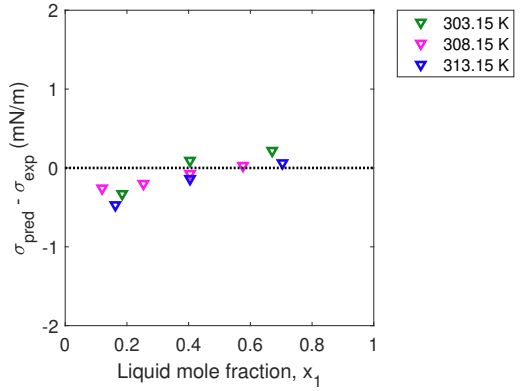

(c) Difference between predicted and experimental surface tension as a function of composition using our new model ($\bigtriangledown$).

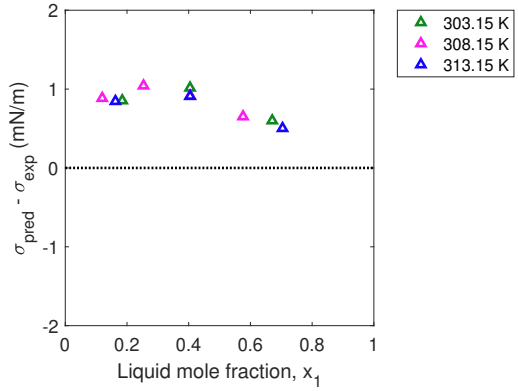

(d) Difference between predicted and experimental surface tension as a function of composition using the parachor model ($\bigtriangleup$).

Figure A.21: Results for *n*-hexane(1) + benzene(2) with data ($\circ$) from Schmidt *et al.* [53].

A.5.2.11 Cyclohexane(1) + Benzene(2)

Figure A.22(a) shows the calculated phase envelopes of cyclohexane(1) + benzene(2) at the temperatures reported in Lam and Benson [25]. At the liquid compositions reported in Lam and Benson [25], we depict our calculated bubble pressures and vapor-phase compositions with + and × symbols, respectively. In Figure A.22(b), surface tension calculated using Equation (3.2) in Chapter 3 with fitting coefficients obtained from data in Herrmann [18, 69] is compared to experimental measurements from Lam and Benson [25] as a function of liquid-phase composition. Figures A.22(c) and (d) show the difference between predicted surface tension and surface tension measured experimentally by Lam and Benson [25] when using our new model (Equation (3.2) in Chapter 3) and the parachor model (Equation (A.22)), respectively.

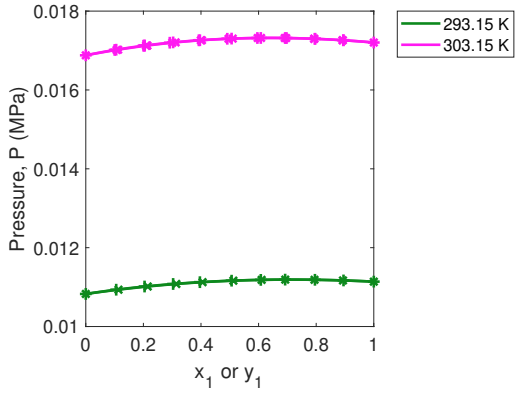

(a) Calculated bubble pressures (+) and vapor (×) compositions at the temperatures and liquid compositions in Lam and Benson [25].

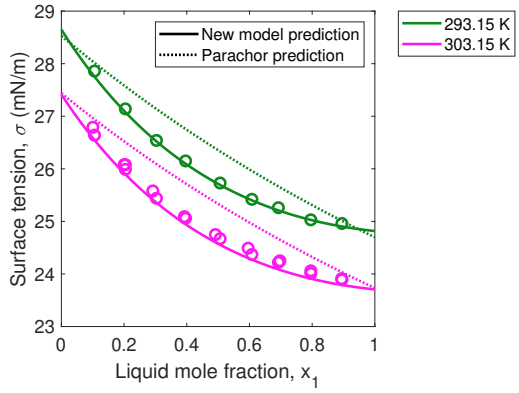

(b) Surface tension predictions using our new model (solid lines) *vs.* liquid composition at elevated temperatures. Parachor predictions are shown by dotted lines.

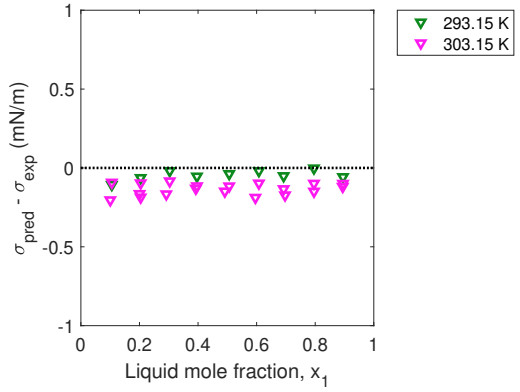

(c) Difference between predicted and experimental surface tension as a function of composition using our new model (▽).

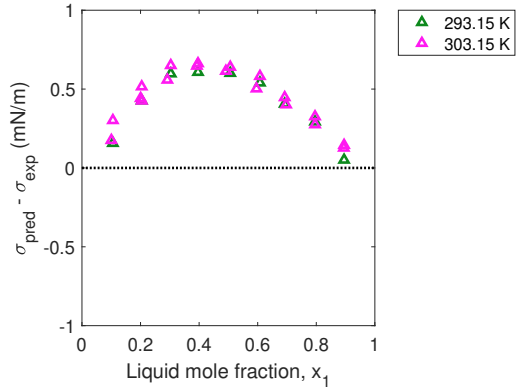

(d) Difference between predicted and experimental surface tension as a function of composition using the parachor model (△).

Figure A.22: Results for cyclohexane(1) + benzene(2) with data (○) from Lam and Benson [25].

Figure A.23(a) shows the calculated phase envelopes of cyclohexane(1) + benzene(2) at the temperatures reported in Konobeev and Lyapin [24, 69]. At the liquid compositions reported in Konobeev and Lyapin [24, 69], we depict our calculated bubble pressures and vapor-phase compositions with + and $\times$ symbols, respectively. In Figure A.23(b), surface tension calculated using Equation (3.2) in Chapter 3 with fitting coefficients obtained from data in Herrmann [18, 69] is compared to experimental measurements from Konobeev and Lyapin [24, 69] as a function of liquid-phase composition. Figures A.23(c) and (d) show the difference between predicted surface tension and surface tension measured experimentally by Konobeev and Lyapin [24, 69] when using our new model (Equation (3.2) in Chapter 3) and the parachor model (Equation (A.22)), respectively.

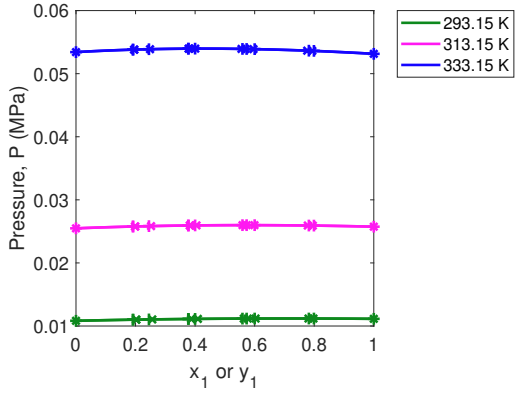

(a) Calculated bubble pressures (+) and vapor ($\times$) compositions at the temperatures and liquid compositions in Konobeev and Lyapin [24, 69].

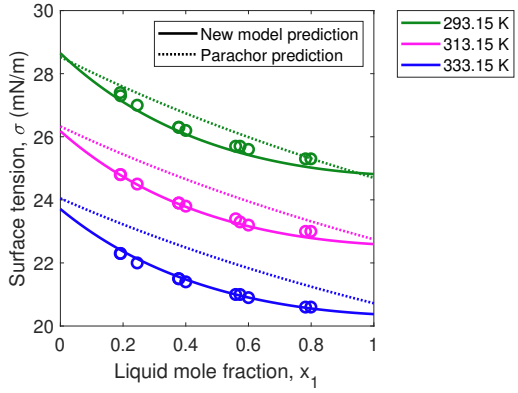

(b) Surface tension predictions using our new model (solid lines) *vs.* liquid composition at elevated temperatures. Parachor predictions are shown by dotted lines.

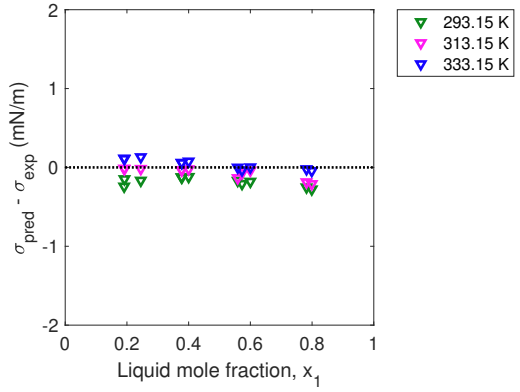

(c) Difference between predicted and experimental surface tension as a function of composition using our new model ($\bigtriangledown$).

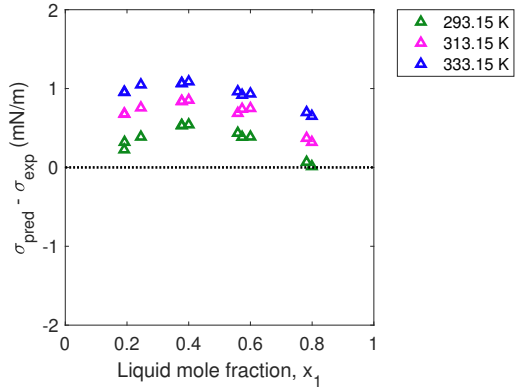

(d) Difference between predicted and experimental surface tension as a function of composition using the parachor model ($\bigtriangleup$).

Figure A.23: Results for cyclohexane(1) + benzene(2) with data ($\circ$) from Konobeev and Lyapin [24, 69].

Figure A.24(a) shows the calculated phase envelopes of cyclohexane(1) + benzene(2) at the temperatures reported in Herrmann [18, 69]. At the liquid compositions reported in Herrmann [18, 69], we depict our calculated bubble pressures and vapor-phase compositions with + and $\times$ symbols, respectively. In Figure A.24(b), surface tension calculated using Equation (3.2) in Chapter 3 is compared to experimental measurements from Herrmann [18, 69] as a function of liquid-phase composition. Figures A.24(c) and (d) show the difference between predicted surface tension and surface tension measured experimentally by Herrmann [18, 69] when using our new model (Equation (3.2) in Chapter 3) and the parachor model (Equation (A.22)), respectively.

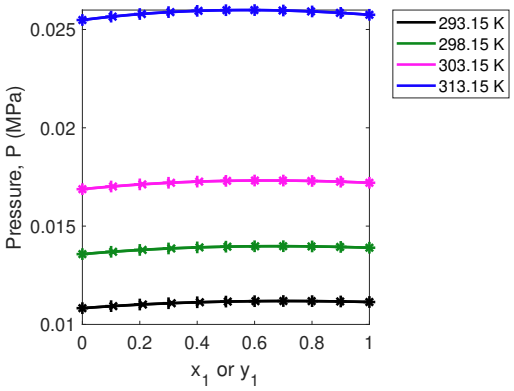

(a) Calculated bubble pressures (+) and vapor ($\times$) compositions at the temperatures and liquid compositions in Herrmann [18, 69].

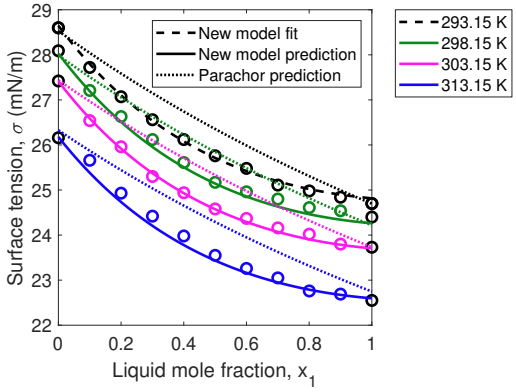

(b) Surface tension fit (black dashed line) and predictions (solid lines) *vs.* liquid composition at elevated temperatures using our new model. Parachor predictions are shown by dotted lines.

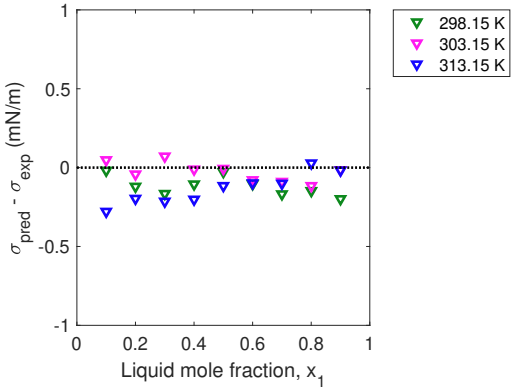

(c) Difference between predicted and experimental surface tension as a function of composition using our new model ($\bigtriangledown$).

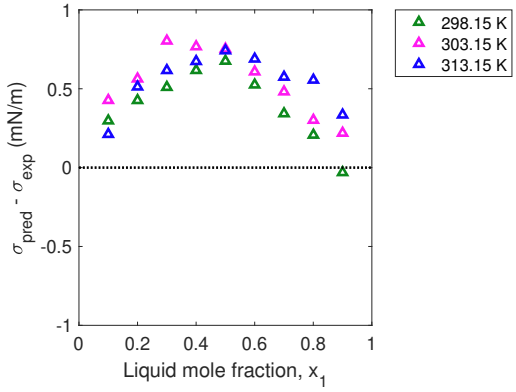

(d) Difference between predicted and experimental surface tension as a function of composition using the parachor model ($\bigtriangleup$).

Figure A.24: Results for cyclohexane(1) + benzene(2) with data ($\circ$) from Herrmann [18, 69].

A.5.2.12 Carbon Tetrachloride(1) + Methyl Iodide(2)

Figure A.25(a) shows the calculated phase envelopes of carbon tetrachloride(1) + methyl iodide(2) at the temperatures reported in Teixeira *et al.* [63]. At the liquid compositions reported in Teixeira *et al.* [63], we depict our calculated bubble pressures and vapor-phase compositions with + and × symbols, respectively. In Figure A.25(b), surface tension calculated using Equation (3.2) in Chapter 3 is compared to experimental measurements from Teixeira *et al.* [63] as a function of liquid-phase composition. Figures A.25(c) and (d) show the difference between predicted surface tension and surface tension measured experimentally by Teixeira *et al.* [63] when using our new model (Equation (3.2) in Chapter 3) and the parachor model (Equation (A.22)), respectively.

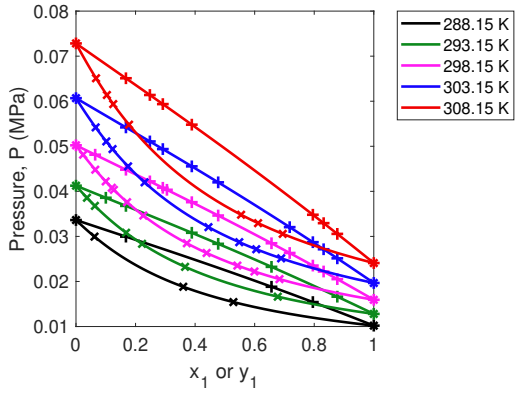

(a) Calculated bubble pressures (+) and vapor (×) compositions at the temperatures and liquid compositions in Teixeira *et al.* [63].

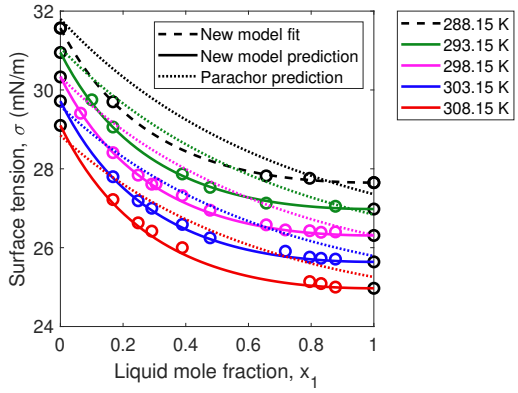

(b) Surface tension fit (black dashed line) and predictions (solid lines) *vs.* liquid composition at elevated temperatures using our new model. Parachor predictions are shown by dotted lines.

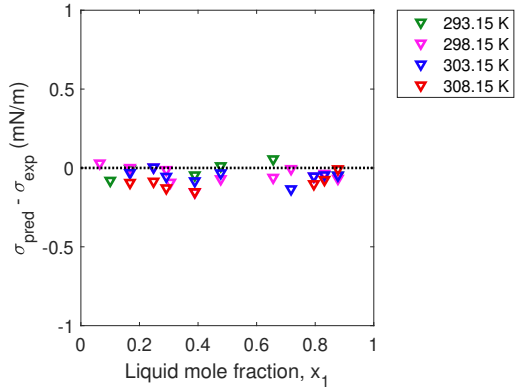

(c) Difference between predicted and experimental surface tension as a function of composition using our new model (▽).

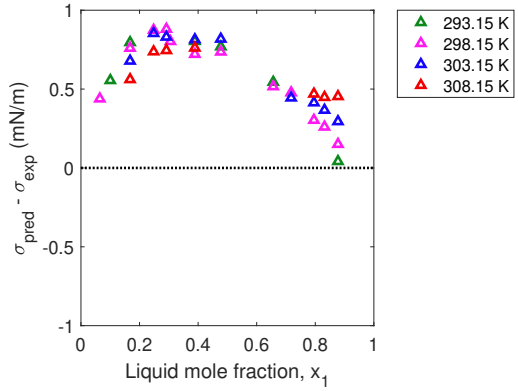

(d) Difference between predicted and experimental surface tension as a function of composition using the parachor model (△).

Figure A.25: Results for carbon tetrachloride(1) + methyl iodide(2) with data (○) from Teixeira *et al.* [63].

A.5.2.13 Carbon Tetrachloride(1) + Acetonitrile(2)

Figure A.26(a) shows the calculated phase envelopes of carbon tetrachloride(1) + acetonitrile(2) at the temperatures reported in Teixeira *et al.* [63]. At the liquid compositions reported in Teixeira *et al.* [63] we depict our calculated bubble pressures and vapor-phase compositions with + and × symbols, respectively. In Figure A.26(b), surface tension calculated using Equation (3.2) in Chapter 3 is compared to experimental measurements from Teixeira *et al.* [63] as a function of liquid-phase composition. Figures A.26(c) and (d) show the difference between predicted surface tension and surface tension measured experimentally by Teixeira *et al.* [63] when using our new model (Equation (3.2) in Chapter 3) and the parachor model (Equation (A.22)), respectively.

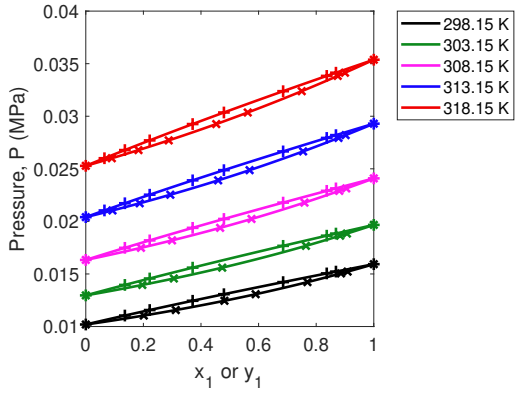

(a) Calculated bubble pressures (+) and vapor (×) compositions at the temperatures and liquid compositions in Teixeira *et al.* [63].

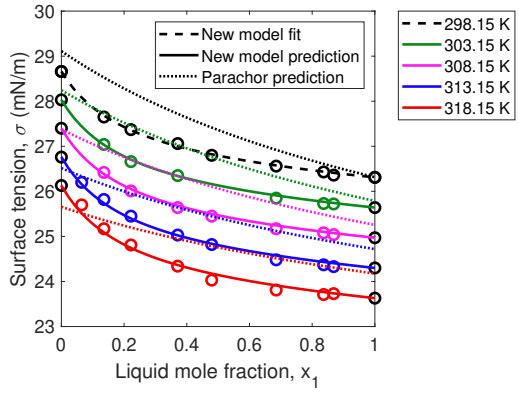

(b) Surface tension fit (black dashed line) and predictions (solid lines) *vs.* liquid composition at elevated temperatures using our new model. Parachor predictions are shown by dotted lines.

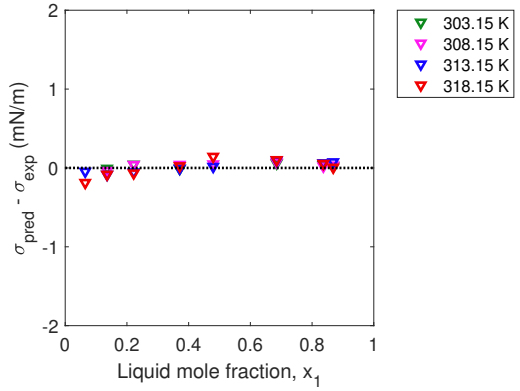

(c) Difference between predicted and experimental surface tension as a function of composition using our new model (▽).

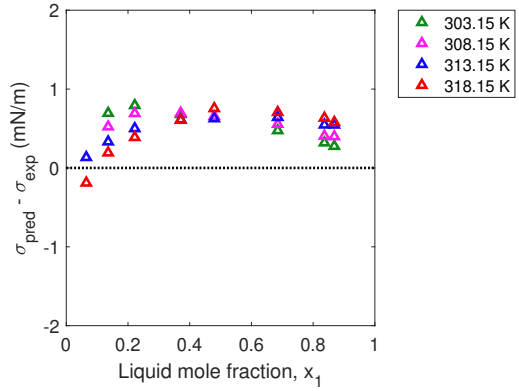

(d) Difference between predicted and experimental surface tension as a function of composition using the parachor model (△).

Figure A.26: Results for carbon tetrachloride(1) + acetonitrile(2) with data (○) from Teixeira *et al.* [63].

A.5.2.14 Carbon Tetrachloride(1) + Carbon Disulfide(2)

Figure A.27(a) shows the calculated phase envelopes of carbon tetrachloride(1) + carbon disulfide(2) at the temperatures reported in Luengo *et al.* [29]. At the liquid compositions reported in Luengo *et al.* [29] we depict our calculated bubble pressures and vapor-phase compositions with + and × symbols, respectively. In Figure A.27(b), surface tension calculated using Equation (3.2) in Chapter 3 is compared to experimental measurements from Luengo *et al.* [29] as a function of liquid-phase composition. Figures A.27(c) and (d) show the difference between predicted surface tension and surface tension measured experimentally by Luengo *et al.* [29] when using our new model (Equation (3.2) in Chapter 3) and the parachor model (Equation (A.22)), respectively.

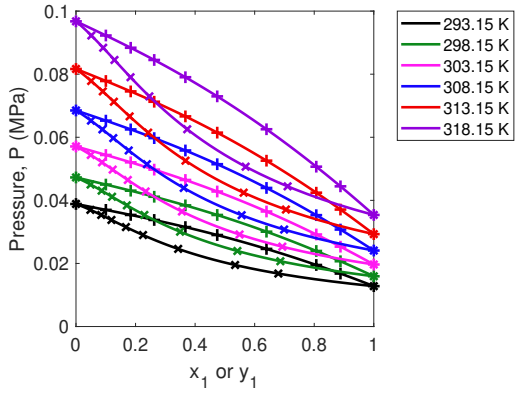

(a) Calculated bubble pressures (+) and vapor (×) compositions at the temperatures and liquid compositions in Luengo *et al.* [29].

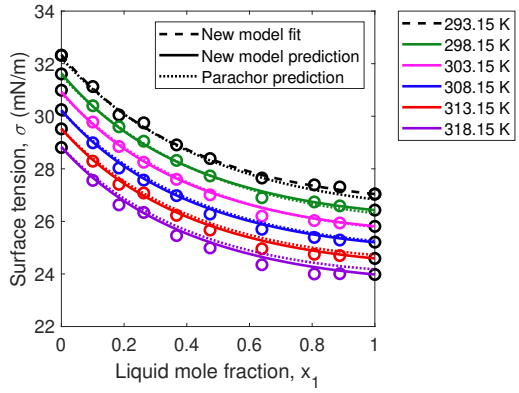

(b) Surface tension fit (black dashed line) and predictions (solid lines) *vs.* liquid composition at elevated temperatures using our new model. Parachor predictions are shown by dotted lines.

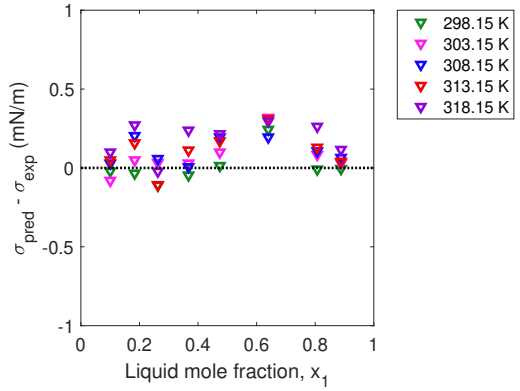

(c) Difference between predicted and experimental surface tension as a function of composition using our new model (▽).

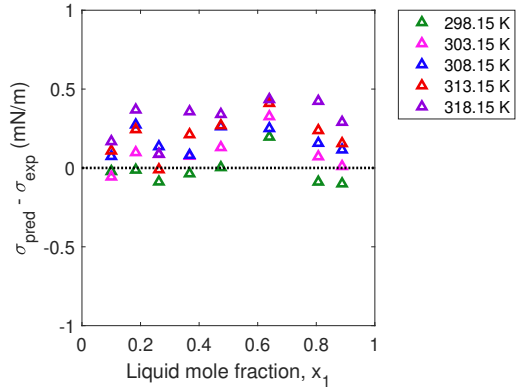

(d) Difference between predicted and experimental surface tension as a function of composition using the parachor model (△).

Figure A.27: Results for carbon tetrachloride(1) + carbon disulfide(2) with data (○) from Luengo *et al.* [29].

A.5.2.15 Dichloromethane(1) + Carbon Disulfide(2)

Figure A.28(a) shows the calculated phase envelopes of dichloromethane(1) + carbon disulfide(2) at the temperatures reported in Aracil *et al.* [4]. At the liquid compositions reported in Aracil *et al.* [4], we depict our calculated bubble pressures and vapor-phase compositions with + and $\times$ symbols, respectively. In Figure A.28(b), surface tension calculated using Equation (3.2) in Chapter 3 is compared to experimental measurements from Aracil *et al.* [4] as a function of liquid-phase composition. Figures A.28(c) and (d) show the difference between predicted surface tension and surface tension measured experimentally by Aracil *et al.* [4] when using our new model (Equation (3.2) in Chapter 3) and the parachor model (Equation (A.22)), respectively.

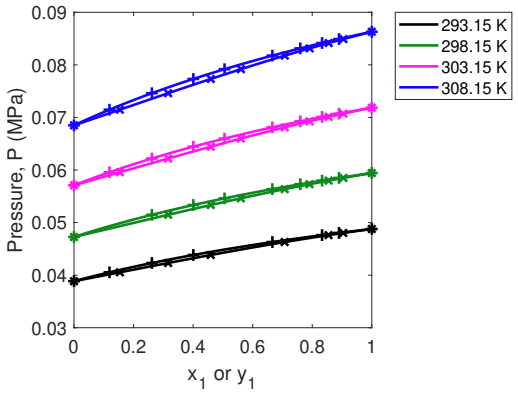

(a) Calculated bubble pressures (+) and vapor ($\times$) compositions at the temperatures and liquid compositions in Aracil *et al.* [4].

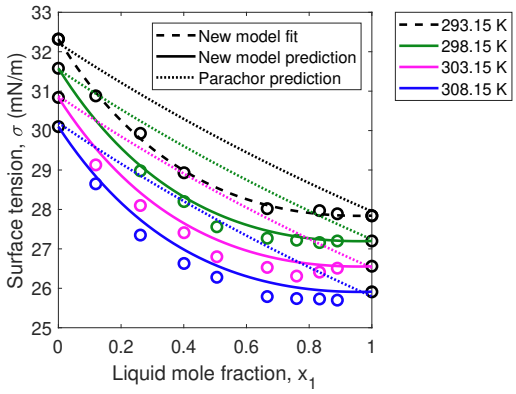

(b) Surface tension fit (black dashed line) and predictions (solid lines) *vs.* liquid composition at elevated temperatures using our new model. Parachor predictions are shown by dotted lines.

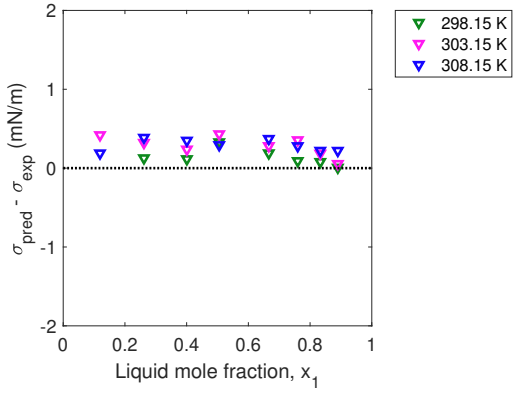

(c) Difference between predicted and experimental surface tension as a function of composition using our new model ($\bigtriangledown$).

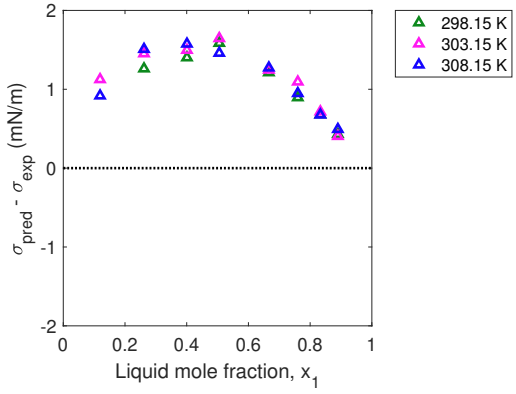

(d) Difference between predicted and experimental surface tension as a function of composition using the parachor model ($\bigtriangleup$).

Figure A.28: Results for dichloromethane(1) + carbon disulfide(2) with data ($\circ$) from Aracil *et al.* [4].

A.6 Discussion of Excluded Datasets

A.6.1 Methane(1) + *n*-Pentane(2)

Li and Firoozabadi [26] and Garrido and Polishuk [14] noted that the surface tensions reported in Amin and Smith [3] are too high for the listed temperatures of 366.48 K and 410.93 K. When we perform flash calculations at these temperatures and reported pressures (Figure A.29(a)), we observe that at pressures above ∼12 MPa, the system is expected to be in the single phase region at 410.93 K, which suggests that experiments could not, in fact, be conducted at this temperature. Thus, it appears that, instead, the reported temperatures were too high, rather than the surface tension values being too high. Figure A.29(b) shows the fit of our new model to data at 310.93 K with $x_{1,\mathrm{cr}} = 0.799$, yielding coefficients $a = -1.74 \pm 1.72$ and $b = 1.77 \pm 0.74$ with a standard deviation of 0.43 mN/m, as well as showing predictions of surface tension at the reported temperatures (solid lines) using our model ($x_{1,\mathrm{cr}}\,(366.48\ \mathrm{K}) = 0.697$ and $x_{1,\mathrm{cr}}\,(410.98\ \mathrm{K}) = 0.546$) and the parachor model (dotted lines).

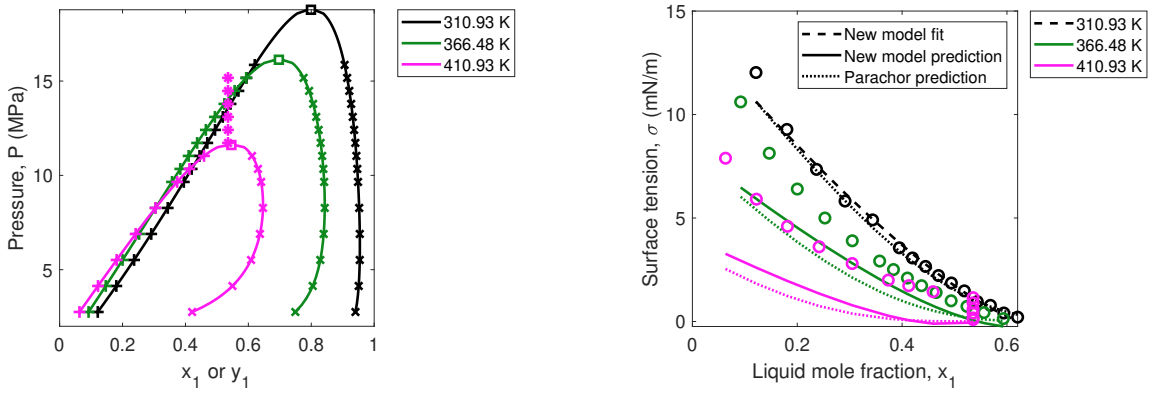

Figure A.29: Results for methane(1) + *n*-pentane(2) with data from Amin and Smith [3] using the reported temperatures. (a) Calculated liquid (+) and vapor (×) compositions at the pressures and temperatures in Amin and Smith [3] and calculated critical compositions (□). (b) Experimental surface tension (○), fit of our new model to experimental data (black dashed line), predicted surface tension using our new model (solid lines), and predicted surface tension using the parachor model (dotted lines) as a function of methane liquid mole fraction at the reported temperatures.

The same paper that studies methane(1) + *n*-pentane(2) mixtures also reports surface tension data for methane(1) + *n*-heptane(2) and methane(1) + *n*-decane(2) [3]. As printed, the temperatures for methane(1) + *n*-pentane(2) are the same as those for the *n*-decane mixture (310.93 K, 366.48 K, and 410.93 K). We suggest that the temperatures for methane(1) + *n*-pentane(2) should instead be the same as the lowest three listed for methane(1) + *n*-heptane(2) (310.93 K,

338.71 K, and 366.48 K). By assuming so, flash calculations yield a two-phase state at the reported pressures, and surface tension values are accurately predicted ($x_{1,\mathrm{cr}}\,(338.71\ \mathrm{K}) = 0.756$ and $x_{1,\mathrm{cr}}\,(366.48\ \mathrm{K}) = 0.697$), as illustrated in Figure A.30. Although they yield accurate results, these temperatures are speculative, however, and thus we do not include this system in our analysis in Chapter 3.

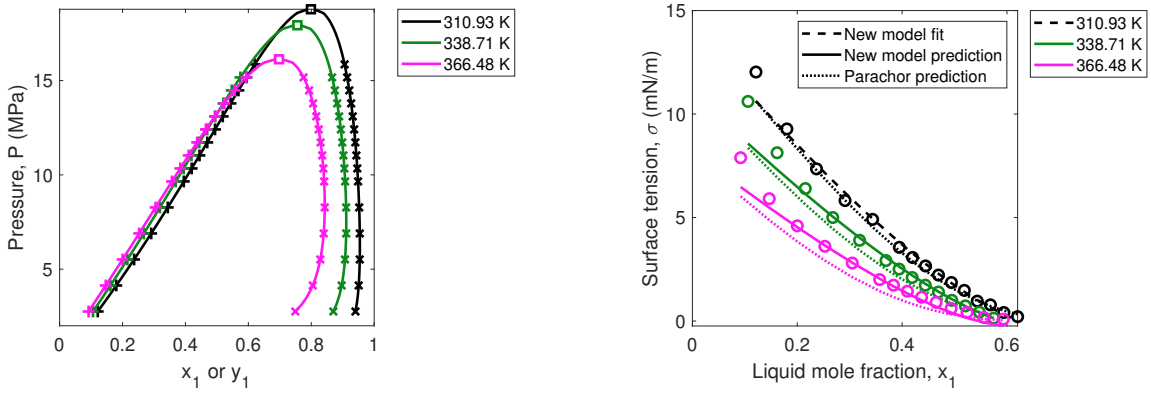

(a) **(b)**

Figure A.30: Results for methane(1) + *n*-pentane(2) with data from Amin and Smith [3] using new temperatures. (a) Calculated liquid (+) and vapor (×) compositions at the pressures in Amin and Smith [3] and calculated critical compositions (□) at 338.71 K and 366.48 K. (b) Experimental surface tension (○), fit of our new model to experimental data (black dashed line), predicted surface tension using our new model (solid lines), and predicted surface tension using the parachor model (dotted lines) as a function of methane liquid mole fraction, but at 338.71 K and 366.48 K instead of 366.48 K and 410.93 K, respectively, reported in Amin and Smith [3].

A.6.2 Methane(1) + *n*-Octane(2)

Figure A.31(a) shows the calculated phase envelopes of methane(1) + *n*-octane(2) at the temperatures reported in Peng *et al.* [40]. At the pressures reported in Peng *et al.* [40], we depict our calculated liquid-phase compositions and vapor-phase compositions with + and $\times$ symbols, respectively. Using the algorithm presented in Figure A.4, the critical composition of the binary mixture is calculated at each temperature, as shown by the $\square$ symbol and summarized in Table A.10.

Table A.10: Our calculated critical composition of methane as a function of the temperatures listed in Peng *et al.* [40] for methane(1) + *n*-octane(2).

methane(1) +	Temperature [K]	Critical Composition $x_{1,\mathrm{cr}}$	Data Reference
n-octane(2)	274.20	0.889	Peng *et al.* [40]
	276.20	0.889	
	278.20	0.888	
	280.20	0.888	
	282.20	0.887	

In Figures A.31(b) and (c), surface tension calculated using Equation (3.2) in Chapter 3 is compared to experimental measurements from Peng *et al.* [40] as a function of liquid-phase composition and pressure, respectively. It can be seen that the mixture surface tension data do not limit to the pure component surface tension determined by the Mulero *et al.* correlation [33] (Equation (3.6) in Chapter 3) as a function of temperature, and thus we exclude this dataset from consideration in Chapter 3. Figures A.31(d) and (e) show the difference between predicted surface tension and surface tension measured experimentally by Peng *et al.* [40] when using our new model (Equation (3.2) in Chapter 3) and the parachor model (Equation (A.22)), respectively.

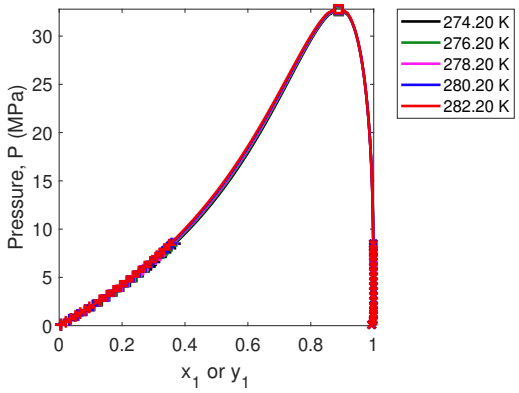

(a) Calculated liquid (+) and vapor (×) compositions at the temperatures and pressures in Peng *et al.* [40] and the calculated critical compositions (□) obtained using the algorithm in Figure A.4.

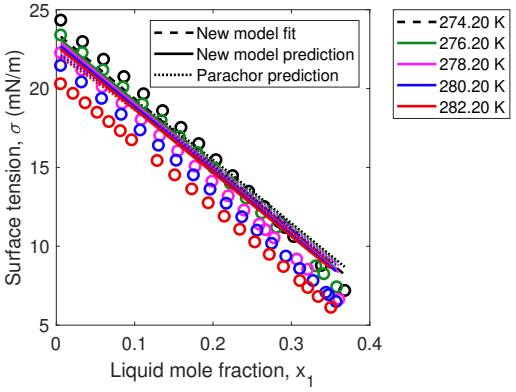

(b) Surface tension fit (black dashed line) and predictions (solid lines) *vs.* liquid composition at elevated temperatures using our new model. Parachor predictions are shown by dotted lines.

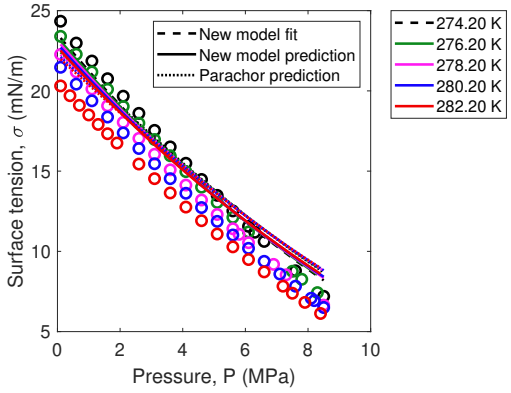

(c) Same as (b), but *vs.* pressure.

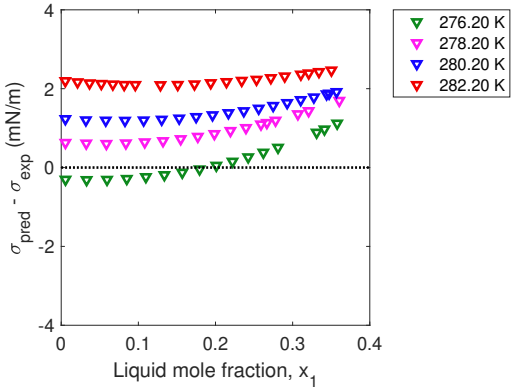

(d) Difference between predicted and experimental surface tension as a function of composition using our new model (▽).

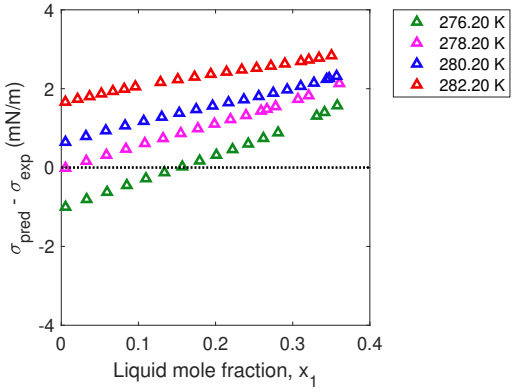

(e) Difference between predicted and experimental surface tension as a function of composition using the parachor model (△).

Figure A.31: Results for methane(1) + *n*-octane(2) with data (○) from Peng *et al.* [40].

A.6.3 Methane(1) + *n*-Nonane(2)

Figure A.32(a) shows the calculated phase envelopes of methane(1) + *n*-nonane(2) at the temperatures reported in Deam and Maddox [8]. At the pressures reported in Deam and Maddox [8], we depict our calculated liquid-phase compositions and vapor-phase compositions with + and $\times$ symbols, respectively. Using the algorithm presented in Figure A.4, the critical composition of the binary mixture is calculated at each temperature, as shown by the $\square$ symbol and listed in Table A.11.

Table A.11: Our calculated critical composition of methane as a function of the temperatures listed in Deam and Maddox [8] for methane(1) + *n*-nonane(2).

methane(1) +	Temperature [K]	Critical Composition $x_{1,\mathrm{cr}}$	Data Reference
n-nonane(2)	238.71	0.903	Deam and Maddox [8]
	249.82	0.903	
	272.04	0.900	
	297.04	0.895	

In Figures A.32(b) and (c), surface tension calculated using Equation (3.2) in Chapter 3 is compared to experimental measurements from Deam and Maddox [8] as a function of liquid-phase composition and pressure, respectively. The fitting coefficients obtained from the data at 238.71 K were $a = -4.7 \pm 22.15$ and $b = 2.62 \pm 9.21$. Although these coefficients can accurately predict surface tension at higher temperatures, the obtained 95% confidence intervals are at least an order of magnitude larger than those for the systems in Chapter 3 (Table 3.2 in Chapter 3). Such large confidence intervals are directly because large changes in coefficients yield only small changes in the predicted surface tension (via the Jacobian). For this dataset in particular, this result is likely due to the small number of data points over a narrow range of compositions being insufficient to capture the functional form. As a result, the fitting procedure iterates towards coefficients with larger magnitudes that result in larger confidence intervals. Figures A.32(d) and (e) show the difference between predicted surface tension and surface tension measured experimentally by Deam and Maddox [8] when using our new model (Equation (3.2) in Chapter 3) and the parachor model (Equation (A.22)), respectively.

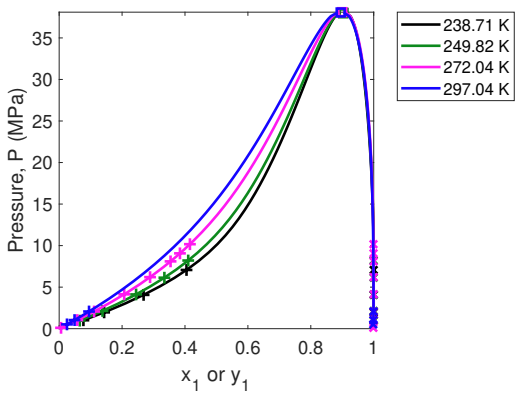

(a) Calculated liquid (+) and vapor (×) compositions at the temperatures and pressures in Deam and Maddox [8] and the calculated critical compositions (□) obtained using the algorithm in Figure A.4.

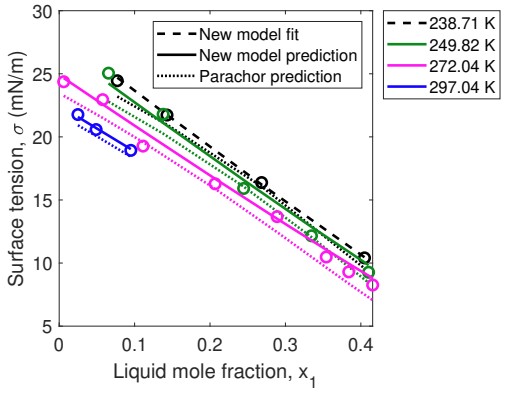

(b) Surface tension fit (black dashed line) and predictions (solid lines) *vs.* liquid composition at elevated temperatures using our new model. Parachor predictions are shown by dotted lines.

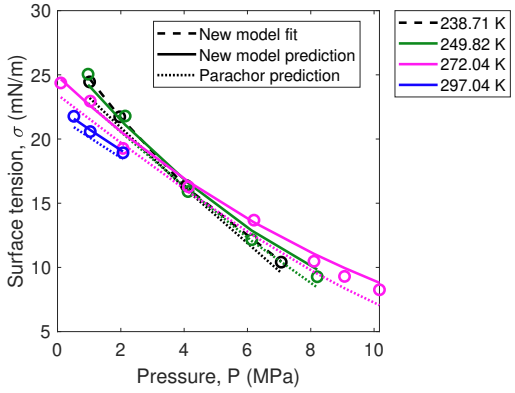

(c) Same as (b), but *vs.* pressure.

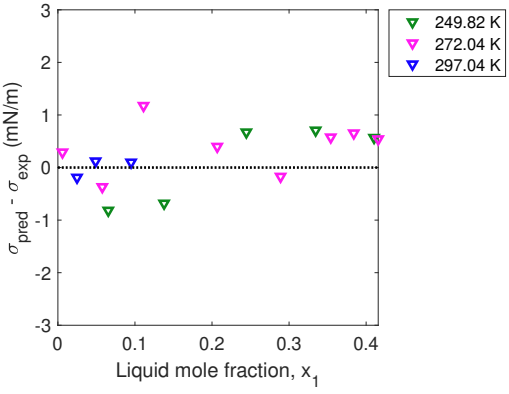

(d) Difference between predicted and experimental surface tension as a function of composition using our new model (▽).

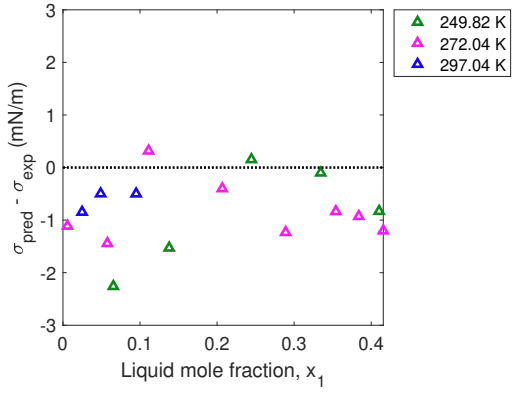

(e) Difference between predicted and experimental surface tension as a function of composition using the parachor model (△).

Figure A.32: Results for methane(1) + *n*-nonane(2) with data (○) from Deam and Maddox [8].

A.6.4 Carbon Dioxide(1) + *n*-Heptane(2)

Figure A.33(a) shows the calculated phase envelopes of carbon dioxide(1) + *n*-heptane(2) at the temperatures reported in Zolghadr *et al.* [70]. At the pressures reported in Zolghadr *et al.* [70], we depict our calculated liquid-phase compositions and vapor-phase compositions with + and $\times$ symbols, respectively. Using the algorithm presented in Figure A.4, the critical composition of the binary mixture is calculated at each temperature, as shown by the $\square$ symbol and listed in Table A.12.

Table A.12: Our calculated critical composition of carbon dioxide as a function of the temperatures listed in Zolghadr *et al.* [70] for carbon dioxide(1) + *n*-heptane(2).

methane(1) +	Temperature [K]	Critical Composition $x_{1,\mathrm{cr}}$	Data Reference
n-heptane(2)	313.15	0.980	Zolghadr *et al.* [70]
	333.15	0.931	
	353.15	0.885	
	373.15	0.848	
	393.15	0.813	

In Figures A.33(b) and (c), surface tension calculated using Equation (3.2) in Chapter 3 with fitting coefficients obtained from data in Niño-Amézquita *et al.* [37] is compared to experimental measurements from Zolghadr *et al.* [70] as a function of liquid-phase composition and pressure, respectively. The limiting values of pure *n*-heptane surface tension are up to 2 mN/m lower than the Mulero *et al.* correlation [33] (Equation (3.6) in Chapter 3), and the mixture data is also consistently lower than reported in Niño-Amézquita *et al.* [37] and Jaeger *et al.* [20] at 353.15 K. Figures A.33(d) and (e) show the difference between predicted surface tension and surface tension measured experimentally by Zolghadr *et al.* [70] when using our new model (Equation (3.2) in Chapter 3) and the parachor model (Equation (A.22)), respectively.

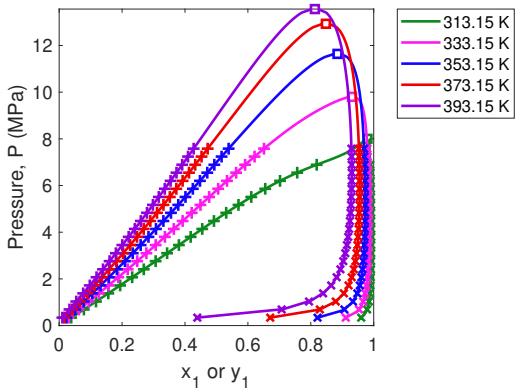

(a) Calculated liquid (+) and vapor (×) compositions at the temperatures and pressures in Zolghadr *et al.* [70] and the calculated critical compositions (□) obtained using the algorithm in Figure A.4.

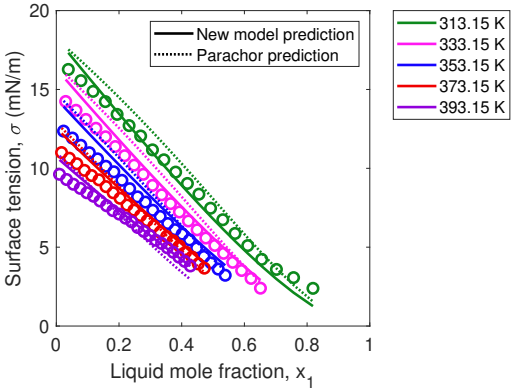

(b) Surface tension predictions (solid lines) *vs.* liquid composition at elevated temperatures using our new model. Parachor predictions are shown by dotted lines.

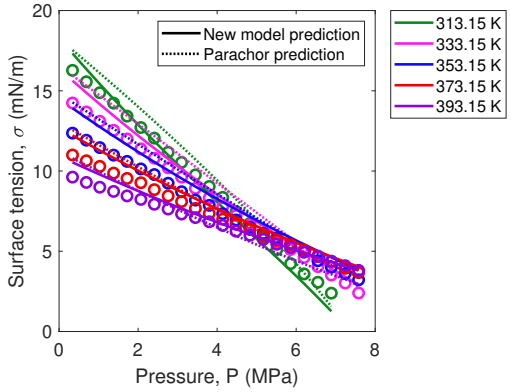

(c) Same as (b), but *vs.* pressure.

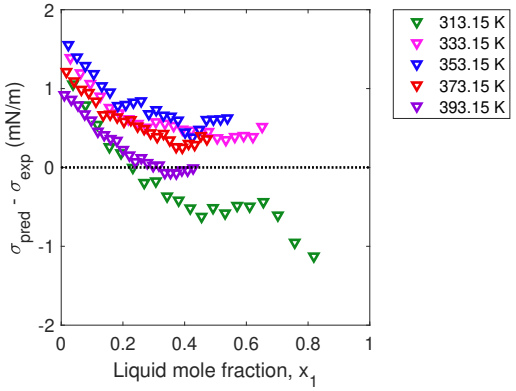

(d) Difference between predicted and experimental surface tension as a function of composition using our new model (▽).

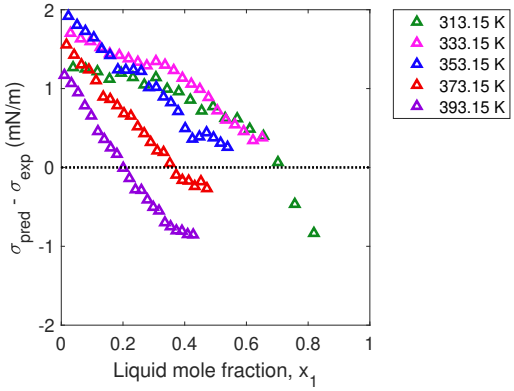

(e) Difference between predicted and experimental surface tension as a function of composition using the parachor model (△).

Figure A.33: Results for carbon dioxide(1) + *n*-heptane(2) with data (○) from Zolghadr *et al.* [70].

A.6.5 Carbon Dioxide(1) + *n*-Decane(2)

For this system, we calculate the critical compositions at each temperature from three literature sources, as listed in Table A.13. All three fitting procedures completed on data from these different literature sources yielded coefficients with very large 95% confidence intervals. As discussed for the methane(1) + *n*-nonane(2) system, this is directly due to the Jacobian of our model (Equation (3.2) in Chapter 3) with respect to the fitting coefficients.

In Nagarajan and Robinson [34] and Pereira *et al.* [44], we attribute the large confidence intervals to the narrow range of liquid-phase compositions available at the lowest temperature. For the dataset with the widest range of liquid-phase compositions (Georgiadis *et al.* [15]), both the fitting coefficients and their confidence intervals are orders of magnitude smaller than those obtained for the datasets with narrow ranges of composition.

Table A.13: Our calculated critical composition of carbon dioxide as a function of the temperatures listed for carbon dioxide(1) + *n*-decane(2).

methane(1) +	Temperature [K]	Critical Composition $x_{1,\mathrm{cr}}$	Data Reference
n-decane(2)	344.30	0.914	Nagarajan and Robinson [34]
	377.60	0.894	
	297.95	1.000	Georgiadis *et al.* [15]
	323.35	0.969	
	343.55	0.915	
	373.45	0.897	
	403.05	0.876	
	443.05	0.841	
	313.50	0.990	Pereira *et al.* [44]
	343.20	0.915	
	392.70	0.884	
	442.50	0.842	

Figure A.34(a) shows the calculated phase envelopes of carbon dioxide(1) + *n*-decane(2) at the temperatures reported in Nagarajan and Robinson [34]. At the pressures reported in Nagarajan and Robinson [34], we depict our calculated liquid-phase compositions and vapor-phase compositions with + and $\times$ symbols, respectively. Using the algorithm presented in Figure A.4, the critical composition of the binary mixture is calculated at each temperature, as shown by the $\square$ symbol. In Figures A.34(b) and (c), surface tension calculated using Equation (3.2) in Chapter 3 is compared to experimental measurements from Nagarajan and Robinson [34] as a function of liquid-phase composition and pressure, respectively. The coefficients from fitting to data at 344.3 K were $a = -41.24 \pm 50.80$ and $b = 4.84 \pm 5.04$, and these were used for making predictions at an elevated temperature. Figures A.34(d) and (e) show

the difference between predicted surface tension and surface tension measured experimentally by Nagarajan and Robinson [34] when using our new model (Equation (3.2) in Chapter 3) and the parachor model (Equation (A.22)), respectively.

Figure A.35(a) shows the calculated phase envelopes of carbon dioxide(1) + *n*-decane(2) at the temperatures reported in Georgiadis *et al.* [15]. At the pressures reported in Georgiadis *et al.* [15], we depict our calculated liquid-phase compositions and vapor-phase compositions with + and $\times$ symbols, respectively. Using the algorithm presented in Figure A.4, the critical composition of the binary mixture is calculated at each temperature, as shown by the $\square$ symbol. In Figures A.35(b) and (c), surface tension calculated using Equation (3.2) in Chapter 3 is compared to experimental measurements from Georgiadis *et al.* [15] as a function of liquid-phase composition and pressure, respectively. The coefficients from fitting to data at 297.95 K were $a = -2.02 \pm 25.65$ and $b = 0.32 \pm 1.98$, and these were used for making predictions at elevated temperatures. Figures A.35(d) and (e) show the difference between predicted surface tension and surface tension measured experimentally by Georgiadis *et al.* [15] when using our new model (Equation (3.2) in Chapter 3) and the parachor model (Equation (A.22)), respectively.

Figure A.36(a) shows the calculated phase envelopes of carbon dioxide(1) + *n*-decane(2) at the temperatures reported in Pereira *et al.* [44]. At the pressures reported in Pereira *et al.* [44], we depict our calculated liquid-phase compositions and vapor-phase compositions with + and $\times$ symbols, respectively. Using the algorithm presented in Figure A.4, the critical composition of the binary mixture is calculated at each temperature, as shown by the $\square$ symbol. In Figures A.36(b) and (c), surface tension calculated using Equation (3.2) in Chapter 3 is compared to experimental measurements from Pereira *et al.* [44] as a function of liquid-phase composition and pressure, respectively. The coefficients from fitting to data at 313.50 K were $a = -3.3 \times 10^4 \pm 7.1 \times 10^8$ and $b = 3.9 \times 10^3 \pm 8.5 \times 10^7$, and these were used for making predictions at elevated temperatures. Figures A.36(d) and (e) shows the difference between predicted surface tension and surface tension measured experimentally by Pereira *et al.* [44] when using our new model (Equation (3.2) in Chapter 3) and the parachor model (Equation (A.22)), respectively.

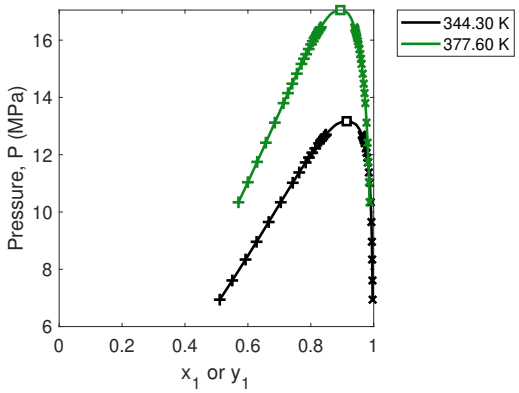

(a) Calculated liquid (+) and vapor (×) compositions at the temperatures and pressures in Nagarajan and Robinson [34] and the calculated critical compositions (□) obtained using the algorithm in Figure A.4.

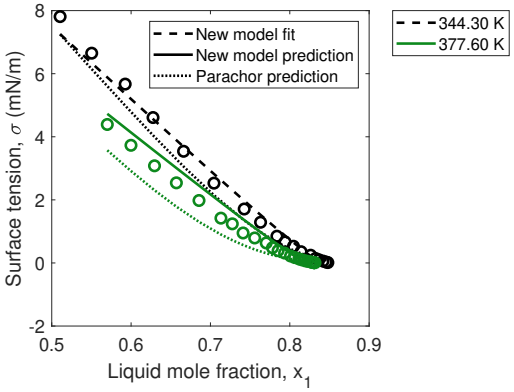

(b) Surface tension fit (black dashed line) and predictions (solid line) *vs.* liquid composition at an elevated temperature using our new model. Parachor predictions are shown by dotted lines.

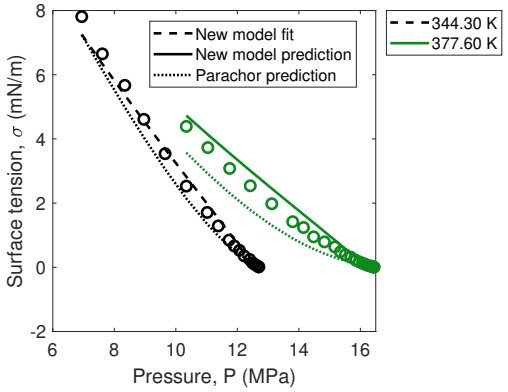

(c) Same as (b), but *vs.* pressure.

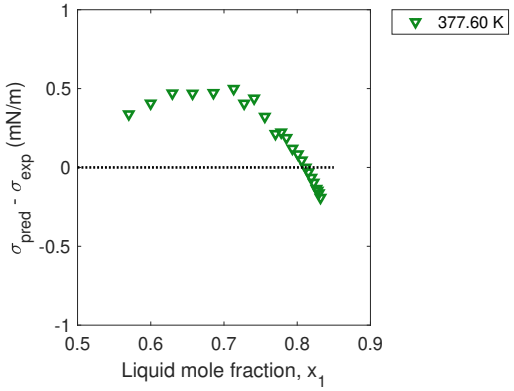

(d) Difference between predicted and experimental surface tension as a function of composition using our new model (▽).

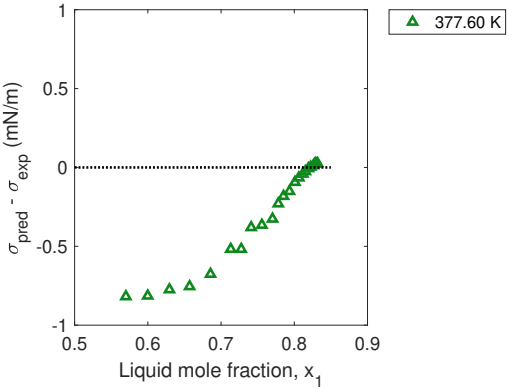

(e) Difference between predicted and experimental surface tension as a function of composition using the parachor model (△).

Figure A.34: Results for carbon dioxide(1) + *n*-decane(2) with data (○) from Nagarajan and Robinson [34].

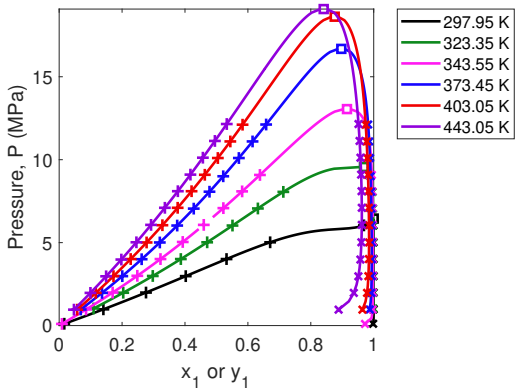

(a) Calculated liquid (+) and vapor (×) compositions at the temperatures and pressures in Georgiadis *et al.* [15] and the calculated critical compositions (□) obtained using the algorithm in Figure A.4.

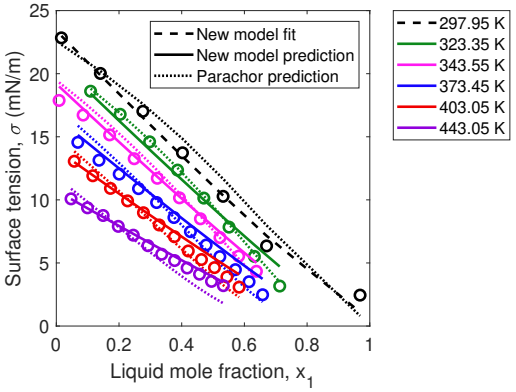

(b) Surface tension fit (black dashed line) and predictions (solid lines) *vs.* liquid composition at elevated temperatures using our new model. Parachor predictions are shown by dotted lines.

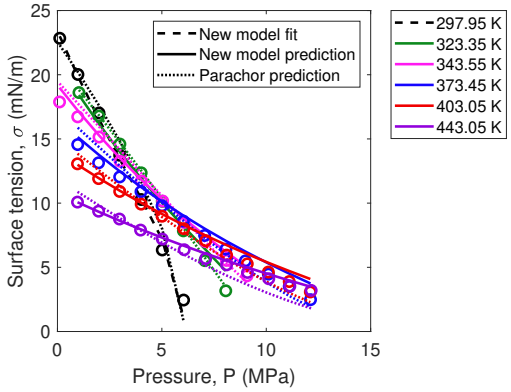

(c) Same as (b), but *vs.* pressure.

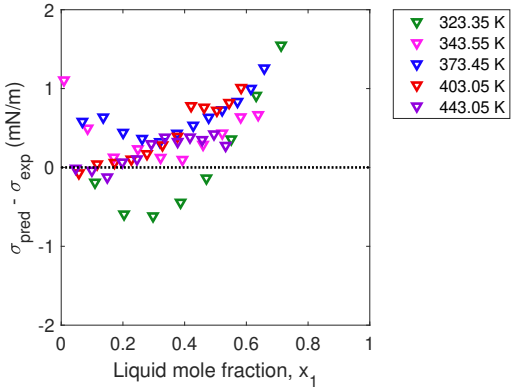

(d) Difference between predicted and experimental surface tension as a function of composition using our new model (▽).

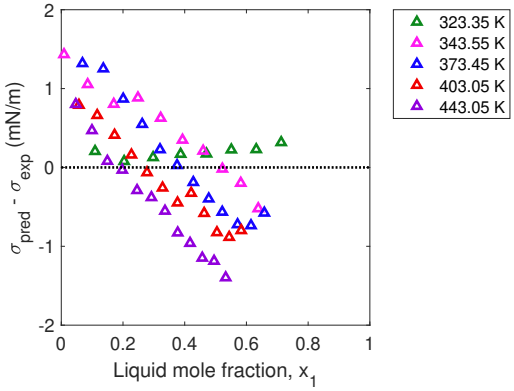

(e) Difference between predicted and experimental surface tension as a function of composition using the parachor model (△).

Figure A.35: Results for carbon dioxide(1) + *n*-decane(2) with data (○) from Georgiadis *et al.* [15].

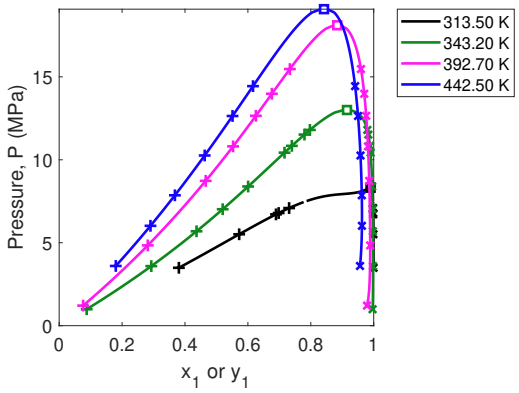

(a) Calculated liquid (+) and vapor (×) compositions at the temperatures and pressures in Pereira *et al.* [44] and the calculated critical compositions (□) obtained using the algorithm in Figure A.4.

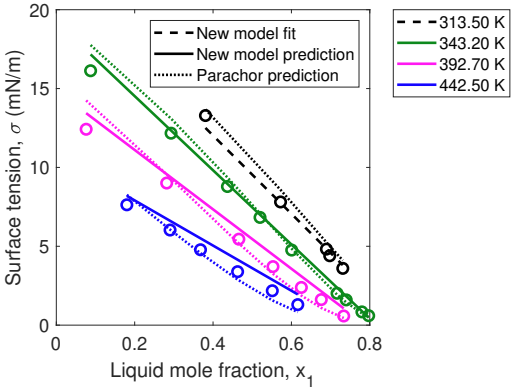

(b) Surface tension fit (black dashed line) and predictions (solid lines) *vs.* liquid composition at elevated temperatures using our new model. Parachor predictions are shown by dotted lines.

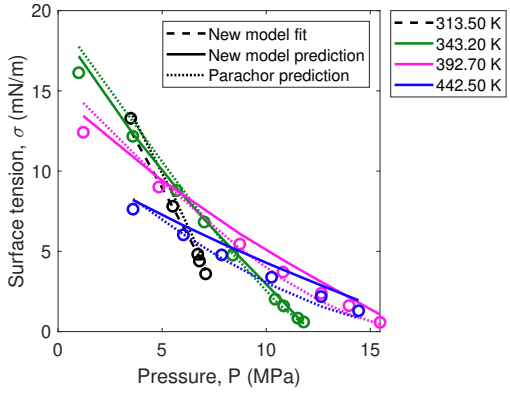

(c) Same as (b), but *vs.* pressure.

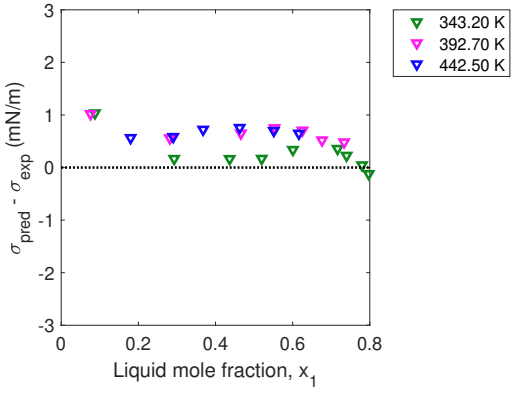

(d) Difference between predicted and experimental surface tension as a function of composition using our new model (▽).

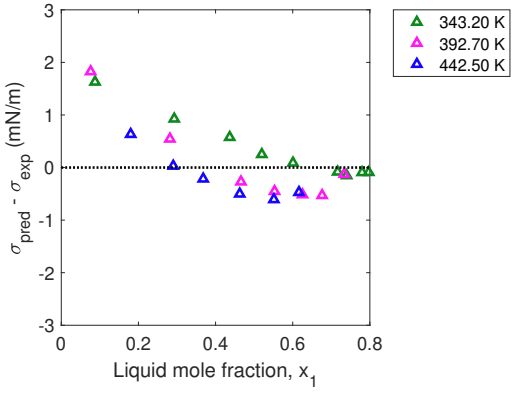

(e) Difference between predicted and experimental surface tension as a function of composition using the parachor model (△).

Figure A.36: Results for carbon dioxide(1) + *n*-decane(2) with data (○) from Pereira *et al.* [44].

A.6.6 Cyclohexane(1) + Benzene(2)

Figure A.37(a) shows the calculated phase envelopes of cyclohexane(1) + benzene(2) at the temperatures reported in Suri and Ramakrishna [62]. At the liquid compositions reported in Suri and Ramakrishna [62], we depict our calculated bubble pressures and vapor-phase compositions with + and $\times$ symbols, respectively. In Figure A.37(b), surface tension calculated using Equation (3.2) in Chapter 3 with fitting coefficients obtained from data in Herrmann [18, 69] is compared to experimental measurements from Suri and Ramakrishna [62] as a function of liquid-phase composition. When compared to the data from the three other literature sources for this system [18, 24, 25], the surface tension measurements at 303.15 K are consistently higher. We thus exclude this data source from consideration. Figures A.37(c) and (d) shows the difference between predicted surface tension and surface tension measured experimentally by Suri and Ramakrishna [62] when using our new model (Equation (3.2) in Chapter 3) and the parachor model (Equation (A.22)), respectively.

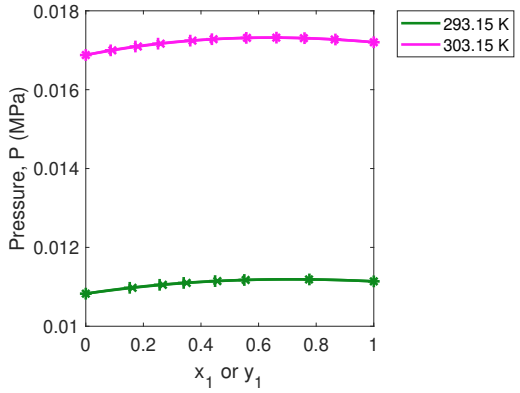

(a) Calculated bubble pressures (+) and vapor (×) compositions at the temperatures and liquid compositions in Suri and Ramakrishna [62].

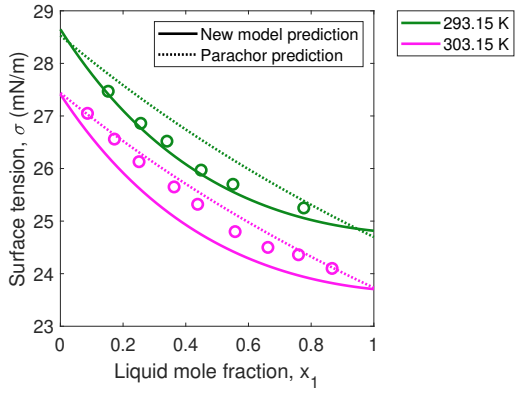

(b) Surface tension predictions (solid lines) vs. liquid composition at elevated temperatures using our new model. Parachor predictions are shown by dotted lines.

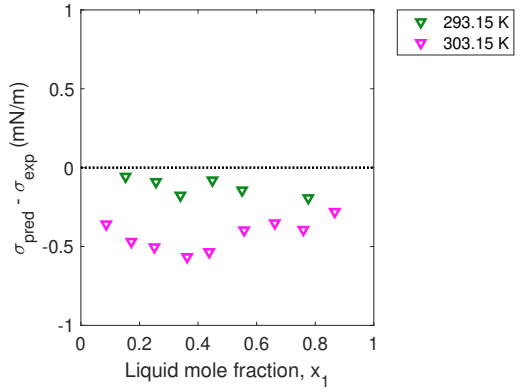

(c) Difference between predicted and experimental surface tension as a function of composition using our new model (▽).

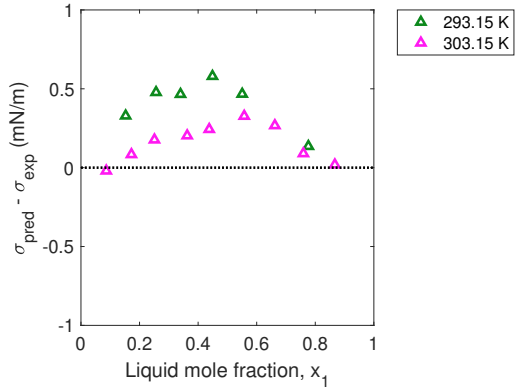

(d) Difference between predicted and experimental surface tension as a function of composition using the parachor model (△).

Figure A.37: Results for cyclohexane(1) + benzene(2) with data (○) from Suri and Ramakrishna [62].

A.7 Discussion of Ternary Mixture Data and Predictions

For multicomponent mixtures, we developed Equation (3.3) in Chapter 3 where the coefficients a_{ji} and b_{ji} are obtained from fitting to surface tension *vs.* composition data for each binary system (component i + component j) that comprises the multicomponent mixture. In the next two subsections, we use Equation (3.3) to predict the surface tension of two ternary mixtures: methanol(1) + ethanol(2) + water(3) and carbon dioxide(1) + *n*-butane(2) + *n*-decane(3).

A.7.1 Methanol(1) + Ethanol(2) + Water(3)

For the ternary mixture of methanol(1) + ethanol(2) + water(3), we use a linear equation for the temperature-dependence of each pure component's surface tension ($\sigma_i = \theta_{0,i} + \theta_{1,i}T$ with coefficients listed in Table A.14; [55]). For the composition-dependence of each constituent binary mixture's surface tension, we use the coefficients obtained in our previous work for methanol(1) + water(3) and ethanol(2) + water(3) [55] (Table A.15), while methanol(1) + ethanol(2) can be considered an ideal mixture [24, 69] so that $a_{21} = 0$, $b_{21} = 0$, and $b_{21}/a_{21} = 1$.

Table A.14: Coefficients from Chapter 2 [55] to describe the surface tension of pure methanol, ethanol, and water as a function of temperature using the equation $\sigma_i = \theta_{0,i} + \theta_{1,i}T$ where σ_i is in mN/m and T is in K.

Component	θ_0 [mN/m]	θ_1 [mN/m/K]
methanol	50.0	−0.092
ethanol	46.3	−0.082
water	120.5	−0.163

Table A.15: Coefficients for use in Equation (3.3) (Chapter 3) to describe the composition-dependence of surface tension for binary mixtures of methanol(1) + ethanol(2), methanol(1) + water(3), and ethanol(2) + water(3). The coefficients for the aqueous mixtures were obtained in Chapter 2 [55] by fitting to experimental data at 293 K.

Mixture	a_{ji}	b_{ji}
methanol(1) + ethanol(2)	0	0
methanol(1) + water(3)	0.8709	0.8314
ethanol(2) + water(3)	0.9583	0.9176

Figure A.38 shows all experimental measurements of surface tension as reported in Kharin *et al.* [22] and all predictions using Equation (3.3) in Chapter 3. Overall, the agreement between experimental measurements and predictions is good with an average absolute deviation of 0.71 mN/m and 2.54%.

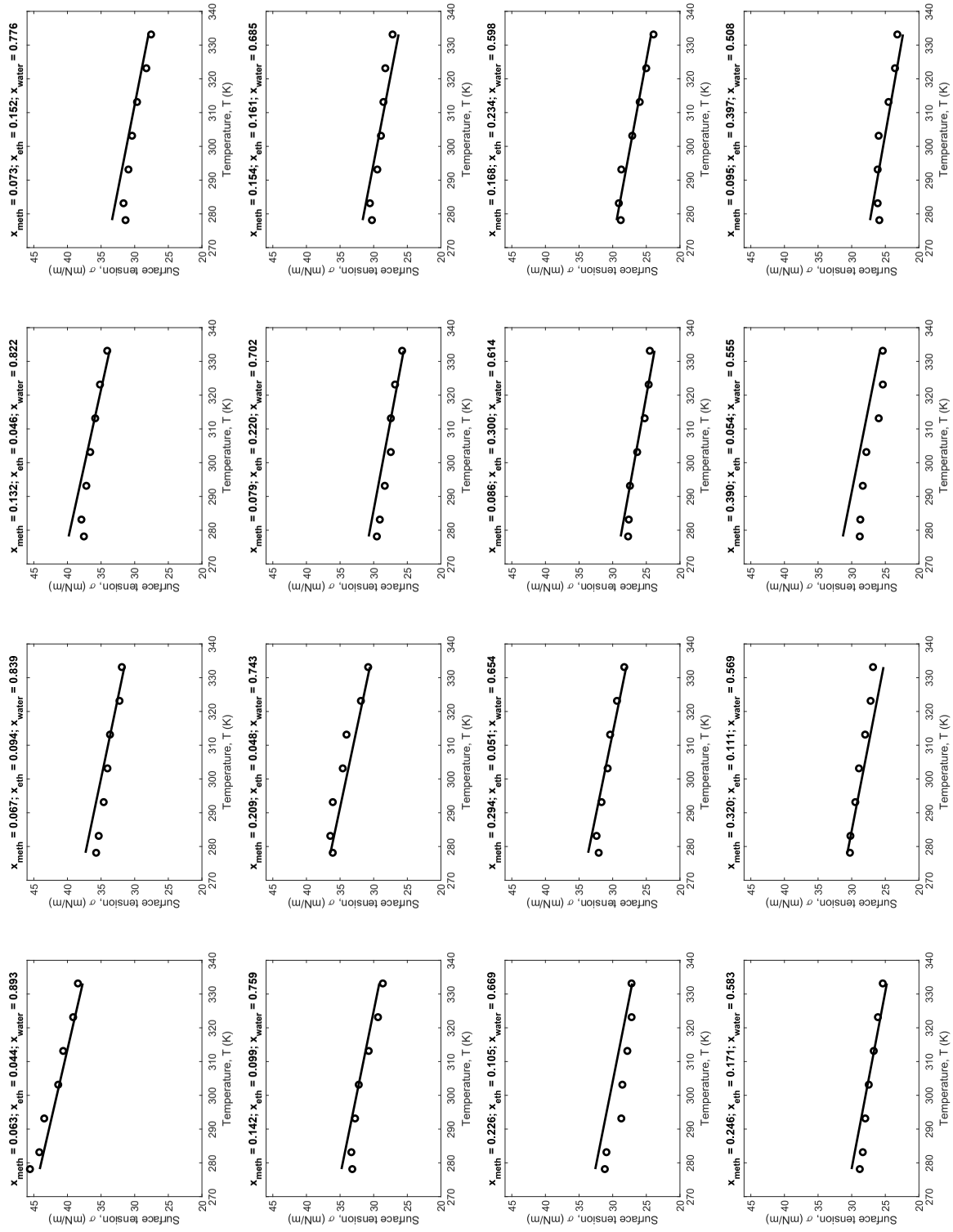
x_{meth} = 0.063; x_{eth} = 0.044; x_{water} = 0.893
x_{meth} = 0.142; x_{eth} = 0.099; x_{water} = 0.759
x_{meth} = 0.226; x_{eth} = 0.105; x_{water} = 0.669
x_{meth} = 0.246; x_{eth} = 0.171; x_{water} = 0.583
x_{meth} = 0.067; x_{eth} = 0.094; x_{water} = 0.839
x_{meth} = 0.209; x_{eth} = 0.048; x_{water} = 0.743
x_{meth} = 0.294; x_{eth} = 0.051; x_{water} = 0.654
x_{meth} = 0.320; x_{eth} = 0.111; x_{water} = 0.569
x_{meth} = 0.132; x_{eth} = 0.046; x_{water} = 0.822
x_{meth} = 0.079; x_{eth} = 0.220; x_{water} = 0.702
x_{meth} = 0.086; x_{eth} = 0.300; x_{water} = 0.614
x_{meth} = 0.390; x_{eth} = 0.054; x_{water} = 0.555
x_{meth} = 0.073; x_{eth} = 0.152; x_{water} = 0.776
x_{meth} = 0.154; x_{eth} = 0.161; x_{water} = 0.685
x_{meth} = 0.168; x_{eth} = 0.234; x_{water} = 0.598
x_{meth} = 0.095; x_{eth} = 0.397; x_{water} = 0.508
Surface tension, σ (mN/m)
Temperature, T (K)

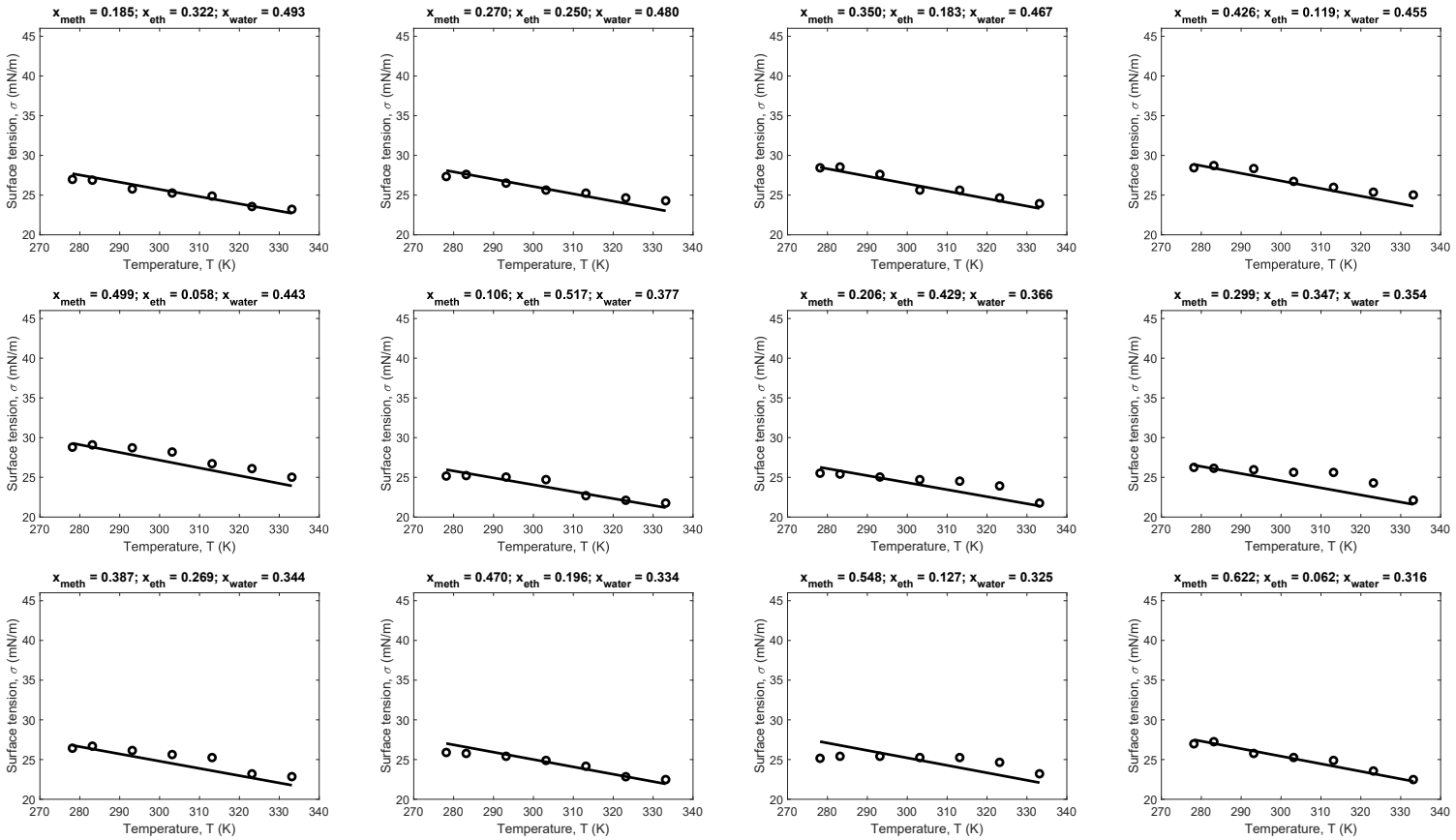

Figure A.38: Surface tension as a function of temperature for mixtures containing methanol(1) + ethanol(2) + water(3), as measured experimentally (○) by Kharin *et al.* [22] and as predicted by Equation (3.3) in Chapter 3 (lines). The mixture compositions (mole fractions of each component computed from the reported weight fractions) are shown in the title of each graph. No fitting coefficients need to be extracted from surface tension data of the ternary mixture.

A.7.2 Carbon Dioxide(1) + *n*-Butane(2) + *n*-Decane(3)

We test the ability of Equation (3.3) in Chapter 3 to predict the surface tension of carbon dioxide(1) + *n*-butane(2) + *n*-decane(3) measured experimentally by Nagarajan *et al.* [35], who studied a mixture with an overall molar composition of 90.2% carbon dioxide, 5.9% *n*-butane, and 3.9% *n*-decane at a temperature of 344.3 K and varying pressures. Four quantities need to be known to evaluate Equation (3.3) in Chapter 3: (*i*) the pure component surface tensions, (*ii*) the binary surface tension parameters a_{ji} and b_{ji}, (*iii*) the liquid-phase compositions, and (*iv*) the critical composition.

For (*i*), the pure component surface tension temperature dependence in Equation (3.3), we use the Mulero *et al.* correlation [33] (Equation (3.6)) with coefficients in Table A.4. For (*ii*), we use the coefficients previously obtained for carbon dioxide(1) + *n*-butane(2) (see Table 3.2 in Chapter 3) and carbon dioxide(1) + *n*-decane(3) (see Section A.6.5, as summarized in Table A.16, where we consider two sets of coefficients for carbon dioxide(1) + *n*-decane(3)). We treat *n*-butane(2) + *n*-decane(3) as an ideal mixture that can be described by $\sigma_{\text{mix}} = \sum \sigma_i x_i$ based on data reported in Deam and Maddox [8] (after performing flash calculations with the PR-EOS assuming a binary interaction coefficient of $k_{23} = 0$), as illustrated in Figure A.39.

Table A.16: Coefficients for use in Equation (3.3) in Chapter 3 to describe the composition-dependence of surface tension for carbon dioxide(1) + *n*-decane(3) from Section A.6.5 and for *n*-butane(2) + *n*-decane(3).

Mixture	a_{ji}	b_{ji}	Data Reference
carbon dioxide(1) + *n*-decane(3)	−41.24	4.84	Nagarajan and Robinson [34]
	−2.02	0.32	Georgiadis *et al.* [15]
n-butane(2) + *n*-decane(3)	0	0	Deam and Maddox [8]

For (*iii*), the liquid-phase compositions at the experimental conditions, we perform flash calculations given the pressure and overall composition using Equations (A.2)–(A.15) in Section A.1. For these vapor–liquid equilibrium calculations, we use binary interaction coefficients of $k_{12} = 0.12$, $k_{13} = 0.11$, and $k_{23} = 0$.

For (*iv*), the critical composition of this ternary mixture, we adapt the algorithm developed in Section A.2 for a binary mixture to perform flash calculations instead of bubble point calculations. This is because the addition of a third component increases the degrees of freedom for vapor–liquid equilibrium by one, and to meet this increase, we specify the overall composition of the mixture at each step of the iterative scheme in addition to temperature and pressure. As our initial guess to the iterative algorithm, we set the composition of carbon dioxide to 85% (around the experimental molar composition), while keeping the ratio of the other two components the

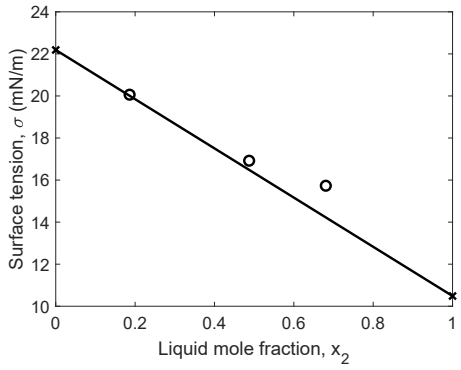

Figure A.39: Surface tension as a function of *n*-butane liquid mole fraction (x_2) for the system *n*-butane(2) + *n*-decane(3), as measured experimentally by Deam and Maddox [8] at 310.93 K ($\circ$) and as predicted by the linear equation $\sigma_{\text{mix}} = \sum \sigma_i x_i$ where pure component values are obtained from the Mulero *et al.* correlation [33] (Equation (3.6) in Chapter 3; shown by $\times$ symbols).

same as studied experimentally (a pseudo-binary mixture). That is, given this mole fraction of carbon dioxide, we split the remaining mole fraction with 60% going to *n*-butane and 40% to *n*-decane (based on the ratio of these components in the experimental molar composition of 5.9% *n*-butane and 3.9% *n*-decane). At this initial composition, we perform a flash calculation at 9 MPa using the PR-EOS to determine the liquid and vapor-phase compositions. For the next iteration, we take the average of the calculated liquid and vapor-phase carbon dioxide composition as the new overall carbon dioxide composition, adjust the *n*-butane and *n*-decane compositions [$z_2 = 0.6(1-z_1)$ and $z_3 = 0.4(1-z_1)$], and perform a flash calculation at an increased pressure at this new overall composition. Further flash calculations are performed until the difference between vapor and liquid phase compositions is less than a threshold value. Using this approach, we calculate a critical composition of carbon dioxide of $x_{1,\text{cr}}(344.3\ K) = 0.867$.

The above four quantities ((*i*) the pure component surface tensions, (*ii*) the binary surface tension parameters a_{ji} and b_{ji}, (*iii*) the liquid-phase compositions, and (*iv*) the critical composition) are substituted into Equation (3.3) in Chapter 3 at each experimental pressure reported in Nagarajan *et al.* [35] to yield predictions of surface tension. Figure A.40 shows predictions of surface tension as a function of pressure when $a_{31} = -41.24$ and $b_{31} = 4.84$ (from a fit to surface tension data in Nagarajan and Robinson [34]), while Figure A.41 shows predictions of surface tension when $a_{31} = -2.02$ and $b_{31} = 0.32$ (from a fit to surface tension data in Georgiadis *et al.* [15]. The accuracy of the predictions is better when the coefficients obtained from a fit to data in Nagarajan and Robinson [34] are used, and this is likely because these coefficients were obtained from data at pressures close to the critical point. On the other hand, the critical region was not experimentally considered in Georgiadis *et al.* [15], and therefore the coefficients

obtained from the data do not adequately describe this region when used for predictions of the ternary mixture in Figure A.41. Regardless of the selected values of a_{31} and b_{31}, the level of accuracy obtained with Equation (3.3) in Chapter 3 is comparable to the predictions of Cárdenas and Mejía [7] obtained using density gradient theory with the variable-range Mie statistical associated fluid theory (SAFT–VR Mie) equation of state, but higher accuracy was obtained by Miqueu *et al.* [32] using density gradient theory with the volume-shifted PR-EOS.

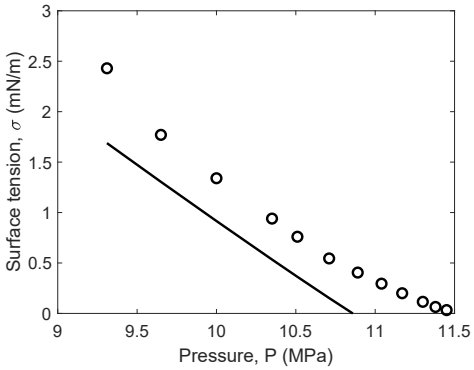

Figure A.40: Surface tension *vs.* pressure for carbon dioxide(1) + *n*-butane(2) + *n*-decane(3), as measured experimentally by Nagarajan *et al.* [35] (○) and as predicted using Equation (3.3) in Chapter 3 (line) with $a_{31} = -41.24$ and $b_{31} = 4.84$ as obtained by fitting to surface tension data for carbon dioxide(1) + *n*-decane(3) in Nagarajan and Robinson [34].

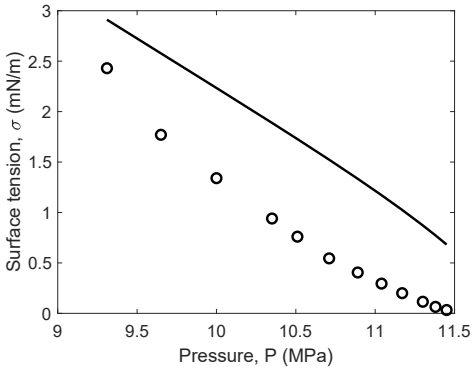

Figure A.41: Surface tension *vs.* pressure for carbon dioxide(1) + *n*-butane(2) + *n*-decane(3), as measured experimentally by Nagarajan *et al.* [35] (○) and as predicted using Equation (3.3) in Chapter 3 (line) with $a_{31} = -2.02$ and $b_{31} = 0.32$ as obtained by fitting to surface tension data for carbon dioxide(1) + *n*-decane(3) in Georgiadis *et al.* [15].

We briefly emphasize that the coefficients used for carbon dioxide(1) + *n*-decane(3) all have very large confidence intervals, as discussed in Section A.6.5, and they are only used here as a conceptual test of the functional form of Equation (3.3) in Chapter 3 for multicomponent mixtures.

A.8 Importance of Surface Tension in Vapor–Liquid Equilibrium at the Nanoscale (Nitrogen(1) + Argon(2))

As a case study, we examine the effect of surface tension on the calculations of dew points for nitrogen(1) + argon(2) mixtures in nanopores. Figure A.42(a) illustrates dew point predictions when Equation (3.1) in Chapter 3 is used to describe how surface tension changes with composition and temperature (see the governing equations for dew point in Chapter 5 [56]), and it can be seen that the predicted dew points are in close agreement with experimental measurements (symbols) for both geometries of adsorption and desorption. In contrast, Figure A.42(b) shows the resulting predictions of dew point if variations in surface tension due to composition are included, but at a constant temperature of 84 K (the temperature for which experimental surface tension is available)—the deviation becomes increasingly poor as the importance of surface tension effects increases (*i.e.*, for $r = -2$ nm compared to $r = -4$ nm). Finally, in Figure A.42(c), we show dew point predictions obtained when surface tension is fixed at one value irrespective of composition and temperature (here, we choose the average of the pure component surface tension values at 84 K), where again, dew point predictions deviate more from experimental measurements as surface tension effects become more significant. We thus emphasize the importance of an accurate description of surface tension as a simultaneous function of composition and temperature, especially where experimental data is unavailable.

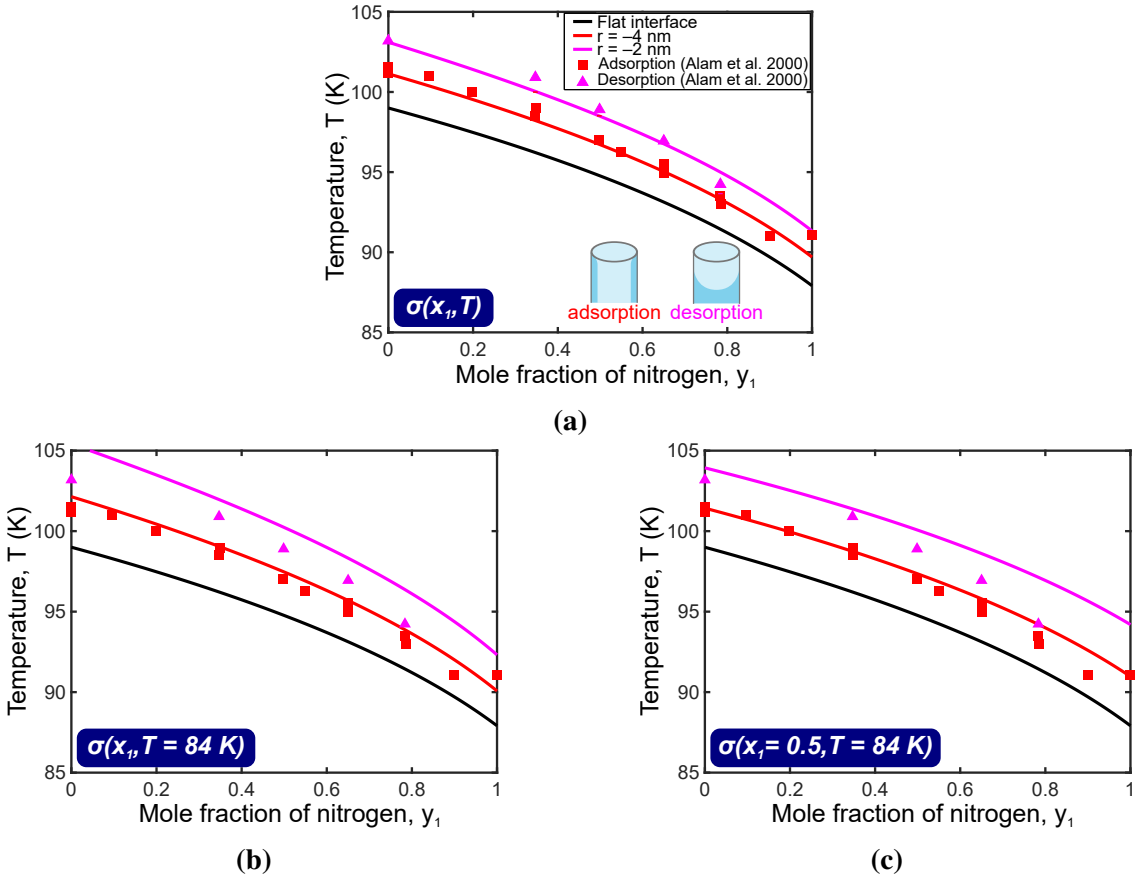

Figure A.42: Dew point predictions (not fits; governing equations are from Chapter 5; Ref. [56]) for nitrogen(1) + argon(2) in Vycor glass with a pore radius of 2 nm at a vapor-phase pressure of 300 kPa (experimental data is from Alam *et al.* [2], and the adsorption/desorption model is adapted from Donohue and Aranovich [10]). We highlight the importance of surface tension in dictating the accuracy of the prediction: (a) dew points calculated using surface tension as a function of composition and temperature as described by Equation (3.1) in Chapter 3 with fitting coefficients from Chapter 5 [56] (a version of this plot was previously shown in Chapter 5 [56]); (b) dew points calculated using surface tension as a function of composition, but at a temperature of 84 K (the only temperature for which experimental data is available); and (c) dew points calculated using the surface tension of an equimolar nitrogen(1) + argon(2) mixture at 84 K. Dew point predictions are accurate when both composition and temperature effects are accounted for—in (a).

References

[1] J. Ahlers and J. Gmehling. "Development of an Universal Group Contribution Equation of State: I. Prediction of Liquid Densities for Pure Compounds with a Volume Translated Peng–Robinson Equation of State". *Fluid Phase Equilibria* 191.1–2 (2001), pp. 177–188 (cited on pp. 172, 174).

[2] M. A. Alam, A. P. Clarke, and J. A. Duffy. "Capillary Condensation and Desorption of Binary Mixtures of N_2–Ar Confined in a Mesoporous Medium". *Langmuir* 16.20 (2000), pp. 7551–7553 (cited on p. 244).

[3] R. Amin and T. N. Smith. "Interfacial Tension and Spreading Coefficient under Reservoir Conditions". *Fluid Phase Equilibria* 142 (1998), pp. 231–241 (cited on pp. 187, 188, 201, 203, 204, 206, 222, 223).

[4] J. Aracil, G. Luengo, B. S. Almeida, M. M. Telo da Gama, R. G. Rubio, and M. Diaz Pena. "Surface Properties of Mixtures of Molecular Fluids: An Experimental and Theoretical Study of Carbon Disulfide + Dichloromethane and Carbon Disulfide + Carbon Tetrachloride". *The Journal of Physical Chemistry* 93 (1989), pp. 3210–3218 (cited on pp. 185, 189, 221).

[5] S. Arbabi and A. Firoozabadi. "Near-Critical Phase Behavior of Reservoir Fluids Using Equations of State". *SPE Advanced Technology Series* 3.1 (1995), pp. 139–145 (cited on p. 175).

[6] V. G. Baidakov, A. M. Kaverin, and M. N. Khotienkova. "Surface Tension of Ethane–Methane Solutions: 1. Experiment and Thermodynamic Analysis of the Results". *Fluid Phase Equilibria* 356 (2013), pp. 90–95 (cited on pp. 187, 191, 192).

[7] H. Cárdenas and A. Mejía. "Phase Behaviour and Interfacial Properties of Ternary System CO_2 + *n*-Butane + *n*-Decane: Coarse-Grained Theoretical Modelling and Molecular Simulations". *Molecular Physics* 114.18 (2016), pp. 2627–2640 (cited on p. 242).

[8] J. R. Deam and R. N. Maddox. "Interfacial Tension in Hydrocarbon Systems". *Journal of Chemical & Engineering Data* 15.2 (1970), pp. 216–222 (cited on pp. 187, 226, 227, 240, 241).

[9] Design Institute for Physical Properties, Sponsored by AIChE. "DIPPR Project 801 - Full Version" (2019) (cited on p. 184).

[10] M. D. Donohue and G. L. Aranovich. "Adsorption Hysteresis in Porous Solids". *Journal of Colloid and Interface Science* 205 (1998), pp. 121–30 (cited on p. 244).

[11] J. Escobedo and G. A. Mansoori. “Surface-Tension Prediction for Liquid Mixtures”. *AIChE Journal* 44.10 (1998), pp. 2324–2332 (cited on p. 189).

[12] A. Firoozabadi. *Thermodynamics and Applications in Hydrocarbon Energy Production*. McGraw-Hill Education, 2016 (cited on pp. 173, 175).

[13] G. Gao, J. L. Daridon, H. Saint-Guirons, P. Xans, and F. Montel. “A Simple Correlation to Evaluate Binary Interaction Parameters of the Peng–Robinson Equation of State: Binary Light Hydrocarbon Systems”. *Fluid Phase Equilibria* 74 (1992), pp. 85–93 (cited on p. 175).

[14] J. M. Garrido and I. Polishuk. “Toward Development of a Universal CP-PC-SAFT-Based Modeling Framework for Predicting Thermophysical Properties at Reservoir Conditions: Inclusion of Surface Tensions”. *Industrial & Engineering Chemistry Research* 57.26 (2018), pp. 8819–8831 (cited on p. 222).

[15] A. Georgiadis, F. Llovell, A. Bismarck, F. J. Blas, A. Galindo, G. C. Maitland, J. P. M. Trusler, and G. Jackson. “Interfacial Tension Measurements and Modelling of (Carbon Dioxide + *n*-Alkane) and (Carbon Dioxide + Water) Binary Mixtures at Elevated Pressures and Temperatures”. *Journal of Supercritical Fluids* 55.2 (2010), pp. 743–754 (cited on pp. 188, 230, 231, 233, 240–242).

[16] D. W. Green and R. H. Perry. “Critical Constants”. In: *Perry’s Chemical Engineers’ Handbook*. 8th ed. McGraw-Hill Professional, 2000 (cited on p. 174).

[17] M. K. Gupta, G. C. Gardner, M. J. Hegarty, and A. J. Kidnay. “Liquid–Vapor Equilibria for the N_2 + CH_4 + C_2H_6 System from 260 to 280 K”. *Journal of Chemical & Engineering Data* 25.4 (1980), pp. 313–318 (cited on pp. 176, 177).

[18] L. Herrmann. “Untersuchung von Struktur und Grenzflächeneigenschaften binärer Systeme”. PhD thesis. Martin-Luther-Universität Halle-Wittenberg, 1994 (cited on pp. 185, 189, 215–217, 235).

[19] J. J.-C. Hsu, N. Nagarajan, and R. L. Robinson. “Equilibrium Phase Compositions, Phase Densities, and Interfacial Tensions for CO_2 + Hydrocarbon Systems. 1. CO_2 + *n*-Butane”. *Journal of Chemical & Engineering Data* 30 (1985), pp. 485–491 (cited on pp. 179, 180, 188, 208, 209).

[20] P. T. Jaeger, M. B. Alotaibi, and H. A. Nasr-El-Din. “Influence of Compressed Carbon Dioxide on the Capillarity of the Gas–Crude Oil–Reservoir Water System”. *Journal of Chemical & Engineering Data* 55.11 (2010), pp. 5246–5251 (cited on pp. 188, 210, 212, 228).

[21] H. Kalra, H. Kubota, D. B. Robinson, and H.-J. Ng. "Equilibrium Phase Properties of the Carbon Dioxide–*n*-Heptane System". *Journal of Chemical & Engineering Data* 23.4 (1978), pp. 317–321 (cited on pp. 179, 180).

[22] S. E. Kharin, A. A. Kniga, and G. S. Sorokina. "Surface Tension of Water–Ethanol–Methanol Solutions". *Izvestiya Vysshikh Uchebnykh Zavedenii Khimiya i Khimicheskaya Tekhnologiya* 12 (1968), pp. 1341–1344 (cited on pp. 237, 239).

[23] J. P. Kohn and W. F. Bradish. "Multiphase and Volumetric Equilibria of the Methane–*n*-Octane System at Temperatures between -110 ° and 150 °C". *Journal of Chemical & Engineering Data* 9.1 (1964), pp. 5–8 (cited on pp. 176, 178).

[24] B. Konobeev and V. Lyapin. "Density, Viscosity, and Surface Tension of Some Binary Systems". *Zhurnal Prikladnoi Khimii* 43.4 (1970), p. 803 (cited on pp. 189, 216, 235, 237).

[25] V. T. Lam and G. C. Benson. "Surface Tension of Binary Liquid Systems I. Mixtures of Nonelectrolytes". *Canadian Journal of Chemistry* 48.24 (1970), pp. 3773–3781 (cited on pp. 189, 215, 235).

[26] Z. Li and A. Firoozabadi. "Interfacial Tension of Nonassociating Pure Substances and Binary Mixtures by Density Functional Theory Combined with Peng–Robinson Equation of State". *The Journal of Chemical Physics* 130 (2009), p. 154108 (cited on pp. 187, 188, 222).

[27] H. M. Lin, H. M. Sebastian, J. J. Simnick, and K. C. Chao. "Gas–Liquid Equilibrium in Binary Mixtures of Methane with *n*-Decane, Benzene, and Toluene". *Journal of Chemical & Engineering Data* 24.2 (1979), pp. 146–149 (cited on pp. 176, 178).

[28] P. J. Linstrom and W. G. Mallard, eds. *NIST Chemistry WebBook, NIST Standard Reference Database Number 69*. https://webbook.nist.gov/chemistry/. Accessed: 2019-04-18. 2018 (cited on p. 174).

[29] G. Luengo, J. Aracil, R. G. Rubio, and M. Diaz Pena. "Bulk and Surface Thermodynamic Properties in Mixtures of Small Rigid Molecules: The Carbon Tetrachloride + Carbon Disulfide System". *The Journal of Physical Chemistry* 92 (1988), pp. 228–234 (cited on pp. 185, 189, 220).

[30] D. B. Macleod. "On a Relation Between Surface Tension and Density". *Transactions of the Faraday Society* 19 (1923), pp. 38–41 (cited on p. 184).

[31] R. Massoudi and A. D. King. "Effect of Pressure on the Surface Tension of *n*-Hexane. Adsorption of Low Molecular Weight Gases on *n*-Hexane at 25 °". *The Journal of Physical Chemistry* 79.16 (1975), pp. 1676–1679 (cited on pp. 186, 187, 198, 199).

[32] C. Miqueu, B. Mendiboure, C. Graciaa, and J. Lachaise. "Modelling of the Surface Tension of Binary and Ternary Mixtures with the Gradient Theory of Fluid Interfaces". *Fluid Phase Equilibria* 218.2 (2004), pp. 189–203 (cited on p. 242).

[33] A. Mulero, I. Cachadiña, and M. I. Parra. "Recommended Correlations for the Surface Tension of Common Fluids". *Journal of Physical and Chemical Reference Data* 41.4 (2012), p. 043105 (cited on pp. 183, 187, 188, 224, 228, 240, 241).

[34] N. Nagarajan and R. L. Robinson. "Equilibrium Phase Compositions, Phase Densities, and Interfacial Tensions for CO_2 + Hydrocarbon Systems. 2. CO_2 + *n*-Decane". *Journal of Chemical & Engineering Data* 31.2 (1986), pp. 168–171 (cited on pp. 188, 230–232, 240–242).

[35] N. Nagarajan, K. A. Gasem, and R. L. Robinson. "Equilibrium Phase Compositions, Phase Densities, and Interfacial Tensions for CO_2 + Hydrocarbon Systems. 6. CO_2 + *n*-Butane + *n*-Decane". *Journal of Chemical & Engineering Data* 35.3 (1990), pp. 228–231 (cited on pp. 240–242).

[36] H. N. Nilssen. *Calculation of Interfacial Tension of Methane + n-Butane Mixture with Gradient Theory near Critical Conditions*. Report prepared for KP8108 Advanced Thermodynamics. Norwegian University of Science and Technology, 2008 (cited on pp. 187, 196, 197).

[37] O. G. Niño Amézquita, S. Enders, P. T. Jaeger, and R. Eggers. "Interfacial Properties of Mixtures Containing Supercritical Gases". *Journal of Supercritical Fluids* 55.2 (2010), pp. 724–734 (cited on pp. 188, 210, 211, 228).

[38] O. G. Niño Amézquita, S. Enders, P. T. Jaeger, and R. Eggers. "Measurement and Prediction of Interfacial Tension of Binary Mixtures". *Industrial & Engineering Chemistry Research* 49.2 (2010), pp. 592–601 (cited on pp. 186, 187, 199, 200).

[39] A. Péneloux, E. Rauzy, and R. Fréze. "A Consistent Correction for Redlich–Kwong–Soave Volumes". *Fluid Phase Equilibria* 8 (1982), pp. 7–23 (cited on p. 174).

[40] B. Z. Peng, C. Y. Sun, B. Liu, Q. Zhang, J. Chen, W. Z. Li, and G. J. Chen. "Interfacial Tension Between Methane and Octane at Elevated Pressure at Five Temperatures from (274.2 to 282.2) K". *Journal of Chemical & Engineering Data* 56.12 (2011), pp. 4623–4626 (cited on pp. 187, 224, 225).

[41] D.-Y. Peng and D. B. Robinson. "A New Two-Constant Equation of State". *Industrial & Engineering Chemistry Fundamentals* 15.1 (1976), pp. 59–64 (cited on pp. 172, 173).

[42] B. Pennington and E. Hough. "Interfacial Tension of the Methane–normal Butane System". *Producers Monthly* 29 (1965), p. 4 (cited on pp. 187, 196, 197).

[43] L. Pereira. “Interfacial Tension of Reservoir Fluids: An Integrated Experimental and Modelling Investigation”. PhD thesis. Heriot-Watt University, 2016 (cited on pp. 187, 188).

[44] L. M. Pereira, A. Chapoy, R. Burgass, and B. Tohidi. “Measurement and Modelling of High Pressure Density and Interfacial Tension of (Gas + *n*-Alkane) Binary Mixtures”. *The Journal of Chemical Thermodynamics* 97 (2016), pp. 55–69 (cited on pp. 186, 188, 204, 207, 230, 231, 234).

[45] K. S. Pitzer, D. Z. Lippmann, R. F. Curl, C. M. Huggins, and D. E. Petersen. “The Volumetric and Thermodynamic Properties of Fluids. II. Compressibility Factor, Vapor Pressure and Entropy of Vaporization”. *Journal of the American Chemical Society* 77.13 (1955), pp. 3433–3440 (cited on p. 174).

[46] H. Rachford and J. Rice. “Procedure for Use of Electronic Digital Computers in Calculating Flash Vaporization Hydrocarbon Equilibrium”. *Journal of Petroleum Technology* 4 (1952), pp. 327–328 (cited on p. 173).

[47] H. H. Reamer and B. H. Sage. “Phase Equilibria in Hydrocarbon Systems. Volumetric and Phase Behavior of the *n*–Decane–CO_2 System”. *Journal of Chemical & Engineering Data* 8.4 (1963), pp. 508–513 (cited on pp. 179, 180).

[48] H. H. Reamer, B. H. Sage, and W. N. Lacey. “Phase Equilibria in Hydrocarbon Systems. Volumetric and Phase Behavior of the Methane–*n*-Heptane System”. *Industrial & Engineering Chemistry - Chemical and Engineering Data Series* 1.1 (1956), pp. 29–42 (cited on pp. 176, 177).

[49] H. H. Reamer, B. H. Sage, and W. N. Lacey. “Phase Equilibria in Hydrocarbon Systems. Volumetric and Phase Behavior of the Methane–Propane System”. *Industrial & Engineering Chemistry - Chemical and Engineering Data Series* 42.3 (1950), pp. 534–539 (cited on pp. 176, 177).

[50] W. E. Reiff, P. Peters-Gerth, and K. Lucas. “A Static Equilibrium Apparatus for (Vapour + Liquid) Equilibrium Measurements at High Temperatures and Pressures: Results for (Methane + *n*-Pentane)”. *The Journal of Chemical Thermodynamics* 19.5 (1987), pp. 467–477 (cited on pp. 176, 177).

[51] D. Robinson and D. Peng. *Research Report 28: The Characterization of the Heptanes and Heavier Fractions for the GPA Peng–Robinson Programs*. Gas Processors Association, 1978 (cited on p. 172).

[52] B. H. Sage, B. L. Hicks, and W. N. Lacey. “Phase Equilibria in Hydrocarbon Systems: The Methane–*n*-Butane System in the Two-Phase Region”. *Industrial & Engineering Chemistry* 32.8 (1940), pp. 1085–1092 (cited on pp. 176, 177).

[53] R. L. Schmidt, J. C. Randall, and H. Lawrence Clever. “The Surface Tension and Density of Binary Hydrocarbon Mixtures: Benzene–*n*-Hexane and Benzene–*n*-Dodecane”. *The Journal of Physical Chemistry* 70.12 (1966), pp. 3912–3916 (cited on pp. 185, 189, 213, 214).

[54] K. N. Seneviratne, T. J. Hughes, M. L. Johns, K. N. Marsh, and E. F. May. “Surface Tension and Critical Point Measurements of Methane + Propane Mixtures”. *The Journal of Chemical Thermodynamics* 111 (2017), pp. 173–184 (cited on pp. 187, 193, 195).

[55] N. Shardt and J. A. W. Elliott. “A Model for the Surface Tension of Dilute and Concentrated Binary Aqueous Mixtures as a Function of Composition and Temperature”. *Langmuir* 33 (2017), pp. 11077–11085 (cited on p. 237).

[56] N. Shardt and J. A. W. Elliott. “Isobaric Vapor–Liquid Phase Diagrams for Multicomponent Systems with Nanoscale Radii of Curvature”. *Journal of Physical Chemistry B* 122.8 (2018), pp. 2434–2447 (cited on pp. 243, 244).

[57] J. Shim and J. P. Kohn. “Multiphase and Volumetric Equilibria of Methane–*n*-Hexane Binary System at Temperatures between -110 ° and 150 °C”. *Journal of Chemical & Engineering Data* 7.1 (1962), pp. 3–8 (cited on pp. 176, 177).

[58] L. M. Shipman and J. P. Kohn. “Heterogeneous Phase and Volumetric Equilibrium in the Methane–*n*-Nonane System”. *Journal of Chemical & Engineering Data* 11.2 (1966), pp. 176–180 (cited on pp. 176, 178).

[59] S. Srivastan, N. A. Darwish, K. A. Gasem, and R. L. Robinson. “Solubility of Methane in Hexane, Decane, and Dodecane at Temperatures from 311 to 423 K and Pressures to 10.4 MPa”. *Journal of Chemical & Engineering Data* 37.4 (1992), pp. 516–520 (cited on pp. 176, 178).

[60] G. L. Stegemeier, B. F. Pennington, E. B. Brauer, and E. W. Hough. “Interfacial Tension of the Methane–normal Decane System”. *SPE Journal* 2.3 (1962), pp. 257–260 (cited on pp. 188, 204, 205).

[61] S. Sugden. “The Variation of Surface Tension with Temperature and Some Related Functions”. *Journal of the Chemical Society* 125 (1923), pp. 32–41 (cited on p. 184).

[62] S. K. Suri and V. Ramakrishna. “Surface Tension of Some Binary Liquid Mixtures”. *The Journal of Physical Chemistry* 72.9 (1968), pp. 3073–3079 (cited on pp. 189, 235, 236).

[63] P. I. C. Teixeira, B. S. Almeida, M. M. Telo da Gama, J. A. Rueda, and R. G. Rubio. "Interfacial Properties of Mixtures of Molecular Fluids: Comparison Between Theory and Experiment; Methyl Iodide + Carbon Tetrachloride and Acetonitrile + Carbon Tetrachloride". *The Journal of Physical Chemistry* 96.21 (1992), pp. 8488–8497 (cited on pp. 185, 189, 218, 219).

[64] S. Vitu, R. Privat, J. N. Jaubert, and F. Mutelet. "Predicting the Phase Equilibria of CO_2 + Hydrocarbon Systems with the PPR78 Model (PR EOS and kij Calculated Through a Group Contribution Method)". *Journal of Supercritical Fluids* 45.1 (2008), pp. 1–26 (cited on p. 179).

[65] H. G. Warren and E. W. Hough. "Interfacial Tension of the Methane–normal Heptane System". *SPE Journal* 10.4 (1970), p. 327 (cited on pp. 187, 201, 202).

[66] C. F. Weinaug and D. L. Katz. "Surface Tensions of Methane–Propane Mixtures". *Industrial & Engineering Chemistry* 35 (1943), pp. 239–246 (cited on pp. 186, 187, 193, 194).

[67] V. Wichterle and R. Kobayashi. "Vapor–Liquid Equilibrium of Methane–Ethane System at Low Temperatures and High Pressures". *Journal of Chemical & Engineering Data* 17.1 (1972), pp. 9–12 (cited on pp. 176, 177).

[68] G. M. Wilson. "A Modified Redlich–Kwong Equation of State, Application to General Physical Data Calculations". In: *65th National AIChE Meeting*. 1969 (cited on p. 173).

[69] C. Wohlfarth and B. Wohlfarth. "Binary Mixtures: Data". In: *Surface Tension of Pure Liquids and Binary Liquid Mixtures*. Ed. by M. D. Lechner. Springer, 1997 (cited on pp. 185, 189, 215–217, 235, 237).

[70] A. Zolghadr, M. Escrochi, and S. Ayatollahi. "Temperature and Composition Effect on CO_2 Miscibility by Interfacial Tension Measurement". *Journal of Chemical & Engineering Data* 58.5 (2013), pp. 1168–1175 (cited on pp. 188, 228, 229).